Intrathecal antibody delivery in health and disease: distribution, osmotic enhancement, and receptor-mediated transport in normal rodents and brain cancer models

By
Michelle E. Pizzo

A dissertation submitted in partial fulfillment of the requirements for the degree of

Doctor of Philosophy
(Pharmaceutical Sciences)

at the
University of Wisconsin-Madison
2018

Date of final oral examination: 10 May 2018

The dissertation is approved by the following members of the Final Oral Committee:
Robert G. Thorne, Assistant Professor, Pharmaceutical Sciences
Ronald Burnette, Professor, Pharmaceutical Sciences
Zsuzsanna Fabry, Professor, Department of Pathology and Laboratory Medicine
M. Elizabeth Meyerand, Professor, Biomedical Engineering
Jamey Weichert, Associate Professor, Radiology

"If I have seen further, it is by standing upon the shoulders of giants."

- Sir Isaac Newton

This thesis is dedicated to the exceptional scientists who came before me, leaving a vast treasure trove of exciting things to discover. I was led on numerous exhilarating adventures to find manuscripts from the 1800s and beautiful hand drawings of original studies (see images from His in 1865 below). I spent many hours on Google translating papers into English, often from the long-ago work of German anatomists or the occasional (and more challenging to translate) French or Japanese study. I am incredibly thankful for their valuable contributions.

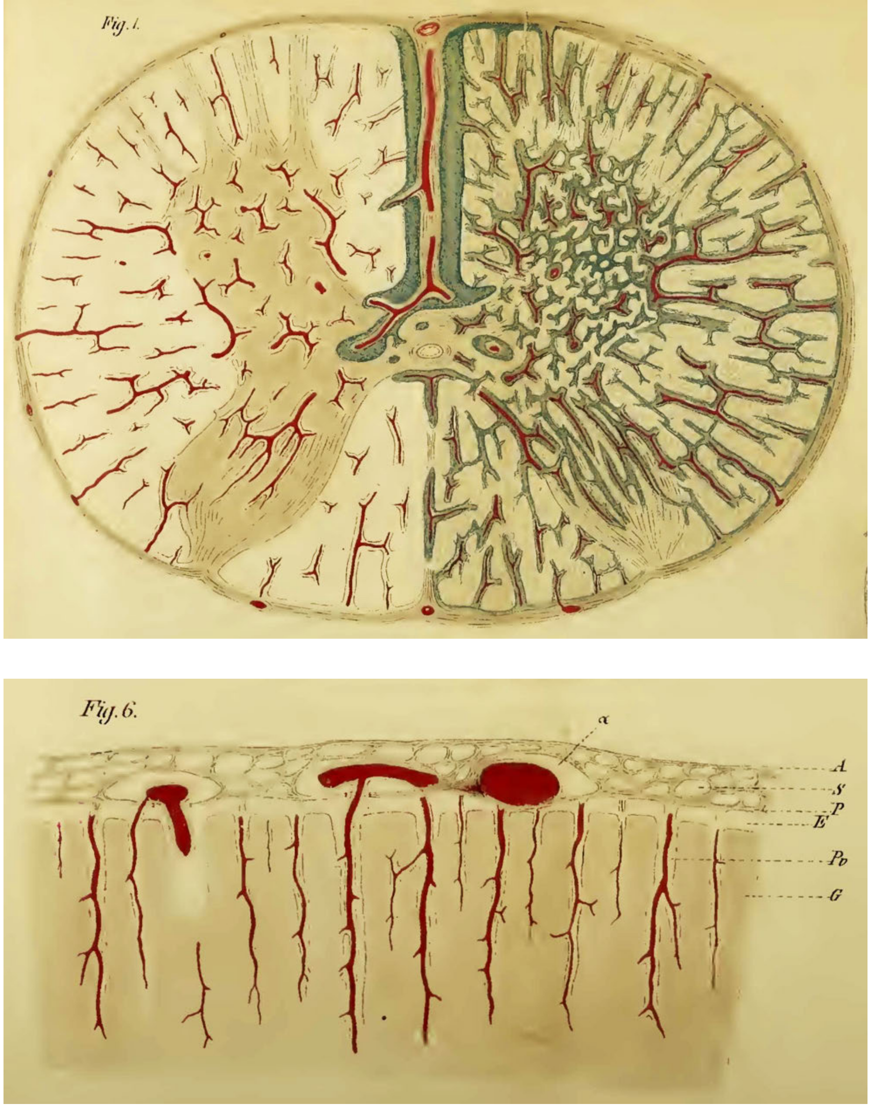

Images of the perivascular spaces around blood vessels by Swiss anatomist Wilhelm His, Sr., the first to attribute a lymphatic role to the perivascular spaces (1865).

Acknowledgments

Completing a PhD is never possible without the help of countless people, but I would first like to thank my advisor, Prof. Robert Thorne, for his continuous guidance and ceaseless support. He is truly an advocate for his students, has a contagious enthusiasm, and pursues science with incredible zeal and integrity. I will forever be grateful for his endless encouragement. I would also like to thank the members of my thesis committee who provided exceptionally helpful advice and wonderful support for myself and this work: Prof. Ronald Burnette, Prof. Zsuzsanna Fabry, Prof. Elizabeth Meyerand, and Prof. Jamey Weichert.

I owe much gratitude to the members of the Thorne Lab who helped me immensely over the years; to former lab members Dr. Jeff Lochhead and Dr. Daniel Wolak for training and guiding me when I was just starting out (and knew quite little), to my classmate Niyanta Kumar with whom I experienced the entirety of grad school (relying on each other got us both through and made it an enjoyable time), to our junior graduate students, Geetika Nehra and Brynna Wilken-Resman who were both a joy to train and work with (I wish you both the best of luck), and to our undergraduate student Gretchen Greene who was always a smiling face and was eager to help with any task (and is bound for great things). I will dearly miss the great times we shared, log-rolling or otherwise.

The scientific work would not be possible without the help of our numerous collaborators. Beth Meyerand and Christina Brunnquell provided critical guidance as to the design of the magnetic resonance imaging studies, helped to determine optimal imaging acquisition parameters, and provided tools for registration of the images; Danica Stanimirovic and Eric Brunette provided and characterized the labeled single-domain antibody for our studies; Lydia Sorokin and Melanie

Hannocks partnered with us to characterize the perivascular spaces (providing critical tools and ideas and arranging for the opportunity for Robert and I to travel to Muenster, Germany to conduct experiments); Joan Abbott collaborated with us and the Sorokin lab and provided incredibly valuable guidance, discussion of ideas, and knowledge; John Kuo and Paul Clark partnered with us to study brain cancer and provided the glioma model; and Sarah Gong and Guojun Chen provided and characterized the unique dual-labeled nanoparticles.

Additionally, a number of people and facilities have shared their equipment and resources with us for these studies including: Arash Bashirullah and Michael Taylor kindly allowed us significant use of their confocal microscopes, the UW Carbone Cancer Center Small Animal Imaging Facility provided MRI acquisition support, and the Biological & Biomaterials Preparation, Imaging, and Characterization Laboratory assisted with processing scanning electron microscopy samples.

Last but most importantly, I would not be where I am today without the support of my family and friends. My parents Keith and Becky Kropf and my sister Sarah Neet provided the utmost love and support for me and my career and never failed to provide encouragement. My wonderful and unbelievably intelligent husband Vincent Pizzo is always there for me (he moved all the way to chilly Wisconsin for me, and will move for me again!); he also served as my primary code-debugger, helping me (and everyone else in the lab) automate menial tasks. Additionally, my fantastic in-laws have been incredibly supportive and are more than excited for our next step.

Abstract

Communication between the cells and fluids of the central nervous system (CNS) is incredibly complex and poorly understood, which has contributed to a paucity of CNS drugs. Despite the relatively limited understanding of drug transport between the cerebrospinal fluid (CSF) and the brain, there are currently three FDA-approved non-small molecule drugs delivered into the CSF for treatment of CNS disorders. Thus, there is a critical need to improve our knowledge of CSF-to-brain transport mechanisms for macromolecule drugs (e.g., antibodies) to aid in interpretation of results from clinical trials.

In the present study, we demonstrated two main mechanisms of CSF-to-brain transport following infusion into the CSF of rats: (i) slow, size-dependent diffusion at brain-CSF interfaces in the brain's extracellular spaces and (ii) rapid, relatively size-independent transport along the cerebral perivascular spaces. We demonstrated using intrathecal infusion of labeled single-domain antibody fragments (4.5 nm), full-length goat IgG (10 nm), and dual-labeled nanoparticles (13.5 nm) that access to the perivascular spaces was size-dependent and could be enhanced for goat IgG by administration of intrathecal hyperosmolar mannitol. Surprisingly, species-matched rat IgG (10 nm) demonstrated extensive access to the perivascular spaces, which was attributed to Fc receptor mediated entry. These results suggested that rat IgG had a physiological role in the perivascular spaces, i.e., for surveillance of antigens. Thus we probed for endogenous rat IgG in untreated animals and revealed endogenous IgG was predominantly localized to CSF interfaces and perivascular spaces, suggesting that rat IgG under physiological conditions *in vivo* utilizes the perivascular pathways extensively for transport into the brain. However, in a primary rat model of glioma intrathecal infusion of rat IgG failed to access the tumor and there was a significant, global reduction in rat IgG access to the perivascular spaces. Altogether, these results illuminate the mechanisms and pathways of macromolecule transport between the CSF and brain and suggest that rapid perivascular transport is likely to provide substantial delivery to the larger human brain. However, size-dependent CSF-to-brain sieving of molecules may significantly hamper distribution of large therapeutic substances, e.g., gene therapy vectors or species-mismatched antibodies and may require strategies to enhance access.

TABLE OF CONTENTS

Dedication .... *i*

Acknowledgements .... *ii-iii*

Abstract .... *iv-v*

Prologue .... *ix-xxxiii*

Prologue Figures .... *xxvi-xxxiii*

CHAPTER 1: THE EXTRACELLULAR AND PERIVASCULAR SPACES OF THE BRAIN ... 1-26

Abstract *2*

Components of the central nervous system (CNS) *2*

The ventricular system and CSF *4*

The extracellular space *6*

Conclusions *15*

Figures *22*

CHAPTER 2: INTRATHECAL ANTIBODY DISTRIBUTION IN THE RAT BRAIN: SURFACE DIFFUSION, PERIVASCULAR TRANSPORT, AND OSMOTIC ENHANCEMENT OF DELIVERY 27-100

Key Points *28*

Abstract *28*

Introduction *29*

Materials and Methods *34*

Results *44*

Discussion *53*

Translational Perspective *70*

Figures *78*

CHAPTER 3: THE ROLE OF BRAIN BARRIERS IN FLUID MOVEMENT IN THE CNS – IS THERE A 'GLYMPHATIC' SYSTEM? 101-151

Abstract *102*

Introduction *103*

History of CSF generation and flow *104*

Pulsatile flow of CSF *106*

The need for CSF – brain ISF exchange *108*

Blood vessels and the perivascular space *110*

Historical considerations: CSF/ISF exchange & flow along low-resistance pathways including the PVS *112*

The 'glymphatic' system: original hypothesis & critical appraisal *115*

Diffusion or flow of the ISF in the brain ECS? *119*

A sieving effect of perivascular astrocyte endfeet? *121*

"ISF bulk flow" *124*

CSF and ISF compartmentalization & drainage pathways *125*

Practical and Clinical Implications of ISF/CSF interaction *126*

CNS pathologies and disturbances of brain fluids *129*

Epilepsy, brain trauma, phosphorylated tau, and enlarged perivascular spaces *131*

Conclusions *133*

Figures *146*

CHAPTER 4: PERIVASCULAR ACCESS OF INTRATHECAL ANTIBODIES TO THE RAT BRAIN IS RECEPTOR-MEDIATED AND IS REDUCED IN A MODEL OF GLIOMA 152-213

Abstract *153*

Introduction *153*

Materials and Methods *157*

Results *166*

Discussion *177*

Conclusions *188*

Figures *195*

CHAPTER 5: ENDOGENOUS IMMUNOGLOBULIN G (IgG) AND ALBUMIN DISTRIBUTION IN THE RODENT BRAIN REVEALS STRIKING DIFFERENCES: IgG IS RESTRICTED TO PERIVASCULAR PATHWAYS AND ALBUMIN IS WIDESPREAD...................................... 214-250

Abstract.. 215

Introduction... 215

Materials and Methods 221

Results... 223

Discussion 226

Conclusions... 236

Figures 243

CHAPTER 6: DUAL-LABELED NANOPARTICLES ALLOW FOR CORRELATIVE IN VIVO MAGNETIC RESONANCE AND EX VIVO FLUORESCENCE IMAGING FOLLOWING INTRATHECAL INFUSION IN RATS 251-289

Abstract.. 252

Introduction... 253

Materials and Methods 254

Results... 262

Discussion 267

Conclusions... 275

Figures 280

EPILOGUE 290-302

Prologue

Michelle Pizzo

Disorders of the central nervous system (comprised of the brain, spinal cord, and encompassed fluids) have been historically difficult to treat due to a lack of successful drugs (Kaitin & Milne, 2011). Several factors likely contribute to the dismal success rate, including off-target side effects (particularly when drugs are administered systemically), a poor pre-clinical to clinical translation (due to species-differences in physiology and size), a lack of knowledgeable biomarkers for gauging the efficacy of drugs once in clinical trials, and most critically, a poor understanding of the brain and its compartments, their communication, and the barriers to drug delivery (Thorne, 2014*a*). The seemingly greatest obstacles to CNS drug delivery are the blood-brain barrier (BBB) and the blood-cerebrospinal fluid (CSF) barriers (BCSFBs), formed by specialized cells joined by tight junctional complexes which exhibit very low rates of transport (Abbott *et al.*, 2006). This excludes most therapeutics from the CNS, whether they are small molecule therapeutics or larger biologics.

Biologics, so-called because they are produced by living organisms, are a highly-promising group of therapeutics for both CNS and non-CNS disease; biologics include peptide and protein therapies (e.g., enzymes and antibodies), nucleotide therapies (e.g., RNA- and DNA-based drugs), viral vectors, and cell therapies. These therapeutics range in size from 1-10 nm for peptides, proteins, and oligonucleotides (Bloomfield *et al.*, 2000; Syková & Nicholson, 2008; Wolak & Thorne, 2013; Wolak *et al.*, 2015) to 20-300 nm for viruses (Davidson & Breakefield, 2003) to 10-30 μm for cell therapies (Hoogduijn *et al.*, 2013), as compared to most small-molecule drugs which are less than approximately 1 nm in size (<1000 Da)(Macielag, 2012). There are over 130 FDA-approved protein and peptide drugs (including full-length antibodies (structure detailed in Fig. 1), antibody fragments, and antibody fusion proteins), which are extremely promising due to their high specificity (and thus, fewer off-target side effects), exceptional potency, and improved tolerability in the body (Leader *et al.*, 2008). Antibody therapies in particular are consistently among the top grossing drugs each year—indeed, six of the top ten drugs were antibodies in 2017 with total sales of $51 billion dollars (Urquhart, 2018), attributed in part to their high cost of production.

However, most biologics are unable to cross the BBB or BCSFBs in sufficient amounts (Abbott et al. 2006; Begley et al. 2008; Calias et al. 2014; Davson and Segal 1995) due to their large size and hydrophilic nature. This illuminates the need for alternative CNS delivery approaches, e.g., non-invasive intranasal administration (Thorne *et al.*, 2004, 2008; Lochhead & Thorne, 2012), invasive delivery directly into the brain parenchyma (e.g., convection enhanced delivery (Bobo *et al.*, 1994)), or semi-invasive administration into the CSF (the focus of the present work). However, even if central access is achieved we still possess an inadequate understanding of the transport limitations imposed by the complex cellular and fluid environment of the brain (Syková and Nicholson 2008; Wolak et al. 2015)—the 'barrier beyond the barrier'. Thus, an improved understanding of the CSF-to-brain distribution mechanisms for these large therapeutics is critically needed because CSF delivery of biologics is ongoing in children and adults (Calias et al. 2014, clinicaltrials.gov), without a clear picture of drug disposition in the brain, the transport limitations, or the mechanisms driving the distribution.

Possible routes of CSF administration include lumbar intrathecal, cisternal intrathecal, or intracerebroventricular (into the lateral, third, or fourth ventricles in the brain's interior)(see (Greenberg, 2010; Schuenke *et al.*, 2010)). Intrathecal lumbar administration can be achieved by direct injection/infusion into the lumbar spinal subarachnoid (CSF) space or by implantable devices which may include a subcutaneous refillable access port (e.g., Soph-a-port Mini S device (clinicaltrials.gov) or Port-a-cath II (Muenzer *et al.*, 2015) in intrathecal trials for lysosomal storage disorders). Catheters can also be inserted at the lumbar level and threaded through the spinal subarachnoid space toward the cranium. Intrathecal cisternal administration can be achieved by direct injection/infusion into the CSF of the cisterna magna; intracisternal administration is often used pre-clinically but is rarely used in humans due to its close proximity to the brainstem (which is critically important for vital functions). Intracerebroventricular administration is generally achieved using an implanted cannula that extends through the skull and brain tissue into the ventricular compartment and is attached to a refillable reservoir fixed to the skull that can be accessed subcutaneously (called an Ommaya reservoir (Ommaya, 1984; Kramer *et al.*, 2007) or Rickham device (Rickham, 1964)). A recent study reviewed the safety and usage of intracerebroventricular devices in patients and suggested that it is a reasonable long-term drug delivery strategy (Cohen-Pfeffer *et al.*, 2017). Additionally, therapeutics can also be administered directly into a surgically created resection cavity following removal of a brain tumor (placed during the time of surgery or after via an inserted catheter; see clinicaltrials.gov).

CSF administration is of increasing clinical interest for delivery of biologics to the CNS because it bypasses the BBB and BCSFBs (Tables 1 and 2, Fig. 2). There are currently over 130 clinical trials administering non-small molecule therapeutics via the CSF (clinicaltrials.gov). Approximately 57 trials are administering proteins and peptides (e.g., 8 peptides, 9 proteins, 20 lysosomal enzymes, and 20 antibodies) for CNS disorders including pain, lysosomal storage disorders, and primary/metastatic CNS cancer; approximately 15 trials are for gene therapy vectors (13 antisense oligonucleotide and 2 adeno-associated virus trials) primarily for spinal muscular atrophy; and approximately 62 trials are for stem cells (mostly autologous or umbilical cord blood derived) predominantly for treatment of CNS injuries.

Table 1. Clinical trials administering peptide and protein drugs into the CSF.

NCT Number	Conditions	CSF biologic[a]	Phase
NCT00002752	Brain and CNS Tumors | Metastatic Cancer	^{131}I-81C6 Neuradiab*	1
NCT00003484	Brain and CNS Tumors | Neuroblastoma	^{131}I-81C6 Neuradiab*	1
NCT00906516	Brain Tumors	^{131}I-81C6 Neuradiab*	2
NCT00615186	Glioblastoma Multiforme	^{131}I-81C6 Neuradiab	3
NCT00003461	Brain and CNS Tumors | Metastatic Cancer | Neuroblastoma	^{131}I-81C6 Neuradiab*	1/2
NCT00089245	Brain and CNS Tumors | Neuroblastoma | Sarcoma	^{131}I-8H9 Burtomab	1
NCT03275402	Neuroblastoma | CNS Metastases | Leptomeningeal Metastases	^{131}I-8H9 Burtomab	2/3
NCT00003022	Brain and CNS Tumors	^{131}I-3F8	1
NCT00445965	Brain and CNS Tumors	^{131}I-3F8	2
NCT00058370	Brain and CNS Tumors	^{131}I-3F8	-
NCT00406016	Acute Spinal Cord Injury	Anti-NogoA mAb	1
NCT00003020	Brain and CNS Tumors	B3(Fv)-PE38	1
NCT03233152	Glioblastoma	Ipilimumab*	1
NCT00002754	Brain and CNS Tumors | Melanoma | Metastatic Cancer	Me1-14 F(ab')$_2$*	1
NCT00002751	Metastatic Cancer	Me1-14 F(ab')$_2$	1/2
NCT03025256	Melanoma | Leptomeningeal Disease	Nivolumab	1/1b
NCT00210340	B cell Lymphoma	Rituximab	1
NCT00221325	CNS Lymphoma | Intraocular Lymphoma	Rituximab	1
NCT00416923	Brain and CNS Tumors | Lymphoma	Rituximab	1
NCT02253264	Primary/Secondary Progressive Multiple Sclerosis	Rituximab	1
NCT01719159	Progressive Multiple Sclerosis	Rituximab	2
NCT02545959	Multiple Sclerosis, Chronic Progressive	Rituximab	2
NCT00244361	Opsoclonus-myoclonus Syndrome	Rituximab	1/2
NCT01212094	Multiple Sclerosis	Rituximab	1/2
NCT01596127	Leukemia | Lymphoid Malignancies | Leptomeningeal metastases	Rituximab	1/2
NCT02774421	Posterior Fossa Ependymoma	Trastuzumab	1
NCT01325207	HER2 Positive Metastatic Breast Cancer	Trastuzumab	1/2
NCT01373710	HER2 Positive Metastatic Breast Cancer	Trastuzumab	1/2
NCT02598427	HER2 Positive Metastatic Breast Cancer	Trastuzumab/Pertuzumab	1
NCT01907087	Late-Infantile Neuronal Ceroid Lipofuscinosis Type 2 (CLN2/Batten)	Cerliponase alfa	1/2
NCT02485899	Late-Infantile Neuronal Ceroid Lipofuscinosis Type 2 (CLN2/Batten)	Cerliponase alfa	1/2
NCT02963350	Late-Infantile Neuronal Ceroid Lipofuscinosis Type 2 (CLN2/Batten)	Cerliponase alfa	EAP
NCT02678689	Late-Infantile Neuronal Ceroid Lipofuscinosis Type 2 (CLN2/Batten)	rhTPP1	2

NCT02232477	Mucopolysaccharidosis I (Hurler Syndrome)	Iduronidase	-
NCT00215527	Mucopolysaccharidosis I (Hurler Syndrome)	Laronidase	1
NCT00638547	Mucopolysaccharidosis I (Hurler Syndrome)	Laronidase	1
NCT00786968	Mucopolysaccharidosis I (Hurler Syndrome)	Laronidase	1
NCT00852358	Mucopolysaccharidosis I (Hurler Syndrome)	Laronidase	-
NCT00920647	Mucopolysaccharidosis II (Hunter Syndrome)	Idursulfase-IT	1/2
NCT01506141	Mucopolysaccharidosis II (Hunter Syndrome)	Idursulfase-IT	1/2
NCT02055118	Mucopolysaccharidosis II (Hunter Syndrome)	Idursulfase-IT	2/3
NCT02412787	Mucopolysaccharidosis II (Hunter Syndrome)	Idursulfase-IT	2/3
NCT01510028	Metachromatic Leukodystrophy (MLD)	rhARSA	1/2
NCT01887938	Metachromatic Leukodystrophy (MLD)	rhARSA	1/2
NCT02060526	Mucopolysaccharidosis IIIA (Sanfilippo A)	rhHNS	2
NCT02350816	Mucopolysaccharidosis IIIA (Sanfilippo A)	rhHNS	2
NCT01155778	Mucopolysaccharidosis IIIA (Sanfilippo A)	rhHNS	1/2
NCT01299727	Mucopolysaccharidosis IIIA (Sanfilippo A)	rhHNS	1/2
NCT02754076	Mucopolysaccharidosis IIIB	rhNAGLU	1/2
NCT01996605	Healthy Volunteers (Hyperalgesia and Allodynia)	Oxytocin	2
NCT02100956	Neuropathic Pain	Oxytocin	2
NCT00996983	Pain | Neuropathic Pain | Intractable / Cancer Pain	Ziconotide	2
NCT00047749	Pain	Ziconotide	3
NCT00076544	Pain	Ziconotide	3
NCT01373983	Peripheral Neuropathy	Ziconotide	4
NCT01992562	Painful Myelopathy | Painful Neuropathy	Ziconotide	4
NCT01888120	Severe Chronic Pain	Ziconotide	-
NCT02193334	Spinal Cord Injuries	KP-100IT HGF	1/2
NCT01999803	Amyotrophic Lateral Sclerosis	rhVEGF	1
NCT02269436	Amyotrophic Lateral Sclerosis	rhVEGF	1
NCT00800501	Amyotrophic Lateral Sclerosis	rhVEGF	1/2
NCT01384162	Amyotrophic Lateral Sclerosis	rhVEGF	1/2
NCT01829867	Parkinson's Disease	rhPDGF-BB	1
NCT01807338	Parkinson's Disease	rhPDGF-BB	-
NCT00866502	Parkinson's Disease	rhPDGF-BB	1/2
NCT02408562	Parkinson's Disease	rhPDGF-BB	1/2

[a] Abbreviations: Nogo-A mAb (neurite outgrowth inhibitor-A monoclonal antibody); Fv (fragment variable region of an antibody); rhARSA (recombinant human arylsulfatase A); rhHNS (recombinant human heparan-N-sulfatase); rhNAGLU (recombinant human α-N-acetylglucosaminidase); rhTPP1 (recombinant human tripeptidyl peptidase-1); HGF (hepatocyte growth factor); rhVEGF (recombinant human vascular endothelial growth factor); rhPDGF-BB (recombinant human platelet-derived growth factor-BB). *Administration into a surgically-created resection cavity following tumor resection. The table is roughly divided into sections by antibodies, enzymes, peptides, and proteins.

Despite the vast number trials for CNS drug delivery **there are only three approved biologics that actually act directly in the CNS—and all three are delivered into the CSF** (Pizzo *et al.*, 2018). These include: **ziconotide**, a 2.6 kDa peptide delivered via lumbar intrathecal infusion approved in 2004 for chronic pain (Jazz Pharmaceuticals, 2004), **nusinersen**, a 7.5 kDa antisense oligonucleotide delivered via lumbar intrathecal injection approved in 2016 for spinal muscular atrophy (Biogen, 2016), and **cerliponase alfa**, a 66 kDa enzyme delivered via intracerebroventricular infusion approved in 2017 for late infantile neuronal ceroid lipofuscinosis type 2 (CLN2) (BioMarin Pharmaceuticals, 2017). CLN2 is unarguably a whole-brain disease for which delivery of the enzyme to every cell is desired; preclinical studies have generally reported pharmacodynamic responses and increased survival (Xu *et al.*, 2011; Vuillemenot *et al.*, 2015), but the whole-brain distribution and potential association with perivascular spaces have not been well-described. This is why preclinical studies of the *mechanisms* for macromolecule delivery in the brain are of the utmost importance for understanding the potential translatability and scalability of intrathecal therapy.

Table 2. Clinical trials of CSF-administered antisense oligonucleotides and gene therapy vectors.

NCT Number[a]	CNS Disorder	CSF Biologic[b]	Trial Phase
NCT01494701	Spinal Muscular Atrophy	ASO (Nusinersen)	1
NCT01703988	Spinal Muscular Atrophy	ASO (Nusinersen)	1/2
NCT01780246	Spinal Muscular Atrophy	ASO (Nusinersen)	1
NCT01839656	Spinal Muscular Atrophy	ASO (Nusinersen)	2
NCT02052791	Spinal Muscular Atrophy	ASO (Nusinersen)	1
NCT02193074	Spinal Muscular Atrophy	ASO (Nusinersen)	3
NCT02292537	Spinal Muscular Atrophy	ASO (Nusinersen)	3
NCT02386553	Spinal Muscular Atrophy	ASO (Nusinersen)	2
NCT02462759	Spinal Muscular Atrophy	ASO (Nusinersen)	2
NCT02594124	Spinal Muscular Atrophy	ASO (Nusinersen)	3
NCT02865109	Spinal Muscular Atrophy	ASO (Nusinersen)	-
NCT02519036	Huntington's Disease	ASO (HTTRx / RG6042)	1/2
NCT02362438	Giant Axonal Neuropathy	scAAV9/JeT-GAN	1
NCT01041222	Familial Amyotrophic Lateral Sclerosis	ASO (SOD1)	1
NCT02725580	Batten Disease (CLN6)	scAAV9.CB.CLN6	1/2

[a] See clinicaltrials.gov for more information. [b] Abbreviations: ASO (antisense oligonucleotide); scAAV9/JeT-GAN (self-complementary AAV serotype 9 vector carrying a codon-optimized human GAN transgene controlled by the minimal synthetic JeT promoter; see (Bailey *et al.*, 2015)); SOD1 (superoxide dismutase 1); scAAV9.CB.CLN6 (self-complementary AAV9 carrying the CLN6 gene under the control of a hybrid CMV enhancer/chicken-β-actin promoter).

The first chapter of this thesis will describe the general components of the CNS—the brain cells, vasculature, and fluids (interstitial fluid and CSF). The anatomical compartments of greatest focus include the **extracellular space** (ECS), i.e., the narrow 40-60 nm (Thorne & Nicholson, 2006) fluid- and matrix-filled spaces between the cells of the brain, and the 5-10 μm **perivascular space** (PVS), i.e., the tubular fluid- and connective tissue-filled spaces between the blood vessels and the brain tissue. The narrow and tortuous ECS is thought to limit transport of molecules through the brain parenchyma to diffusion—slow, size-dependent movement of molecules along a concentration gradient (Syková & Nicholson, 2008; Wolak & Thorne, 2013). However, the much larger PVS is thought to allow for substantially faster transport by convective flow (Cserr *et al.*, 1977; Szentistványi *et al.*, 1984; Iliff *et al.*, 2012) or dispersion (Asgari *et al.*, 2016) due to its significantly higher hydraulic conductivity compared to the ECS (Wolak & Thorne, 2013).

The second chapter investigates the CSF-to-brain distribution of two proteins infused into the CSF of rats using *ex vivo* fluorescence microscopy and *in vivo* magnetic resonance imaging (MRI). Our interest in macromolecule therapeutic distribution within the brain is in part due to the unique transport phenomena they will likely experience because of their large size. Thus, we first probed the **size-dependent transport differences** between a fluorescently-labeled **single-domain antibody fragment** (4.5 nm) and a fluorescently-labeled or MRI contrast agent-labeled **full-length immunoglobulin G** (IgG; species-mismatched goat or bovine IgG) antibody (10 nm); all antibodies were non-targeted and were not expected to have significant binding within the rat brain. Numerous pilot studies were first performed to develop an MRI-compatible method for intracisternal infusion in normal rats (detailed in Fig. 3). Importantly, we also carefully considered the flow rate at which to infuse the antibodies so as to minimize perturbations to the compartment, which could alter the normal transport mechanisms within the CNS. Ultimately, we decided on a rate of 1.6 μL/min for intrathecal infusion in rats because it is approximately half the rat CSF production rate (see Table 3 for CSF physiological parameters) and has demonstrated negligible alterations to intracranial pressure in rats (Yang *et al.*, 2013; Bedussi *et al.*, 2017). We demonstrated that transport of both antibodies was consistent with diffusion into the brain surface from the CSF but was limited to < 1 mm depth of penetration. This superficial penetration would be expected to be similar to the penetration in larger human brains because diffusion in the brain is the same across species, attributed to the highly-conserved extracellular volume fraction of the brain (Nicholson & Syková, 1998; Nicholson, 2001; Syková & Nicholson, 2008).

Table 3. CSF physiological parameters in the human, rat, and mouse.

	Human	**Rat**	**Mouse**
CSF secretion rate	350-370 μL/min[a, b,c]	2.1-5.4 μL/min[c,f]	0.33-0.38 μL/min[c]
CSF clearance rate	16-20 mL/hr[a]		
% per minute (turnover time)	0.3-0.4 (6-7 hrs)[a,b,c]	0.7-1.7 (1-2.5 hrs)[c]	0.9 (2 hrs)[c]
Total CSF volume	140-150 mL[a,b]	200-300 μL[c,d]	37-40 μL[c]
SAS CSF	~115 mL[a]	190 μL[d]	
Ventricular CSF	~25 mL[a]	10-12 μL[d]	
Intracranial Pressure	65-195 mmH$_2$0[a]	~56 mmH$_2$0[e]	

[a]Laterra & Goldstein, 2012; [b]Nicholson, 1999; [c]Davson & Segal, 1995; [d]Fenstermacher *et al.*, 1999; [e]Barth *et al.*, 1992; [f]Cserr, 1965. See also (Thorne, 2014*b*). SAS: subarachnoid space.

We also observed rapid transport along the PVS for both antibodies revealing a relatively size-independent mechanism (i.e., convection or dispersion), but limited *access* of the larger goat IgG to the PVS demonstrated a size-dependent *entry* into the PVS. This CSF-to-brain sieving was hypothesized to be caused by **pores or 'stomata' in leptomeningeal cells** (and/or their associated connective tissue) ensheathing blood vessels on the surface of the brain. These leptomeningeal cells separate the CSF from the PVS creating an apparently semi-permeable barrier. However, an **osmotic enhancement strategy** (intrathecal infusion of mannitol) **improved IgG entry into the PVS,** presumably by manipulation of leptomeningeal cells (Fig. 4). We also show that both antibodies are cleared from the CNS along previously described lymphatic drainage pathways via the olfactory nerves to reach the nasal mucosa and cervical lymph nodes.

The third chapter reviews older studies and recent work that have demonstrated **agreement or disagreement with components of the 'glymphatic' hypothesis** proposed by Nedergaard, Iliff, and colleagues (Iliff *et al.*, 2012; Nedergaard, 2013; Jessen *et al.*, 2015). The 'glymphatic' hypothesis involves three main steps of transport with a suggested lymphatic-like role for the brain: i) influx of CSF-borne tracers along the PVS of arteries, ii) a transparenchymal flow through the narrow ECS facilitated by the aquaporin-4 water channel on glial (astrocyte) endfeet (hence the name glial + lymphatic → 'glymphatic'), and iii) efflux of tracers (and/or brain waste) along the PVS of veins. A substantial amount of experimental and modeling evidence opposes the idea of flow through the narrow ECS (see discussion in (Abbott *et al.*, 2018)) and recent studies attempting to replicate the involvement of aquaporin 4 failed to do so (Smith *et al.*, 2017). However, there is a general consensus in the field that the perivascular spaces indeed allow for rapid transport of CSF-borne molecules into the brain, though the direction of transport and precise anatomical compartments involved are controversial.

The fourth chapter reveals **species-specific** antibody transport into the brain. Using the same infusion paradigm, a species-matched rat IgG (structure detailed in Fig. 1) was intrathecally-infused into normal rats. Despite the ability of rat IgG to rapidly and reversibly bind to receptors in the rat brain (which our lab has demonstrated *slows* IgG transport within the ECS; Wolak et al. *unpublished*), **rat IgG showed exceptional and widespread entry into the perivascular spaces**. Rat IgG accessed significantly more perivascular spaces than the goat IgG used previously and competition by an excess of unlabeled IgG prevented widespread access to the PVS, suggesting an **Fc receptor-mediated transcytosis of IgG into the PVS** (Fig. 5). Additionally, rat IgG was also infused into **rats bearing primary brain tumors** and showed an inability to deliver IgG to the tumor and a **widespread reduction in perivascular transport**. This striking result requires further investigation to assess the causes but is an alarming outcome considering the number of clinical trials ongoing using intrathecal antibodies for treatment of brain cancer.

The fifth chapter investigates antibody transport in the brain by probing for ***endogenous*** **rat IgG and albumin** (among the most abundant proteins in the CSF (Davson & Segal, 1995)) in untreated rats. We hypothesized that the receptor-mediated transport of intrathecal rat IgG into the PVS represented a likely transport pathway for endogenous IgG to survey the brain for antigens, as the PVS is a known route for surveillance by immune cells (Fabry *et al.*, 2008; Ransohoff & Engelhardt, 2012; Engelhardt *et al.*, 2017). Indeed, we revealed that **endogenous IgG was predominantly localized to the PVS**, brain-CSF interfaces, and circumventricular organs. In contrast, **endogenous albumin showed a widespread distribution through the rat brain**, perhaps suggesting that albumin's smaller size allows it to diffuse throughout the brain, while IgG is restricted from entering the parenchyma and constrained to the PVS under normal conditions.

The sixth chapter reveals the CSF-to-brain distribution of **novel dual-labeled nanoparticles** (13.5 nm) infused intrathecally. *In vivo* MRI utilized the gadolinium labeling and demonstrated the kinetic profile of the nanoparticles in both parenchymal brain regions and CSF spaces. Dual-labeling with a fluorophore allowed for high resolution *ex vivo* fluorescence microscopy in the same animal after MRI. The **nanoparticles showed a limited distribution in the brain**, accessing fewer perivascular spaces compared to the 10 nm IgG, supporting the hypothesis that entry into the PVS is size-dependent. This study also illuminated that substances of this size (or greater, e.g., viral vectors) are likely to have a severely restricted distribution in the brain.

In addition to the work reported in Chapters 1-6, we also developed a method for **intracisternal withdrawal in rats**. We utilized this withdrawal technique to show that intranasally-administered matrix metalloproteinase-9 (MMP-9; thought to act as a *local* nasal permeability enhancer) did not elevate CSF levels of MMP-9 (Lochhead *et al.*, 2015). In another study we developed a method to withdraw **separate, sequential CSF fractions** every 10 minutes (by incorporation of a low dead volume HPLC valve into the setup) following intranasal administration of a radiolabeled IgG. The study revealed increasing levels in the CSF with time that reached a CSF/blood ratio of 0.016, an order of magnitude higher than with systemic administration (Kumar *et al.*, 2018; *unpublished*). We also used the withdrawal technique to determine levels of intranasally-administered perillyl alcohol in the CSF to determine if it may be crossing the BBB and if intranasal application improved brain targeting (Nehra et al., *unpublished*). We have also adapted this technique for **intrathecal infusion in mice**, which provided some technical challenges associated with the substantially smaller animal size. Preliminary studies of three different infusion rates (0.2 μL/min or 0.4 μL/min for 50 minutes, and 1 μL/min for 10 minutes) in mice showed a very limited entry of mouse IgG into the PVS (Fig. 6), in sharp contrast to rat IgG infusion in rats which demonstrated widespread, receptor-mediated perivascular access. Staining of endogenous IgG in rats and mice (Chapter 5) may suggest that this is due to species differences in endogenous IgG transport within the brain. This would indicate a significant species-difference in antibody surveillance of the brain and requires additional investigation. Additionally, we have launched an in-depth study of **Fc receptor localization** in the brain of normal rats and tumor-bearing rats to better understand their role in IgG distribution throughout the brain.

Finally, the Epilogue summarizes several key findings of this work and important implications for CNS physiology and drug delivery. It also includes a discussion of critical future experiments that would further improve our understanding of macromolecule transport in the CNS in health and disease, with the hopes of guiding interpretation of clinical trial successes and failures and improving intrathecal drug delivery.

References

Abbas AK, Lichtman AH & Pillai S (2015). *Cellular and Molecular Immunology*, 8th edn.ed. Abbas AK, Lichtman AH & Pillai S. Elsevier Saunders, Philadelphia.

Abbott NJ, Pizzo ME, Preston JE, Janigro D & Thorne RG (2018). The role of brain barriers in fluid movement in the CNS: is there a 'glymphatic' system? *Acta Neuropathol* **135,** 387–407.

Abbott NJ, Rönnbäck L & Hansson E (2006). Astrocyte-endothelial interactions at the blood-brain barrier. *Nat Rev Neurosci* **7,** 41–53.

Asgari M, de Zélicourt D & Kurtcuoglu V (2016). Glymphatic solute transport does not require bulk flow. *Sci Rep* **6,** 38635.

Bailey RM, Armao D, Nagabhushan Kalburgi S & Gray SJ (2015). Development of Intrathecal scAAV9 Gene Therapy for Giant Axonal Neuropathy. *Mol Ther* **23,** S6–S7.

Barth KN, Onesti ST, Krauss WE & Solomon RA (1992). A simple and reliable technique to monitor intracranial pressure in the rat: technical note. *Neurosurgery* **30,** 138–140.

Bedussi B, van der Wel NN, de Vos J, van Veen H, Siebes M, VanBavel E & Bakker EN (2017). Paravascular channels, cisterns, and the subarachnoid space in the rat brain: A single compartment with preferential pathways. *J Cereb Blood Flow Metab* **37,** 1374–1385.

Biogen (2016). SPINRAZA (nusinersen) injection, for intrathecal use. *Highlights Prescr Inf.*

BioMarin Pharmaceuticals (2017). BRINEURA (cerliponase alfa) injection, for intraventricular use.

Bloomfield VA, Crothers DM & Tinoco Jr. I (2000). *Nucleic Acids: Structures, Properties, and Functions*.

Bobo RH, Laske DW, Akbasak A, Morrison PF, Dedrick RL & Oldfield EH (1994). Convection-enhanced delivery of macromolecules in the brain. *Proc Natl Acad Sci U S A* **91,** 2076–2080.

Burmeister WP, Huber AH & Bjorkman PJ (1994). Crystal structure of the complex of rat neonatal Fc receptor with Fc. *Nature* **372,** 379–383.

Cloyd MW & Low FN (1974). Scanning electron microscopy of the subarachnoid space in the dog. I. Spinal cord levels. *J Comp Neurol* **153,** 325–368.

Cohen-Pfeffer JL, Gururangan S, Lester T, Lim DA, Shaywitz AJ, Westphal M & Slavc I (2017). Intracerebroventricular Delivery as a Safe, Long-Term Route of Drug Administration. *Pediatr Neurol* **67,** 23–35.

Cserr H (1965). Potassium exchange between cerebrospinal fluid, plasma, and brain. *Am J Physiol* **209,** 1219–1226.

Cserr HF, Cooper DN & Milhorat TH (1977). Flow of cerebral interstitial fluid as indicated by the removal of extracellular markers from rat caudate nucleus. *Exp Eye Res* **25 Suppl,** 461–473.

Davidson BL & Breakefield XO (2003). Viral vectors for gene delivery to the nervous system. *Nat Rev Neurosci* **4,** 353–364.

Davson H & Segal MB (1995). *Phyioslogy of the CSF and Blood-Brain Barriers*, 1st edn.ed. Davson H & Segal MB. CRC Press, Inc, Boca Raton.

Engelhardt B, Vajkoczy P & Weller RO (2017). The movers and shapers in immune privilege of the CNS. *Nat Immunol* **18,** 123–131.

Fabry Z, Schreiber H a., Harris MG & Sandor M (2008). Sensing the microenvironment of the central nervous system: immune cells in the central nervous system and their pharmacological manipulation. *Curr Opin Pharmacol* **8,** 496–507.

Fenstermacher JD, Nagaraja TN, Wei L & Ghersi-Egea J-F (1999). Surprises and peculiarities in the distribution of material from cerebrospinal fluid to brain tissues and blood. In *Brain Barrier Systems: Alfred Benzon Symposium*, pp. 494–505. Munksgaard, Copenhagen.

Firan M, Bawdon R, Radu C, Ober RJ, Eaken D, Antohe F, Ghetie V & Ward ES (2001). The MHC class I-related receptor, FcRn, plays an essential role in the maternofetal transfer of γ-globulin in humans. *Int Immunol* **13,** 993–1002.

Frederickson RG & Low FN (1969). Blood vessels and tissue space associated with the brain of the rat. *Am J Anat* **125,** 123–145.

Greenberg MS (2010). *Handbook of Neurosurgery*, 7th edn. Thieme, New York.

Hannocks M-J, Pizzo ME, Huppert J, Despande T, Abbott NJ, Thorne RG & Sorokin L (2017). Molecular characterization of perivascular drainage pathways in the murine brain. *J Cereb Blood Flow Metab*.

Hebel R & Stromberg MW (1976). *Anatomy of the Laboratory Rat*. Williams & Wilkins, Baltimore.

Holliger P & Hudson PJ (2005). Engineered antibody fragments and the rise of single domains. *Nat Biotechnol* **23,** 1126–1136.

Hoogduijn MJ, van den Beukel JC, Wiersma LCM & Ijzer J (2013). Morphology and size of stem cells from mouse and whale: observational study. *BMJ* **347,** f6833.

Iliff JJ, Wang M, Liao Y, Plogg BA, Peng W, Gundersen GA, Benveniste H, Vates GE, Deane R, Goldman SA, Nagelhus EA & Nedergaard M (2012). A paravascular pathway facilitates CSF flow through the brain parenchyma and the clearance of interstitial solutes, including amyloid ?? *Sci Transl Med*; DOI: 10.1126/scitranslmed.3003748.

Jazz Pharmaceuticals (2004). PRIALT (ziconotide) solution, intrathecal infusion.

Jessen NA, Munk ASF, Lundgaard I & Nedergaard M (2015). The Glymphatic System: A Beginner's Guide. *Neurochem Res* **40,** 2583–2599.

Jones EG (1970). On the mode of entry of blood vessels into the cerebral cortex. *J Anat* **106,** 507–520.

Kaitin KI & Milne CP (2011). A dearth of new meds. *Sci Am* **305,** 16.

Kramer K, Humm JL, Souweidane MM, Zanzonico PB, Dunkel IJ, Gerald WL, Khakoo Y, Yeh SD, Yeung HW, Finn RD, Wolden SL, Larson SM & Cheung N-K V (2007). Phase I study of targeted radioimmunotherapy for leptomeningeal cancers using intra-Ommaya 131-I-3F8. *J Clin Oncol* **25,** 5465–5470.

Kristoffersen EK & Matre R (1996). Co-localization of the neonatal Fc gamma receptor and IgG in human placental term syncytiotrophoblasts. *Eur J Immunol* **26,** 1668–1671.

Kumar NN, Lochhead JJ, Pizzo ME, Nehra G, Boroumand S, Greene G & Thorne RG (2018). Delivery of immunoglobulin G antibodies to the rat nervous system following intranasal administration: distribution, dose-response and mechanisms of delivery. *Submitted*.

Laterra J & Goldstein G (2012). The Blood-Brain Barrier, Choroid Plexus, and Cerebrospinal Fluid. In *Principles of Neural Science, Fifth Edition*, 5th edn., ed. Kandel ER, Schwartz JH, Jessell TM, Siegelbaum SA & Hudspeth AJ, pp. 1565–1580. McGraw-Hill Professional, New York.

Leach JL, Sedmak DD, Osborne JM, Rahill B, Lairmore MD & Anderson CL (1996). Isolation from human placenta of the IgG transporter, FcRn, and localization to the syncytiotrophoblast: implications for maternal-fetal antibody transport. *J Immunol* **157,** 3317–3322.

Leader B, Baca QJ & Golan DE (2008). Protein therapeutics: a summary and pharmacological classification. *Nat Rev Drug Discov* **7,** 21–39.

Lochhead JJ & Thorne RG (2012). Intranasal delivery of biologics to the central nervous system. *Adv Drug Deliv Rev* **64,** 614–628.

Lochhead JJ, Wolak DJ, Pizzo ME & Thorne RG (2015). Rapid transport within cerebral perivascular spaces underlies widespread tracer distribution in the brain after intranasal administration. *J Cereb Blood Flow Metab* **35,** 371–381.

Macielag M (2012). Chemical properties of antibacterials and their uniqueness. In *Antibiotic Discovery and Development*, ed. Dougherty T & Pucci M, pp. 793–820. Springer, New York.

Muenzer J, Hendriksz CJ, Fan Z, Vijayaraghavan S, Perry V, Santra S, Solanki G a., Mascelli MA, Pan L, Wang N, Sciarappa K & Barbier AJ (2015). A phase I/II study of intrathecal idursulfase-IT in children with severe mucopolysaccharidosis II. *Genet Med*1–9.

Nedergaard M (2013). Garbage truck of the brain. *Science (80-)* **340,** 1529–1530.

Nicholson C (1999). Signals that go with the flow. *Trends Neurosci* **22,** 143–145.

Nicholson C (2001). Diffusion and related transport mechanisms in brain tissue. *Reports Prog Phys* **64,** 815–884.

Nicholson C & Syková E (1998). Extracellular space structure revealed by diffusion analysis. *Trends Neurosci* **21,** 207–215.

Ommaya AK (1984). Implantable devices for chronic access and drug delivery to the central nervous system. *Cancer Drug Deliv* **1,** 169–179.

Pizzo ME, Wolak DJ, Kumar NN, Brunette E, Brunnquell CL, Hannocks M-J, Abbott NJ, Meyerand ME, Sorokin L, Stanimirovic DB & Thorne RG (2018). Intrathecal antibody distribution in the rat brain: surface diffusion, perivascular transport and osmotic enhancement of delivery. *J Physiol* **596,** 445–475.

Ransohoff RM & Engelhardt B (2012). The anatomical and cellular basis of immune surveillance in the central nervous system. *Nat Rev Immunol* **12,** 623–635.

Rickham PP (1964). A ventriculostomy reservoir. *Br Med J* **2,** 173.

Rohen JW, Yokochi C & Romrell LJ (1994). *Color atlas of anatomy: A photographic study of the human body*, 3rd edn. Igaku-Shoin Medical Pub, Tokyo.

Schuenke M, Schulte E & Schumacher U (2010). *Thieme Atlas of Anatomy: Head and Neuroanatomy*, 1st edn. Thieme, New York.

Simister NE & Mostov KE (1989). An Fc receptor structurally related to MHC class I antigens. *Nature* **337,** 184–187.

Simister NE, Story CM, Chen HL & Hunt JS (1996). An IgG-transporting Fc receptor expressed in the syncytiotrophoblast of human placenta. *Eur J Immunol* **26,** 1527–1531.

Smith AJ, Yao X, Dix JA, Jin B & Verkman AS (2017). Test of the "glymphatic" hypothesis demonstrates diffusive and aquaporin-4-independent solute transport in rodent brain parenchyma. *Elife*; DOI: 10.7554/eLife.27679.

Syková E & Nicholson C (2008). Diffusion in brain extracellular space. *Physiol Rev* **88,** 1277–1340.

Szentistványi I, Patlak CS, Ellis RA & Cserr HF (1984). Drainage of interstitial fluid from different regions of rat brain. *Am J Physiol* **246,** 35–44.

Thorne RG (2014*a*). Preface. In *Drug Delivery to the Brain: Physiological Concepts, Methodologies, and Approaches*, ed. Hammarlund-Udenaes M, de Lange E & Thorne RG. Springer-Verlag, New York.

Thorne RG (2014*b*). Primer on Central Nervous System Structure/Function and the Vasculature, Ventricular System, and Fluids of the BRain. In *Drug Delivery to the Brain: Physiological Concepts, Methodologies, and Approaches*, ed. Hammarlund-Udenaes M, de Lange E & Thorne RG, pp. 685–707. Springer-Verlag, New York.

Thorne RG, Hanson LR, Ross TM, Tung D & Frey WH (2008). Delivery of interferon-beta to the monkey nervous system following intranasal administration. *Neuroscience* **152,** 785–797.

Thorne RG & Nicholson C (2006). In vivo diffusion analysis with quantum dots and dextrans predicts the width of brain extracellular space. *Proc Natl Acad Sci USA* **103,** 5567–5572.

Thorne RG, Pronk GJ, Padmanabhan V & Frey WH (2004). Delivery of insulin-like growth factor-I to the rat brain and spinal cord along olfactory and trigeminal pathways following intranasal administration. *Neuroscience* **127,** 481–496.

Urquhart L (2018). Market watch: Top drugs and companies by sales in 2017. *Nat Rev Drug Discov* **17,** 232.

Vorbrodt AW, Dobrogowska DH, Tarnawski M & Lossinsky AS (1994). A quantitative immunocytochemical study of the osmotic opening of the blood-brain barrier to endogenous albumin. *J Neurocytol* **23,** 792–800.

Vuillemenot BR, Kennedy D, Cooper JD, Wong AMS, Sri S, Doeleman T, Katz ML, Coates JR, Johnson GC, Reed RP, Adams EL, Butt MT, Musson DG, Henshaw J, Keve S, Cahayag R, Tsuruda LS & O'Neill CA (2015). Nonclinical evaluation of CNS-administered TPP1 enzyme replacement in canine CLN2 neuronal ceroid lipofuscinosis. *Mol Genet Metab* **114,** 281–293.

Wolak DJ, Pizzo ME & Thorne RG (2015). Probing the extracellular diffusion of antibodies in brain using in vivo integrative optical imaging and ex vivo fluorescence imaging. *J Control Release* **197,** 78–86.

Wolak DJ & Thorne RG (2013). Diffusion of macromolecules in the brain: implications for drug delivery. *Mol Pharm* **10,** 1492–1504.

Woof JM & Burton DR (2004). Human antibody–Fc receptor interactions illuminated by crystal structures. *Nat Rev Immunol* **4,** 89–99.

Xu S, Wang L, El-Banna M, Sohar I, Sleat DE & Lobel P (2011). Large-volume Intrathecal Enzyme Delivery Increases Survival of a Mouse Model of Late Infantile Neuronal Ceroid Lipofuscinosis. *Mol Ther* **19,** 1842–1848.

Yang L, Kress BT, Weber HJ, Thiyagarajan M, Wang B, Deane R, Benveniste H, Iliff JJ & Nedergaard M (2013). Evaluating glymphatic pathway function utilizing clinically relevant intrathecal infusion of CSF tracer. *J Transl Med* **11,** 107.

Zervas NT, Liszczak TM, Mayberg MR & Black PM (1982). Cerebrospinal fluid may nourish cerebral vessels through pathways in the adventitia that may be analogous to systemic vasa vasorum. *J Neurosurg* **56,** 475–481.

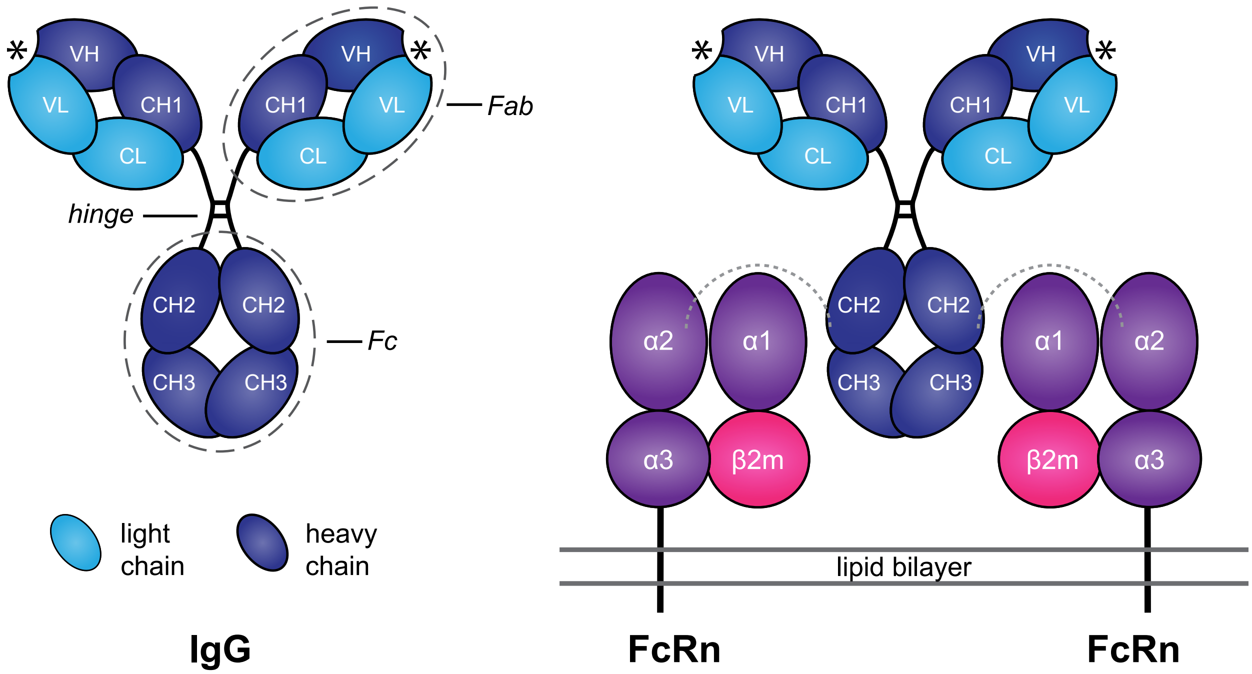

Figure 1. Structure and binding of immunoglobulin G (IgG) and Fc receptors. IgG is composed of two heavy chains (dark blue) and two light chains (light blue). The heavy chain consists of three constant regions (CH1-3) and a variable region (VH) and the light chain consists of a constant region (CL) and a variable region (VL). IgG can be divided into one crystallizable fragment (Fc) connected by a hinge region to two antigen binding fragments (Fab), the latter of which contains the antigen binding sites (*)(see (Woof & Burton, 2004; Holliger & Hudson, 2005; Abbas et al., 2015) for more details). The neonatal Fc receptor (FcRn) is comprised of a β2-microglobulin subunit (pink) non-covalently associated with a larger subunit major histocompatibility complex (MHC) class I-like heavy chain, which contains three extracellular loops (α1, α2, and α3; purple) and a transmembrane region (Simister & Mostov, 1989). A region at the junction of the CH2 and CH3 Fc region of IgG binds to the α2 domain of FcRn (gray dashed line), and also interacts with the α1 domain and the β2-microglobulin subunit (Burmeister et al., 1994).

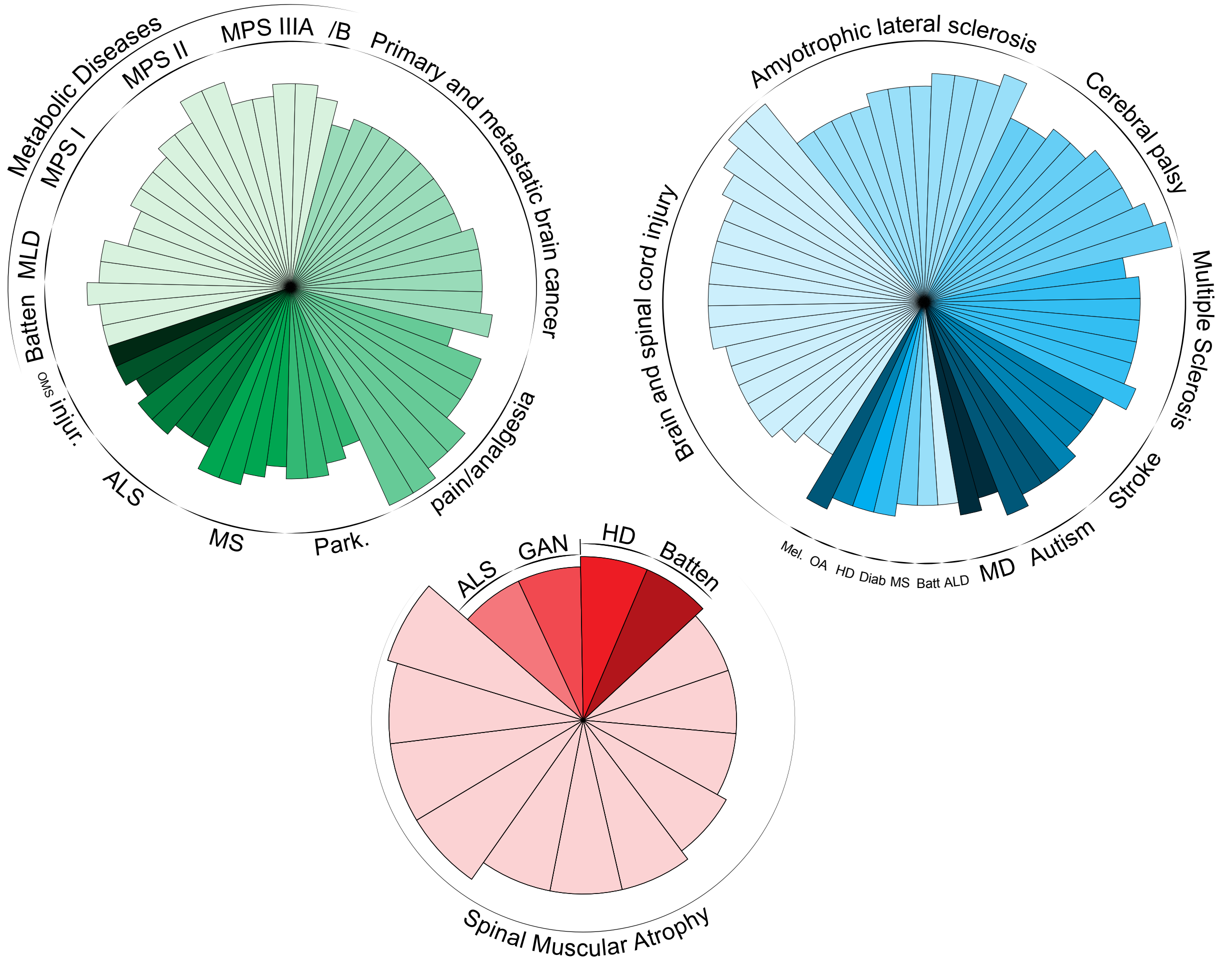

Figure 2. Summary of clinical trials administering non-small molecule therapeutics into the cerebrospinal fluid (CSF). Shades of green represent protein and peptide therapeutics, shades of blue represent cell therapies, and shades of red represent antisense oligonucleotide and adeno-associated virus therapies for various CNS disease groups. The length of each segment represent the trial phase, increasing in length from Phase 1 → 4 or expanded access program). Abbreviations: Batten (disease, including neuronal ceroid lipofuscinosis); MLD (); MPS I (); MPS II (); MPS IIIA (); MPS IIIB (); Park (Parkinson’s disease); MS (multiple sclerosis); ALS (amyotrophic lateral sclerosis); injur. (spinal cord injury); OMS (opsoclonus-myoclonus syndrome); MD (muscular dystrophy); ALD (adrenoleukodystrophy); Batt (Batten disease); MSA (multiple system atrophy); Diab. (diabetes mellitus); HD (Huntington’s disease); OA (optic atrophy); Mel. (metastatic melanoma); GAN (giant axonal neuropathy).

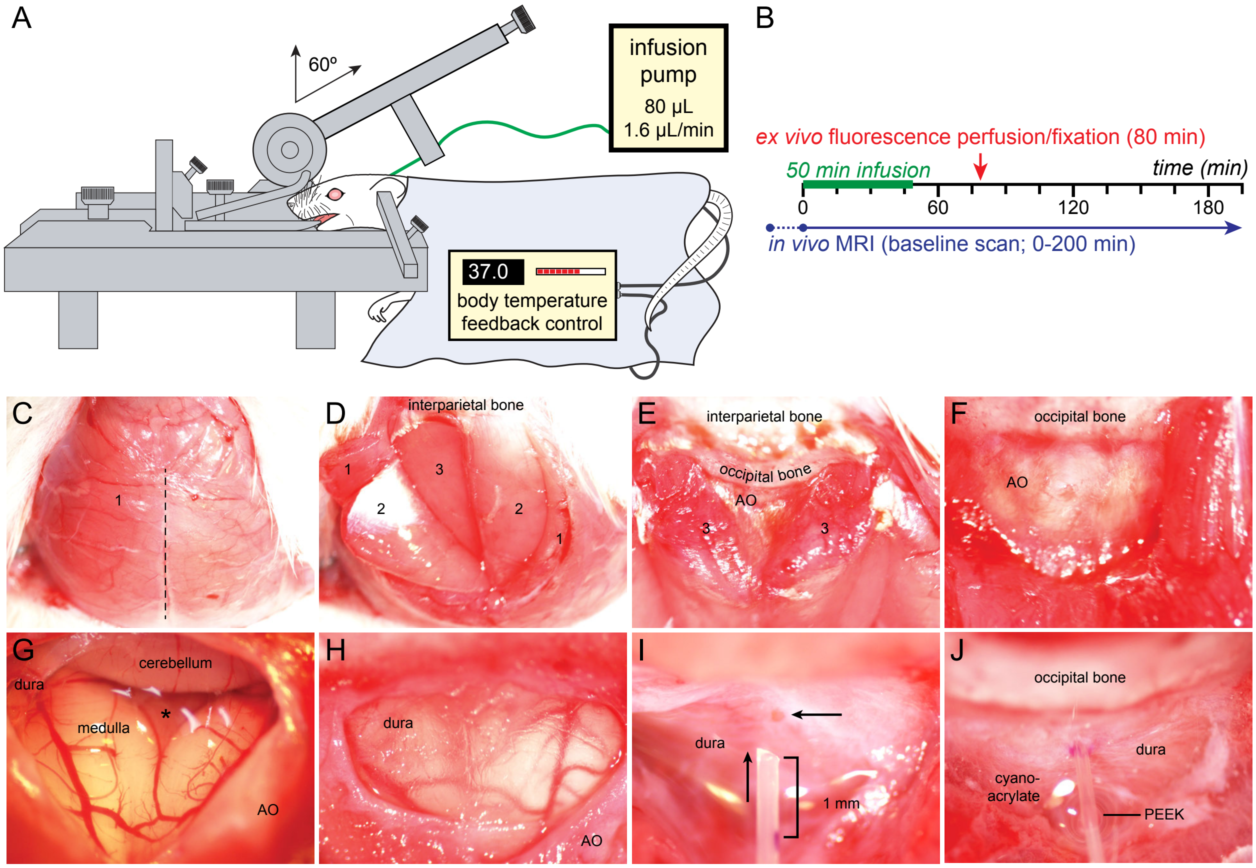

Figure 3. Method of MRI-compatible intracisternal infusion in rats. (A-B) To perform the surgery and infusion, an anesthetized rat placed into a stereotaxic frame in the flat skull position while temperature is maintained by a homeothermic blanket. A custom cannula is inserted into the cisterna magna at 60º from the vertical and 80 µL of the solution of interest is infused at 1.6 µL/min for 50 minutes. For MRI experiments, the cannula is implanted, baseline MRI scans are performed, then MR images are acquired throughout the duration of the infusion and for 2-3 hours after the infusion has completed. For ex vivo fluorescence experiments, immediately after completion of the infusion the abdominal aorta is cannulated and 30 minutes post-infusion the rat is perfused and fixed. Surgical exposure of the cisterna magna in rats first involves dissection of the subcutaneous muscles of the dorsal aspect of the neck. (C) A dorsal midline incision of the skin exposes the first muscle layer (1; putative splenius capitis (human) or biventer cervicis (rat)), which is incised down the midline and retracted laterally. (D) The second layer of muscle (2; putative semispinalis capitis (human) or longissimus capitis (rat)) is cut on the left and right

sides from the occipital bone and retracted, revealing the third muscle layer (3). (E) The third and deepest muscle layer (3; putative rectus capitis posterior minor (human) or rectus capitis dorsalis major (rat)) is cut from the occipital bone and retracted from the underlying atlanto-occipital membrane (AO) to which it is adhered. (F) The atlanto-occipital membrane is adhered to the underlying dura and obscures the view of the cisterna magna; thus, it is carefully retracted. (G) Complete removal of the dura reveals the CSF of the cisterna magna and provides a clear view of the cerebellum and medulla (with posterior spinal arteries on either side); the fourth ventricle is separated from the cisterna magna by a thin translucent membrane, the inferior medullary velum (*). (H) The dura is not removed for intracisternal infusion but is left intact after sufficient removal of the AO membrane to provide a clear view of the desired insertion site. (I-J) A custom cannula made of 33 GA polyetheretherketone (PEEK) is connected to polyethylene tubing controlled by an infusion pump and is filled prior to insertion. A 30 GA dental needle us used to puncture the dura and the PEEK tubing is immediately inserted 1 mm into the cisterna magna and sealed to the dura with cyanoacrylate. Human and rat anatomy referenced in (Hebel & Stromberg, 1976; Rohen, 2011). For more information regarding surgical preparation (Wolak et al., 2015; Pizzo et al., 2018).

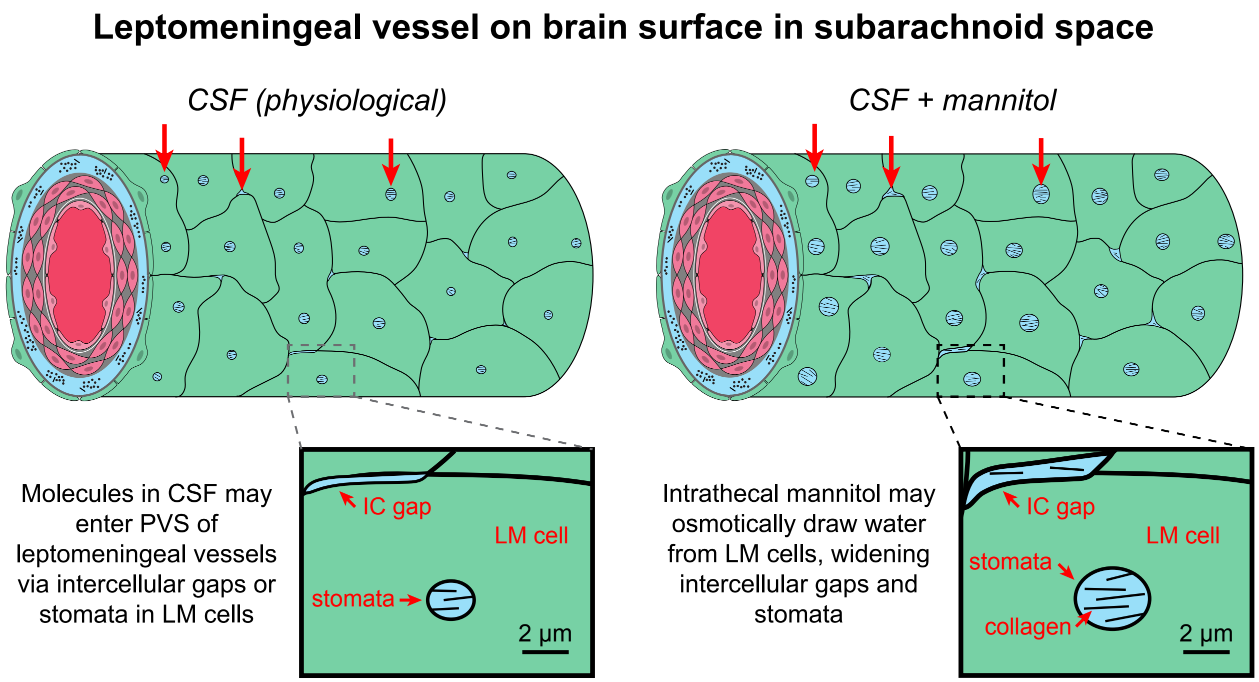

Figure 4. Hypothesized entry into the perivascular space from the CSF and osmotic enhancement strategy. (*Left*) A schematic of a leptomeningeal (LM) artery on the brain surface demonstrates a layer of leptomeningeal fibroblasts (Hannocks et al., 2017) which separate the CSF from the underlying perivascular space (light blue) and connective tissue (e.g., perivascular collagen). We hypothesize that pores or 'stomata' which are present in the leptomeningeal cells of rats (Pizzo et al., 2018) and cats (Zervas et al., 1982) may govern entry into to perivascular space from the CSF, in addition to intercellular gaps (IC) between leptomeningeal cells or the pia mater (Frederickson & Low, 1969; Jones, 1970; Cloyd & Low, 1974). (*Right*) We speculate that co-infusion of hyperosmolar mannitol intrathecally draws water out of the leptomeningeal cells, possibly causing cells to shrink and therefore stomata and intercellular gaps to widen, facilitating perivascular entry. It is also possible that hyperosmolar mannitol in the CSF increases transcytosis across leptomeningeal cells, as has been demonstrated for mannitol and the blood-brain barrier (Vorbrodt et al., 1994).

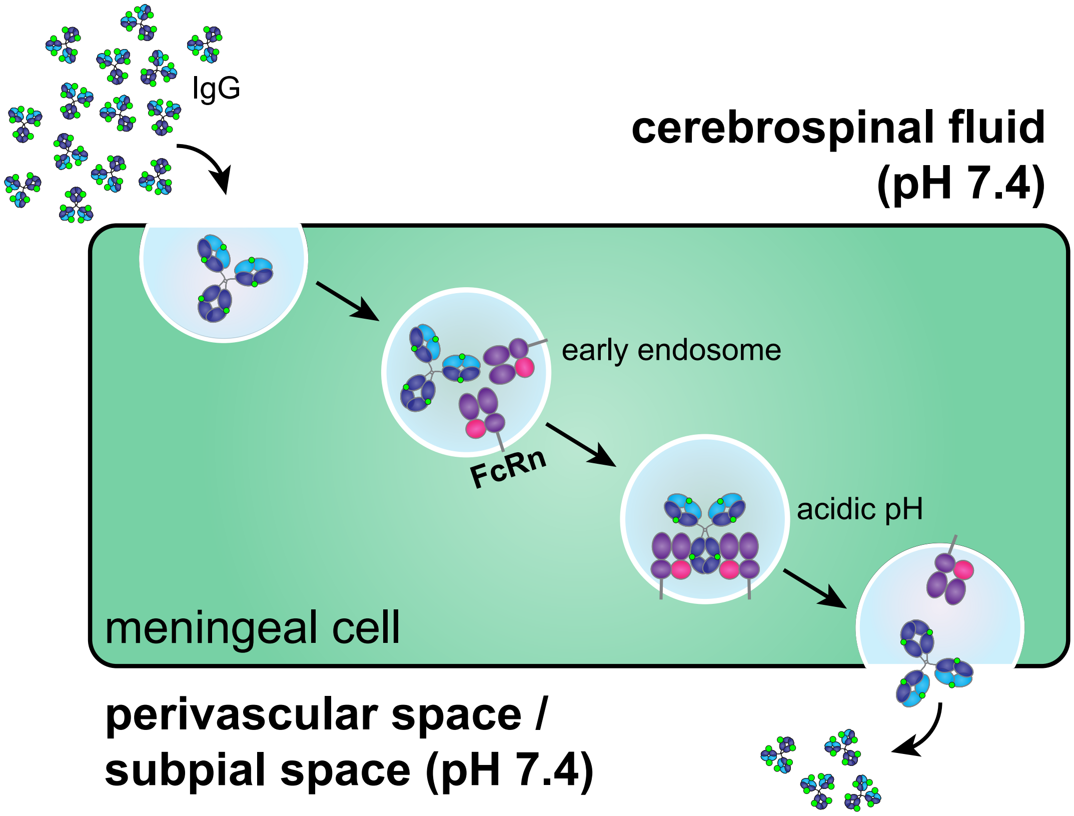
IgG
cerebrospinal fluid
(pH 7.4)
early endosome
FcRn
acidic pH
meningeal cell
perivascular space /
subpial space (pH 7.4)

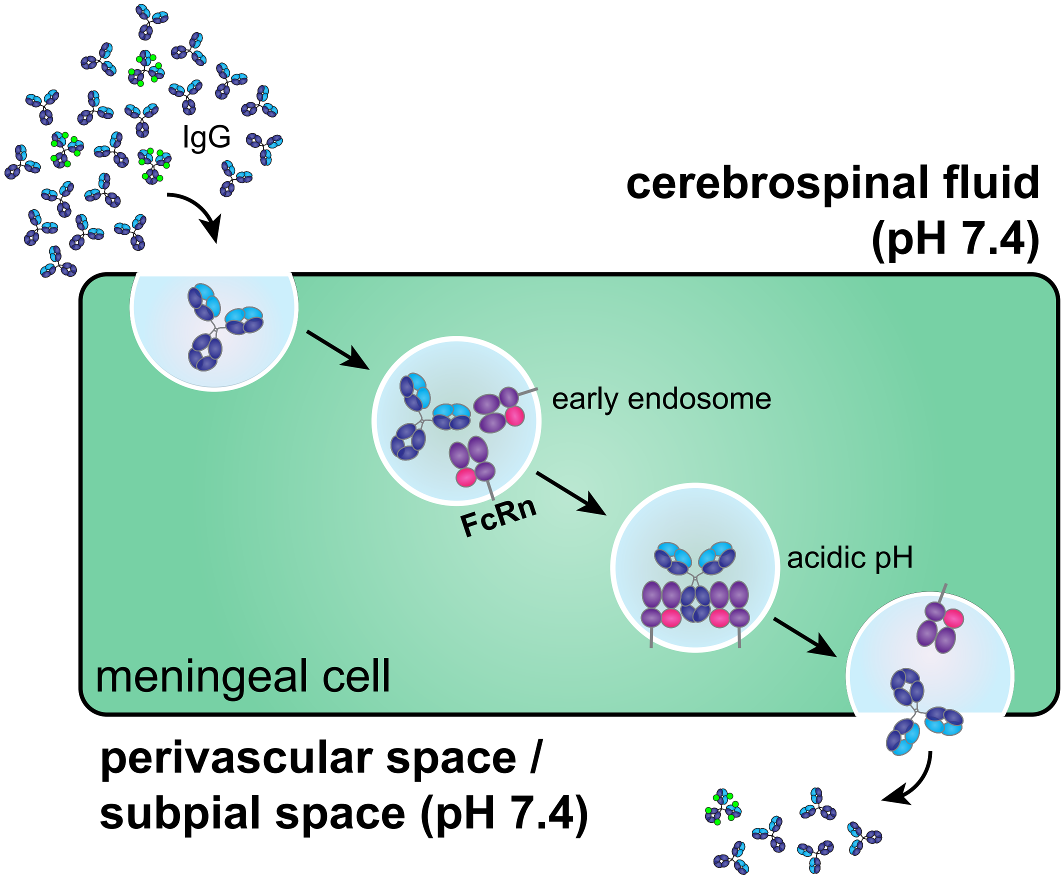
IgG
cerebrospinal fluid
(pH 7.4)
early endosome
FcRn
acidic pH
meningeal cell
perivascular space /
subpial space (pH 7.4)

Figure 5. Hypothesized mechanism of receptor-mediated IgG transport into the perivascular space from the CSF. Rat IgG demonstrated a specific, carried-mediated transfer from the CSF into the perivascular spaces across the rat brain. FcRn is a pH-depednent IgG-binding receptor that has demonstrated the ability to transcytose IgG across other barriers in the body, e.g., the syncytiotrophoblasts of the placenta (Simister et al., 1996; Kristoffersen & Matre, 1996; Leach et al., 1996; Firan et al., 2001), and thus was hypothesized to be involved in CSF-to-perivascular transport. The general premise is: (*Top*) Labeled IgG in the CSF enters meningeal cells by nonspecific or specific mechanisms, reaches the acidified endosome where it can bind with high affinity to FcRn in a 2:1 (receptor:IgG) stoichiometry, the FcRn IgG complex is trafficked to the other side, and IgG is released from FcRn upon reaching the physiological pH of the perivascular compartment. (*Bottom*) When an excess of unlabeled IgG if co-infused into the CSF with labeled IgG, the unlabeled IgG is more likely to be internalized into meningeal cells and thus competes for receptor-mediated transcytosis, resulting in few labeled IgG molecules from reachin the perivascular space.

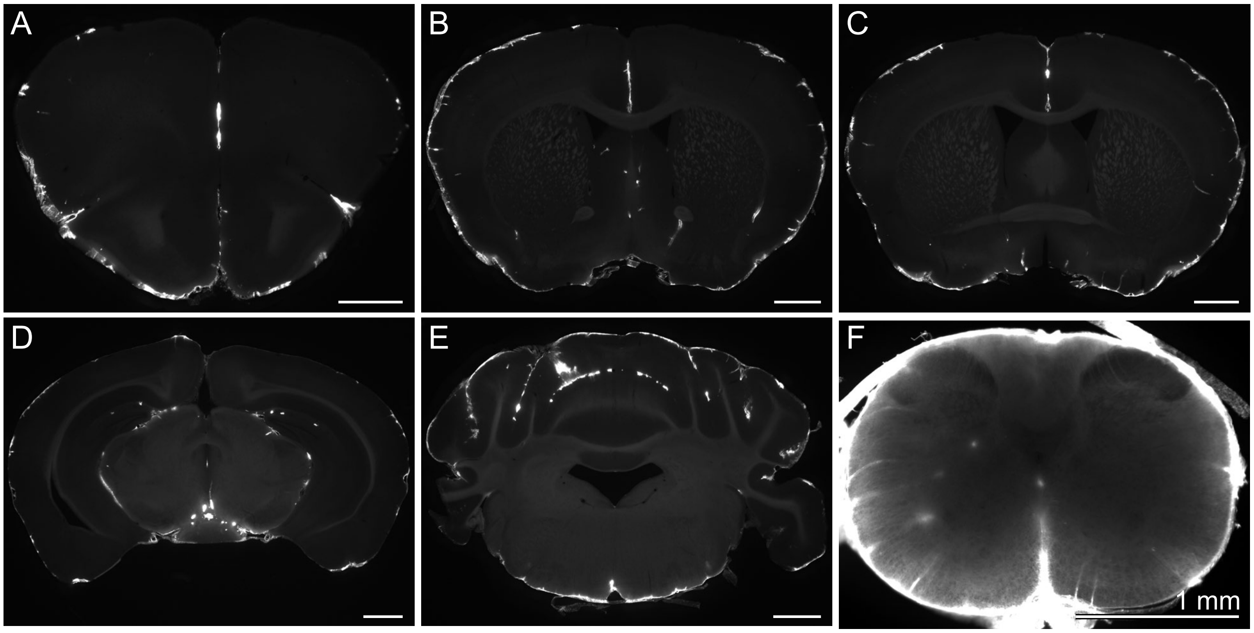

Figure 6. Preliminary brain distribution of intrathecally-infused mouse IgG in mice. In this mouse 20 μL fluorescently-labeled, normal, pooled, non-targeted mouse IgG was infused into the cisterna magna over 50 minutes at a rate of 0.4 μL/min. Thirty minutes post-infusion the mouse was perfused with phosphate buffered saline followed by paraformaldehyde. (A-F) The distribution of intrathecally-infused mouse IgG showed a fairly limited distribution throughout coronal mouse brain sections. Signal was present at the brain-CSF interfaces, but only penetrated into the brain along a few perivascular spaces (e.g., vessels in the striatum, in B, punctate profiles in the dorsal hippocampus in D, or a few profiles in the spinal cord, in F).

CHAPTER 1
The extracellular and perivascular spaces of the brain

Michelle E. Pizzo[1,2] & Robert G. Thorne[1-5]
[1]School of Pharmacy, Division of Pharmaceutical Sciences; [2]Clinical Neuroengineering Training Program; [3]Neuroscience Training Program; [4]Cellular and Molecular Pathology Graduate Program; [5]Institute for Clinical and Translational Research; University of Wisconsin-Madison

Adapted in part with permission from:
Pizzo ME & Thorne RG (2017). The extracellular and perivascular spaces of the brain. In *Brain Edema: From Molecular Mechanisms to Clinical Practice*, 1st edn., ed. Badaut J & Plesnila N, pp. 103–128. Academic Press.

Abstract

The central nervous system is an extraordinarily complex cellular and fluid environment. Much evidence exists to suggest that short-range, local distribution in the microenvironment of the neuropil is normally governed by diffusion in the narrow, tortuous brain extracellular space (ECS). Long-range distribution within the central compartment occurs via convection or bulk flow within the cerebrospinal fluid and cerebral perivascular fluid spaces and perhaps also within white matter.

Components of the central nervous system (CNS)

The central nervous system (CNS) can be generally divided into three main components—the cells, fluids, and vasculature. First, there are the cells of the brain and spinal cord parenchyma, or tissue, which consist of two main types, neurons and glia. There is remarkable variation in the ~ 100 billion neurons that make up the human brain while the remaining ~100 billion glial cells include astrocytes, microglia, and oligodendrocytes (Peters *et al.*, 1991; Paxinos & Mai, 2004; Watson *et al.*, 2010; Kandel *et al.*, 2013; Thorne, 2014). Between all of these cells and their processes is an extracellular space (ECS) compartment that is filled with interstitial fluid (ISF); ISF is carefully regulated because its ionic composition and volume are critical parameters for neurotransmission. Cerebrospinal fluid (CSF) is also present within and surrounding the brain and spinal cord. CSF composition and volume are carefully regulated and optimized to provide mechanical support (making the brain buoyant so it does not deform under the forces of gravity) and mechanical protection (preventing the brain from striking the skull with regular movement), as well as to maintain ion homeostasis (Davson & Segal, 1995; Sakka *et al.*, 2011). The third component is the cerebral vasculature. Cerebral blood vessels are uniquely designed to separate the blood and its contents from the cells and fluids of the CNS (the CSF and ISF), providing highly selective blood-brain and blood-CSF barriers. The blood-brain barrier (BBB), is primarily formed by microvessel endothelial cells, which lack fenestrations, possess tight junctions that prevent paracellular transport, have very low rates of transcytosis, and also have a variety of influx and efflux transporters to allow selective entry of some molecules (e.g., glucose) while selectively rejecting others (e.g., toxic substances). In this fashion, the BBB functions to supply the cells of the brain with nutrients, allow for removal of waste products, maintain the ionic homeostasis of the brain (by preventing the alteration of brain ions when plasma levels fluctuate), and to selectively regulate the entry and exit of molecules (e.g., proteins and neurotransmitters) between the blood and brain compartments (Abbott, 2004; Abbott *et al.*, 2006). An important feature is the proximity of the vasculature to the brain cells—neurons are usually not located further than ~ 10-20 μm from capillaries (Schlageter *et al.*, 1999; Mabuchi *et al.*, 2005), a short distance likely optimized for oxygen, glucose, and other essential molecules to reach all brain cells efficiently by diffusive transport.

The brain and spinal cord are contained within the meninges, which include (external to internal) the dura mater, arachnoid mater, and pia mater. The outermost external layer is the dura (a tough membrane composed largely of collagen), which lies between the skull and the underlying leptomeninges. The leptomeninges, or “thin” meninges, include the arachnoid and pia, between which lies the CSF-filled subarachnoid space (SAS). Many large blood vessels travel in the SAS and trabeculae (strings or sheets of leptomeningeal cells) also cross the SAS connecting the arachnoid and pia. Beneath all these meningeal layers lies the brain; at the surface of the brain as well as along parenchymal blood vessels, astrocyte (glial) endfeet and their basement membrane form the glia limitans, partly partitioning the brain from the subpial and perivascular spaces (Zhang *et al.*, 1990; Davson & Segal, 1995; Nolte, 2009).

The ventricular system and CSF

The CSF of mammals is contained within several cavities (ventricles) within the brain along with the subarachnoid space that surrounds the brain and spinal cord (Fig. 1). Each of the brain's four ventricles contain a choroid plexus, consisting of fenestrated vasculature and specialized secretory epithelia that produce CSF by active transport/secretion (Davson & Segal, 1995). Additionally, CSF is produced in the brain parenchyma, by fluid entering across the BBB (Cserr, 1971; Szentistványi *et al.*, 1984; Davson & Segal, 1995). The ependymal cells lining the ventricles possess cilia, which, in addition to the respiratory and cardiac pulsations, aid in CSF movement through the ventricular system (Davson & Segal, 1995; Brinker *et al.*, 2014; Faubel *et al.*, 2016). The conventional CSF flow pattern is generally described as follows: CSF is produced by the choroid plexuses of two paired lateral ventricles, where it flows through two interventricular foramina (of Monro) to enter the third ventricle; the third ventricle choroid plexus produces additional CSF, which flows through a narrow cerebral aqueduct (of Sylvius) to enter the fourth ventricle; the fourth ventricle choroid plexus produces additional CSF, which exits via three foramen, two lateral foramina (of Luschka) and one medial foramen (of Magendie), to enter the SAS (though some CSF continues down the central canal in the center of the spinal cord). Once CSF enters the SAS, it fills the SAS surrounding the brain parenchyma and spinal cord. In some brain areas there is a thin layer of SAS between the brain and the dura/skull, while in other areas there are large pockets of SAS referred to as cisterns (Davson & Segal, 1995; Schuenke *et al.*, 2010). From the SAS, CSF may drain along arachnoid (Pacchionian) granulations or villi into the blood of the dural venous sinuses, or along cranial nerves (e.g., along olfactory nerves to the nasal lymphatics) to the deep cervical lymph nodes (Faber, 1937; Bradbury *et al.*, 1981; Bradbury & Westrop, 1983; Szentistványi *et al.*, 1984; Weller *et al.*, 1992; Kida *et al.*, 1993) (reviewed in reference (Koh *et al.*, 2005)), or along spinal nerves to the deep cervical, intercostal, and other lymph nodes (reviewed in reference (Koh *et al.*, 2005)), which ultimately drain into the blood. Recently, it has been shown that CSF may also drain to dural lymphatic vessels that also appear to drain to the deep cervical lymph nodes (Kida *et al.*, 1993; Aspelund *et al.*, 2015; Louveau *et al.*, 2015). It is thought that all these routes to the lymphatic system are important for CNS antigen drainage and immune function (Harling-Berg *et al.*, 1989; Cserr *et al.*, 1992; Knopf *et al.*, 1998; Walter *et al.*, 2006*a*; Louveau *et al.*, 2016; Kipnis, 2016). Key questions going forward concern how all the different CSF / lymphatic drainage pathways work in concert with each other, their relative importance, species differences, and alterations in their function / relative importance during different disease processes.

In addition to the BBB, there is a blood-cerebrospinal fluid barrier (BCSFB) preventing free communication between the blood and CSF. One region of the BCSFB is created by tight junctions between arachnoid epithelial cells (Nabeshima *et al.*, 1975), which prevents plasma contents from fenestrated blood vessels in the dura from entering the CSF of the subarachnoid space. Tight junctions between choroid plexus epithelial cells create the other region of the BCSFB (Becker *et al.*, 1967). As already mentioned, choroid plexus blood vessels are fenestrated, which aids in CSF production from plasma water. Thus, like the BBB, the BCSFB has transporters to allow selective entry of ions and molecules from the blood compartment, and also plays a role in immune regulation/response (Davson & Segal, 1995; Strazielle & Ghersi-Egea, 2000; Engelhardt & Sorokin, 2009; Damkier *et al.*, 2013).

The extracellular space

The ECS refers to the interstitial fluid-filled environment that separates brain cells and their processes (Fig. 2A). Much work suggests that the ECS accounts for approximately 20% of the total tissue volume in the normal, adult brain *in vivo* (Nicholson & Phillips, 1981; Nicholson & Syková, 1998). This ECS volume fraction ($\alpha \sim 0.2$) appears highly conserved between most brain regions and across most species that have been studied to date, including mammals (e.g., rat, mouse, guinea pig, rabbit, dog, and human tissue), reptiles (e.g., turtle), amphibians (e.g., frog), and fish (e.g., skate) (Levin *et al.*, 1970; Nicholson, 2001; Syková & Nicholson, 2008; Wolak & Thorne, 2013). Careful study of the rodent brain during postnatal development has revealed that the ECS in both the gray and white matter is about twice its adult value in the newborn ($\alpha \sim 0.4$ (Lehmenkühler *et al.*, 1993; Vorisek & Sykova, 1997)) and that the gray matter ECS appears to decline in aged animals at the end of the lifespan (e.g., $\alpha = 0.13 – 0.16$ in 17-25 month old mice (Syková *et al.*, 2005)). It is worth noting that the above information about ECS volume comes primarily from the method of real-time iontophoresis performed in either anesthetized animals *in vivo* or in acute brain slice preparations (e.g., see references (Syková & Nicholson, 2008; Wolak & Thorne, 2013) for review). A recent report utilizing this same method has suggested that the ECS volume may be reduced in the superficial parietal association cortex of awake mice as compared to measurements in the same area of either sleeping or anesthetized adult mice ($\alpha \sim 0.14$ in awake versus $\alpha \sim 0.23$ in sleeping or ketamine/xylazine anesthetized animals (Xie *et al.*, 2013);

however, this interesting finding awaits replication and further study across other brain regions and species.

Another important parameter describing the brain ECS is its width (Fig. 2B), as this will impose constraints on how larger macromolecules diffuse through the tortuous paths between brain cells. While early estimates of ECS width from electron microscopy suggested a narrow ECS width of ~ 20 nm or less, it was long appreciated that these estimates were likely confounded by redistribution of extracellular water due to tissue ischemia and processing (associated with animal sacrifice and preparation of samples for microscopy) because the ECS volume in this material often appeared much smaller than physiological estimates had clearly provided (Thorne & Nicholson, 2006; Wolak & Thorne, 2013). More recent estimates from *in vivo* diffusion measurements in anesthetized rat neocortex suggest the actual ECS width is approximately 40-60 nm in adult animals (Thorne & Nicholson, 2006). At least for the gray matter, a large body of evidence from numerous tracer diffusion and distribution studies suggests that these narrow spaces are unlikely to accommodate bulk flow (convection) because basic diffusion theory has been sufficient to fully describe such transport under a variety of experimental conditions in normal animals (e.g., (Rosenberg *et al.*, 1980; Ichimura *et al.*, 1991; Wolak *et al.*, 2015); for review see (Abbott, 2004; Syková & Nicholson, 2008; Wolak & Thorne, 2013)). ECS transport is most likely governed by diffusion because the hydraulic conductivity (ease of flow) is likely too low (and the resistance to flow too high) to allow for appreciable convective flow (Bear, 1972; Fenstermacher & Patlak, 1976). In simple terms, diffusion is a size-dependent, slow random-walk migration of molecules along a concentration gradient (Berg, 1993). Studies employing tracers of varying size/chemistry and using a variety of methods have demonstrated that molecular transport in the brain tissue is consistent with Fick's second law relating changes in concentration with time to a diffusion coefficient (Fenstermacher & Patlak, 1976; Thorne *et al.*, 2004; Thorne & Nicholson, 2006; Syková & Nicholson, 2008; Wolak & Thorne, 2013).

An important aspect of the ECS that can further affect transport concerns its structural organization. Brain regions that lack homogeneity (e.g., inhomogeneity is evident in tissue with complex patterns of different layers such as the cerebellum and olfactory bulb) and/or isotropy (e.g., anisotropic aligned fibers within the white matter) display regional variations in diffusion characteristics (Syková & Nicholson, 2008). Most neocortical areas that have been examined to date, e.g., somatosensory cortex (Nicholson & Tao, 1993; Tao & Nicholson, 1996; Mazel *et al.*, 1998; Thorne *et al.*, 2004; Wolak *et al.*, 2015)**,** have been characterized by isotropic diffusion (diffusion coefficients are the same along any axis so that point source injections result in spherically symmetrical diffusion clouds). The white matter of the corpus callosum provides an example of a brain area where diffusion anisotropy exists, e.g., extracellular diffusion of the small tetramethylammonium ion tracer is significantly greater along the long cylindrical axis of myelinated axons in this region (Vorísek & Syková, 1997).

Convincing experimental evidence suggests that convective transport (flow) within and around the brain and spinal cord is limited to the ventricular and subarachnoid space CSF compartments, perivascular spaces, and possibly also the white matter; all of these areas are expected to exhibit substantially higher hydraulic conductivity (i.e., lower resistance to flow) than the neuropil of the gray matter (Fenstermacher & Patlak, 1976; Wolak & Thorne, 2013). While the white matter has a normal ECS volume similar to the gray matter in adult animals and diffusive transport likely dominates under normal conditions (Lehmenkühler *et al.*, 1993; Vorisek & Sykova, 1997), experimental evidence suggests that the white matter ECS paths oriented along fibers likely can undergo significant expansion when exposed to higher than normal pressures or osmotic challenge such that measureable flow occurs (Cserr *et al.*, 1977; Rosenberg *et al.*, 1980). This preferential poroelastic expansion of the white matter ECS may help to explain the marked periventricular white matter edema that occurs with hydrocephalus while the central gray matter and neocortex remain relatively unaffected, even in severe conditions (Weller, 1998).

The ECS is not simply an empty fluid space; it is also contains hyaluronic acid, heparan sulfate and chondroitin sulfate proteoglycans, glycoproteins, laminins, and collagen, which may be attached to cells or free floating (Novak & Kaye, 2000). All of these ECM components, as well as the cell membranes and associated cell surface molecules together comprise the ECS boundaries and can impact the transport of endogenous and exogenous molecules (Fig. 2B). Molecules which interact (e.g., transiently bind) with ECM components and/or fixed elements on cell surfaces may therefore diffuse more slowly through brain ECS than comparably sized inert molecules that lack such interactions (Syková & Nicholson, 2008; Wolak & Thorne, 2013; Wolak *et al.*, 2015). Examples where alterations in measured diffusive transport parameters due to binding to cell surface receptors or extracellular matrix components have recently been described. First, a direct ECM effect where rapid, reversible binding to endogenous heparan sulfate proteoglycans slowed the extracellular diffusion of the iron-binding protein lactoferrin was shown *in vivo* (Thorne *et al.*, 2008). This study took advantage of a comparison between lactoferrin and the closely related transferrin protein to isolate the heparan sulfate proteoglycan binding effect on measured extracellular diffusion parameters; both lactoferrin and transferrin are bilobal ~ 80 kDa proteins but only lactoferrin contains a region of basic amino acids near its amino terminus allowing it to bind polyanions, such as heparin, heparan sulfate, and DNA. The study showed that lactoferrin's effective diffusion coefficient was reduced by ~ 60% due to its binding the relative fixed, endogenous heparan sulfate binding sites arrayed in brain ECS (Thorne *et al.*, 2008). Second, IgG antibody binding to endogenous Fc receptors on cell surfaces has also been shown to significantly hinder extracellular diffusion in the somatosensory cortex *in vivo* (Wolak *et al.*, 2015); administering an excess of unlabeled Fc (competing away the binding of the labeled IgG domain which specifically binds the endogenous Fc receptors) facilitated improved IgG diffusion (Wolak *et al.*, 2015).

While it is thought that diffusion governs transport in the ECS, it is well agreed upon that there are also pathways in the brain for convective, or bulk fluid flow, where molecules in a fluid, independent of size, move at the same rate of fluid flow. Convective flow is driven by a pressure gradient and is substantially faster than diffusion, particularly over longer distances (Abbott, 2004; Wolak & Thorne, 2013). Transport of mass within a fluid may be described in terms of a diffusive flux component (always present as long as the diffusing molecules are mobile) and a convective flux component (present when a volume of fluid containing the molecules is transported at some velocity). Diffusion is caused by Brownian motion (random walks), resulting in a net flux down a concentration gradient, and is directly proportional to a molecule's diffusion coefficient according to Fick's first law. In contrast, convection most often refers to a flow driven by a pressure difference. Darcy's law states that convective flux is directly proportional to the hydraulic permeability (a property influenced by both the material's pores for fluid flow and the fluid itself). Intrinsic hydraulic permeability is a useful component of the hydraulic permeability—it varies directly with the square of the mean pore diameter through which fluid must flow and can be used to understand how convection is dramatically favored within the brain along lower resistance pathways (i.e., those with much larger effective ‘pores’ than the 40-60 nm wide neuropil; (Thorne & Nicholson, 2006) such as the ventricular and subarachnoid CSF spaces, the perivascular spaces of the cerebrovasculature, and potentially the white matter). For example, measurements of perivascular space widths in mammals (e.g., arteriole perivascular spaces commonly appear ~5−10 μm or larger in rodents and humans (Pollock *et al.*, 1997; Foley *et al.*, 2012; Iliff *et al.*, 2012); suggest the intrinsic hydraulic permeability of the perivascular space is at least ~10,000-fold higher than the ECS of the neuropil (Wolak & Thorne, 2013). Several tracer experiments have now demonstrated that molecules administered into the CNS spread quickly, much faster than diffusion would allow, along preferential pathways in the brain that include the perivascular spaces and extracellular compartments associated with white matter tracts (Cserr & Ostrach, 1974; Cserr *et al.*, 1977; Bradbury *et al.*, 1981; Cserr *et al.*, 1981; Szentistványi *et al.*, 1984; Rennels *et al.*, 1985, 1990; Ichimura *et al.*, 1991; Cserr & Patlak, 1992; Weller *et al.*, 1992; Ghersi-Egea *et al.*, 1996; Fenstermacher *et al.*, 1997; Proescholdt *et al.*, 2000; Iliff *et al.*, 2012, 2013*a*). Most research suggests that the convective flow in the PVS is driven by the pulsations of the arteries (Rennels *et al.*, 1985; Hadaczek *et al.*, 2006; Iliff *et al.*, 2013*b*), as reducing the pulsations with drugs, physical ligation of vessels, or euthanization reduces transport in the PVS.

There is now great interest in how perivascular spaces, fluid-filled channels surrounding arteries, arterioles, veins, venules and possibly even microvessels, may offer potential pathways for rapid convective flows into and out of the brain parenchyma. In light of this, we shall briefly summarize the work of several groups (see Fig. 3) to generally define the perivascular compartment

(Frederickson & Low, 1969; Wagner *et al.*, 1974; Krahn, 1982). The perivascular space exists around vessels in the subarachnoid space and follows the vessels (at least for some distance) as they penetrate the brain tissue, narrowing as the vessel diameter narrows. The vessel continues until the fluid compartment lies between the astrocyte (glial) basement membrane which walls off the brain parenchyma and the vessel wall. At the level of the capillaries, where the blood vessel wall and its components consist of the endothelial cell, its basement membrane, and pericytes, it has been unclear if a perivascular fluid space still remains. Indeed, whether a pericapillary space exists, or if the endothelial BM and the glial BM fuse to obliterate the space has been a matter of debate for some time (Maynard *et al.*, 1957; Jones, 1970; Cervós-Navarro & Ferszt, 1973; Peters *et al.*, 1991).

As a pathway, the perivascular space likely has several functions in normal physiology, many of which are still emerging or have only been recently proposed. It may play a role in the distribution and delivery of nutrients and neuromodulators (Rennels *et al.*, 1985; Jessen *et al.*, 2015) to specific brain regions or the entire brain, which therefore may make it an excellent medium/route for drug delivery. For example, it was once proposed that the perivascular space may provide nutrients to the cells in the thick vessel walls, as cerebral vessels lack vasa vasorum which supply the vessel walls of large vessels in the periphery (Zervas *et al.*, 1982). It may be involved in solute and waste clearance from the brain, for example, transporting metabolic products like amyloid beta out of the interstitial fluid (Iliff *et al.*, 2012; Xie *et al.*, 2013), and impairment of this system could be related to several pathologies such as Alzheimer's disease (AD), cerebral amyloid angiopathy, and traumatic brain injury (Preston *et al.*, 2003; Weller *et al.*, 2008; Iliff *et al.*, 2014; Kress *et al.*, 2014). Additionally, many researchers (Casley-Smith *et al.*, 1976; Szentistványi *et al.*, 1984;

Rennels *et al.*, 1985; Földi, 1996; Weller *et al.*, 2009; Iliff *et al.*, 2012) have suggested that the perivascular spaces may very well be functioning as lymphatics (or pre-lymphatics) for the brain (this was in fact first suggested by His in 1865!), partly because the brain noticeably lacks traditional lymphatic vessels for the drainage of interstitial fluid and antigens. As mentioned already, the CSF and ISF have been shown to drain along cranial nerves and via dural lymphatic vessels to the deep cervical lymph nodes, and antigens in the CSF and ISF can induce a specific immune response via the cervical lymph nodes (Harling-Berg *et al.*, 1989; Walter *et al.*, 2006*a*, 2006*b*). It is possible that drainage along the perivascular space is an initial step in the CSF / ISF to nasal lymphatic/dural lymphatic to cervical lymph node pathway; surprisingly, the precise direct and/or indirect connections between the ISF and cervical lymph nodes have yet to be firmly established.

While the perivascular space likely plays a role in normal physiology, it also is linked to several neuropathologies. It has been suggested that in Alzheimer's disease, a failure of the perivascular drainage pathway may result in reduced drainage of amyloid-beta from the interstitial fluid, forming plaques in the perivascular space and blocking drainage further, worsening the disease (Weller *et al.*, 2008; Iliff *et al.*, 2014; Kress *et al.*, 2014). In cerebral amyloid angiopathy, amyloid-beta is found in the basement membrane of the vessel walls, perhaps also indicating a failure in the perivascular drainage of amyloid-beta (Preston *et al.*, 2003).

Many studies have also implicated a role for aquaporin water channel proteins in the regulation of brain water homeostasis (see content elsewhere in this volume; reviewed in (Badaut *et al.*, 2014). Briefly, 3 of the at least 13 aquaporin (AQP) family members appear to be prominently expressed in the central nervous system: AQP1, AQP4, and AQP9 (Frigeri *et al.*, 1995; Nielsen *et al.*, 1997; Nagelhus *et al.*, 2004; Badaut, 2010; Badaut *et al.*, 2014). AQP4 is highly expressed on astrocyte processes forming the glia limitans at the pial brain surface (i.e., the brain interface with the subarachnoid space CSF) as well as on astrocyte endfeet contacting blood vessels (i.e., forming part of the wall separating the perivascular space from the surrounding parenchyma in large vessels and facing the basal lamina of the neurovascular unit in microvessels); it is the most abundant water channel in the CNS and is thought to play a major role in water homeostasis (Badaut *et al.*, 2014). AQP1 is prominently expressed in the choroid plexus epithelia, where it likely plays a role in CSF formation (Badaut *et al.*, 2014), while AQP9, an aquaglyceroporin permeable to water as well as glycerol and urea, is widely expressed in astrocytes and more selectively expressed in neurons of the catecholaminergic system (Badaut, 2010). The prominent expression of AQP4 at brain tissue interfaces with the CSF and blood vessels has long suggested a role for AQP4 in the regulation of brain ECS water. As mentioned above, brain ECS volume fraction declines significantly from birth ($\alpha \sim 0.4$) to reach its smaller adult volume ($\alpha \sim 0.2$); this change occurs in parallel with glial proliferation and increasing AQP4 expression over the same period (Wen, 1999). Furthermore, careful measurements of somatosensory cortex ECS volume in AQP4-deficient adult mice have revealed a small but significant increase in ECS volume (α change from 0.18 to 0.23 (Yao *et al.*, 2008)), further suggesting a prominent role for AQP4 in regulating extracellular water volume. While measurements of PVS width in AQP4-null adult mice have suggested that PVS volume is not significantly affected by a lack of AQP4 at the perivascular astrocytic endfeet, tracer influx from the CSF to the parenchyma appeared noticeably reduced (Iliff *et al.*, 2012). Further research is needed to better define the different roles that aquaporins may play in normal brain water circulation as well as in pathological processes resulting in cerebral edema.

Conclusions

Much evidence exists to suggest that molecular distribution in the brain microenvironment is normally governed by diffusion in the narrow, tortuous ECS of the neuropil in combination with convection or bulk flow within the CSF compartments (ventricular and subarachnoid spaces) and cerebral perivascular fluid spaces and perhaps also within the white matter. ECS and PVS volumes and physiological attributes may be altered in a variety of neurological disease states, including those conditions accompanied by brain edema. The narrow ECS of the gray matter in adult animals appears well suited to resist volume expansion in the face of increasing pressure, providing a possible explanation for numerous observations that transport in the gray matter ECS appears limited to size-dependent diffusion and thus the gray matter ECS would be better capable of maintaining a stable fluid environment for the ionic gradients that underlie neurotransmission. The cerebral perivascular spaces and white matter tracts appear to be a path-of-less-resistance with a role in clearing edema constituents from the brain to the CSF via bulk flow. Both of these pathways show a connection to the downstream CSF drainage route to the cervical lymph nodes, but the precise details remain unclear. Understanding the formation of edema fluid, the mechanisms and pathways of edema fluid removal, and the balance between them will allow for improved, physiologically-based treatment of cerebral edema. Central to this endeavor is developing a more complete understanding of just how the fluid compartments of the brain ECS and PVS are regulated under normal conditions as well as during pathological processes accompanied by edema.

References

Abbott NJ (2004). Evidence for bulk flow of brain interstitial fluid: significance for physiology and pathology. *Neurochem Int* **45,** 545–552.

Abbott NJ, Rönnbäck L & Hansson E (2006). Astrocyte-endothelial interactions at the blood-brain barrier. *Nat Rev Neurosci* **7,** 41–53.

Aspelund A, Antila S, Proulx ST, Karlsen TV, Karaman S, Detmar M, Wiig H & Alitalo K (2015). A dural lymphatic vascular system that drains brain interstitial fluid and macromolecules. *J Exp Med* **212,** 991–999.

Badaut J (2010). Aquaglyceroporin 9 in brain pathologies. *Neuroscience* **168,** 1047–1057.

Badaut J, Fukuda AM, Jullienne A & Petry KG (2014). Aquaporin and brain diseases. *Biochim Biophys Acta - Gen Subj* **1840,** 1554–1565.

Bear J (1972). *Dynamics of fluids in porous media*. American Elsevier Pub. Co., New York.

Becker NH, Novikoff AB & Zimmerman HM (1967). Fine structure observations of the uptake of intravenously injected peroxidase by the rat choroid plexus. *J Histochem Cytochem* **15,** 160–165.

Berg HC (1993). *Random walks in biology*. Princeton University Press, Princeton.

Del Bigio MR, da Silva MC, Drake JM & Tuor UI (1994). Acute and chronic cerebral white matter damage in neonatal hydrocephalus. *Can J Neurol Sci* **21,** 299–305.

Blaumanis OR, Rennels ML & Grady PA (1990). Focal cerebral edema impedes convective fluid/tracer movement through paravascular pathways in cat brain. *Adv Neurol* **52,** 385–389.

Bradbury MW, Cserr HF & Westrop RJ (1981). Drainage of cerebral interstitial fluid into deep cervical lymph of the rabbit. *Am J Physiol* **240,** F329-36.

Bradbury MW & Westrop RJ (1983). Factors influencing exit of substances from cerebrospinal fluid into deep cervical lymph of the rabbit. *J Physiol* **339,** 519–534.

Brinker T, Stopa E, Morrison J & Klinge P (2014). A new look at cerebrospinal fluid circulation. *Fluids Barriers CNS* **11,** 10.

Casley-Smith JR, Földi-Börsök E & Földi M (1976). The prelymphatic pathways of the brain as revealed by cervical lymphatic obstruction and the passage of particles. *Br J Exp Pathol* **57,** 179–188.

Cervós-Navarro J & Ferszt R (1973). Connective tissue in pericapillary spaces of the human spinal cord. *Acta Neuropathol* **24,** 178–183.

Csanda E, Földi M, Obál F & Zoltán OT (1968). Cerebral oedema as a consequence of experimental cervical lymphatic blockage. *Angiologica* **5,** 55–63.

Cserr HF (1971). Physiology of the choroid plexus. *Physiol Rev* **51,** 273–311.

Cserr HF, Cooper DN & Milhorat TH (1977). Flow of cerebral interstitial fluid as indicated by the removal of extracellular markers from rat caudate nucleus. *Exp Eye Res* **25 Suppl,** 461–473.

Cserr HF, Cooper DN, Suri PK & Patlak CS (1981). Efflux of radiolabeled polyethylene glycols and albumin from rat brain. *Am J Physiol* **240,** F319-28.

Cserr HF, DePasquale M, Harling-Berg CJ, Park JT & Knopf PM (1992). Afferent and efferent arms of the humoral immune response to CSF-administered albumins in a rat model with normal blood-brain barrier permeability. *J Neuroimmunol* **41,** 195–202.

Cserr HF & Ostrach LH (1974). Bulk flow of interstitial fluid after intracranial injection of blue dextran 2000. *Exp Neurol* **45,** 50–60.

Cserr HF & Patlak CS (1992). Secretion and bulk flow of interstitial fluid. In *Physiology and Pharmacology of the Blood-Brain Barrier*, ed. Bradbury MW, Handbook of Experimental Pharmacology, pp. 245–261. Springer-Verlag, Berlin Heidelberg.

Damkier HH, Brown PD & Praetorius J (2013). Cerebrospinal fluid secretion by the choroid plexus. *Physiol Rev* **93,** 1847–1892.

Davson H & Segal MB (1995). *Phyioslogy of the CSF and Blood-Brain Barriers*, 1st edn.ed. Davson H & Segal MB. CRC Press, Inc, Boca Raton.

Ebisu T, Naruse S, Horikawa Y, Ueda S, Tanaka C, Uto M, Umeda M & Higuchi T (1993). Discrimination between Different Types of White Matter Edema with Diffusion-weighted MR Imaging. *J Magn Reson Im* **3,** 863–868.

Engelhardt B & Sorokin L (2009). The blood-brain and the blood-cerebrospinal fluid barriers: function and dysfunction. *Semin Immunopathol* **31,** 497–511.

Faber WM (1937). The nasal mucosa and the subarachnoid space. *Am J Anat* **62,** 121–148.

Faubel R, Westendorf C, Bodenschatz E & Eichele G (2016). Cilia-based flow network in the brain ventricles. *Science* **353,** 176–178.

Fenstermacher JD, Ghersi-Egea JF, Finnegan W & Chen JL (1997). The rapid flow of cerebrospinal fluid from ventricles to cisterns via subarachnoid velae in the normal rat. *Acta Neurochir Suppl* **70,** 285–287.

Fenstermacher JD & Kaye T (1988). Drug "diffusion" within the brain. *Ann N Y Acad Sci* **531,** 29–39.

Fenstermacher JD & Patlak CS (1976). The Movements of Water and Solutes in the Brains of Mammals. In *Dynamics of Brain Edema*, ed. Pappius HM & Feindel W, pp. 87–94. Springer Berlin Heidelberg.

Fenstermacher JD, Patlak CS & Blasberg RG (1974). Transport of material between brain extracellular fluid, brain cells and blood. *Fed Proc* **33,** 2070–2074.

Földi M (1996). The brain and the lymphatic system (I). *Lymphology* **29,** 1–9.

Foley CP, Nishimura N, Neeves KB, Schaffer CB & Olbricht WL (2012). Real-time imaging of perivascular transport of nanoparticles during convection-enhanced delivery in the rat cortex. *Ann Biomed Eng* **40,** 292–303.

Frederickson RG & Low FN (1969). Blood vessels and tissue space associated with the brain of the rat. *Am J Anat* **125,** 123–145.

Frigeri A, Gropper MA, Umenishi F, Kawashima M, Brown D & Verkman AS (1995). Localization of MIWC and GLIP water channel homologs in neuromuscular, epithelial and glandular tissues. *J Cell Sci* **108 (Pt 9,** 2993–3002.

Geer CP & Grossman SA (1997). Interstitial fluid flow along white matter tracts: A potentially important mechanism for the dissemination of primary brain tumors. *J Neurooncol* **32,** 193–201.

Ghersi-Egea JF, Finnegan W, Chen JL, Fenstermacher JD & Hospital HF (1996). Rapid distribution of intraventricularly administered sucrose into cerebrospinal fluid cisterns via subarachnoid velae in rat. *Neuroscience* **75,** 1271–1288.

Hadaczek P, Yamashita Y, Mirek H, Tamas L, Bohn MC, Noble C, Park JW & Bankiewicz K (2006). The "perivascular pump" driven by arterial pulsation is a powerful mechanism for the distribution of therapeutic molecules within the brain. *Mol Ther* **14,** 69–78.

Harling-Berg C, Knopf PM, Merriam J & Cserr HF (1989). Role of cervical lymph nodes in the systemic humoral immune response to human serum albumin microinfused into rat cerebrospinal fluid. *J Neuroimmunol* **25,** 185–193.

Hossmann KA (1976). Development and Resolution of Ischemic Brain Swelling. In *Dynamics of Brain Edema*, ed. Pappius HM & Feindel W, pp. 219–227. Springer Berlin Heidelberg.

Ichimura T, Fraser PAA & Cserr HF (1991). Distribution of extracellular tracers in perivascular spaces of the rat brain. *Brain Res* **545,** 103–113.

Iliff JJ, Chen MJ, Plog BA, Zeppenfeld DM, Soltero M, Yang L, Singh I, Deane R & Nedergaard M (2014). Impairment of Glymphatic Pathway Function Promotes Tau Pathology after Traumatic Brain Injury. *J Neurosci* **34,** 16180–16193.

Iliff JJ, Lee H, Yu M, Feng T, Logan J, Nedergaard M & Benveniste H (2013*a*). Brain-wide pathway for waste clearance captured by contrast-enhanced MRI. *J Clin Invest* **123,** 1299–1309.

Iliff JJ, Wang M, Liao Y, Plogg BA, Peng W, Gundersen GA, Benveniste H, Vates GE, Deane R, Goldman SA, Nagelhus EA & Nedergaard M (2012). A paravascular pathway facilitates CSF flow through the brain parenchyma and the clearance of interstitial solutes, including amyloid β. *Sci Transl Med* **4,** 147ra111.

Iliff JJ, Wang M, Zeppenfeld DM, Venkataraman A, Plog B a, Liao Y, Deane R & Nedergaard M (2013*b*). Cerebral arterial pulsation drives paravascular CSF-interstitial fluid exchange in the murine brain. *J Neurosci* **33,** 18190–18199.

Jessen NA, Munk ASF, Lundgaard I & Nedergaard M (2015). The Glymphatic System: A Beginner's Guide. *Neurochem Res*1–17.

Jones EG (1970). On the mode of entry of blood vessels into the cerebral cortex. *J Anat* **106,** 507–520.

Kalimo H, Fredriksson K, Nordborg C, Auer RN, Olsson Y & Johansson B (1986). The spread of brain oedema in hypertensive brain injury. *Med Biol* **64,** 133–137.

Kandel ER, Schwartz JH, Jessell TM, Siegelbaum SA & Hudspeth AJ eds. (2013). *Principles of Neural Science*, 5th edn. McGraw Hill Medical, New York.

Kida S, Pantazis A & Weller RO (1993). CSF drains directly from the subarachnoid space into nasal lymphatics in the rat. Anatomy, histology and immunological significance. *Neuropathol Appl Neurobiol* **19,** 480–488.

Kipnis J (2016). Multifaceted interactions between adaptive immunity and the central nervous system. *Science* **353,** 766–771.

Klatzo I (1967). Presidental address. Neuropathological aspects of brain edema. *J Neuropathol Exp Neurol* **26,** 1–14.

Klatzo I (1987). Pathophysiological aspects of brain edema. *Acta Neuropathol* **72,** 236–239.

Knopf PM, Harling-Berg CJ, Cserr HF, Basu D, Sirulnick EJ, Nolan SC, Park JT, Keir G, Thompson EJ & Hickey WF (1998). Antigen-dependent intrathecal antibody synthesis in the normal rat brain: tissue entry and local retention of antigen-specific B cells. *J Immunol* **161,** 692–701.

Koh L, Zakharov A & Johnston M (2005). Integration of the subarachnoid space and lymphatics: is it time to embrace a new concept of cerebrospinal fluid absorption? *Cerebrospinal Fluid Res* **2,** 6.

Krahn V (1982). The pia mater at the site of the entry of blood vessels into the central nervous system. *Anat Embryol (Berl)* **164,** 257–263.

Kress BT, Iliff JJ, Xia M, Wang M, Wei HS, Zeppenfeld D, Xie L, Kang H, Xu Q, Liew JA, Plog BA, Ding F, Deane R & Nedergaard M (2014). Impairment of paravascular clearance pathways in the aging brain. *Ann Neurol* **76,** 845–861.

Lehmenkühler A, Syková E, Svoboda J, Zilles K & Nicholson C (1993). Extracellular space parameters in the rat neocortex and subcortical white matter during postnatal development determined by diffusion analysis. *Neuroscience* **55,** 339–351.

Levin VA, Fenstermacher JD & Patlak CS (1970). Sucrose and inulin space measurements of cerebral cortex in four mammalian species. *Am J Physiol* **219,** 1528–1533.

Louveau A, Da Mesquita S & Kipnis J (2016). Lymphatics in Neurological Disorders: A Neuro-Lympho-Vascular Component of Multiple Sclerosis and Alzheimer's Disease? *Neuron* **91,** 957–973.

Louveau A, Smirnov I, Keyes TJ, Eccles JD, Rouhani SJ, Peske JD, Derecki NC, Castle D, Mandell JW, Lee KS, Harris TH & Kipnis J (2015). Structural and functional features of central nervous system lymphatic vessels. *Nature* **523,** 337–341.

Mabuchi T, Lucero J, Feng A, Koziol J a & del Zoppo GJ (2005). Focal cerebral ischemia preferentially affects neurons distant from their neighboring microvessels. *J Cereb Blood Flow Metab* **25,** 257–266.

Maynard EA, Schultz RL & Pease DC (1957). Electron microscopy of the vascular bed of rat cerebral cortex. *Am J Anat* **100,** 409–433.

Mazel T, Simonová Z & Syková E (1998). Diffusion heterogeneity and anisotropy in rat hippocampus. *Neuroreport*

9, 1299–1304.

McLone DG, Bondareff W & Raimondi AJ (1971). Brain edema in the hydrocephalic hy-3 mouse: submicroscopic morphology. *J Neuropathol Exp Neurol* **30,** 627–637.

Nabeshima S, Reese TS, Landis DM & Brightman MW (1975). Junctions in the meninges and marginal glia. *J Comp Neurol* **164,** 127–169.

Nag S, Manias JL & Stewart DJ (2009). Pathology and new players in the pathogenesis of brain edema. *Acta Neuropathol* **118,** 197–217.

Nagelhus EA, Mathiisen TM & Ottersen OP (2004). Aquaporin-4 in the central nervous system: cellular and subcellular distribution and coexpression with KIR4.1. *Neuroscience* **129,** 905–913.

Nicholson C (2001). Diffusion and related transport mechanisms in brain tissue. *Reports Prog Phys* **64,** 815–884.

Nicholson C & Phillips JM (1981). Ion diffusion modified by tortuosity and volume fraction in the extracellular microenvironment of the rat cerebellum. *J Physiol* **321,** 225–257.

Nicholson C & Syková E (1998). Extracellular space structure revealed by diffusion analysis. *Trends Neurosci* **21,** 207–215.

Nicholson C & Tao L (1993). Hindered diffusion of high molecular weight compounds in brain extracellular microenvironment measured with integrative optical imaging. *Biophys J* **65,** 2277–2290.

Nielsen S, Nagelhus EA, Amiry-Moghaddam M, Bourque C, Agre P & Ottersen OP (1997). Specialized membrane domains for water transport in glial cells: high-resolution immunogold cytochemistry of aquaporin-4 in rat brain. *J Neurosci* **17,** 171–180.

Nolte J (2009). *The Human Brain: An Introduction to its Functional Anatomy*, 6th edn. Elsevier, Amsterdam.

Novak U & Kaye AH (2000). Extracellular matrix and the brain: components and function. *J Clin Neurosci* **7,** 280–290.

Ohata K & Marmarou A (1992). Clearance of brain edema and macromolecules through the cortical extracellular space. *J Neurosurg* **77,** 387–396.

Ohata K, Marmarou A & Povlishock JT (1990). An immunocytochemical study of protein clearance in brain infusion edema. *Acta Neuropathol* **81,** 162–177.

Paxinos G & Mai JK (2004). *The Human Nervous System*. Elsevier Inc., Amsterdam.

Peters A, Palay SSL & Webster H deF. (1991). *The fine structure of the nervous system: neurons and their supporting cells*, 3rd edn. Oxford University Press, New York.

Pollock H, Hutchings M, Weller RO & Zhang ET (1997). Perivascular spaces in the basal ganglia of the human brain: their relationship to lacunes. *J Anat* **191 (Pt 3,** 337–346.

Preston SD, Steart P V., Wilkinson A, Nicoll J a R & Weller RO (2003). Capillary and arterial cerebral amyloid angiopathy in Alzheimer's disease: defining the perivascular route for the elimination of amyloid beta from the human brain. *Neuropathol Appl Neurobiol* **29,** 106–117.

Proescholdt MG, Hutto B, Brady LS & Herkenham M (2000). Studies of cerebrospinal fluid flow and penetration into brain following lateral ventricle and cisterna magna injections of the tracer [14C]inulin in rat. *Neuroscience* **95,** 577–592.

Rennels ML, Blaumanis OR & Grady PA (1990). Rapid solute transport throughout the brain via paravascular fluid pathways. *Adv Neurol* **52,** 431–439.

Rennels ML, Gregory TF, Blaumanis OR, Fujimoto K & Grady PA (1985). Evidence for a "paravascular" fluid circulation in the mammalian central nervous system, provided by the rapid distribution of tracer protein throughout the brain from the subarachnoid space. *Brain Res* **326,** 47–63.

Reulen HJ, Graham R, Spatz M & Klatzo I (1977). Role of pressure gradients and bulk flow in dynamics of vasogenic brain edema. *J Neurosurg* **46,** 24–35.

Reulen HJ, Tsuyumu M, Tack A, Fenske AR & Prioleau GR (1978). Clearance of edema fluid into cerebrospinal fluid: A mechanism for resolution of vasogenic brain edema. *J Neurosurg* **48,** 754–764.

Rosenberg GA, Kyner WT & Estrada E (1980). Bulk flow of brain interstitial fluid under normal and hyperosmolar conditions. *Am J Physiol* **238,** F42–F49.

Sakka L, Coll G & Chazal J (2011). Anatomy and physiology of cerebrospinal fluid. *Eur Ann Otorhinolaryngol Head Neck Dis* **128,** 309–316.

Schlageter KE, Molnar P, Lapin GD & Groothuis DR (1999). Microvessel organization and structure in experimental brain tumors: microvessel populations with distinctive structural and functional properties. *Microvasc Res* **58,** 312–328.

Schuenke M, Schulte E & Schumacher U (2010). *Thieme Atlas of Anatomy: Head and Neuroanatomy*, 1st edn. Thieme, New York.

Shima K & Marmarou A (1990). Clearance of infusion edema fluid at high and low levels of intracranial pressure. **1990/01/01,** 285–287.

Strazielle N & Ghersi-Egea JF (2000). Choroid plexus in the central nervous system: biology and physiopathology. *J Neuropathol Exp Neurol* **59,** 561–574.

Syková E & Nicholson C (2008). Diffusion in brain extracellular space. *Physiol Rev* **88,** 1277–1340.

Syková E, Vorísek I, Antonova T, Mazel T, Meyer-Luehmann M, Jucker M, Hájek M, Ort M & Bures J (2005). Changes in extracellular space size and geometry in APP23 transgenic mice: a model of Alzheimer's disease. *Proc Natl Acad Sci U S A* **102,** 479–484.

Szentistványi I, Patlak CS, Ellis RA & Cserr HF (1984). Drainage of interstitial fluid from different regions of rat brain. *Am J Physiol* **246,** 35–44.

Tao L & Nicholson C (1996). Diffusion of albumins in rat cortical slices and relevance to volume transmission. *Neuroscience* **75,** 839–847.

Thorne RG (2014). Primer on Central Nervous System Structure/Function and the Vasculature, Ventricular System, and Fluids of the BRain. In *Drug Delivery to the Brain: Physiological Concepts, Methodologies, and Approaches*, ed. Hammarlund-Udenaes M, de Lange E & Thorne RG, pp. 685–707. Springer-Verlag, New York.

Thorne RG, Hrabetová S & Nicholson C (2004). Diffusion of epidermal growth factor in rat brain extracellular space measured by integrative optical imaging. *J Neurophysiol* **92,** 3471–3481.

Thorne RG, Lakkaraju A, Rodriguez-Boulan E & Nicholson C (2008). In vivo diffusion of lactoferrin in brain extracellular space is regulated by interactions with heparan sulfate. *Proc Natl Acad Sci USA* **105,** 8416–8421.

Thorne RG & Nicholson C (2006). In vivo diffusion analysis with quantum dots and dextrans predicts the width of brain extracellular space. *Proc Natl Acad Sci USA* **103,** 5567–5572.

Verbalis JG (2010). Brain volume regulation in response to changes in osmolality. *Neuroscience* **168,** 862–870.

Vorisek I & Sykova E (1997). Ischemia-induced changes in the extracellular space diffusion parameters, K+, and pH in the developing rat cortex and corpus callosum. *J Cereb Blood Flow Metab* **17,** 191–203.

Vorísek I & Syková E (1997). Evolution of anisotropic diffusion in the developing rat corpus callosum. *J Neurophysiol* **78,** 912–919.

Wagner HJ, Pilgrim C & Brandl J (1974). Penetration and removal of horseradish peroxidase injected into the cerebrospinal fluid: Role of cerebral perivascular spaces, endothelium and microglia. *Acta Neuropathol* **27,** 299–315.

Walter BA, Valera VA, Takahashi S, Matsuno K & Ushiki T (2006*a*). Evidence of antibody production in the rat cervical lymph nodes after antigen administration into the cerebrospinal fluid. *Arch Histol Cytol* **69,** 37–47.

Walter BA, Valera VA, Takahashi S & Ushiki T (2006*b*). The olfactory route for cerebrospinal fluid drainage into the peripheral lymphatic system. *Neuropathol Appl Neurobiol* **32,** 388–396.

Watson C, Kirkcaldie M & Paxinos G (2010). *The Brain: An Introduction to Functional Neuroanatomy*. Academic Press.

Weller RO (1998). Pathology of cerebrospinal fluid and interstitial fluid of the CNS: significance for Alzheimer disease, prion disorders and multiple sclerosis. *J Neuropathol Exp Neurol* **57,** 885–894.

Weller RO, Djuanda E, Yow H-Y & Carare RO (2009). Lymphatic drainage of the brain and the pathophysiology of neurological disease. *Acta Neuropathol* **117,** 1–14.

Weller RO, Kida S & Zhang ET (1992). Pathways of fluid drainage from the brain--morphological aspects and immunological significance in rat and man. *Brain Pathol* **2,** 277–284.

Weller RO, Subash M, Preston SD, Mazanti I & Carare RO (2008). Perivascular drainage of amyloid-beta peptides from the brain and its failure in cerebral amyloid angiopathy and Alzheimer's disease. *Brain Pathol* **18,** 253–266.

Wen H (1999). Ontogeny of water transport in rat brain: Postnatal expression of the aquaporin-4 water channel. *Eur J Neurosci* **11,** 935–945.

Wilson MH, Newman S & Imray CH (2009). The cerebral effects of ascent to high altitudes. *Lancet Neurol* **8,** 175–191.

Wolak DJ, Pizzo ME & Thorne RG (2015). Probing the extracellular diffusion of antibodies in brain using in vivo integrative optical imaging and ex vivo fluorescence imaging. *J Control Release* **197,** 78–86.

Wolak DJ & Thorne RG (2013). Diffusion of macromolecules in the brain: implications for drug delivery. *Mol Pharm* **10,** 1492–1504.

Xie L, Kang H, Xu Q, Chen MJ, Liao Y, Thiyagarajan M, O'Donnell J, Christensen DJ, Nicholson C, Iliff JJ, Takano T, Deane R & Nedergaard M (2013). Sleep drives metabolite clearance from the adult brain. *Science* **342,** 373–377.

Yao X, Hrabetova S, Nicholson C & Manley GT (2008). Aquaporin-4-Deficient Mice Have Increased Extracellular Space without Tortuosity Change. *J Neurosci* **28,** 5460–5464.

Zervas NT, Liszczak TM, Mayberg MR & Black PM (1982). Cerebrospinal fluid may nourish cerebral vessels through pathways in the adventitia that may be analogous to systemic vasa vasorum. *J Neurosurg* **56,** 475–481.

Zhang ET, Inman CB & Weller RO (1990). Interrelationships of the pia mater and the perivascular (Virchow-Robin) spaces in the human cerebrum. *J Anat* **170,** 111–123.

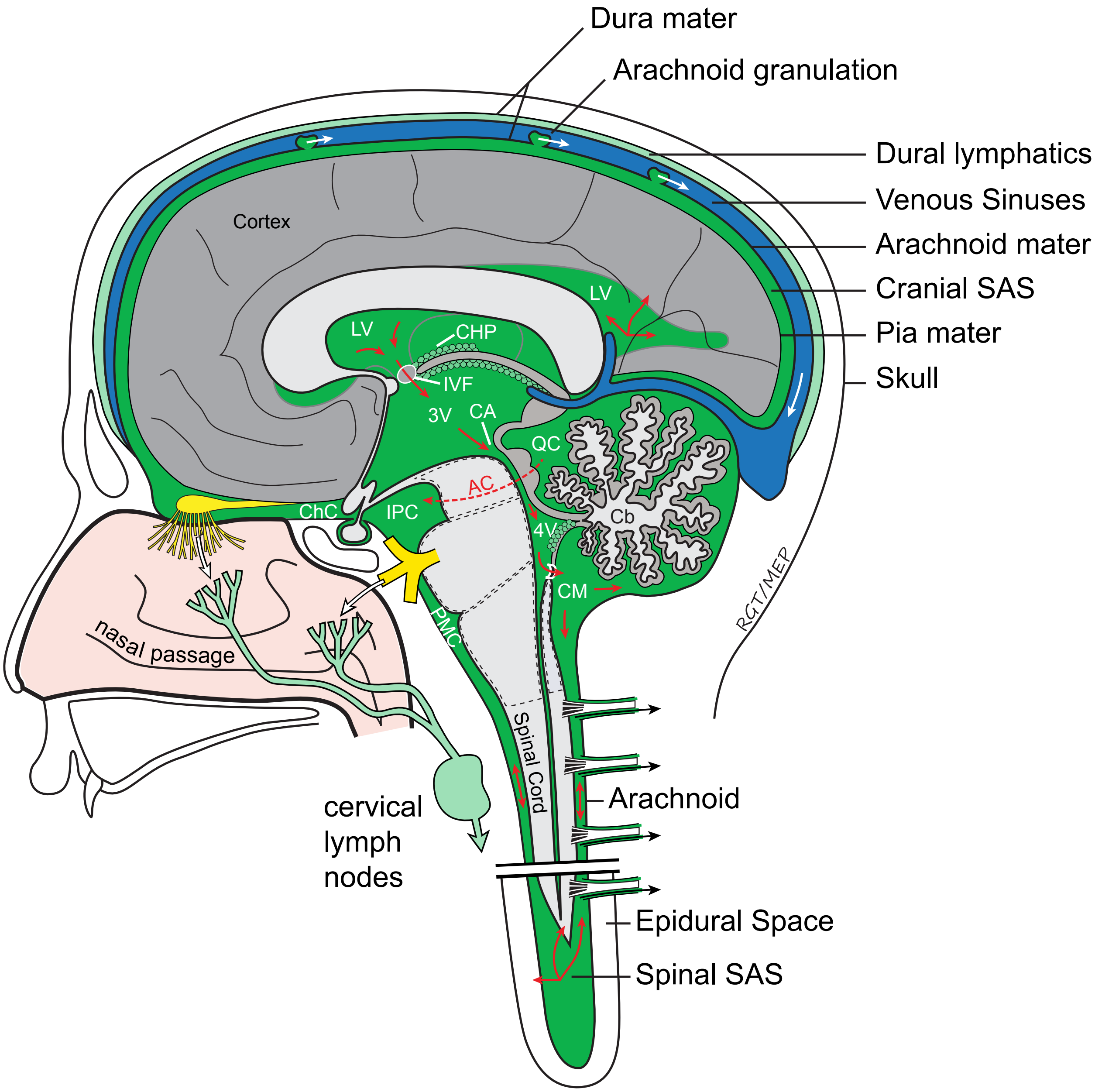

Figure 1. Cerebrospinal fluid compartments, flow pattern, and drainage routes. The CSF (green) flows through the ventricular system (red arrows) and into the subarachnoid space surrounding the brain and spinal cord. The CSF exit pathways (white arrows) include drainage into the venous sinuses of the dura via arachnoid granulations, drainage along cranial nerves (i.e., olfactory nerves and trigeminal nerves) into the nasal mucosa and deep cervical lymph nodes, and drainage along spinal nerves to intercostal and other lymph nodes. Additionally, lymphatic vessels in the dura may be a route for CSF to drain to the cervical lymph nodes. Abbreviations: SAS = subarachnoid space;

LV = lateral ventricle; CHP = choroid plexus; IVF = interventricular foramen; 3V = third ventricle; CA = cerebral aqueduct; 4V = fourth ventricle; CM = cisterna magna (cerebellomedullary cistern); QC = quadrigeminal cistern; AC = ambient cistern; ChC = chiasmatic cistern; IPC = interpeduncular cistern; PMC = pontomedullary cistern; Cb = cerebellum.

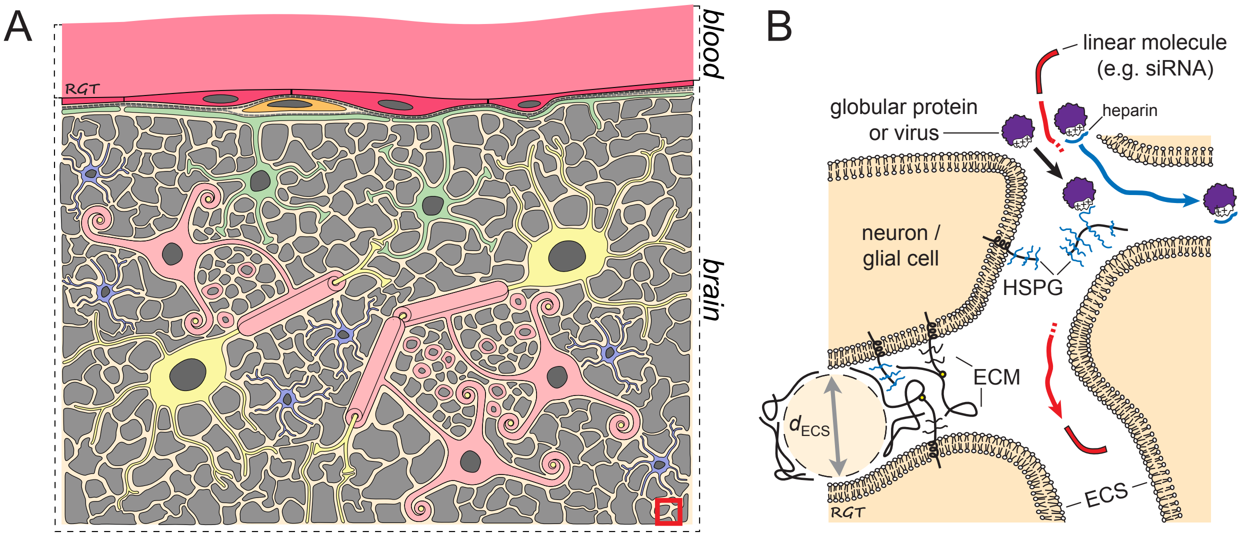

Figure 2. The brain microenvironment—blood-brain barrier and extracellular space. (A) The brain parenchyma is composed of several different cell types including neurons (yellow), oligodendrocytes (pink), microglia (blue), and astrocytes (green); these cells and their processes (gray) create a very narrow and tortuous extracellular space (ECS). Brain microvessels are composed of endothelial cells (dark pink) and their basement membrane (dashed dark gray line) and associated pericytes (light orange). Astrocyte foot processes and their basement membrane (dashed light gray line) further separate the blood vessels from the brain parenchyma and the extracellular spaces of the brain. (B) A magnified view of the ECS (red box) illustrates how linear molecules (e.g., siRNA) or globular macromolecules and macromolecular assemblies (e.g., proteins or viral vectors) are believed to diffuse through the ECS, and how the extracellular matrix (ECM) components (e.g., heparan sulfate proteoglycans) and the ECS width (dECS) may influence their diffusion. It is possible to improve transport of substances through the ECS by reducing binding to ECM components, for example, complexing heparin to lactoferrin to reduce lactoferrin binding to heparan sulfate proteoglycans (blue line).

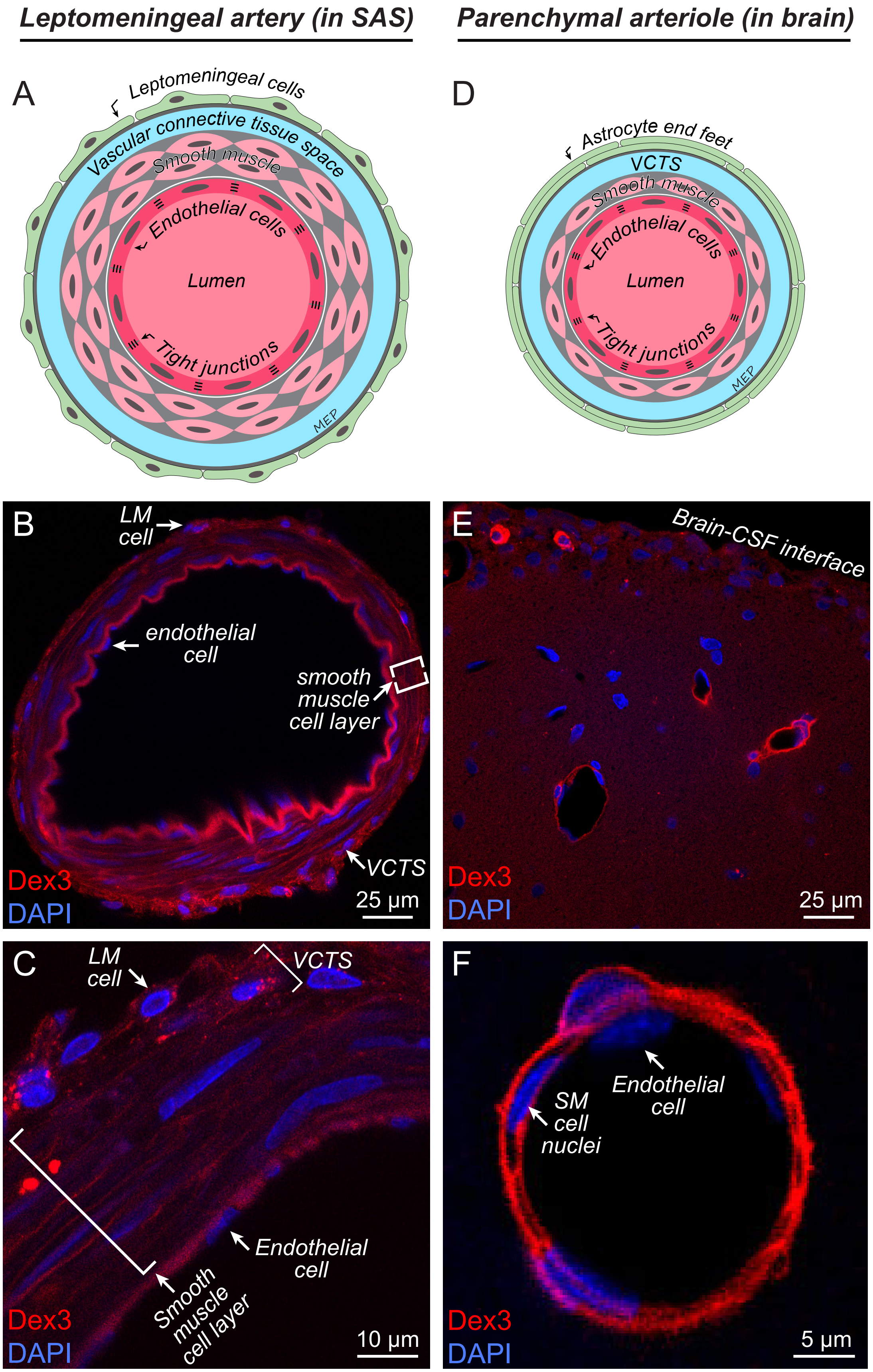
Leptomeningeal artery (in SAS)
Parenchymal arteriole (in brain)
A
Leptomeningeal cells
Vascular connective tissue space
Smooth muscle
Endothelial cells
Lumen
Tight junctions
MEP
D
Astrocyte end feet
VCTS
Smooth muscle
Endothelial cells
Lumen
Tight junctions
MEP
B
LM cell
endothelial cell
smooth muscle cell layer
VCTS
Dex3
DAPI
25 µm
E
Brain-CSF interface
Dex3
DAPI
25 µm
C
LM cell
VCTS
Endothelial cell
Smooth muscle cell layer
Dex3
DAPI
10 µm
F
Endothelial cell
SM cell nuclei
Dex3
DAPI
5 µm

Figure 3. The perivascular space of cerebral blood vessels. (A) Schematic of the layers of a leptomeningeal artery in the subarachnoid space on the brain surface. The blood vessel is ensheathed by a layer of leptomeningeal cells (light green) and a vascular connective tissue space (VCTS), generally referred to as the perivascular space (light blue). The artery wall consists of (outer to inner): circumferentially arranged smooth muscle (SM) cells (light pink) which may be several layers thick, and their surrounding SM basement membrane (gray); an internal elastic lamina (white line); and the endothelial cell basement membrane (gray) and endothelial cells (dark pink), joined by tight junctions. (B) Texas Red labeled 3 kDa dextran was infused for 50 minutes into the cisterna magna in rats (for method details, see reference (Wolak et al., 2015)) and the distribution in brain slices observed using ex vivo confocal microscopy. A cross section of the intracranial internal carotid artery, a large leptomeningeal artery, shows 3 kDa dextran around leptomeningeal (LM) cells, in the perivascular/ vascular connective tissue space (adventitia), and around smooth muscle cells (tunica media), most likely in the smooth muscle basement membrane, demonstrating that CSF can access the perivascular space and the arterial wall. (C) A magnified image of the wall of the artery of a branch of the anterior cerebral artery also demonstrates 3 kDa dextran in and around the arterial wall. (D) Schematic of an arteriole in the brain parenchyma. The arteriole has fewer smooth muscle cell layers and is separated from the brain parenchyma by astrocyte endfeet (light green) and their basement membrane (gray). (E) After infusion of 3 kDa dextran into the CSF, the dextran has entered into the perivascular spaces of various-sized blood vessels in the cortical parenchyma near the brain surface. A putative arteriole in the frontal cortex shows dextran distributed throughout the arteriole wall, surrounding SM cells (empty pockets, some show DAPI staining of SM cell nuclei), likely distributed within the SM and endothelial basement membranes. Note, the spaces in the schematic drawings are not necessarily drawn to scale, but the vascular connective tissue space/perivascular space is not generally visible in light microscopy (i.e., around the arteriole in F) due to changes in the tissue with aldehyde fixation and processing.

CHAPTER 2
Intrathecal antibody distribution in the rat brain: surface diffusion, perivascular transport, and osmotic enhancement of delivery

Michelle E. Pizzo[1,2], Daniel J. Wolak[1,2], Niyanta N. Kumar[1], Eric Brunette[9], Christina L. Brunnquell[3], Melanie-Jane Hannocks[10,11], N. Joan Abbott[8], M. Elizabeth Meyerand[2-4], Lydia Sorokin[10,11], Danica B. Stanimirovic[9], Robert G. Thorne[1,2,5-7]
[1]School of Pharmacy, Division of Pharmaceutical Sciences; [2]Clinical Neuroengineering Training Program; [3]Department of Medical Physics; [4]Department of Biomedical Engineering; [5]Neuroscience Training Program; [6]Cellular and Molecular Pathology Graduate Program; [7]Institute for Clinical and Translational Research; University of Wisconsin-Madison, USA; [8]Institute of Pharmaceutical Science, King's College London, UK; [9]Human Health Therapeutics Research Centre, National Research Council of Canada, Ottawa, Canada; [10]Institute of Physiological Chemistry and Pathobiochemistry, [11]Cells-in-Motion Cluster of Excellence, Muenster University, Muenster, Germany

Reproduced with permission from:
Pizzo ME, Wolak DJ, Kumar NN, Brunette E, Brunnquell CL, Hannocks M-J, Abbott NJ, Meyerand ME, Sorokin L, Stanimirovic DB & Thorne RG (2018). Intrathecal antibody distribution in the rat brain: surface diffusion, perivascular transport and osmotic enhancement of delivery. J Physiol 596, 445–475.

Key Points

- It has been unclear precisely how macromolecules, e.g., endogenous proteins and exogenous immunotherapeutics, access brain tissue from the cerebrospinal fluid (CSF).
- We show that transport at the brain-CSF interface involves a balance between Fickian diffusion in the extracellular spaces at the brain surface and convective transport in perivascular spaces of cerebral blood vessels.
- Intrathecally-infused antibodies exhibited size-dependent access to the perivascular spaces and tunica media basement membranes of leptomeningeal arteries; perivascular access and distribution of full-length IgG could be enhanced by intrathecal co-infusion of hyperosmolar mannitol.
- Pores or stomata present on CSF-facing leptomeningeal cells ensheathing blood vessels in the subarachnoid space may provide unique entry sites into the perivascular spaces from the CSF.
- These results illuminate new mechanisms likely to govern antibody trafficking at the brain-CSF interface with relevance for immune surveillance in the healthy brain and insights into the distribution of therapeutic antibodies.

Abstract

The precise mechanisms governing the central distribution of macromolecules from the cerebrospinal fluid (CSF) to the brain and spinal cord remain poorly understood, despite their importance for physiological processes such as antibody trafficking for central immune surveillance as well as several ongoing intrathecal clinical trials. Here, we clarify how immunoglobulin G (IgG) and smaller single-domain antibodies (sdAb) distribute throughout the whole brain in a size-dependent manner after intrathecal infusion in rats using *ex vivo* fluorescence and *in vivo* 3D magnetic resonance imaging. Antibody distribution was characterized by diffusion at the brain surface and widespread distribution to deep brain regions along perivascular spaces of all vessel types, with sdAb accessing 4-7 times greater brain area than IgG. Perivascular transport involved blood vessels of all caliber and putative smooth muscle and astroglial basement membrane compartments. Perivascular access to smooth muscle basement membrane compartments also exhibited size-dependence. Electron microscopy was used to show stomata on leptomeningeal coverings of blood vessels in the subarachnoid space as potential access points for substances in the CSF to enter the perivascular space. Osmolyte co-infusion significantly enhanced perivascular access of the larger antibody from the CSF, with intrathecal 0.75 M mannitol increasing the number of perivascular profiles per slice area accessed by IgG by approximately 50%. Our results reveal potential distribution mechanisms for endogenous IgG, one of the most abundant proteins in the CSF, as well as provide new insights needed to understand and improve drug delivery of macromolecules to the central nervous system via the intrathecal route.

Introduction

Extracellular transport of molecules between the cerebrospinal fluid (CSF) and the interstitial fluid (ISF) of the central nervous system (CNS) has long been thought to involve size-dependent diffusional transport in brain extracellular space (ECS) and potentially size-independent convective flow pathways elsewhere (Abbott, 2004; Syková & Nicholson, 2008; Wolak & Thorne, 2013); however, it has recently been suggested that a clearance process exists that relies in some part on convective flow through the brain parenchyma (Iliff *et al.*, 2012; Nedergaard, 2013). While the precise mechanisms of distribution for endogenous and therapeutic macromolecules between the CSF and brain ISF are not yet fully established, an abundance of physiological evidence has nevertheless indicated that transport in the brain parenchyma is governed by diffusion in the small (40-60 nm (Thorne & Nicholson, 2006)), tortuous ECS of the neuropil (Fenstermacher & Patlak, 1976; Thorne *et al.*, 2004; Thorne & Nicholson, 2006; Syková & Nicholson, 2008; Wolak & Thorne, 2013). Faster convective or bulk flow occurs in the CSF (Davson & Segal, 1995) and decades-old experimental work has also suggested flow could potentially occur in the perivascular (PV) spaces (PVS), white matter tracts, and the subependymal region (Cserr *et al.*, 1977; Szentistványi *et al.*, 1984; Ichimura *et al.*, 1991). Indeed, there is now great interest regarding the specific mechanisms of distribution and the role of the PVS in fluid and solute exchange in the CNS (Iliff *et al.*, 2012; Xie *et al.*, 2013; Jin *et al.*, 2016; Asgari *et al.*, 2016).

Brain delivery of substances other than small molecules has so far proven extremely difficult (Hammarlund-Udenaes *et al.*, 2014), particularly for biologics with limited-to-negligible permeability at the blood-brain barrier (Davson & Segal, 1995; Abbott *et al.*, 2006; Calias *et al.*, 2014) and further transport limitations within the CNS (Syková & Nicholson, 2008; Wolak *et al.*, 2015). There is a critical unmet need for alternative delivery approaches, including semi-invasive strategies such as administration into the CSF (Papisov *et al.*, 2013). Delivering biologics (e.g., antibodies) to the CNS via the CSF has been the focus of pre-clinical and early stage clinical work (Thakker *et al.*, 2009; Calias *et al.*, 2014), but the specific mechanisms of transport and detailed patterns of distribution are still in question (Wolak & Thorne, 2013), despite numerous clinical trials testing intrathecal infusions in children and adults (Calias *et al.*, 2014; clinicaltrials.gov). Although diffusional transport over the large distances required for whole brain delivery from the CSF is unlikely for all but the smallest species (Wolak & Thorne, 2013; Wolak *et al.*, 2015), growing evidence suggests the cerebrovascular PVS may offer a unique route for achieving rapid, widespread drug distribution via convective/bulk flow (Lochhead *et al.*, 2015).

The PVS (Fig. 1) is a compartment surrounding both leptomeningeal blood vessels and parenchymal blood vessels typically described as being filled with fluid, connective tissue, scattered cells, and possibly basement membranes (BM); it is thought to be analogous to the vessel adventitia (Frederickson & Low, 1969; Jones, 1970; Krisch *et al.*, 1984; Zhang *et al.*, 1990; Sixt *et al.*, 2001; Wu *et al.*, 2009) and possibly also the BM of the tunica media (Carare *et al.*, 2008; Weller *et al.*, 2008). Such a space has been demonstrated in many species from rodents (Frederickson & Low, 1969) to cats (Jones, 1970) to humans (Zhang *et al.*, 1990). The natural dimensions of the rodent PVS appear to be on the order of ~5-10 μm wide at the brain surface (Ichimura *et al.*, 1991; Foley *et al.*, 2012; Iliff *et al.*, 2012), becoming smaller as the vessel diameter narrows in the parenchyma (Frederickson & Low, 1969); the PVS is therefore substantially larger than the brain ECS and far more likely to accommodate flow due to a much lower hydraulic resistance (Wolak & Thorne, 2013). The PVS appears to be in communication with the subpial space (Krisch *et al.*, 1984; Hutchings & Weller, 1986; Ichimura *et al.*, 1991) and possibly also the subarachnoid space (SAS) via fenestrations in the pia mater (Frederickson & Low, 1969; Jones, 1970; Cloyd & Low, 1974; Ichimura *et al.*, 1991) and/or in the leptomeningeal sheaths around subarachnoid blood vessels (Jones, 1970; Cloyd & Low, 1974; Zervas *et al.*, 1982), but such fenestrations have not been well described for rodents (Frederickson & Low, 1969; Oda & Nakanishi, 1984).

Much evidence suggests that bulk flow occurs in the PVS (Cserr *et al.*, 1977, 1981; Rennels *et al.*, 1985; Ichimura *et al.*, 1991; Ghersi-Egea *et al.*, 1996*a*; Proescholdt *et al.*, 2000; Abbott, 2004; Hadaczek *et al.*, 2006*b*), potentially driven by arterial pulsations (Rennels *et al.*, 1985; Hadaczek *et al.*, 2006*b*; Iliff *et al.*, 2013*b*); indeed, the PVS has been described as a conduit for the rapid influx (Rennels *et al.*, 1985; Iliff *et al.*, 2012), efflux (Cserr *et al.*, 1977; Szentistványi *et al.*, 1984; Ichimura *et al.*, 1991; Zhang *et al.*, 1992; Carare *et al.*, 2008), and possible circulation of a variety of experimentally applied tracer substances (Rennels *et al.*, 1985; Iliff *et al.*, 2012; Nedergaard, 2013). Pioneering work by Helen Cserr and others long suggested a possible lymphatic role for the PVS (Casley-Smith *et al.*, 1976; Bradbury *et al.*, 1981; Cserr *et al.*, 1981; Yamada *et al.*, 1991; Zhang *et al.*, 1992; Kida *et al.*, 1993), since the brain parenchyma appeared to lack the lymphatic vessels typical of non-CNS tissues (Cserr *et al.*, 1977, 1981; Engelhardt *et al.*, 2017). The PVS also may provide a pathway for cellular migration for the purpose of CNS immune surveillance (Fabry *et al.*, 2008; Ransohoff & Engelhardt, 2012; Engelhardt *et al.*, 2017). Lastly, the PVS may play some role in CSF/ISF clearance, in addition to drainage pathways along nerves (Faber, 1937; Bradbury & Westrop, 1983; Weller *et al.*, 1992; Cserr & Knopf, 1992; Kida *et al.*, 1993; Koh *et al.*, 2005) and dural lymphatics (Kida *et al.*, 1993; Furukawa *et al.*, 2008; Aspelund *et al.*, 2015; Louveau *et al.*, 2015) to the cervical lymph nodes.

Several unresolved issues remain regarding transport in and around the PVS. First, it is not yet clear what precise anatomical boundaries define where transport can occur (Rennels *et al.*, 1985; Carare *et al.*, 2008). Second, there is uncertainty over the factors dictating whether peri-capillary transport is possible (Maynard *et al.*, 1957; Jones, 1970; Cervós-Navarro & Ferszt, 1973; Peters *et al.*, 1991). Third, a lack of consensus is evident regarding the specific sites of PV influx, PV efflux, and the potential for PV circulation (Rennels *et al.*, 1985; Zhang *et al.*, 1992; Carare *et al.*, 2008; Iliff *et al.*, 2012), e.g., what is the direction of PV flow along arteries versus veins (Ichimura *et al.*, 1991; Wang & Olbricht, 2011; Morris *et al.*, 2016; Coloma *et al.*, 2016)? Fourth, there has been speculation that a PV circulation involves convective flow through the ECS of the neuropil from peri-arterial to peri-venous spaces that is facilitated by glial aquaporin-4 water channels (the 'glymphatic' hypothesis (Iliff *et al.*, 2012; Nedergaard, 2013)), although such a flow through the parenchyma has been questioned (Wolak & Thorne, 2013; Hladky & Barrand, 2014; Jin *et al.*, 2016; Asgari *et al.*, 2016); indeed, numerous experimental studies have shown transport in brain ECS to be diffusive in nature (Fenstermacher & Patlak, 1976; Thorne *et al.*, 2004; Thorne & Nicholson, 2006; Syková & Nicholson, 2008; Wolak & Thorne, 2013). Finally, where and how CSF-borne molecules enter the PVS has not yet been clearly addressed. Here, we have utilized *ex vivo* fluorescence and *in vivo* magnetic resonance imaging (MRI) with intrathecal infusions of well-characterized, non-targeted full-length immunoglobulin G (IgG) and single-domain antibody (sdAb) conjugates to address many of these issues. IgG and sdAb span a size range (~15 kDa – 150 kDa) that brackets most major endogenous biomolecules, particularly proteins in highest concentration in the CSF (e.g., albumin, IgG (Davson & Segal, 1995)), as well as proteins with high clinical/therapeutic potential (e.g., lysosomal enzymes, antibody fragments, and full-length antibodies (Calias *et al.*, 2014)). Our results demonstrate that extracellular parenchymal diffusion and perivascular flow together produce unique size-dependent distribution of antibodies from CSF-to-brain and that perivascular IgG access can be osmotically manipulated to increase brain distribution.

Materials and Methods

Ethical Approval

Experiments were carried out at the University of Wisconsin-Madison in accordance with the National Institutes of Health Guide for the Care and Use of Laboratory Animals (2011), local Institutional Animal Care and Use Committee regulations, and *The Journal of Physiology's* guidelines on animal ethics. Rats had access to food and water *ad libitum* and were housed in a climate-controlled room on a 12 hour light/dark cycle. All experiments were terminal and every effort was made to minimize the animal's pain and distress.

Intracisternal infusions in rats

Female Sprague-Dawley rats (180-230 g; approximately 9-14 weeks of age; Harlan/Envigo) were anesthetized with urethane (1.3 g/kg i.p.) and supplemented (0.375 g/kg urethane i.p.) to effect as determined by the absence of a pedal reflex. Body temperature was maintained at 37°C using a homeothermic blanket system (Harvard Apparatus). Rats were then tracheotomized, subcutaneously administered 0.05 mL 2% lidocaine hydrochloride at the scalp for analgesia, and placed in a stereotaxic frame (Stoelting). Atropine sulfate (0.1 mg/kg every two hours) was administered subcutaneously to diminish bronchial secretions. Rats underwent a dorsal, midline neck incision followed by resection of subcutaneous tissues and posterior vertebral muscles to expose the atlanto-occipital membrane. The atlanto-occipital membrane was then retracted to reveal the dura overlying the cisterna magna for cannula insertion. A custom cannula consisting of 1.5 cm 33 GA polyetheretherketone tubing (PEEK; Plastics One) connected via PE-10 tubing (Solomon Scientific) to a Hamilton syringe controlled by an infusion pump (Quintessential Stereotaxic Injector, Stoelting) was filled with infusate prior to insertion. A small hole was created in the dura with a 30 GA dental needle (Exel International) and the PEEK cannula was immediately advanced 1 mm into the cisterna magna, at a 30-degree angle from the horizontal and with the head approximately in the flat skull position; after insertion, the cannula was carefully fixed in place by cyanoacrylate with the dura tightly sealed around it.

Non-targeted AlexaFluor488 single-domain antibody (sdAb; llama-derived A20.1 V_HH antibody fragment against *C. difficile* toxin, with no known mammalian target (DBS; Farrington *et al.*, 2014)) or AlexaFluor488 goat-anti-rabbit IgG (IgG; A-11034, Life Technologies; characterized in a previous study (Wolak *et al.*, 2015)) was infused intracisternally at 1.6 µL/min for 50 min (80 µL total). Following infusion, the abdominal aorta was cannulated with the animal supine, and 50 mL ice-cold 0.01 M phosphate-buffered saline (PBS; pH 7.4) was perfused at 15 mL/min (beginning 30 min post-infusion), euthanizing animals by exsanguination, followed by perfusion with 450 mL 4% paraformaldehyde in 0.1 M phosphate buffer. 0.5 mL blood was withdrawn one min prior to perfusion through the abdominal aorta cannula in a subset of animals.

Ex vivo fluorescence imaging

The whole brain, cervical lymph nodes, nasal passages, and spinal cord were removed/dissected and imaged immediately using an Olympus MVX10 Macroview microscope equipped with an Orca-flash 2.8 CMOS camera (Hamamatsu) and Lumen Dynamics X-Cite 120Q illuminator using the appropriate filter set (Chroma, U-M49002XL). Whole brains and nasal passages were imaged in 2-3 overlapping sections and at multiple planes of focus; each section was first auto-blended and then overlapping sections were manually aligned and auto-blended into a single larger image using Photoshop CC (Adobe). After post-fixation in 4% PFA overnight at 4°C brains were sectioned on a vibratome (100 μm; Leica VT1000S) and immediately imaged on a wet petri dish. Lymph nodes and nasal passages were put in 20% sucrose overnight at 4°C, frozen in isopentane on dry ice, sectioned (25 μm) using a cryostat (Leica CM1950), and mounted onto slides (Prolong Gold or Diamond Antifade, with or without DAPI, Life Technologies).

Plasma levels

Following intrathecal infusion and just prior to perfusion (79 min) in some animals, 0.5 mL blood was drawn via cardiac puncture or abdominal aorta cannula, added to a collection tube with heparin, and kept on ice. Blood was spun for 10 min at 3,000 × *g* and the supernatant then spun for 10 min at 10,000 × *g*. The supernatant was removed for fluorescence quantification on a microplate reader (FLUOstar Omega, BMG LABTECH). Untreated or saline infused animals (*N*=6) were used as controls. IgG concentration in plasma was determined by comparison with a standard curve.

Magnetic Resonance Imaging (MRI)

All MRI experiments utilized an Agilent 4.7T small animal MRI acquired using VnmrJ software. After scout scans, and optional T2 anatomical scans, isotropic 3D T1-weighted spoiled gradient echo scans were used to detect gadolinium diethylenetriaminepentacetate (Gd-DTPA) labeled bovine IgG (Gd-IgG; Biopal) using the following sequence parameters: TR = 9.3 ms, TE = 4.7 ms, flip angle = 20°, field of view = 60×30×30 mm or 70×35×35 mm, resolution = 256×128×128, averages = 4, resulting in a scan time of ~10 min 17 sec per imaging time point and a voxel size of ~234-273 μm. Animals were prepared identically as described for fluorescence imaging experiments except that, once the cannula was inserted into the cisterna magna and sealed, rats were carefully placed in a transmitting/receiving volume coil in the prone position. Animals were maintained at 37°C using a warm air blower and heart and respiratory rates were monitored to ensure basic physiological parameters were in the normal range throughout the experiment. A baseline scan was acquired prior to the infusion, after which the subsequent scan and the infusion (1.6 µL/min, 80 µL total) were begun simultaneously; animals were then scanned continuously for the remainder of the infusion and typically for a further 1-2 hours post-infusion. Animals were then euthanized after the experiment by intracardiac KCl (1 M).

MRI processing

If necessary, registration was performed using a rigid body registration in Matlab (The MathWorks Inc.). All additional processing and analysis was performed using Fiji (Schindelin *et al.*, 2012). Multiple regions of interest (ROIs) were outlined on raw MRI slices to analyze various CSF or brain ROIs (e.g., interpeduncular cistern or striatum), and the average pixel intensity (and other properties, e.g., max, min, and mode) measured for each time point. The percent change in intensity from the pre-infusion baseline for several areas (depicted in Fig. 2) was then averaged across animals; negative values were set to zero. As Gd-IgG interacts differently with different molecular environments (e.g., CSF versus gray or white matter), the percent change from baseline cannot unambiguously be compared between different brain areas (i.e., a 10% increase in signal in a CSF region versus a parenchymal brain region may not be the result of equivalent increases in Gd-IgG concentration). However, changes within a region and their kinetics are instructive. For 3D dynamic visualization, the pre-infusion baseline image was subtracted from subsequent scans using Fiji. Negative values were set to zero and surrounding background tissue signal (e.g., neck muscles) cropped. Baseline-subtracted data was rendered in 4D (3D with time) using the 3D

Viewer plugin (volume, no resampling) (Schmid *et al.*, 2010). 3D baseline-subtracted data from individual time points was rendered in the Volume Viewer plugin (Barthel, 2005) using maximum projection mode and trilinear interpolation (e.g., Fig. 5*C*).

Immunohistochemistry and confocal microscopy

Free-floating 100 μm brain sections (following *ex vivo* fluorescence imaging) were washed three times in PBS for 5 min, blocked with 3% goat serum for one hour at room temperature, and incubated with mouse-anti-rat endothelial cell antigen-1 (RECA-1) primary antibody (Abcam ab9774; 1:1000 dilution) overnight at 4°C. Sections were next washed in PBS, incubated with goat-anti-mouse AlexaFluor405 (Life Technologies A-31553; 1:500 dilution) or donkey-anti-mouse AlexaFluor 647 (Abcam ab150107; 1:500 dilution) for one hour at room temperature, washed again in PBS, and mounted on slides using Prolong Gold or Diamond Antifade (Life Technologies). After secondary incubation, some sections were also incubated with DAPI (Life Technologies; 2 μg/mL) for 20 min at room temperature and then washed in PBS before mounting. Slides were imaged on an Olympus FV1000 confocal microscope using FLUOVIEW software or a Nikon A1R confocal microscope with NIS Elements software. For laminin staining, sections were blocked in 1% BSA with 0.5% Triton X-100 for 2 hours at room temperature and incubated overnight in laminin γ1 primary antibody (Sorokin laboratory, clone D18, 3 μg/mL). Sections were washed in PBS, incubated 2-3 hours at room temperature with secondary antibody (Cy3 goat-anti-mouse, 1:600, Dianova 115-165-062), washed in PBS, and mounted for imaging on a Zeiss LSM 700 confocal microscope using ZEN software.

Measurements of extracellular diffusion at the brain section surface following intrathecal infusion

Coronal sections were analyzed for diffusion at the brain surface, as previously described (Wolak *et al.*, 2015). Briefly, images were opened in Fiji (Schindelin *et al.*, 2012) and a line (~80 µm wide and ~500-1200 µm deep) was drawn normal to the brain surface and the fluorescence intensity gradient along the line fitted to the appropriate equations (Wolak *et al.*, 2015) to estimate an effective diffusion coefficient (D^*_{infus}) for antibody transport at the brain surface. Several lines were drawn per section, and several sections were analyzed per animal at coronal levels of approximately 1.5 mm anterior to bregma (± 0.5 mm; IgG) or 3 mm posterior to bregma (± 1 mm; IgG and sdAb) from bregma (Paxinos & Watson, 2007). For IgG, only D^*_{infus} fits where the R-squared was greater than 0.8 and the difference between the maximum and minimum (background) intensity was greater than 500 arbitrary units were included for analysis. For sdAb, 6-8 lines were drawn per section and, as sdAb gradients extended further into the tissue than IgG gradients, a selection of the best fit lines (highest R-squared values; 4 lines from two sections for a total of 8 per animal) were included for analysis. Animals co-infused with mannitol were not analyzed due to low signal-to-noise at the pial surface. Brain sections from saline-infused control animals did not show any surface gradient, but rather a random distribution of low level intensities (background) with a slight increase in intensity as opposed to the decrease in signal intensity seen for antibody-infused animals. No significant difference was found between dorsal D^*_{infus} values or ventral D^*_{infus} values obtained for IgG at different coronal levels (+1.5 mm and -3 mm) so results were pooled for dorsal and ventral D^*_{infus} reported values.

Mannitol co-infusion

AlexaFluor 488 goat-anti-rabbit IgG was prepared in 0.27 M or 0.75 M mannitol in 0.01M PBS (pH 7.4) using 0.5 mL Amicon Ultra 100 kDa molecular weight cutoff centrifugal filters for buffer exchange (Millipore). IgG solution was added to the filter and washed/spun from 0.5 mL three times with 0.27 M or 0.75 M mannitol solution (final osmolality 507-564 mOsm/kg and 988-1124 mOsm/kg, respectively); each spin was 10 min at 14,000 × *g*. Recovery spin was 2 min at 1,000 × *g*. Concentration of IgG protein (absorbance at 280 nm) was measured using a NanoDrop 2000C (Thermo Fisher) before and after filtration, and the protein concentration adjusted after filtration so animals received identical amounts of IgG whether administered in provided buffer or mannitol solution. The lower concentration of mannitol (0.27 M) was chosen because its isomer sorbitol (which is expected to have a similar osmotic effect as mannitol) has been used to stabilize AAV formulations that have been administered into the CSF (e.g., (Samaranch *et al.*, 2013)) and brain (e.g., (Hadaczek *et al.*, 2006*a*)), and the higher mannitol concentration (0.75 M) was chosen to be near the upper limit of mannitol solubility at room temperature (Mullin, 2001). Each of these concentrations was well-tolerated in anesthetized rats over the duration of the experiment; previous work has also showed fair tolerability after intracisternal bolus dosing of mannitol in rats (Speck *et al.*, 1988).

Point source diffusion measurements in free solution and in brain using integrative optical imaging (IOI)

Single-domain antibody diffusion was evaluated in free solution and in the rat neocortex *in vivo* using IOI, as previously described (Thorne & Nicholson, 2006; Thorne *et al.*, 2008; Wolak *et al.*, 2015). IOI is a well-characterized method that utilizes epifluorescence microscopy and quantitative image analysis to measure the diffusion of fluorescently-labeled molecules. After a brief pulse injection, successive images of the diffusion cloud were recorded at regular intervals of 1-8 s using a custom program in MatLab (The MathWorks) provided by C. Nicholson and L. Tao (Nicholson & Tao, 1993). Image analysis was performed using a second MatLab program to fit images with expressions that describe how the 3D clouds resulting from each point source injection project on to the 2D CCD camera according to diffusion theory (Nicholson & Tao, 1993):

$$I_i(r, \gamma_i) = E_i \exp\left[-\left(\frac{r}{\gamma_i}\right)^2\right] \qquad [1]$$

and

$$\gamma_i^2 = 4D(t_i + t_0) \qquad [2]$$

where I_i is the fluorescence intensity of the ith image at radial distance r from the source point, and E_i incorporates the defocused point spread function of the microscope objective. To account for deviation from the point source approximation, a time offset, t_0, was added to the measured time from injection, t_i. Eq. 1 was fit to the upper 90% of the fluorescence intensity curves using a nonlinear simplex algorithm, providing estimates of a parameter, γ^2, at a succession of t_i intervals. A linear regression plot of $\gamma^2/4$ versus t_i returned a slope equal to the effective diffusion coefficient ($D*$) or free diffusion coefficient (D) based on Eq. 2. Measurements of D were made at 37 ± 1°C using 0.3% NuSieve GTG agarose (FMC) in 154 mM NaCl and measurements of D^* were at a depth of 200 μm below the pial surface in the primary somatosensory area (barrel field and trunk region) *in vivo*. D was further used to calculate the apparent hydrodynamic diameter (d_H) using the Stokes-Einstein equation [$d_H = (kT)/(3\pi\eta D)$, where k is Boltzmann's constant, T is absolute temperature, and η is the viscosity of water (6.9152×10^{-4} Pa·s at $T = 310$ K)] (Thorne *et al.*, 2004).

Diffusion parameters for IgG were taken from a previously published IOI study with the same AlexaFluor488-IgG conjugate as used here.

Perivascular quantification

Quantification of perivascular profiles and area accessed by intrathecal probes was performed using the Fiji image processing package (Schindelin *et al.*, 2012), with the general strategy depicted in Fig. 3. First, the area of each *ex vivo* fluorescence brain section (in pixels^2 and mm^2) was determined by adjusting the threshold to delineate the section boundaries within the image and then by using the wand tool to outline the entire section. Ventricles were excluded from all slice areas. Thresholds were next adjusted until background autofluorescence (typically from white matter) was no longer detectable; thresholds were set equally for all sections within each animal. Three coronal levels were analyzed for antibody signal (coordinates according to (Paxinos & Watson, 2007)): approximately 1.5 mm anterior to bregma (± 1 mm; 8 sections per animal), 2.5 mm posterior to bregma (± 1 mm; 7 sections per animal), and 5.5 mm posterior to bregma (± 0.25 mm; 3-4 sections per animal). Next, the slice area was divided into two ROIs, a dorsal portion and ventral portion (a simple division that still allowed us to distinguish some degree of regional heterogeneity). For sections 1.5 mm anterior to bregma, the dorsal/ventral horizontal division line was placed at approximately half the vertical distance from the dorsal-ventral extent of the lateral ventricles; for sections 2.5 mm posterior to bregma, the horizontal division line was placed just inferior to the dorsal hippocampus and dorsal third ventricle; for sections 5.5 mm posterior to bregma, the horizontal division line was placed just superior to the cerebral aqueduct. The ‘analyze particles’ command was used to count, characterize, and outline perivascular signal or diffuse surface/white matter signal above the set threshold in each defined dorsal or ventral ROI; no restriction was set on circularity but only profiles greater than 2 pixels were included (i.e., single pixels were not counted). The number of perivascular counts per mm^2 slice area was determined by using the raw number of perivascular counts divided by the total slice area. The number of PV profiles per slice area was not quantified for sdAb because the strong, diffuse surface signal associated with sdAb obscured PV profiles and complicated interpretation.

Scanning Electron Microscopy (SEM)

Rats were anesthetized with urethane and perfused with ~50 mL ice cold 0.01M PBS and fixed with ~500 mL 2% paraformaldehyde and 2.5% glutaraldehyde in 0.1M phosphate buffer via the abdominal aorta. The brain was removed and certain brain regions carefully dissected. Tissue samples were post-fixed overnight in 2% PFA with 2.5% glutaraldehyde at 4°C, and dehydrated in increasing levels of ethanol at room temperature. Tissue was then dried using a CO_2 critical point dryer (Tousimis_Sandri 780A) and sputter coated with ~3-5 nm 60:40 gold:palladium using a SeeVac Auto ConductVac IV prior to imaging (10kV, 25-10,000X) on a Hitachi S570 SEM or LEO 1530 field emission SEM.

Statistics

A Student's two-tailed t-test was used to determine statistical differences for all two-way comparisons (e.g., IgG vs sdAb), with *p* values listed in the text. A Kruskal-Wallis one-way ANOVA on ranks ($p<0.001$) was performed for group comparisons (e.g., IgG vs IgG with 0.27 M or 0.75 M mannitol) where at least one group did not pass normality or equal variance tests, followed by post hoc pairwise testing using Dunn's method (unless otherwise specified) with $p<0.05$. A one-way analysis of variance was performed ($p<0.001$) for one group comparison characterized by normal distribution and equal variance (as noted in the figure legend), followed by a Bonferroni post hoc test ($p<0.001$). Statistical analyses were performed using SigmaPlot (Systat Software). All values listed as mean ± s.e.m; *N* animals, *n* measurements.

Results

Whole brain ex vivo fluorescence imaging

We initially characterized antibody probes using IOI *D* measurements (Nicholson & Tao, 1993; Thorne *et al.*, 2004, 2008), confirming monomeric behavior and yielding Stokes-Einstein apparent hydrodynamic diameters (d_H) for AlexaFluor488-labeled sdAb (16.8 kDa (Farrington *et al.*, 2014); $D = 14.7 \pm 0.3 \times 10^{-7}$ cm^2/s and $d_H = 4.47 \pm 0.11$ nm; n=43; Fig. 4) and AlexaFluor488-labeled IgG (150 kDa; $D = 6.47 \times 10^{-7}$ cm^2/s and $d_H = 10.15$ nm ((Wolak *et al.*, 2015)). Anesthetized, Sprague-Dawley rats were placed in a stereotaxic frame and a cannula placed in the cisterna magna. Antibodies were intrathecally infused, with animals in a prone position, for 50 min at a flow rate of 1.6 μL/min (approximately half the CSF production rate (Davson & Segal, 1995)), followed by a post-infusion distribution time of 30 min then perfusion-fixation; others have recently utilized similar infusion site/rates and infusion/post-infusion durations in rats with other intrathecal tracers (Iliff *et al.*, 2013*a*; Yang *et al.*, 2013; Bedussi *et al.*, 2017) and shown such a flow rate does not appreciably elevate intracranial pressure (Yang *et al.*, 2013; Bedussi *et al.*, 2017). Whole brains were removed and *ex vivo* imaging of the ventral and dorsal brain surfaces demonstrated high PV signal for both sdAb (*N*=6) and IgG (*N*=10) along cerebral arteries (Fig. 5). Antibody signal was apparent, albeit lower, around surface veins (e.g., the caudal rhinal vein; Fig. 5 *J* and *K*). Antibody associated with the PVS of penetrating vessels perpendicular to the brain surface appeared as punctate signal (circled in Fig. 5*G*). High signal was particularly prominent at brain-CSF interfaces (e.g., at the olfactofrontal and quadrigeminal cisterns), the olfactory bulbs, and around cranial (e.g., II, V, VIII, and XII) and spinal nerves (Fig. 5 *F-I* & Fig. 5*L*). There was a noticeable size-dependent surface distribution—generally, sdAb signal appeared brighter and more diffuse while IgG signal appeared more restricted to the PVS (e.g., Fig. 5 *F* and *G*); in addition, diffuse and PV signal on the ventral brain surface appeared greater than dorsal signal for both antibodies (Fig. 5 *A* and *B* & *D* and *E*). Saline-infused animals showed relatively low fluorescence (Fig. 5 *B* and *E* insets).

In vivo 3D MRI of intrathecal IgG

In vivo 3D T1-weighted MRI allowed tracking of a Gd-DTPA contrast agent conjugated to full-length IgG (Gd-IgG) over time using the same infusion paradigm and animal positioning as above. Compared to whole brain *ex vivo* fluorescence, 3D baseline-subtracted T1-weighted image contrast enhancement associated with Gd-IgG signal showed a similar distribution of PV signal along cerebral arteries, as expected (Fig. 5 *C*). Representative raw sagittal MRI slices showed high signal in CSF cisterns, particularly ventrally (correlating with *ex vivo* fluorescence signal), and increasing signal in the brain parenchyma with time (Fig. 6 *A-D* and Fig. S2 *A-I*). Gd-IgG signal in the SAS was sparse over the dorsal cortex; anatomical T2 scans (not shown) and past studies suggest this is likely due to less CSF/SAS in these areas (Pease & Schultz, 1958; Morse & Low, 1972; Oda & Nakanishi, 1984). The percent signal change from pre-infusion baseline for several ROIs (Fig. 2) over time yielded strikingly different kinetics (e.g., time to peak change) in CSF ROIs (Fig. 6*E* and Table 1) versus parenchymal ROIs (Fig. 6*F*). Signal in CSF ROIs tended to increase during the infusion and then fall as or shortly after the infusion finished whereas parenchymal ROIs tended to progressively increase throughout the experiment (even in two animals imaged for greater than 2 hours post-infusion). CSF ROIs nearest the infusion site

Table 1. Peak times and peak % changes with Gd-IgG infusion for selected MRI cerebrospinal fluid regions of interest.

	Approximate distance from CM infusion site (mm)[†]	Peak % Change[‡]	Peak Time (minutes)
ventral spinal SAS	4	185 ± 20%[a]	53.7 ± 2.6
interpeduncular cistern	14	101 ± 10%[b]	60.0 ± 0.0
ambient cistern	18	76.1 ± 7%	64.0 ± 2.5
quadrigeminal cistern	22	57.1 ± 5%	91.3 ± 19
olfactofrontal cistern	30	34.2 ± 5%	109 ± 5.9

Values listed indicate mean ± s.e.m.

[†] A ventral path and general ventral-to-dorsal and caudal-to-rostral flow pattern as suggested by MRI was assumed in calculating distances.

[‡] Peak % change in intensity from pre-infusion baseline MRI. Mean peak % change values were significantly different by one-way ANOVA (p<0.001); pairwise post-hoc comparisons using the Holm-Sidak method showed [a] ventral spinal SAS peak % change values were significantly greater than values for the interpeduncular (p=0.011), ambient (p=0.002), quadrigeminal (p<0.001), and olfactofrontal cisterns (p<0.001) and the [b] interpeduncular cistern peak % change value was significantly higher than the value for the olfactofrontal cistern (p=0.04).

demonstrated a higher peak % change from baseline and a lower time to peak change than CSF ROIs further from the infusion site, i.e., the ventral spinal subarachnoid space had a significantly higher peak % change compared to all other more rostral CSF cisterns (Table 1). Carefully-selected ROIs within the lateral ventricles or fourth ventricle (Fig. 6 *G* and *H*) were also analyzed, showing ventricular Gd-IgG signal increased with time, with a kinetic profile similar to parenchymal ROIs, but the lack of differences between the sampled lateral ventricle and fourth ventricle ROIs suggest backflow through the ventricular system was not the source of this signal increase (Fig. 6*I*). Raw coronal MRI slices at the upper cervical level showed the greatest signal increase (relative to pre-infusion baseline) in the SAS and butterfly-shaped spinal cord gray matter (Fig. 6 *J*, *K*, *T*, and *U*); greater contrast in the spinal gray versus white matter corresponded with dramatically higher vascularity in the spinal gray (Fig. 6*L*) and agreed well with markedly higher PV signal seen in that region in *ex vivo* fluorescence experiments (discussed below). 3D contrast enhancement with time clearly demonstrated a rostrally-directed flow around the brain towards CSF efflux routes such as the olfactory nerves.

Ex vivo fluorescence imaging of coronal brain sections

Imaging of coronal brain sections revealed striking parenchymal sdAb and IgG distributions of two basic types: (i) hundreds of PV signal profiles in deeper brain regions at a variety of cortical and subcortical locations and (ii) a tight yet observable surface gradient at brain-CSF interfaces (Fig. 7 *A-D*). Perivascular signal was evident along the entire neural axis for both sdAb and IgG, with a distribution that was more prominent ventrally (Fig. 7 *A* and *B* & Fig. 8). Antibody distribution was quantified in brain sections using Fiji software, yielding percent slice area with antibody signal (Fig. 3). Signal was analyzed in dorsal or ventral halves of brain slices at three different coronal levels. A significantly greater percent area with signal was measured for sdAb than for IgG in both dorsal and ventral regions at all levels ($p<0.001$; Fig. 7 *E* and Table 2); averaging values over the 7 mm rostral-caudal distance sampled, the approximate mean areas accessed by sdAb and IgG were 11.6% and 1.95%, respectively (expressed as % of the total slice area; Table 2). Greater sdAb signal was particularly evident at brain surfaces, within periventricular white matter, and in the PVS throughout each slice.

Diffuse signal at the brain surface was analyzed for sdAb and IgG using Fiji. Fluorescence intensity gradients were extracted along lines perpendicular to the brain surface (Fig. 7*F*). The resulting profiles were then fit to the appropriate diffusion equation (Wolak *et al.*, 2015) to assess agreement with diffusion theory (Fig. 7*G*) and, if so, to estimate a diffusion coefficient in brain after intrathecal infusion (D^*_{infus}). The D^*_{infus} was then compared with the effective diffusion coefficient measured in the cortex beneath the brain surface *in vivo* using the well-established method of IOI

Table 2. Summary of antibody signal quantification from *ex vivo* fluorescence imaging of brain sections.

	% Area with antibody signal (N, n)		
Infused Antibody	+ 1.5 mm	- 2.5 mm	-5.5 mm
sdAb			
dorsal	6.02 ± 0.33 (5, 40)	9.33 ± 0.30 (5, 35)	5.79 ± 0.40 (5, 20)
ventral	20.14 ± 0.44 (5, 40)	13.46 ± 0.63 (5, 35)	14.87 ± 1.11 (5, 20)
IgG			
dorsal	1.42 ± 0.14 (5, 40)	1.63 ± 0.17 (6, 42)	1.17 ± 0.33 (5, 20)
ventral	3.46 ± 0.23 (5, 40)	1.77 ± 0.12 (6, 42)	2.26 ± 0.26 (5, 20)
IgG + 0.27 M mannitol			
dorsal	2.37 ± 0.15 (6, 48)	2.17 ± 0.28 (6, 42)	2.40 ± 0.45 (6, 24)
ventral	4.95 ± 0.23 (6, 48)	2.39 ± 0.09 (6, 42)	5.14 ± 0.47 (6, 24)
IgG + 0.75 M mannitol			
dorsal	2.34 ± 0.14 (9, 72)	2.82 ± 0.23 (8, 56)	3.10 ± 0.25 (7, 26)
ventral	6.21 ± 0.23 (9, 72)	3.24 ± 0.16 (8, 56)	4.85 ± 0.44 (7, 26)

	Number of PV profiles per mm^2 slice area (N, n)		
Infused Antibody	+ 1.5 mm	- 2.5 mm	-5.5 mm
IgG			
dorsal	5.37 ± 0.28 (5, 40)	3.58 ± 0.30 (6, 42)	2.97 ± 0.5 (5, 20)
ventral	14.00 ± 0.45 (5, 40)	7.51 ± 0.28 (6, 42)	8.13 ± 0.31 (5, 20)
IgG + 0.27 M mannitol			
dorsal	7.01 ± 0.46 (6, 48)	5.80 ± 0.45 (6, 42)	6.46 ± 0.81 (6, 24)
ventral	15.08 ± 0.74 (6, 48)	9.84 ± 0.55 (6, 42)	10.95 ± 0.97 (6, 24)
IgG + 0.75 M mannitol			
dorsal	8.48 ± 0.47 (9, 72)	6.20 ± 0.33 (8, 56)	6.33 ± 0.29 (7, 26)
ventral	17.85 ± 0.81 (9, 72)	10.47 ± 0.55 (8, 56)	11.52 ± 0.6 (7, 26)

Antibody signal above a background threshold was quantified using Fiji to measure the % area with antibody signal within dorsal or ventral halves of brain slices (1.5 mm anterior or 2.5 mm and 5.5 mm posterior to bregma) and the number of perivascular profiles normalized by slice area (mm^2). Values represent mean ± s.e.m.; N animal experiments and n brain sections per treatment group.

(D^*_{IOI}); this allowed us to evaluate whether the antibody surface gradients from intrathecal infusions in a closed system were consistent with parenchymal diffusion in deeper brain measured using open cranial windows and point source intraparenchymal injections with IOI (Fig. 7*H*). D^*_{infus} for sdAb at the ventral brain surface after intrathecal infusion ($D^*_{\text{infus}}=32 \pm 0.7 \times 10^{-8}$ cm^2/s; $n=32$, $N=4$, Fig. 4) agreed remarkably well with parenchymal values from IOI ($D^*_{\text{IOI}}=31 \pm 1$ x

10^{-8} cm^2/s; n=19, N=4; p=0.47; D^* at the dorsal brain surface could not be determined due to the difficulty of sampling around extensive PV signal at that site). IgG surface gradients were clearly diffusive in nature (Fig. 7*G*) but D^*_{infus} at the ventral brain surface ($D^*_{infus}=3.4 \pm 0.3 \times 10^{-8}$ cm^2/s; n=50, N=5) was reduced compared to D^*_{IOI} measured previously at a depth of 200 μm from the pial surface ($D^*_{IOI}=6.7 \pm 0.3 \times 10^{-8}$ cm^2/s; ((Wolak *et al.*, 2015)). Furthermore, a noticeably steeper IgG gradient at the dorsal brain surface yielded an even lower value ($D^*_{infus}=1.8 \pm 0.1 \times 10^{-8}$ cm^2/s; n=34, N=5) compared to the ventral brain surface.

Ex vivo confocal microscopy of perivascular antibody distribution

Representative sections were chosen for immunohistochemistry and confocal microscopy to examine PV localization. Both sdAb and IgG signal surrounded leptomeningeal surface arteries (endothelial cells immunolabeled with rat endothelial cell antigen-1) in the fluid- and connective tissue-space of the presumed adventitia, but sdAb had markedly greater access to the tunica media (i.e., putative BM between smooth muscle cells (alpha smooth muscle actin+)) compared to IgG (Fig. 9 *A* and *E*). Both antibodies were distributed along parenchymal PVS including putative arteries/arterioles (Fig. 9 *B* and *F*; with characteristic circumferential bands of signal associated with the smooth muscle BM), putative veins/venules (Fig. 9 *C* and *G*), and microvessels (Fig. 9 *D, H,* arrow in *I*; as small as 4 μm in diameter), based on vessel size and morphology. Overall, sdAb had a more continuous distribution within the PVS and more diffuse signal in the neuropil surrounding the PVS compared to IgG. Antibody signal for both sdAb and IgG was prominent at the brain surface, likely associated with the pia and/or subpial space, and often exhibited a punctate appearance within putative macrophages (Iba1/Cd11b/Lyve-1+) in the SAS and in the PVS (arrowheads in Fig. 9 *B* and *F*). PV signal was consistently prominent around lenticulostriate vessels (Fig. 9*I*), where a pan-laminin BM marker demonstrated that IgG co-localized with astrocyte BM and smooth muscle BM, but not endothelial BM (Fig. 9*I* inset).

Electron microscopy of potential perivascular entry points on leptomeningeal vessel sheaths

Potential routes of entry from the CSF into the PVS of rodents have received surprisingly little attention, despite their obvious importance and potential to screen or filter CSF-borne macromolecules. We investigated whether stomata, leptomeningeal fenestrations/pores that have been shown on the adventitial cell layer bordering the CSF of surface vessels in the cat (Zervas *et al.*, 1982), could be demonstrated on the adventitial surface of major leptomeningeal vessels in the rat using SEM. Untreated rats were perfused, fixed, and several tissue areas around the anterior cerebral, middle cerebral, basilar and vertebral arteries and the optic, interpeduncular, and quadrigeminal cisterns were processed for SEM. Careful investigation revealed the presence of numerous stomata on the adventitial surface (i.e., at the site of the green leptomeningeal cells depicted in Fig. 1 *A* and *B*) of all vessels examined (Fig. 10 *A-D*), with a strikingly similar appearance to those in the cat (Zervas *et al.*, 1982). These pore-like structures typically exhibited a uniform, smooth rim, with diameters mostly in the range of 1-3 μm. A dense meshwork of underlying connective tissue, presumably fibrillar collagen, was also clearly visible through the pores (Fig. 10 *B* (inset), *C,* and *D*).

Enhanced perivascular access of IgG with co-infusion of mannitol

Our results showing an inverse correlation between PV access/distribution and probe size suggested a size-dependent filtration process may restrict PV access from the CSF (possibly due to sieving by stomata and their associated connective tissue, as described above, or by similar structures present on the pia). We hypothesized that intrathecal co-infusion of an osmolyte might increase the larger IgG's access to the PVS, e.g., by osmotically drawing water out of leptomeningeal lining cells on the adventitial surface of vessels in the SAS. IgG was prepared in either 0.27 M (5%; *N*=6) or 0.75 M mannitol (14%; *N*=9) and then infused intrathecally using the same infusion parameters as described above. *Ex vivo* fluorescence imaging of brain sections and subsequent quantification using Fiji (Fig. 3) indicated that mannitol co-infusion enhanced IgG PV access in a dose-dependent manner (Fig. 11 *A-D*), resulting in a significantly increased percent slice area with IgG signal (Fig. 11*E*) and greater number of PV profiles per mm^2 (Fig. 11*F*). Co-infusion with 0.27 M mannitol yielded a significantly increased percent area accessed by IgG in 4/6 areas sampled (dorsal or ventral halves of brain slices at three different coronal levels, as above) and a significantly increased number of PV counts per mm^2 in 3/6 areas sampled compared to IgG alone. Co-infusion of IgG with 0.75 M mannitol yielded a significantly increased percent area and a significantly increased number of PV counts per mm^2 in all areas sampled compared to IgG alone. Co-infusion of IgG with 0.75 M mannitol also resulted in a significantly increased percent area in 3/6 areas sampled and showed more prominent spread of IgG along periventricular white matter compared to 0.27 M mannitol co-infusions, confirming mannitol dose-dependence. In summary, co-infusion with 0.75 M mannitol dramatically increased the brain area accessed by IgG by ~93% and increased the number of PV profiles per slice area by 1.46-fold compared to IgG alone (Table 2). Mannitol co-infusion also markedly increased PV access of IgG in the spinal gray matter (Fig. 11 *G-I*). Confocal imaging demonstrated that mannitol co-infusion increased IgG access to the innermost smooth muscle BM layers of large leptomeningeal arteries (Fig. 11 *J-M*) and allowed more continuous PV distribution along penetrating vessels. Co-infusion of 0.75 M mannitol did not appreciably alter the distribution of the smaller sdAb (data not shown), suggesting mannitol elicited increased perivascular access in a size-dependent fashion.

CSF drainage routes

Intrathecal infusions of both sdAb and IgG resulted in high signal in the olfactory mucosa and deep cervical lymph nodes (Fig. 12), CSF efflux routes that have been previously identified in many other studies (Faber, 1937; Bradbury *et al.*, 1981; Bradbury & Westrop, 1983; Szentistványi *et al.*, 1984; Zhang *et al.*, 1992; Kida *et al.*, 1993; Koh *et al.*, 2005) although nasally-directed CSF efflux has recently been called into question (Louveau *et al.*, 2015). Within the nasal passages, most of the antibody signal was localized to the olfactory mucosa and cribriform plate (Fig. 12 *A-D*); confocal microscopy of olfactory mucosa coronal cryosections demonstrated that IgG signal was present throughout the lamina propria where it surrounded putative blood vessels, lymphatic vessels, and nerve bundles, with signal stopping abruptly at the basal lamina (Fig. 12 *E-I*). Antibody drainage to the deep cervical lymph nodes (consistent with much past work (Bradbury *et al.*, 1981; Bradbury & Westrop, 1983; Szentistványi *et al.*, 1984)) was indicated by prominent signal in all animals intrathecally administered either sdAb or IgG (Fig. 12 *A* and *B* inset) and all animals receiving IgG with either 0.27 M mannitol or 0.75 M mannitol. Often, at least one superficial cervical lymph node exhibited signal (consistent with past work (Szentistványi *et al.*, 1984)) although, when present, it always appeared of lower intensity than the deep cervical lymph node signal. IgG signal was also noticeably present around nerves (e.g., the nerve layer of the olfactory bulb surface, the optic, trigeminal, and hypoglossal nerves (see Fig. 5 *A*, *B*, and *F-I*), and spinal nerves (see Fig. 5*L*)), possibly associated with cranial and spinal nerve-associated efflux routes (Faber, 1937; Bradbury & Westrop, 1983; Weller *et al.*, 1992; Cserr & Knopf, 1992; Kida *et al.*, 1993; Koh *et al.*, 2005) and clearance along dural lymphatic vessels (Aspelund *et al.*, 2015). Clearance of IgG to the plasma compartment 30 min post-infusion, presumably via arachnoid villi and lymphatic drainage routes, resulted in low plasma concentrations: 26.8 ± 1.3 nM after intrathecal IgG (*N*=9); 28.6 ± 1.7 nM after co-infusion of IgG with 0.27 M mannitol (*N*=5); 35.1 ± 0.85 nM after co-infusion of IgG with 0.75 M mannitol (*N*=9). Although 0.75 M mannitol co-infusion yielded a small yet significant elevation in plasma IgG concentration compared to IgG alone and 0.27 M mannitol co-infusion, these levels were orders of magnitude below the infused IgG concentration (13 μM) and the low μM CSF levels likely to have resulted from the infusion after taking into account CSF dilution.

Discussion

The major findings of the present study are: (i) fluorescence intensity gradients within the neuropil at the brain surface were consistent with diffusive transport and exhibited clear antibody size-dependence; (ii) sdAb and IgG each appeared to distribute perivascularly to some degree along all vessel types studied, i.e., arteries, arterioles, microvessels, venules, and veins; (iii) the percent brain area accessed was strikingly greater for the smaller sdAb than for the larger IgG; (iv) perivascular access to the smooth muscle BM of the tunica media exhibited size-dependence; (v) intrathecal co-infusion of an osmolyte, mannitol, markedly increased access of IgG to PV compartments in a dose-dependent manner; and (vi) CNS clearance of antibodies was prominent along olfactory pathways to the olfactory mucosa and cervical lymph nodes. Finally, SEM revealed numerous leptomeningeal vessel stomata (micron-sized pores on the CSF-facing outer surface cell layer of the vessels, not to be confused with the inner surface endothelial cell layer) in rodents. We speculate that these unique fenestrations may play a role in the size-dependent PVS access of CSF-borne macromolecules. Our results provide strong support for two principal mechanisms governing transport of antibodies from CSF to brain: diffusion from the CSF into the ECS at the brain surface and convection in the PVS of cerebral blood vessels to deep brain regions.

Diffusion in the extracellular space of the neuropil

Recent intracisternal infusion studies in mice (Iliff *et al.*, 2012; Xie *et al.*, 2013) and rats (Iliff *et al.*, 2013*a*; Yang *et al.*, 2013) have led to speculation that aquaporin-4 water channels on astrocyte endfeet allow a convective flux or flow of CSF/ISF through the parenchymal ECS, facilitating convective transport of various tracer substances along brain-wide pathways (termed 'glymphatic' due to a proposed reliance on glia and role in lymphatic-like brain drainage) out of the arterial PVS through the brain ECS and into the PVS of veins for clearance (Nedergaard, 2013). However, the occurrence of convective flow through the ECS of the neuropil has been called into question based on theoretical considerations and modeling results that suggest diffusion to be a more plausible mechanism (Wolak & Thorne, 2013; Jin *et al.*, 2016; Asgari *et al.*, 2016). Our experimental results using the same infusion site/rate and similar infusion/post-infusion durations as used with other tracers in the experimental work underlying the 'glymphatic' concept (Iliff *et al.*, 2013*a*; Yang *et al.*, 2013) provides further evidence that diffusion, and not convection, is likely to be the predominant transport process governing distribution in the ECS of the neuropil. Fluorescence intensity brain surface gradients from intrathecal infusions were extracted from different coronal sections several mm apart and the resulting profiles fit with the appropriate 1-dimensional solution to the diffusion equation (Wolak *et al.*, 2015), similar to an older approach pioneered by Fenstermacher et al. with radiotracer perfusions (reviewed in (Syková & Nicholson, 2008; Wolak & Thorne, 2013)). The excellent fit of these profiles strongly suggests diffusive transport as the dominant transport mechanism at least 200 μm (IgG) to 800 μm (sdAb) deep into the brain surface from the CSF. Further, the sdAb effective diffusion coefficient obtained from the ventral brain surface profiles after intrathecal infusion was nearly identical to that obtained using the IOI method, where intraparenchymal injections were performed in somatosensory cortex at a depth of 200 μm in separate animals. This striking agreement, despite the application of entirely different methods and *in vivo* animal preparations to arrive at sdAb D^*_{infus} and D^*_{IOI} values, provides strong evidence in support of diffusion limiting parenchymal gradients at the brain surface (and experimentally obtained isotropic radial profiles around point sources in the parenchyma such as with IOI). While diffusion theory also fit intrathecal IgG brain surface profiles quite well, the resulting D^*_{infus} values were lower than previously obtained D^*_{IOI} values from the point source IOI method with the same IgG fluorescent conjugate (Wolak *et al.*, 2015). The reasons for this are not entirely clear although we speculate that the environment for IgG diffusion into the brain across the pial surface may exhibit subtle differences from the parenchyma several hundred microns below, e.g., structural complexity associated with the extensive surface glia limitans (Ghersi-Egea *et al.*, 1996*a*; Fenstermacher *et al.*, 1997) and/or site-dependent differences in astrocytic expression of Fcγ receptors (Okun *et al.*, 2010) may result in greater sieving of IgG and/or more pronounced IgG hindrance due to rapid, reversible Fc binding; size-dependent diffusional hindrance and reduced effective diffusion due to binding in the brain have been previously demonstrated (Thorne & Nicholson, 2006; Thorne *et al.*, 2008). We did observe differences in the relative signal intensities associated with brain surface profiles (and their apparent depth of penetration) across different sites, but such differences should not affect the calculated diffusion coefficient. It is very likely that CSF antibody levels varied at different brain-CSF interfaces; indeed, MRI appeared to demonstrate greater exposure of ventral brain regions to Gd-IgG in the

CSF, with little CSF (as seen by T2 MRI) or Gd-IgG contrast over the dorsal brain region. Lastly, distributions often exhibited many profiles consistent with concentration gradient-driven radial diffusion out from the PVS of parenchymal vessels, particularly microvessels (e.g., Fig. 9*D*); similar radial profiles around parenchymal vessels have been observed by others, e.g., following intraventricular acid sphingomyelinase or intracisternal adeno-associated virus infusions in macaques (Ziegler *et al.*, 2011; Samaranch *et al.*, 2013).

Recently, it has been suggested that the brain ECS volume in mice is reduced during the awake state as compared to during sleep or under ketamine/xylazine anesthesia (Xie *et al.*, 2013), so it remains possible that certain aspects of our results may have been different (e.g., more limited brain surface profiles due to hindered extracellular diffusion resulting from reduced ECS width; Thorne & Nicholson, 2006) had the experiments been conducted in awake rats rather than the urethane-anesthetized animals utilized here. This possibility awaits further study along with replication of the awake brain ECS volume reduction finding (Xie *et al.*, 2013) by other laboratories and in other species such as the rat. Importantly, urethane anesthesia has been shown to cause only modest effects on both excitatory and inhibitory neurotransmission compared to other anesthetics (e.g., isoflurane, ketamine (Hara & Harris, 2002)) and induce a sleep-like state in rodents (Clement *et al.*, 2008), so it may also be useful to carefully evaluate diffusion and perivascular transport in future studies by comparing intrathecal tracer distributions using different anesthetics.

Perivascular access and distribution characteristics for antibodies

Intrathecal infusions of both fluorescently labeled sdAb and IgG resulted in abundant PV signal throughout the brain, including cortical and subcortical regions far deeper than reached by the diffusive brain surface gradients discussed above. Comparison of PV IgG signal associated with major surface vessels obtained by *ex vivo* fluorescence imaging and *in vivo* MRI (with Gd-IgG infusion) revealed excellent agreement between the two methods. Importantly, all parenchymal brain ROIs analyzed (e.g., olfactory bulbs, cortex, striatum) exhibited increasing Gd-IgG signal with time, consistent with Gd-IgG distribution to and accumulation in and around the parenchymal PVS (as shown by *ex vivo* fluorescence imaging). Indeed, accumulating Gd-IgG signal in the upper cervical spinal cord close to the intracisternal infusion site easily distinguished the highly vascular spinal gray from the less vascular surrounding white matter (i.e., more PV Gd-IgG signal was presumably associated with the spinal gray's higher vascularity), again in agreement with *ex vivo* fluorescence imaging results (e.g., compare Fig. 6 *K* and *L* with Fig. 11*G*). Our results were generally consistent with other studies where a variety of non-antibody tracer substances, e.g., horseradish peroxidase, ovalbumin, and small and large molecular weight dextrans, have been infused into the CSF of rodents, cats, and dogs (Wagner *et al.*, 1974; Rennels *et al.*, 1985; Iliff *et al.*, 2012, 2013*a*, 2013*b*; Xie *et al.*, 2013). While a previous rat study (Iliff *et al.*, 2013*a*) compared the intrathecal distribution of two gadolinium non-dextran contrast agents with fluorescent dextran tracers in three parenchymal CNS areas of the rat, our study is the first to correlate findings across MRI and *ex vivo* fluorescence imaging using a single physiologically and therapeutically relevant protein, IgG, with a much expanded list of parenchymal and CSF ROIs reported. Much work suggests the driving force for this PV transport is related to vessel pulsatility (Rennels *et al.*, 1985; Hadaczek *et al.*, 2006*b*; Iliff *et al.*, 2013*b*), with the result being a convective flow in the PVS (Cserr *et al.*, 1977, 1981; Rennels *et al.*, 1985; Ichimura *et al.*, 1991; Ghersi-Egea *et al.*, 1996*a*; Proescholdt *et al.*, 2000; Abbott, 2004; Hadaczek *et al.*, 2006*b*; Iliff *et al.*, 2012, 2013*a*), although modeling has suggested transport processes other than bulk flow (e.g., dispersion due to local fluid motion) may also provide an explanation for fast PV tracer transport (Asgari *et al.*, 2016).

Our *ex vivo* fluorescence imaging results showed some degree of sdAb and IgG signal around vessels of all caliber, i.e., from arteries/arterioles to capillaries to venules/veins, and our *in vivo* MRI data for IgG was consistent with a net PV flow first appearing around the largest surface arteries (presumably the PV compartment) and later around cortical surface veins (e.g., the caudal rhinal vein). *In vivo* two-photon imaging has been used previously to show that CSF-infused fluorescent dextran conjugates appear first in PV compartments associated with arteries and then later in PV compartments associated with veins (Iliff *et al.*, 2012), suggesting a natural PV transport pathway traveling in the same direction as blood flow (Iliff *et al.*, 2012, 2013*a*; Xie *et al.*, 2013), as proposed decades ago (Rennels *et al.*, 1985). It is worth noting that other studies have proposed intramural PV transport (i.e., along the BM of arterial smooth muscle cells in the tunica media and possibly also along the capillary basal lamina) may occur in the opposite direction to flow under certain conditions (Carare *et al.*, 2008; Morris *et al.*, 2016). Further work is needed to settle the direction of PV tracer transport in different vessels and their different compartments as well as the mechanisms underlying such transport.

An important aspect of our results was the demonstration that both sdAb and IgG reached the PVS of microvessels (i.e., typical of capillaries, arbitrarily assigned as vessels with a lumen diameter less than 8 μm); whether convection may occur at these sites is unknown, in part because it is unclear if a peri-capillary fluid space exists or if fused astrocyte and endothelial BMs result in a matrix compartment without an actual fluid space (Maynard *et al.*, 1957; Jones, 1970; Cervós-Navarro & Ferszt, 1973; Peters *et al.*, 1991). Nevertheless, assuming flow in the PVS continues down to the region of exchange vessels such as capillaries, there are numerous possibilities for peri-capillary transport, e.g., diffusion and possibly also convection within either a fused BM or fluid space compartment. Whether peri-capillary convection is possible would in theory depend upon pressure gradients, porosity, viscosity, and the dimensions of the space (Wolak & Thorne, 2013); further work is needed to explore likely possibilities. However, our results with both sdAb and IgG do confirm older reports from Wagner et al. (Wagner *et al.*, 1974) and Rennels et al. (Rennels *et al.*, 1985), as well as more recent reports from others (Jolly *et al.*, 2011; Iliff *et al.*, 2012), that macromolecule tracers infused into the CSF may distribute to a peri-capillary compartment. Peri-capillary transport after tracer infusion into the CSF is significant for at least two reasons: (i) it may be theoretically possible to access the PVS of all vessel types from the CSF, with the prospect of true global CNS delivery provided there is sufficient diffusion into the neuropil from the peri-capillary region (neurons are rarely more than 10-20 μm from capillaries (Wolak & Thorne, 2013), a short distance optimal for diffusion) and (ii) it may also be theoretically possible for circulation along the entire perivascular tree (e.g., from the PVS of arteries → arterioles → capillaries → venules → veins), as suggested previously (Rennels *et al.*, 1985), without requiring transport through the neuropil to reach peri-venous spaces (in contrast with a proposed convection through the neuropil as suggested in the 'glymphatic' concept (Iliff *et al.*, 2012; Nedergaard, 2013)). If such a directed circulation throughout the perivascular tree is indeed observed, it is unlikely that large molecules transported out of the brain from peri-venous compartments drain directly into the CSF. Many prior studies have demonstrated that labeled macromolecules (e.g., albumin or a poly(ethylene glycol)-dye conjugate) injected into the brain parenchyma drain primarily to cervical lymph nodes ipsilateral to the injection site (Bradbury *et al.*, 1981; Szentistványi *et al.*, 1984; Yamada *et al.*, 1991; Aspelund *et al.*, 2015), while tracers applied to the CSF drain to cervical lymph nodes with no apparent lateralization (Bradbury *et al.*, 1981), as seen in the present study. These different drainage patterns may be important for mechanisms related to CNS immune privilege, as it has long been known that tissue grafts (and their associated antigens) generate far more potent immune responses when transplanted into CSF compartments than when transplanted into brain parenchyma (Engelhardt *et al.*, 2017).

We also observed a striking size-dependent access to PV pathways, with sdAb signal covering a 4-fold to 7-fold greater percentage of slice area compared to IgG at each slice location analyzed. Averaging values over the entire rostral-caudal distance sampled (Table 2), we obtained approximate mean % areas accessed of 11.6% and 1.95% for sdAb and IgG, respectively. Nedergaard et al. have previously noted size-dependent access for intracisternally infused dextran tracers in mice (Iliff *et al.*, 2012; Lee *et al.*, 2015; Peng *et al.*, 2016) (and rats (Iliff *et al.*, 2013*a*)), although the reported % mean areas accessed have markedly varied across different studies by this group for unknown reasons (e.g., from approximately 5% (Lee *et al.*, 2015) to 50% (Iliff *et al.*, 2012) for 3 kDa dextran in mice), so comparisons with the values reported here may not be meaningful. One of the most striking differences we observed between sdAb and IgG concerned the prominent disposition of sdAb, but not IgG, in the smooth muscle BM of the tunica media in leptomeningeal arteries as shown by confocal imaging of the vessel wall (Fig. 9 *A* and *E* & Fig. 11 *J-M*). Such an apparent size-dependent access to the tunica media compartment following intrathecal infusions has to our knowledge not been previously identified, although Carare et al. have noted that 15 nm gold nanoparticles do not access the BM between smooth muscle cells (Morris *et al.*, 2016). Coupling the (i) greatly reduced IgG access to the smooth muscle BM of large leptomeningeal arteries relative to sdAb with (ii) significant peri-capillary access for both sdAb and IgG suggests the existence of a low-resistance peri-capillary compartment that may not easily distinguish sdAb and IgG based on size, as expected for a peri-capillary fluid space *in vivo* rather than a fused astrocyte/endothelial BM compartment (Maynard *et al.*, 1957; Jones, 1970; Cervós-Navarro & Ferszt, 1973; Peters *et al.*, 1991).

It seems likely that the unique pattern of perivascular signal associated with intrathecal sdAb and IgG across the rostral-caudal neural axis (Fig. 8) is dependent in some complex way on specific vessel branching patterns, continuity, pulsatility, and regional variations in PV hydraulic conductivity, i.e., the pattern of PV signal likely depends on characteristics of the blood vessels that supply and drain specific CNS regions. The cerebrovascular architecture of rat surface arteries and their associated PVS have been recently described (Lochhead *et al.*, 2015), based on multiple sources (e.g., (Scremin, 2004; Hammarlund-Udenaes *et al.*, 2014)), and can be divided into an anterior circulation (principally the internal carotid and the anterior and middle cerebral arteries, along with their associated branches) and a posterior circulation (principally the vertebral arteries, basilar artery and the posterior cerebral arteries, along with their associated branches). The olfactory bulbs and tracts consistently exhibited high PV signal in all animals, suggesting robust PV access and distribution associated with their arterial supply (nasal-olfactory, olfactofrontal, and ventral olfactory arteries, all principally branching from the anterior cerebral artery (Lochhead *et al.*, 2015)); other ventromedial brain regions (e.g., the septal nucleus and striatum) supplied by the anterior cerebral artery also exhibited consistently high PV signal while dorsomedial territories exhibited somewhat variable PV signal. Striatal and ventrolateral cortical regions associated with the middle cerebral artery exhibited consistently high PV signal while dorsolateral territories exhibited more variable PV signal. In general, ventral brain areas associated with proximal branches of posterior circulation vessels such as the diencephalon, midbrain, and hindbrain exhibited consistently high PV signal (e.g., hypothalamus, a small portion of the ventromedial thalamus, and ventromedial midbrain supplied by thalamo-perforating and median mesencephalic branches of the posterior cerebral/basilar arteries) while areas supplied by more distal branches exhibited little or no PV signal (e.g., anterior/dorsal thalamus and anterior/dorsal hippocampus, e.g., 2.5 mm posterior to bregma). The very sparse PV signal in parts of the brainstem and cerebellar cortex was also surprising, given these areas are supplied by branches of the vertebral and basilar arteries, which were nearest to the infusion site and exhibited the highest PV signal on the brain surface. Taken together, the overall pattern of PV signal distribution was most prominent at ventral sites nearest the origin of arterial branches and less prominent at more distal sites. Further, mannitol co-infused with IgG resulted in a somewhat global PV signal increase compared to that of IgG alone, i.e., PV signal was increased across many different areas supplied by both the anterior and posterior circulations.

Enhanced perivascular access of IgG with co-infusion of mannitol

Previous studies have shown intrathecal infusions of hypertonic mannitol solutions to be reasonably well tolerated in animals (Speck *et al.*, 1988) and 5% (0.27 M) sorbitol (an isomer of mannitol and a glucose metabolite) has been routinely used as a stabilizing excipient for viral gene therapy vectors intended for cisternal infusion (e.g., (Samaranch *et al.*, 2013)). However, our results represent the first characterization of the effects and possible mechanisms of intrathecally co-infused osmolytes on macromolecule distribution in the central compartment. We used *ex vivo* fluorescence imaging to evaluate intrathecal co-infusion of IgG with mannitol at two different mannitol concentrations (0.27 and 0.75 M), revealing a mannitol concentration-dependent increase in IgG signal for both the % brain area accessed and PV counts per mm^2 slice area. Interestingly, fluorescence intensity brain surface gradients did not appear affected by infusion of mannitol into the CSF at either concentration (Fig. 8), suggesting parenchymal diffusion was not enhanced by CSF mannitol and that the major contribution to increased IgG signal in brain likely came from a local effect on CSF-facing lining cells of leptomeningeal vessels (and possibly also pial cells) resulting in increased PV access.

Intrathecal mannitol infusions were well-tolerated in our experiments. Hyperosmolar mannitol has been used in past studies to modify BBB permeability characteristics (e.g., (Rapoport *et al.*, 1980; Neuwelt *et al.*, 1982; Cserr *et al.*, 1987)) but there has been little guidance on how intrathecal mannitol may impact the BBB or blood-CSF barriers. We expect that our intrathecal paradigm with 0.27 and 0.75 M mannitol minimally affected CNS barriers because (i) endpoint (30 min post-infusion) plasma IgG levels were unaffected by 0.27 M mannitol and minimally affected by 0.75 M mannitol, consistent with mannitol not altering central IgG clearance to the systemic compartment, (ii) we employed a slow intrathecal infusion which likely subjected mannitol to continuous dilution due to CSF production and clearance, and (iii) extrapolation suggests the CSF mannitol levels likely to have resulted from our infusions were well below levels associated with BBB modulation with systemically applied mannitol. Even if intrathecal mannitol had been administered as a bolus rather than a slow infusion over 50 min, we estimate it would have been diluted approximately 3-fold in the CSF (considering a bolus 80 μL volume of 0.75 M mannitol infused into ~ 250 μL of total subarachnoid CSF; total CSF volumes in the rat range from ~150-300 μL (Davson & Segal, 1995; Fenstermacher *et al.*, 1999; Preston, 2001)). Such a dilution would have resulted in a concentration of ~0.24 M mannitol assuming instantaneous mixing. The threshold for increasing BBB permeability with systemic mannitol has been reported to necessitate mannitol dosing resulting in blood concentrations (assuming 250 g rats with a blood volume of approximately 13 mL (Everett *et al.*, 1956)) of approximately 0.39 - 0.57 M mannitol (Rapoport *et al.*, 1980; Neuwelt *et al.*, 1982; Cserr *et al.*, 1987). Previous work has also shown a fairly short time window of increased BBB permeability in rats (~ 1 hr) with systemic mannitol application (Rapoport *et al.*, 1980). We therefore expect the effects of intrathecal mannitol to be temporary and reversible. Nevertheless, additional studies to investigate the kinetics and full range of actions for intrathecal mannitol infusions are warranted.

Periventricular white matter signal

Interestingly, animals infused with the smaller sdAb or, to a lesser extent, with IgG exhibited diffuse antibody signal in periventricular white matter areas surrounding the lateral ventricles (e.g., corpus callosum, external capsule, deep cerebral white matter) and extending rostrally into the olfactory ventricles (Fig. 8). *Ex vivo* fluorescence after sdAb infusion demonstrated this periventricular white matter signal in all animals. Infusion of IgG revealed a substantially smaller area of spread in 4/6 animals. Co-infusion of 0.27 M mannitol did not show apparent differences from IgG alone (signal present in 3/6 animals), but co-infusion of 0.75 M mannitol resulted in substantial diffuse IgG signal in periventricular white matter in 8/9 animals, though the spread was still less than for sdAb. The precise origin of this periventricular signal is at present not clear and will require further study. Multiple findings suggest that backflow from the cisterna magna into the ventricular compartment (i.e., from cisterna magna → fourth ventricle (4V) via foramina of Luschka and Magendie → third ventricle (3V) via cerebral aqueduct of Sylvius → lateral ventricles (LV) via intraventricular foramina of Monro) did not account for periventricular signal in our experiments. First, our infusion rate of 1.6 µl/min has been demonstrated by others to be below the rate (~3 µl/min) at which an infusion-dependent acute elevation in intracranial pressure first occurs in the rat (Yang *et al.*, 2013; Bedussi *et al.*, 2017); such an elevation, were it to occur, might in principle be accompanied by backflow from the subarachnoid space into the ventricles. Second, close examination of *ex vivo* fluorescence in coronal sections spanning across the brain (Fig. 8) revealed prominent periventricular signal in the lateral ventricles, with far less periventricular signal adjacent to the third and fourth ventricles; backflow would have been expected to produce the opposite gradient due to a dilution effect (i.e., with expected signal levels adjacent to the ventricles in the order of 4V > 3V > lateral ventricles). Third, MRI comparison of Gd-IgG signal associated with lateral ventricle and fourth ventricle ROIs (Fig. 6 *G-I*) showed that our infusion paradigm did not result in signal change from baseline suggestive of backflow (i.e., where 4V changes would be expected to exceed and precede LV changes). Furthermore, the kinetics of percent change from baseline in Gd-IgG contrast in LV and 4V ROIs resembled parenchymal ROIs rather than CSF ROIs from subarachnoid cisterns (compare Fig. 6*I* with Fig. 6 *E* and *F*). Taken together, the results suggest that infused antibodies gained entry to tissue compartments adjacent to the lateral ventricle and perhaps other ventricular compartments via other pathways.

We speculate two pathways may have contributed to this observed periventricular signal: (i) spillover from PV compartments associated with the choroidal arteries and (ii) alternative cistern-to-ventricle flow paths associated with the LV choroidal fissure, velum interpositum and medullary velae. The former possibility is supported by the observation that the choroid plexus often exhibited fluorescence, particularly with sdAb infusions. Transport within the PVS of the posterior cerebral artery, which branches to provide anterior, posterior lateral, and posterior medial choroidal arteries supplying the ventricular choroid plexuses that are most abundant within the lateral ventricles (Coyle, 1975), may have resulted in some spillover in these regions with subsequent flow along low resistance periventricular pathways associated with adjacent white matter or subependymal areas (Cserr *et al.*, 1977; Szentistványi *et al.*, 1984; Ichimura *et al.*, 1991). The latter possibility is suggested by several observations by others in which direct connections have been inferred between the ventricular spaces and cisterns at specialized sites where the pia, ependyma, and leptomeningeal vessels are in close proximity; such sites, revealed by labeled tracer infusions, may include the LV choroidal fissure (Bedussi *et al.*, 2017), the velum interpositum (Ghersi-Egea *et al.*, 1996*a*), and the superior medullary velum (Ghersi-Egea *et al.*, 1996*a*). Other studies employing low flow rate infusions in rats have also reported tracer signal in ventricular compartments such as the LV (Bedussi *et al.*, 2017) and mesencephalic 4V (Iliff *et al.*, 2013*a*); indeed, Benveniste et al. have reported size-dependent signal accumulation with two different cisternally-infused MRI contrast agents (938 Da Gd-DPTA >> 200 kDa GadoSpinP) at the cerebral aqueduct/4V (Iliff *et al.*, 2013*a*) using the same infusion rate as in the present study.

Potential PVS access sites

Very little information exists from past rodent studies regarding the nature of the transport barrier(s) that might be responsible for the size-dependent PV access from the CSF (and its manipulation by mannitol) seen in this study. SEM studies in other species have indicated the presence of fenestration-like stomata between CSF-facing lining cells of leptomeningeal vessels in the subarachnoid space (Cloyd & Low, 1974; Zervas *et al.*, 1982) with a potential role in supplying nutrients to large cerebral vessels that lack the vasa vasorum present elsewhere in the body (Zervas *et al.*, 1982), but the possibility that such pores exist in rodents has thus far only been suggested by isolated observations from two previous transmission electron microscopy studies (Frederickson & Low, 1969; Oda & Nakanishi, 1984). Here, we used SEM to show the presence of numerous micron-sized stomata on leptomeningeal cells of subarachnoid vessels from both the anterior and posterior circulations in the rat. The general dimensions, circularity, and dense, underlying connective tissue of these stomata closely resemble leptomeningeal vessel fenestrations seen with SEM in the cat (Zervas *et al.*, 1982) (as well as pial fenestrations that have been observed with SEM in dogs (Cloyd & Low, 1974) and humans (Reina *et al.*, 2004)). We speculate that sieving by such structures (stomata and their closely associated connective tissue) may be responsible at least in part for the reduced PV access we observed for the larger IgG relative to the smaller sdAb. Further, our result that mannitol co-infusions significantly increased PV access of IgG appear consistent with an osmotic effect on stomata and/or intercellular gaps between leptomeningeal vessel lining cells (or pial cells). More work is needed to investigate such structures, their regional distribution, and their possible modulation.

Involvement of the olfactory clearance route for CNS antibody drainage

Drainage of CSF- or parenchymally-administered tracer substances along olfactory nerves to the nasal mucosa and then to the cervical lymph nodes has been suggested in many prior studies (reviewed in (Weller *et al.*, 1992; Koh *et al.*, 2005)), mostly using tracers such as India ink (e.g., (Kida *et al.*, 1993)), radiocontrast (e.g., (Faber, 1937)), or radiolabeled substances (e.g., (Bradbury & Westrop, 1983)), but this communication route has recently been questioned (Louveau *et al.*, 2015). Here, we have shown with *ex vivo* fluorescence and confocal imaging that intrathecal infusions of sdAb and IgG resulted in (i) prominent signal in the nasal mucosa, predominantly associated with the olfactory region, (ii) IgG signal throughout the olfactory lamina propria, and

(iii) prominent signal in the deep cervical lymph nodes. Confocal imaging of the olfactory mucosa demonstrated IgG associated with connective tissue and numerous vessels throughout the lamina propria (Fig. 12 *E-I*), in proximity to areas shown with SEM to contain lymphatics (Furukawa *et al.*, 2008), and *ex vivo* fluorescence imaging of olfactory bulb sections showed sdAb and IgG throughout the olfactory nerve layer. These results are consistent with IgG clearance/drainage along olfactory perivascular/perineural spaces and/or lymphatics across the cribriform plate to the olfactory mucosa, as demonstrated by others using different tracers (Faber, 1937; Kida *et al.*, 1995; Koh *et al.*, 2005; Aspelund *et al.*, 2015). Preferential drainage of sdAb and IgG to the olfactory region (with much less drainage to the nasal respiratory mucosa) may be functionally important as the olfactory mucosa exhibits significantly lower relative vascularity and vascular permeability that have been speculated to favor lymphatic drainage from the olfactory lamina propria to regional lymph nodes (e.g., deep cervical) (Kumar *et al.*, 2016). Antibody signal was also evident in proximity to several cranial and spinal nerves, some of which seemed to be in the ensheathing dura, possibly associated with dural lymphatics (Aspelund *et al.*, 2015); dissection and imaging of dorsal cranial dura revealed intrathecally infused IgG signal localized around sinuses, a portion of which may have been associated with dural lymphatics (Aspelund *et al.*, 2015; Louveau *et al.*, 2015).

Significance for CNS physiology, pathology, and drug delivery

Endogenous IgG antibodies are the second most abundant proteins in CSF (after albumin), representing ~7-12% of total CSF protein (Davson & Segal, 1995), yet surprisingly little is known about their precise distribution pathways from the CSF into brain; indeed, the nature and limits of the PV pathways taken by endogenous antibodies as they traffic into the brain may have significant implications for immune surveillance (Schmitt *et al.*, 2012). We have shown that CSF-borne IgG (10 nm d_H) has difficulty accessing the BM between smooth muscle cells while the smaller sdAb (4.5 nm d_H) appears to penetrate the tunica media compartment fully. We speculate that a smaller protein than sdAb, e.g., the soluble 40-residue form of beta-amyloid (Aß$_{1\text{-}40}$), might also be expected to also easily access the BM compartment between smooth muscle cells from the CSF and, once there, to remain relatively hidden from perivascular circulating IgG (endogenous or exogenous) originating from the CSF. Indeed, others have speculated that cerebrovascular amyloid in Alzheimer's disease, characterized in large part by Aß$_{1\text{-}40}$ deposition in the BM between smooth muscle cells, may originate from CSF Aß$_{1\text{-}40}$ (Ghersi-Egea *et al.*, 1996*b*); interestingly, such amyloid deposition has proven difficult to clear by either systemic or centrally administered antibody (discussed in (Koenigsknecht-Talboo *et al.*, 2008)). We speculate that the perivascular trafficking of IgG and other proteins may have unique relevance for cerebral amyloid angiopathy (Weller *et al.*, 2008), autoimmune disease (Asgari *et al.*, 2015), and other conditions where IgG surveillance pathways between the CSF and parenchyma may affect pathogenesis. Stomata on leptomeningeal lining cells of subarachnoid vessels may also provide unique pathways for the trafficking of immune cells (Merchant & Low, 1977). Our results also reaffirm the importance of olfactory drainage pathways for CSF clearance, with previously described potential implications for central antigen drainage (Bradbury & Westrop, 1983; Kida *et al.*, 1993; Knopf *et al.*, 1995; Engelhardt *et al.*, 2017). Finally, our results may have unique relevance for understanding, optimizing, and translating several CNS drug delivery approaches, particularly the central infusion of antibodies and other proteins by the intrathecal and/or intraventricular routes, as it emphasizes the critical importance of PV pathways in achieving more extensive central distribution. In agreement with much past work (Fenstermacher & Patlak, 1976; Thorne *et al.*, 2004; Thorne &

Nicholson, 2006; Syková & Nicholson, 2008; Wolak & Thorne, 2013), our results confirm that brain surface gradients of sdAb and IgG are consistent with diffusive transport into the brain from the CSF; we infer from this result that transport through the neuropil of the gray matter adjacent to the PV pathways is also likely to be diffusive in nature under normal conditions. Importantly, gradients produced by diffusion are not expected to scale with increasing brain size (Wolak & Thorne, 2013; Wolak *et al.*, 2015), while it appears increasingly likely that circulation/distribution of CSF and ISF within the ventricles, extraventricular sites, and the PVS do represent scalable phenomena (Rennels *et al.*, 1985; Jolly *et al.*, 2011; Samaranch *et al.*, 2013). Taken together, the significance of these findings for central drug delivery is that access to and distribution within PV pathways may ultimately dictate the success or failure of a variety of different approaches (e.g., intranasal (Lochhead *et al.*, 2015), intrathecal, or intraventricular administration) aimed at whole brain delivery. Understanding the key physiologic determinants of central distribution may in the end allow optimization strategies (e.g., use of smaller active drug fragments or osmolyte co-infusion, as we have described) to enhance the prospects for success in translating pre-clinical CNS drug delivery studies to the clinic.

Translational Perspective

Mechanistic understanding of methods for traversing or bypassing the barriers between the blood and CNS in order to achieve effective delivery of biologics (e.g., peptides, proteins, oligonucleotides, and gene therapies) to the brain and spinal cord has been a major challenge in biomedical research. The past several decades have witnessed many preclinical and clinical trials aimed at demonstrating efficacy for biologics in the treatment of CNS disorders but successful translation to the clinic has been rare; although most such trials have centered around strategies attempting to deliver a biologic or conjugate across the blood-brain barrier, today there are only three examples of clinically approved biologics (U.S. & E.U.) that are unequivocally delivered to CNS target sites and each of these involve bypassing the CNS barriers with CSF infusions (intrathecal ziconotide, a peptide, for chronic pain; intrathecal nusinersen, an antisense oligonucleotide, for spinal muscular atrophy; intracerebroventricular cerliponase alfa, an enzyme replacement therapy, for a form of neuronal ceroid lipofuscinosis). However, detailed descriptions of the factors that govern the distribution of biologics, particularly therapeutically promising antibodies and antibody fragments, from the CSF to brain tissue have been surprisingly limited. Our findings illuminate how the CSF-to-brain transfer of antibodies occurs in rats, showing the physiological and anatomical correlates that underlie intrathecal antibody delivery as well as the trafficking of endogenous antibodies. Our results suggest that perivascular access and distribution of antibodies, and likely other biologics, has been underappreciated as a key physiologic determinant of whether extensive central distribution is achievable with CSF infusions.

References

Abbott NJ (2004). Evidence for bulk flow of brain interstitial fluid: significance for physiology and pathology. *Neurochem Int* **45,** 545–552.

Abbott NJ, Rönnbäck L & Hansson E (2006). Astrocyte-endothelial interactions at the blood-brain barrier. *Nat Rev Neurosci* **7,** 41–53.

Asgari M, de Zélicourt D & Kurtcuoglu V (2016). Glymphatic solute transport does not require bulk flow. *Sci Rep* **6,** 38635.

Asgari N, Berg CT, Mørch MT, Khorooshi R & Owens T (2015). Cerebrospinal fluid aquaporin-4-immunoglobulin G disrupts blood brain barrier. *Ann Clin Transl Neurol* **2,** 857–863.

Aspelund A, Antila S, Proulx ST, Karlsen TV, Karaman S, Detmar M, Wiig H & Alitalo K (2015). A dural lymphatic vascular system that drains brain interstitial fluid and macromolecules. *J Exp Med* **212,** 991–999.

Barthel KU (2005). *Volume Viewer*. Berlin, Germany.

Bedussi B, van der Wel NN, de Vos J, van Veen H, Siebes M, VanBavel E & Bakker EN (2017). Paravascular channels, cisterns, and the subarachnoid space in the rat brain: A single compartment with preferential pathways. *J Cereb Blood Flow Metab* **37,** 1374–1385.

Bradbury MW, Cserr HF & Westrop RJ (1981). Drainage of cerebral interstitial fluid into deep cervical lymph of the rabbit. *Am J Physiol* **240,** F329-36.

Bradbury MW & Westrop RJ (1983). Factors influencing exit of substances from cerebrospinal fluid into deep cervical lymph of the rabbit. *J Physiol* **339,** 519–534.

Calias P, Banks WA, Begley D, Scarpa M & Dickson P (2014). Intrathecal delivery of protein therapeutics to the brain: A critical reassessment. *Pharmacol Ther* **144,** 114–122.

Carare RO, Bernardes-Silva M, Newman TA, Page AM, Nicoll JAR, Perry VH & Weller RO (2008). Solutes, but not cells, drain from the brain parenchyma along basement membranes of capillaries and arteries: significance for cerebral amyloid angiopathy and neuroimmunology. *Neuropathol Appl Neurobiol* **34,** 131–144.

Casley-Smith JR, Földi-Börsök E & Földi M (1976). The prelymphatic pathways of the brain as revealed by cervical lymphatic obstruction and the passage of particles. *Br J Exp Pathol* **57,** 179–188.

Cervós-Navarro J & Ferszt R (1973). Connective tissue in pericapillary spaces of the human spinal cord. *Acta Neuropathol* **24,** 178–183.

Clement EA, Richard A, Thwaites M, Ailon J, Peters S & Dickson CT (2008). Cyclic and sleep-like spontaneous alternations of brain state under urethane anaesthesia. *PLoS One*; DOI: 10.1371/journal.pone.0002004.

Cloyd MW & Low FN (1974). Scanning electron microscopy of the subarachnoid space in the dog. I. Spinal cord levels. *J Comp Neurol* **153,** 325–368.

Coloma M, Schaffer JD, Carare RO, Chiarot PR & Huang P (2016). Pulsations with reflected boundary waves: a hydrodynamic reverse transport mechanism for perivascular drainage in the brain. *J Math Biol* **73,** 469–490.

Coyle P (1975). Arterial patterns of the rat rhinencephalon and related structures. *Exp Neurol* **49,** 671–690.

Cserr HF, Cooper DN & Milhorat TH (1977). Flow of cerebral interstitial fluid as indicated by the removal of extracellular markers from rat caudate nucleus. *Exp Eye Res* **25 Suppl,** 461–473.

Cserr HF, Cooper DN, Suri PK & Patlak CS (1981). Efflux of radiolabeled polyethylene glycols and albumin from rat brain. *Am J Physiol* **240,** F319-28.

Cserr HF, DePasquale M & Patlak CS (1987). Volume regulatory influx of electrolytes from plasma to brain during acute hyperosmolality. *Am J Physiol* **253,** F530-7.

Cserr HF & Knopf PM (1992). Cervical lymphatics, the blood-brain barrier and the immunoreactivity of the brain: a new view. *Immunol Today* **13,** 507–512.

Davson H & Segal MB (1995). *Phyioslogy of the CSF and Blood-Brain Barriers*, 1st edn.ed. Davson H & Segal MB. CRC Press, Inc, Boca Raton.

Engelhardt B, Vajkoczy P & Weller RO (2017). The movers and shapers in immune privilege of the CNS. *Nat Immunol* **18,** 123–131.

Everett NB, Simmons B & Lasher EP (1956). Distribution of blood (Fe 59) and plasma (I 131) volumes of rats determined by liquid nitrogen freezing. *Circ Res* **4,** 419–424.

Faber WM (1937). The nasal mucosa and the subarachnoid space. *Am J Anat* **62,** 121–148.

Fabry Z, Schreiber H a., Harris MG & Sandor M (2008). Sensing the microenvironment of the central nervous system: immune cells in the central nervous system and their pharmacological manipulation. *Curr Opin Pharmacol* **8,** 496–507.

Farrington GK, Caram-Salas N, Haqqani AS, Brunette E, Eldredge J, Pepinsky B, Antognetti G, Baumann E, Ding W, Garber E, Jiang S, Delaney C, Boileau E, Sisk WP & Stanimirovic DB (2014). A novel platform for engineering blood-brain barrier-crossing bispecific biologics. *FASEB J* **28,** 4764–4778.

Fawcett DW (1986). Blood and lymph vascular systems. In *A textbook of histology*, 11th edn., pp. 367–405. W.B. Saunders Company, Philadelphia.

Fenstermacher JD, Ghersi-Egea JF, Finnegan W & Chen JL (1997). The rapid flow of cerebrospinal fluid from ventricles to cisterns via subarachnoid velae in the normal rat. *Acta Neurochir Suppl* **70,** 285–287.

Fenstermacher JD, Nagaraja TN, Wei L & Ghersi-Egea J-F (1999). Surprises and peculiarities in the distribution of material from cerebrospinal fluid to brain tissues and blood. In *Brain Barrier Systems: Alfred Benzon Symposium*, pp. 494–505. Munksgaard, Copenhagen.

Fenstermacher JD & Patlak CS (1976). The Movements of Water and Solutes in the Brains of Mammals. In *Dynamics of Brain Edema*, ed. Pappius HM & Feindel W, pp. 87–94. Springer Berlin Heidelberg.

Foley CP, Nishimura N, Neeves KB, Schaffer CB & Olbricht WL (2012). Real-time imaging of perivascular transport of nanoparticles during convection-enhanced delivery in the rat cortex. *Ann Biomed Eng* **40,** 292–303.

Frederickson RG & Low FN (1969). Blood vessels and tissue space associated with the brain of the rat. *Am J Anat* **125,** 123–145.

Furukawa M, Shimoda H, Kajiwara T, Kato S & Yanagisawa S (2008). Topographic study on nerve-associated lymphatic vessels in the murine craniofacial region by immunohistochemistry and electron microscopy. *Biomed Res* **29,** 289–296.

Ghersi-Egea JF, Finnegan W, Chen JL, Fenstermacher JD & Hospital HF (1996*a*). Rapid distribution of intraventricularly administered sucrose into cerebrospinal fluid cisterns via subarachnoid velae in rat. *Neuroscience* **75,** 1271–1288.

Ghersi-Egea JF, Gorevic PD, Ghiso J, Frangione B, Patlak CS & Fenstermacher JD (1996*b*). Fate of cerebrospinal fluid-borne amyloid beta-peptide: rapid clearance into blood and appreciable accumulation by cerebral arteries. *J Neurochem* **67,** 880–883.

Hadaczek P, Kohutnicka M, Krauze MT, Bringas J, Pivirotto P, Cunningham J & Bankiewicz K (2006*a*). Convection-enhanced delivery of adeno-associated virus type 2 (AAV2) into the striatum and transport of AAV2 within monkey brain. *Hum Gene Ther* **17,** 291–302.

Hadaczek P, Yamashita Y, Mirek H, Tamas L, Bohn MC, Noble C, Park JW & Bankiewicz K (2006*b*). The “perivascular pump” driven by arterial pulsation is a powerful mechanism for the distribution of therapeutic molecules within the brain. *Mol Ther* **14,** 69–78.

Hammarlund-Udenaes M, de Lange E & Thorne RG eds. (2014). *Drug Delivery to the Brain: Physiological Concepts, Methodologies and Approaches*. Springer-Verlag, New York.

Hara K & Harris RA (2002). The anesthetic mechanism of urethane: the effects on neurotransmitter-gated ion channels. *Anesth Analg* **94,** 313–318.

Hladky SB & Barrand MA (2014). Mechanisms of fluid movement into, through and out of the brain: evaluation of the evidence. *Fluids Barriers CNS* **11,** 26.

Hutchings M & Weller RO (1986). Anatomical relationships of the pia mater to cerebral blood vessels in man. *J Neurosurg* **65,** 316–325.

Ichimura T, Fraser PAA & Cserr HF (1991). Distribution of extracellular tracers in perivascular spaces of the rat brain. *Brain Res* **545,** 103–113.

Iliff JJ, Lee H, Yu M, Feng T, Logan J, Nedergaard M & Benveniste H (2013*a*). Brain-wide pathway for waste clearance captured by contrast-enhanced MRI. *J Clin Invest* **123,** 1299–1309.

Iliff JJ, Wang M, Liao Y, Plogg BA, Peng W, Gundersen GA, Benveniste H, Vates GE, Deane R, Goldman SA, Nagelhus EA & Nedergaard M (2012). A paravascular pathway facilitates CSF flow through the brain parenchyma and the clearance of interstitial solutes, including amyloid β. *Sci Transl Med* **4,** 147ra111.

Iliff JJ, Wang M, Zeppenfeld DM, Venkataraman A, Plog B a, Liao Y, Deane R & Nedergaard M (2013*b*). Cerebral arterial pulsation drives paravascular CSF-interstitial fluid exchange in the murine brain. *J Neurosci* **33,** 18190–18199.

Jin B-J, Smith AJ & Verkman AS (2016). Spatial model of convective solute transport in brain extracellular space does not support a "glymphatic" mechanism. *J Gen Physiol* **148,** 489–501.

Jolly RD, Marshall NR, Perrott MR, Dittmer KE, Hemsley KM & Beard H (2011). Intracisternal enzyme replacement therapy in lysosomal storage diseases: Routes of absorption into brain. *Neuropathol Appl Neurobiol* **37,** 414–422.

Jones EG (1970). On the mode of entry of blood vessels into the cerebral cortex. *J Anat* **106,** 507–520.

Kida S, Pantazis A & Weller RO (1993). CSF drains directly from the subarachnoid space into nasal lymphatics in the rat. Anatomy, histology and immunological significance. *Neuropathol Appl Neurobiol* **19,** 480–488.

Kida S, Weller RO, Zhang ET, Phillips MJ & Iannotti F (1995). Anatomical pathways for lymphatic drainage of the brain and their pathological significance. *Neuropathol Appl Neurobiol* **21,** 181–184.

Knopf PM, Cserr HF, Nolan SC, Wu TY & Harling-Berg CJ (1995). Physiology and immunology of lymphatic drainage of interstitial and cerebrospinal fluid from the brain. *Neuropathol Appl Neurobiol* **21,** 175–180.

Koenigsknecht-Talboo J, Meyer-Luehmann M, Parsadanian M, Garcia-Alloza M, Finn MB, Hyman BT, Bacskai BJ & Holtzman DM (2008). Rapid microglial response around amyloid pathology after systemic anti-Abeta antibody administration in PDAPP mice. *J Neurosci* **28,** 14156–14164.

Koh L, Zakharov A & Johnston M (2005). Integration of the subarachnoid space and lymphatics: is it time to embrace a new concept of cerebrospinal fluid absorption? *Cerebrospinal Fluid Res* **2,** 6.

Krisch B, Leonhardt H & Oksche A (1984). Compartments and perivascular arrangement of the meninges covering the cerebral cortex of the rat. *Cell Tissue Res* **238,** 459–474.

Kumar NN, Gautam M, Lochhead JJ, Wolak DJ, Ithapu V, Singh V & Thorne RG (2016). Relative vascular permeability and vascularity across different regions of the rat nasal mucosa: implications for nasal physiology and drug delivery. *Sci Rep* **6,** 31732.

Lee H, Xie L, Yu M, Kang H, Feng T, Deane R, Logan J, Nedergaard M & Benveniste H (2015). The Effect of Body Posture on Brain Glymphatic Transport. *J Neurosci* **35,** 11034–11044.

Lochhead JJ, Wolak DJ, Pizzo ME & Thorne RG (2015). Rapid transport within cerebral perivascular spaces underlies widespread tracer distribution in the brain after intranasal administration. *J Cereb blood flow Metab* **35,** 371–381.

Louveau A, Smirnov I, Keyes TJ, Eccles JD, Rouhani SJ, Peske JD, Derecki NC, Castle D, Mandell JW, Lee KS, Harris TH & Kipnis J (2015). Structural and functional features of central nervous system lymphatic vessels. *Nature* **523,** 337–341.

Maynard EA, Schultz RL & Pease DC (1957). Electron microscopy of the vascular bed of rat cerebral cortex. *Am J Anat* **100,** 409–433.

Merchant RE & Low FN (1977). Scanning electron microscopy of the subarachnoid space in the dog. V. Macrophages challenged by bacillus Calmette-Guerin. *J Comp Neurol* **172,** 381–407.

Morris AWJ, Sharp MM, Albargothy NJ, Fernandes R, Hawkes CA, Verma A, Weller RO & Carare RO (2016). Vascular basement membranes as pathways for the passage of fluid into and out of the brain. *Acta Neuropathol*; DOI: 10.1007/s00401-016-1555-z.

Morse DE & Low FN (1972). The fine structure of the pia mater of the rat. *Am J Anat* **133,** 349–367.

Mullin JW ed. (2001). Appendix. In *Crystallization*, 4th edn., pp. 478–535. Butterworth-Heinemann: Oxford, Boston.

Nabeshima S, Reese TS, Landis DM & Brightman MW (1975). Junctions in the meninges and marginal glia. *J Comp Neurol* **164,** 127–169.

Nedergaard M (2013). Neuroscience. Garbage truck of the brain. *Science* **340,** 1529–1530.

Neuwelt EA, Barnett P a, Bigner DD & Frenkel EP (1982). Effects of adrenal cortical steroids and osmotic blood-brain barrier opening on methotrexate delivery to gliomas in the rodent: the factor of the blood-brain barrier. *Proc Natl Acad Sci* **79,** 4420–4423.

Nicholson C & Tao L (1993). Hindered diffusion of high molecular weight compounds in brain extracellular microenvironment measured with integrative optical imaging. *Biophys J* **65,** 2277–2290.

Oda Y & Nakanishi I (1984). Ultrastructure of the mouse leptomeninx. *J Comp Neurol* **225,** 448–457.

Okun E, Mattson MP & Arumugam T V. (2010). Involvement of Fc receptors in disorders of the central nervous system. *NeuroMolecular Med* **12,** 164–178.

Papisov MI, Belov V V & Gannon KS (2013). Physiology of the intrathecal bolus: the leptomeningeal route for macromolecule and particle delivery to CNS. *Mol Pharm* **10,** 1522–1532.

Paxinos G & Watson C (2007). *The Rat Brain in Stereotaxic Coordinates*, 6th edn. Academic Press, London.

Pease DC & Schultz RL (1958). Electron microscopy of rat cranial meninges. *Am J Anat* **102,** 301–321.

Peng W, Achariyar TM, Li B, Liao Y, Mestre H, Hitomi E, Regan S, Kasper T, Peng S, Ding F, Benveniste H, Nedergaard M & Deane R (2016). Suppression of glymphatic fluid transport in a mouse model of Alzheimer's disease. *Neurobiol Dis* **93,** 215–225.

Peters A, Palay SSL & Webster H deF. (1991). *The fine structure of the nervous system: neurons and their supporting cells*, 3rd edn. Oxford University Press, New York.

Preston JE (2001). Ageing choroid plexus-cerebrospinal fluid system. *Microsc Res Tech* **52,** 31–37.

Proescholdt MG, Hutto B, Brady LS & Herkenham M (2000). Studies of cerebrospinal fluid flow and penetration into brain following lateral ventricle and cisterna magna injections of the tracer [14C]inulin in rat. *Neuroscience* **95,** 577–592.

Ransohoff RM & Engelhardt B (2012). The anatomical and cellular basis of immune surveillance in the central nervous system. *Nat Rev Immunol* **12,** 623–635.

Rapoport SI, Fredericks WR, Ohno K & Pettigrew KD (1980). Quantitative aspects of reversible osmotic opening of the blood-brain barrier. *Am J Physiol* **238,** R421-31.

Reina MA, De León Casasola ODL, Villanueva MC, López A, Machés F & De Andrés JA (2004). Ultrastructural findings in human spinal pia mater in relation to subarachnoid anesthesia. *Anesth Analg* **98,** 1479–1485.

Rennels ML, Gregory TF, Blaumanis OR, Fujimoto K & Grady PA (1985). Evidence for a "paravascular" fluid circulation in the mammalian central nervous system, provided by the rapid distribution of tracer protein throughout the brain from the subarachnoid space. *Brain Res* **326,** 47–63.

Samaranch L, Salegio EA, San Sebastian W, Kells AP, Bringas JR, Forsayeth J & Bankiewicz KS (2013). Strong Cortical and Spinal Cord Transduction After AAV7 and AAV9 Delivery into the Cerebrospinal Fluid of Nonhuman Primates. *Hum Gene Ther* **24,** 526–532.

Schindelin J, Arganda-Carreras I, Frise E, Kaynig V, Longair M, Pietzsch T, Preibisch S, Rueden C, Saalfeld S, Schmid B, Tinevez J-Y, White DJ, Hartenstein V, Eliceiri K, Tomancak P & Cardona A (2012). Fiji: an open-source platform for biological-image analysis. *Nat Methods* **9,** 676–682.

Schmid B, Schindelin J, Cardona A, Longair M & Heisenberg M (2010). A high-level 3D visualization API for Java and ImageJ. *BMC Bioinformatics* **11,** 274.

Schmitt C, Strazielle N & Ghersi-Egea J-F (2012). Brain leukocyte infiltration initiated by peripheral inflammation or experimental autoimmune encephalomyelitis occurs through pathways connected to the CSF-filled compartments of the forebrain and midbrain. *J Neuroinflammation* **9,** 187.

Scremin OU (2004). Cerebral vascular system. In *The rat nervous system*, 3rd edn., ed. Paxinos G, pp. 1167–1199. Academic Press, San Diego.

Sixt M, Engelhardt B, Pausch F, Hallmann R, Wendler O & Sorokin LM (2001). Endothelial cell laminin isoforms, laminins 8 and 10, play decisive roles in T cell recruitment across the blood-brain barrier in experimental autoimmune encephalomyelitis. *J Cell Biol* **153,** 933–945.

Speck U, Press WR & Mützel W (1988). Osmolality-related effects of injections into the central nervous system. *Invest Radiol* **23 Suppl 1,** S114–S117.

Swanson LW (1998). *Brain Maps: Structure of the rat brain*. Elsevier, Amsterdam.

Syková E & Nicholson C (2008). Diffusion in brain extracellular space. *Physiol Rev* **88,** 1277–1340.

Szentistványi I, Patlak CS, Ellis RA & Cserr HF (1984). Drainage of interstitial fluid from different regions of rat brain. *Am J Physiol* **246,** 35–44.

Thakker DR, Weatherspoon MR, Harrison J, Keene TE, Lane DS, Kaemmerer WF, Stewart GR & Shafer LL (2009). Intracerebroventricular amyloid-beta antibodies reduce cerebral amyloid angiopathy and associated micro-hemorrhages in aged Tg2576 mice. *Proc Natl Acad Sci* **106,** 4501–4506.

Thorne RG, Hrabetová S & Nicholson C (2004). Diffusion of epidermal growth factor in rat brain extracellular space measured by integrative optical imaging. *J Neurophysiol* **92,** 3471–3481.

Thorne RG, Lakkaraju A, Rodriguez-Boulan E & Nicholson C (2008). In vivo diffusion of lactoferrin in brain extracellular space is regulated by interactions with heparan sulfate. *Proc Natl Acad Sci USA* **105,** 8416–8421.

Thorne RG & Nicholson C (2006). In vivo diffusion analysis with quantum dots and dextrans predicts the width of brain extracellular space. *Proc Natl Acad Sci USA* **103,** 5567–5572.

Wagner HJ, Pilgrim C & Brandl J (1974). Penetration and removal of horseradish peroxidase injected into the cerebrospinal fluid: Role of cerebral perivascular spaces, endothelium and microglia. *Acta Neuropathol* **27,** 299–315.

Wang P & Olbricht WL (2011). Fluid mechanics in the perivascular space. *J Theor Biol* **274,** 52–57.

Weller RO, Kida S & Zhang ET (1992). Pathways of fluid drainage from the brain--morphological aspects and immunological significance in rat and man. *Brain Pathol* **2,** 277–284.

Weller RO, Subash M, Preston SD, Mazanti I & Carare RO (2008). Perivascular drainage of amyloid-beta peptides from the brain and its failure in cerebral amyloid angiopathy and Alzheimer's disease. *Brain Pathol* **18,** 253–266.

Wolak DJ, Pizzo ME & Thorne RG (2015). Probing the extracellular diffusion of antibodies in brain using in vivo integrative optical imaging and ex vivo fluorescence imaging. *J Control Release* **197,** 78–86.

Wolak DJ & Thorne RG (2013). Diffusion of macromolecules in the brain: implications for drug delivery. *Mol Pharm* **10,** 1492–1504.

Wu C, Ivars F, Anderson P, Hallmann R, Vestweber D, Nilsson P, Robenek H, Tryggvason K, Song J, Korpos E, Loser K, Beissert S, Georges-Labouesse E & Sorokin LM (2009). Endothelial basement membrane laminin alpha5 selectively inhibits T lymphocyte extravasation into the brain. *Nat Med* **15,** 519–527.

Xie L, Kang H, Xu Q, Chen MJ, Liao Y, Thiyagarajan M, O'Donnell J, Christensen DJ, Nicholson C, Iliff JJ, Takano T, Deane R & Nedergaard M (2013). Sleep drives metabolite clearance from the adult brain. *Science* **342,** 373–377.

Yamada S, DePasquale M, Patlak CS & Cserr HF (1991). Albumin outflow into deep cervical lymph from different regions of rabbit brain. *Am J Physiol* **261,** H1197-204.

Yang L, Kress BT, Weber HJ, Thiyagarajan M, Wang B, Deane R, Benveniste H, Iliff JJ & Nedergaard M (2013). Evaluating glymphatic pathway function utilizing clinically relevant intrathecal infusion of CSF tracer. *J Transl Med* **11,** 107.

Zervas NT, Liszczak TM, Mayberg MR & Black PM (1982). Cerebrospinal fluid may nourish cerebral vessels through pathways in the adventitia that may be analogous to systemic vasa vasorum. *J Neurosurg* **56,** 475–481.

Zhang ET, Inman CB & Weller RO (1990). Interrelationships of the pia mater and the perivascular (Virchow-Robin) spaces in the human cerebrum. *J Anat* **170,** 111–123.

Zhang ET, Richards HK, Kida S & Weller RO (1992). Directional and compartmentalised drainage of interstitial fluid and cerebrospinal fluid from the rat brain. *Acta Neuropathol* **83,** 233–239.

Ziegler R, Salegio E, Dodge J, Bringas J, Treleaven C, Bercury S, Tamsett T, Shihabuddin L, Hadaczek P, Fiandaca M, Bankiewicz K & Scheule R (2011). Distribution of acid sphingomyelinase in rodent and non-human primate brain after intracerebroventricular infusion. *Exp Neurol* **231,** 261–271.

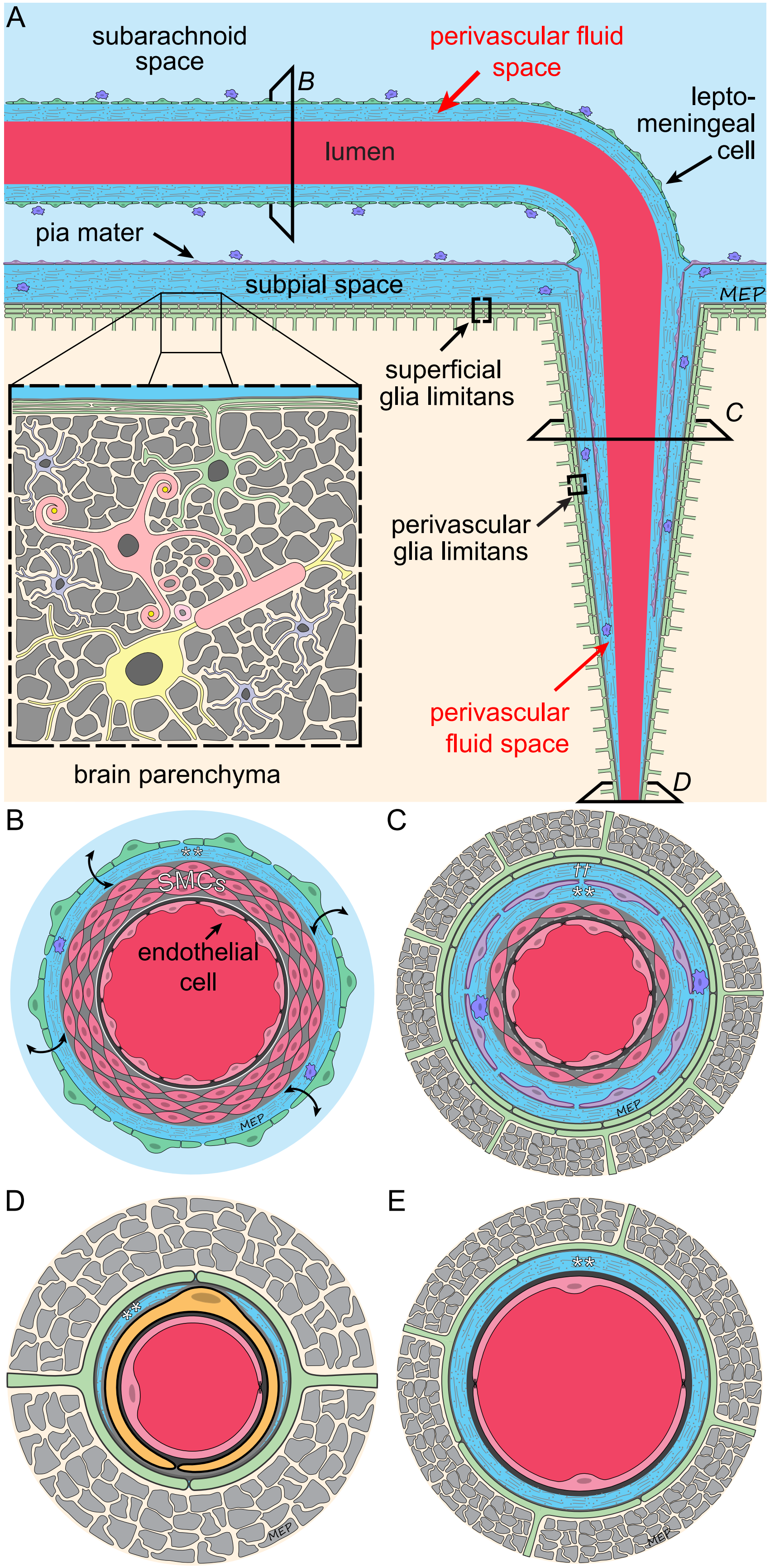
A
subarachnoid space
perivascular fluid space
B
lepto-meningeal cell
lumen
pia mater
subpial space
MEP
superficial glia limitans
C
perivascular glia limitans
perivascular fluid space
D
brain parenchyma
B
**
SMCs
endothelial cell
MEP
C
††
**
MEP
D
**
MEP
E
**
MEP

Figure 1. Schematic of the subarachnoid and perivascular spaces and their relationship to the brain parenchyma. (A) The cerebrospinal fluid (CSF, light blue) of the subarachnoid space (SAS) is contained between the arachnoid mater and pia mater (light purple). Leptomeningeal blood vessels traverse the CSF of the SAS on the brain's surface; these vessels are covered by a layer of leptomeningeal cells (green), sometimes referred to as the adventitial cell layer. Beneath the pia and its BM (thin gray line) is the subpial space containing connective tissue (e.g., collagen), cells (e.g., macrophages, purple), and subpial vessels. Studies suggest the PVS is continuous between blood vessels in the SAS, the subpial space, and the parenchyma (Krisch et al., 1984; Zhang et al., 1990; Ichimura et al., 1991). Separating the subpial space and PVS from the brain parenchyma is the glia limitans, composed of astrocyte endfeet (light green) and their associated basement membrane (thin gray line). Within the brain parenchyma (inset), cells (neurons in yellow, oligodendrocytes in pink, microglia in light blue, astrocytes in light green) and associated processes (gray) create a narrow and tortuous extracellular space (beige) filled with interstitial fluid (Wolak & Thorne, 2013). The PVS is surrounded by different components depending on the level, as viewed in cross-section (B-E). (B) A leptomeningeal artery on the brain surface has three main layers: the intima (consisting of endothelial cells (pink), endothelial cell BM (dark gray), and the internal elastic lamina (white)), the media (consisting of a few layers of circumferentially arranged smooth muscle cells (pink) and their BM (gray)), and the adventitia (which is made of loose connective tissue (e.g., collagen), scattered cells (e.g., macrophages, purple), and fluid (thus the perivascular fluid space, darker blue). This adventitial space (**) is generally referred to as the subarachnoid PVS, and is surrounded by a layer of leptomeningeal cells (green) which separate the blood vessel wall and PVS from the CSF (light blue), with potential points of entry as discussed in the text (e.g., fenestrations or stomata, intercellular clefts, and possibly other structures; depicted with arrows). (C) A rodent arteriole soon after entering the parenchyma typically has 1-2 layers of smooth muscle cells and is surrounded by a compartment (**) continuous with the subarachnoid PVS. A layer of pial cells (purple) and their BM (thin gray line) surround the vessel for some distance into the parenchyma, incompletely separating the vessel and fluid space from another fluid compartment continuous with

the subpial space (††). The vessel and PVS are physically separated from the parenchyma by the glia limitans, which consists of layers of astrocyte endfeet (green) and their basement membrane (gray). (D) A capillary in the brain consists of the endothelial cell (pink) and endothelial BM (dark gray) and the pericyte (orange) and pericyte BM (light gray), alongside the astrocyte BM (gray) and astrocyte endfeet (light green). At the level of the capillary it is unclear if the endothelial/pericyte BM and astrocyte BM are entirely fused or open to some extent (i.e., with a peri-capillary space; **), potentially allowing communication along the perivascular space of the entire vascular tree from arteriole to capillary to venule. (E) Parenchymal venules (not depicted in (A)) in the rodent have sparse or no smooth muscle cells and little surrounding pia, thus the endothelial BM (gray) is directly exposed to the PVS fluid compartment (**). Information compiled from multiple sources (Frederickson & Low, 1969; Jones, 1970; Nabeshima et al., 1975; Zervas et al., 1982; Krisch et al., 1984; Fawcett, 1986; Zhang et al., 1990; Peters et al., 1991) and our own findings.

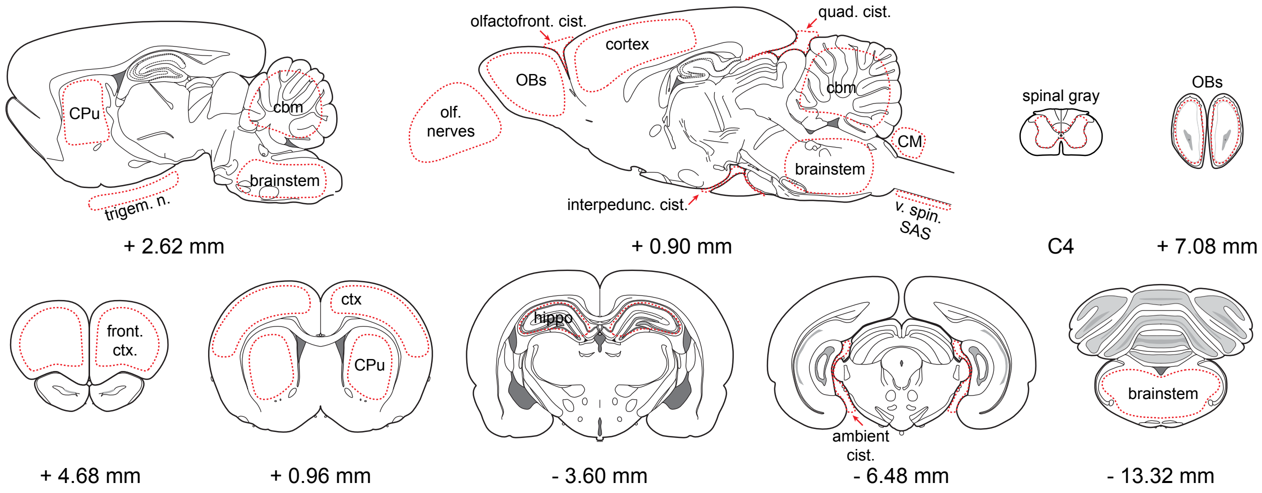

Figure 2. Approximate regions of interest for MRI quantification. Red dashed lines indicate the approximate regions of interest (ROIs) used for analysis throughout various brain areas (based on (Paxinos & Watson, 2007)). For parenchymal brain areas ROIs were carefully defined, avoiding tissue edges to ensure no contamination from subarachnoid signal. Multiple ROIs were collected for most brain areas, from both hemispheres where applicable, and from both coronal (cor) and sagittal (sag) slices if possible. For each animal, *n* ROIs were sampled for each of the following areas: olfactory nerves: 5 (3 sag, 2 cor), olfactofrontal cistern: 3 (sag), quadrigeminal cistern: 3 (sag), interpeduncular cistern: 3 (sag), ventral spinal SAS: 3 (sag), cisterna magna: 3 (sag), ambient cistern: 2 (cor), cerebellum (cbm): 3 (sag), trigeminal nerve: 2 (sag); olfactory bulbs (OBs): 6 (4 sag, 2 cor), striatum/caudoputamen (CPu): 6 (4 sag, 2 cor), cortex: 6 (2 sag, 4 cor—2 frontal cortex, 2 somatosensory/motor cortex near bregma), brainstem: 3 (2 sag, 1 cor), hippocampus: 2 (cor), spinal gray matter: 3 (cor). Overall, we sampled from *N*=3 animals, so that multiplying the above n yields the total ROIs sampled for a given area (e.g., olfactory nerves, total *n*=3•5=15; spinal gray matter, total *n*=3•3=9).

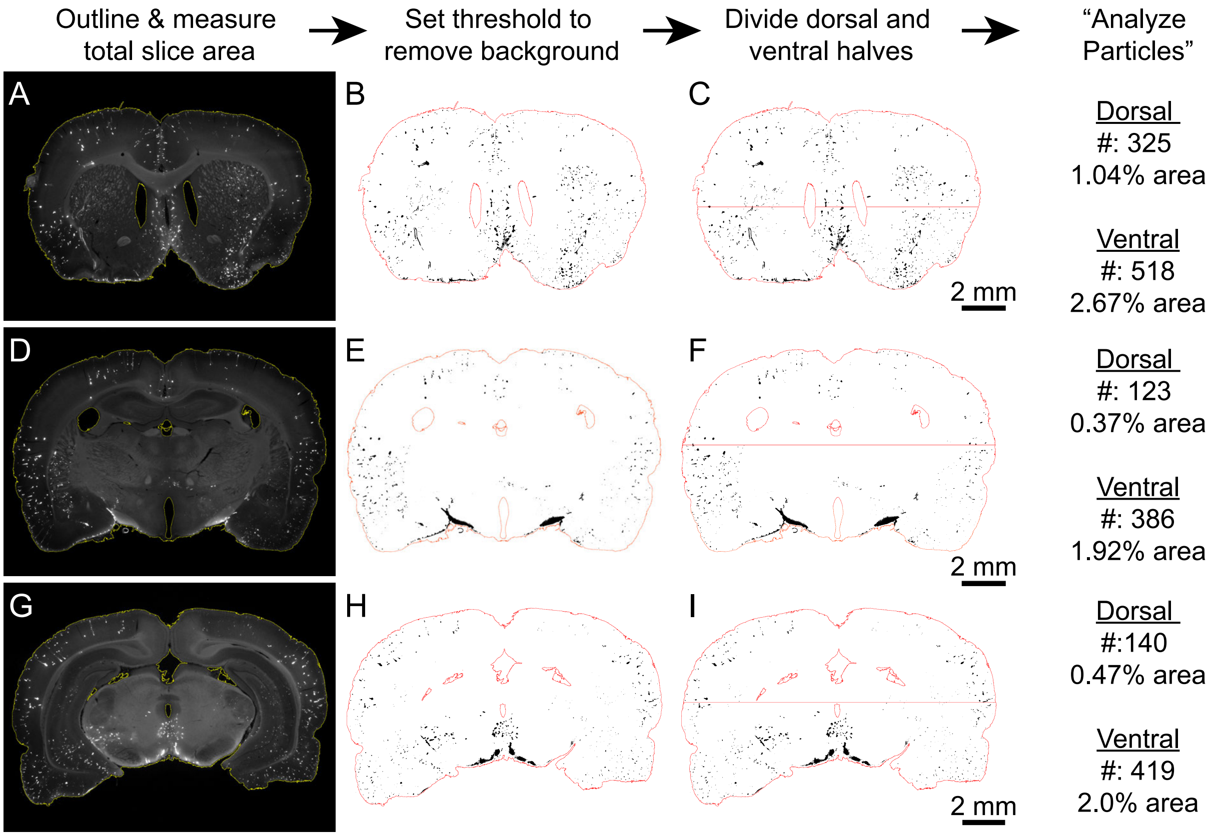

Figure 3. Method of quantifying percent area with antibody signal and number of perivascular profiles per mm^2 using Fiji. (A, D, G) First, the *ex vivo* fluorescence section image was opened in Fiji (sections shown corresponded to IgG infusion). The threshold was then adjusted so that the slice area could easily be selected using the wand tool (shown as yellow outline) and the slice area measured; ventricular or cisternal areas were excluded. (B, E, H) Second, the threshold for signal was then set for the fluorescence image so that signal could be separated from background (with background set as the level of white matter autofluorescence). Black profiles indicate antibody signal. (C, F, I) Third, each slice was divided into dorsal and ventral halves, using the following anatomical landmarks for reference: (C) For + 1.5 mm sections (8 per animal), the horizontal division line was drawn at approximately half the vertical distance between the dorsal-ventral extent of the lateral ventricles; (F) For -2.5 mm sections (7 per animal), the horizontal line was drawn just below the dorsal third ventricles and dorsal hippocampus; (I) For -5.5 mm sections (3-4 per animal), the horizontal line was drawn at the dorsal edge of the cerebral aqueduct. Lastly,

after dividing each slice into dorsal and ventral regions, the Fiji command “Analyze Particles” was run to count and characterize perivascular profiles (particles) within each region of interest. Individual values for the example sections are shown.

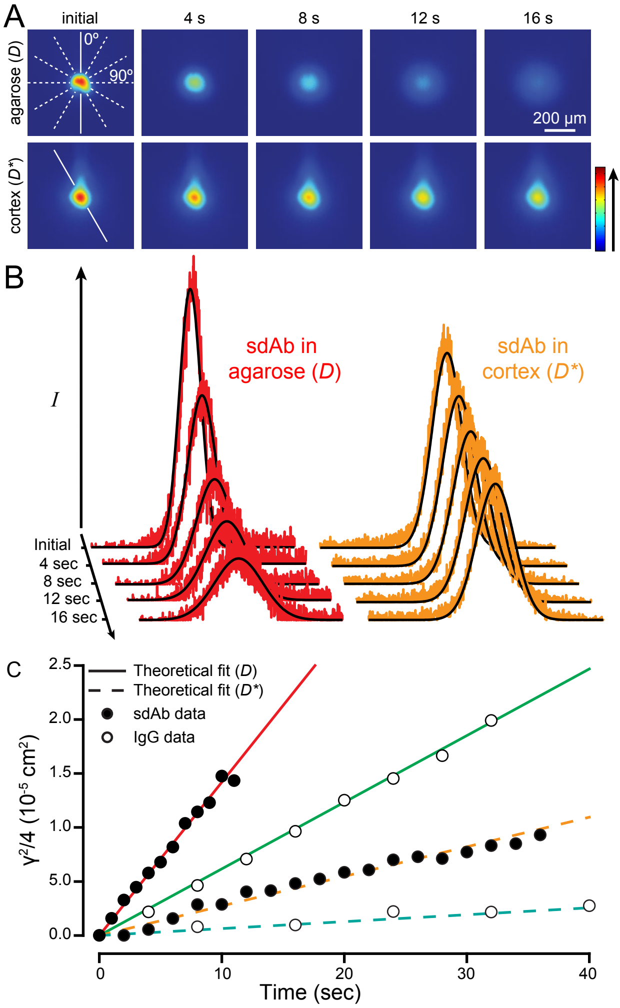

Figure 4. Diffusion measurements of single-domain antibody in free media or brain using integrative optical imaging (IOI). (A) Representative images acquired with IOI following injection of fluorescently-labeled sdAb into dilute agarose gel for measurement of the free diffusion coefficient (*D*; *n*=43 measurements) or into rat cortex for measurement of the effective diffusion coefficient in brain (D^*_{IOI}; *N*=4 animals, *n*=19 measurements). (B) Example fluorescence intensity data extracted along one image axis (white line in (A)) and fit to the diffusion equation (Eq. 1). The data are in shown in color (agarose, red; cortex, orange) to facilitate comparison to the curve fits at each time point (black). (C) Curve fitting at each point from (A) & (B) returns a parameter, $\gamma^2/4$, that produces a line with a slope equal to *D* or D^*_{IOI} after linear regression on time (data transformed to a zero y-intercept for comparison between molecules). Linear regression fits for sdAb and IgG free diffusion coefficients (solid lines) and effective diffusion coefficients (dashed lines) obtained in the present study (sdAb; filled circles) and from a previous study (IgG (Wolak et al., 2015); open circles).

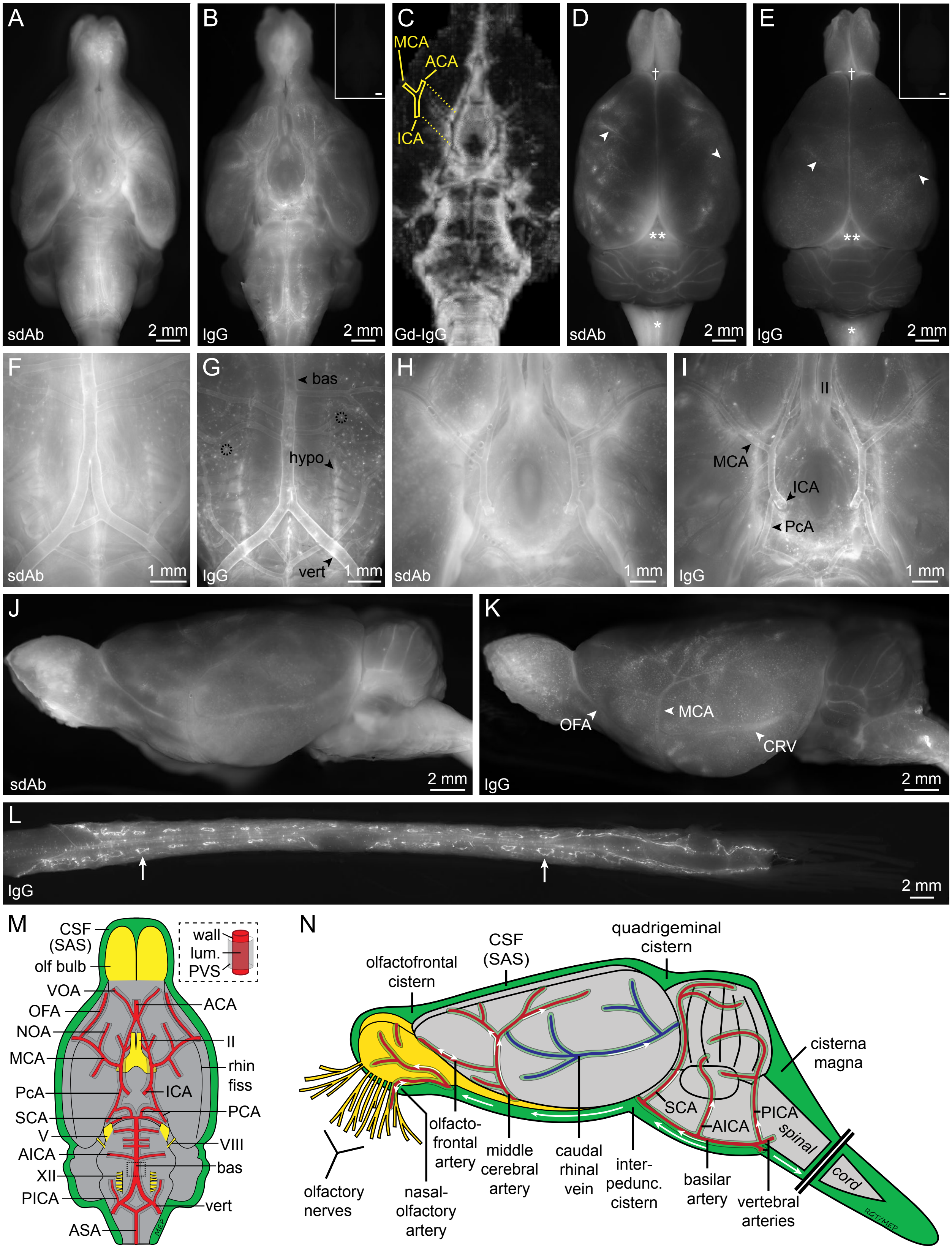
A
sdAb
2 mm
B
IgG
2 mm
C
MCA
ACA
ICA
Gd-IgG
D
†
**
*
sdAb
2 mm
E
†
**
*
IgG
2 mm
F
sdAb
1 mm
G
bas
hypo
vert
IgG
1 mm
H
sdAb
1 mm
I
II
MCA
ICA
PcA
IgG
1 mm
J
sdAb
2 mm
K
OFA
MCA
CRV
IgG
2 mm
L
IgG
2 mm
M
CSF
(SAS)
olf bulb
wall
lum.
PVS
VOA
OFA
NOA
MCA
PcA
SCA
V
AICA
XII
PICA
ASA
ACA
II
rhin
fiss
ICA
PCA
VIII
bas
vert
MEP
N
olfactofrontal
cistern
CSF
(SAS)
quadrigeminal
cistern
cisterna
magna
SCA
AICA
PICA
spinal
cord
olfactory
nerves
olfacto-
frontal
artery
nasal-
olfactory
artery
middle
cerebral
artery
caudal
rhinal
vein
inter-
pedunc.
cistern
basilar
artery
vertebral
arteries
RGT/MEP

Figure 5. Whole brain surface distribution of sdAb and IgG after intrathecal infusion. Representative *ex vivo* fluorescence ventral surface distribution of (A) sdAb and (B) IgG at 30 min post-infusion revealed antibodies along major surface arteries and certain cranial nerves (e.g., II, V, VIII, and XII); overall, sdAb signal appeared more diffuse, while IgG appeared predominantly in perivascular (PV) areas. (C) Ventral view of a representative baseline-subtracted 3D MR image of Gd-IgG distribution 12 min post-infusion. Gd-IgG signal was prominent around major surface arteries, correlating well with *ex vivo* fluorescence in (B). (D, E) Corresponding dorsal brain surface for (A) following sdAb infusion or for (B) following IgG infusion demonstrated high sdAb and IgG signal along the PVS of many dorsal branches of the middle cerebral artery (arrowheads), as well high signal at brain-CSF interfaces facing the olfactofrontal cistern (†), quadrigeminal cistern (**), and the infusion site at the cisterna magna (*). As with the ventral brain surface (A and B) sdAb signal appeared overall more diffuse compared to IgG, but both showed prominent punctate signal associated with the PVS of penetrating vessels. The dorsal brain surfaces had a lower overall signal compared to the ventral brain surfaces for both sdAb and IgG (ventral images A and B and dorsal images D and E represent a single animal experiment, and the same linear contrast was equally applied to dorsal and ventral images). Control animals infused with saline (*N*=2) did not show any fluorescent signal on the ventral (B inset) or dorsal (E inset) brain surfaces (images taken at same exposure and magnification as sdAb and IgG images; contrasted equally to IgG images). IgG co-infused with 0.27 M mannitol or 0.75 M mannitol did not show apparent differences in surface signal compared to IgG alone. *Ex vivo* fluorescence of the vertebral and basilar arteries demonstrated strong PV signal of sdAb (F) and IgG (G) and signal associated with the hypoglossal nerves. Punctate signal in (F and G) corresponds to PV signal around penetrating vessels entering the parenchyma perpendicular to the surface; the dark lumen of some penetrating vessels contrasts with the bright PV signal (see circles). The major ventral surface arteries of the circle of Willis demonstrated sdAb (H) and IgG (I) signal associated with the PVS and the arterial wall. A lateral view of the brain after (J) sdAb infusion or (K) IgG infusion again showed PV signal around the middle cerebral artery and olfactofrontal artery,

signal in the olfactory bulbs and near the infusion site, and PV signal along the caudal rhinal vein. (L) The spinal cord showed IgG signal along its entire length (image shown for ventral side), with the highest signal on the surface (some appearing to be associated with meninges) and around spinal nerve roots (arrows), which again appeared similar for IgG with mannitol co-infusion. The vasculature of the ventral brain surface is detailed in (M). (N) Schematic of a lateral view of the brain, showing major surface vessels, CSF cisterns, and a presumed general CSF and PVS flow pattern (arrows) for IgG infused into the cisterna magna. Not all features indicated in M and N are easily visible in A-I. CSF: cerebrospinal fluid; SAS: subarachnoid space; VOA: ventral olfactory artery; OFA: olfactofrontal artery; ACA: anterior cerebral artery; NOA: nasal olfactory artery; MCA: middle cerebral artery; II: optic nerve; rhin fiss: rhinal fissure; ICA: internal carotid artery; PcA: posterior communicating artery; PCA: posterior cerebral artery; SCA: superior cerebellar artery; V: trigeminal nerve; VIII: vestibulocochlear nerve; AICA: anterior inferior cerebellar artery; bas: basilar artery; XII: hypoglossal nerves; PICA: posterior inferior cerebellar artery; vert: vertebral arteries; ASA: anterior spinal artery.

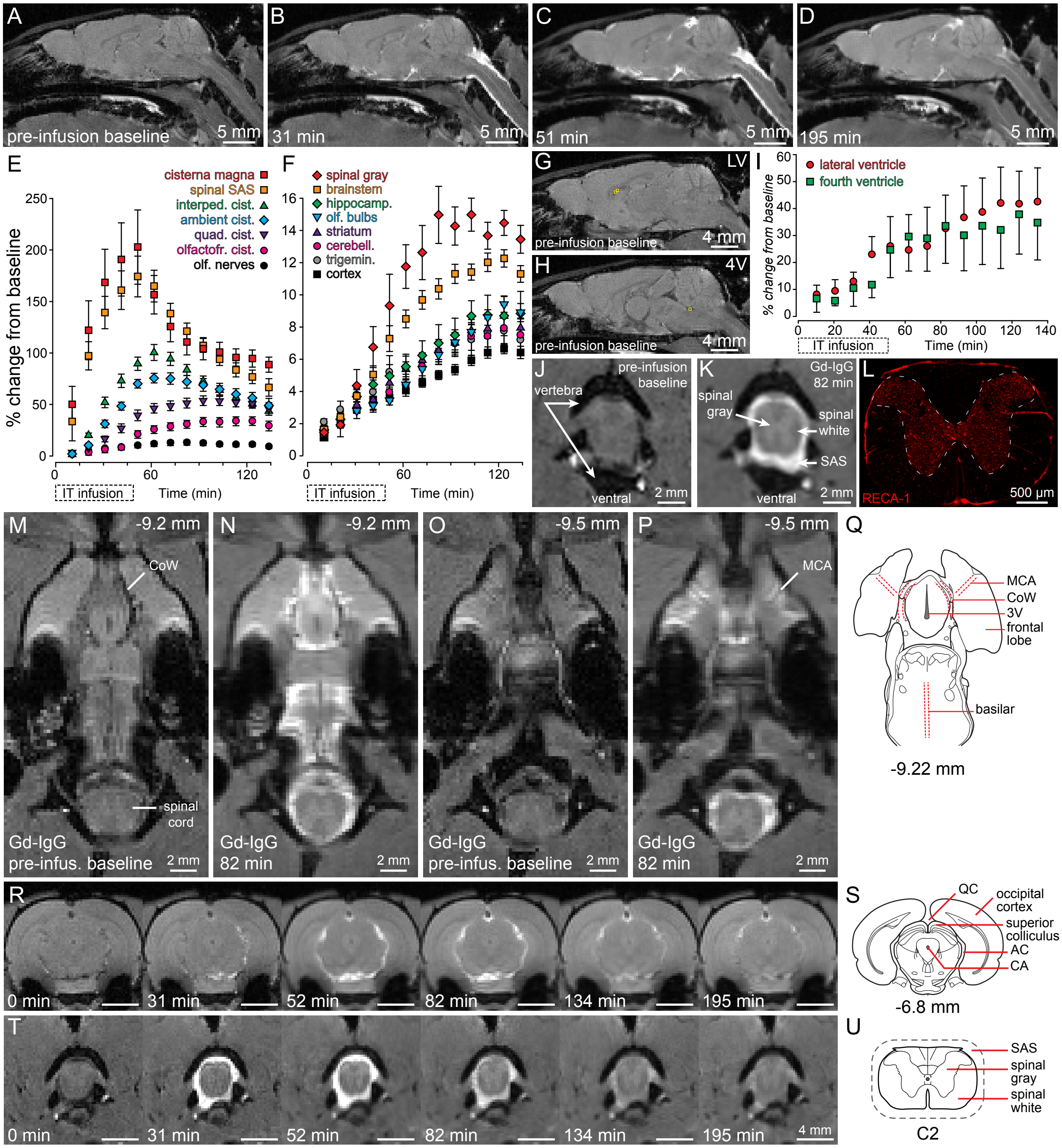

Figure 6. Distribution of Gd-IgG *in vivo* using dynamic 3D T1-weighted MRI. (A-D) Mid-sagittal view (approximately 0.5 mm lateral to the midline) of representative raw MRI slices over time demonstrated high levels of Gd-IgG contrast in CSF cisterns (cisterna magna, interpeduncular, quadrigeminal, olfactofrontal; see Fig. 5N) during the 50-min infusion, as well as increasing levels in the parenchyma (e.g., see cortex and striatum) with time. The percent change in Gd-IgG signal from pre-infusion baseline was quantified in specific CSF (E) or parenchymal brain (F) regions of

interest (ROIs; *N*=3; Fig. 2). (G-I) Quantification of % change from baseline in the lateral ventricle (LV) and fourth ventricle (4V) from MRI. Small, carefully-chosen regions of interest (ROIs; yellow boxes) were selected in the lateral ventricle (G; approximately 1.5 lateral to the midline) or fourth ventricle (H; approximately at the midline). (I) Quantification of % change in Gd-IgG signal from pre-infusion baseline revealed similar signal magnitudes and kinetics over time for the lateral ventricle (*n*=6, *N*=3) and fourth ventricle (*n*=3, *N*=3) ROIs. Cross-sections of the upper cervical spinal cord pre-infusion (J) and 30 min post-infusion (K) demonstrated high Gd-IgG signal in the spinal SAS and gray matter. (L) High vascularity of the spinal gray compared to spinal white matter, shown with staining for rat endothelial cell antigen-1 (RECA-1; dashed line denotes approximate spinal gray matter). (M-P) Raw MRI horizontal slices with time. (M) Dark vessels of the circle of Willis are visible in the horizontal plane before the infusion of Gd-IgG. (N) Approximately 30 minutes post-infusion Gd-IgG signal is evident surrounding the dark vessels of the circle of Willis and the basilar artery, as well as in the subarachnoid space around the spinal cord, where the spinal gray matter has had a noticeable signal increase. (O) The dark lumen of the middle cerebral artery is visible pre-infusion as it branches laterally, and is surrounded by Gd-IgG signal (P) approximately 30-minutes post-infusion. (Q) Schematic depicting the approximate location of structures in M-P. (R) Coronal brain or (T) spinal cord sections before, during, and after 50 min Gd-IgG infusion. Gd-IgG signal is prominent in parenchymal and subarachnoid CSF spaces. (S, U) Schematics depicting the approximate location of structures in R and T, respectively. Corresponding sections in Q, S, and U adapted from (Paxinos & Watson, 2007).

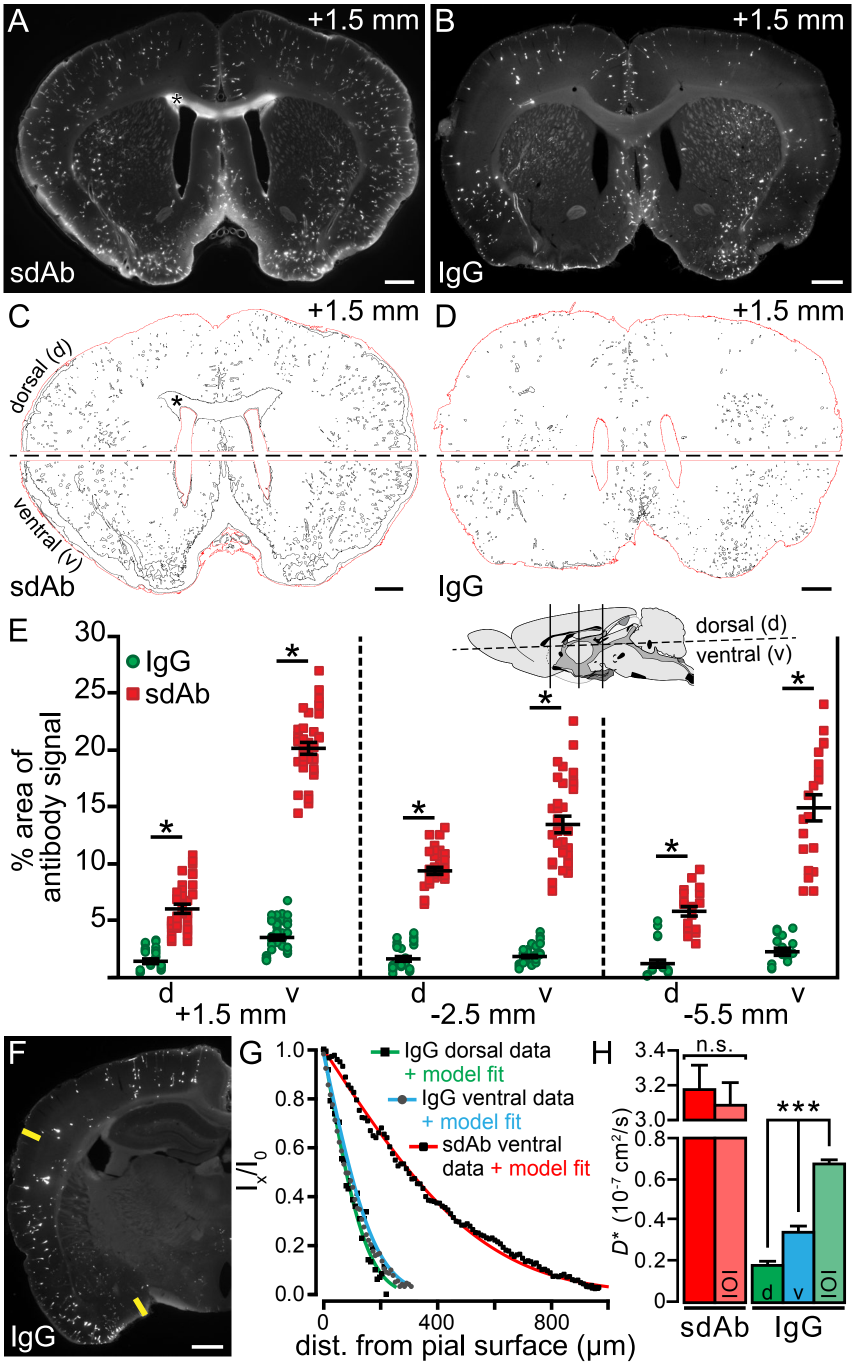

Figure 7. *Ex vivo* fluorescence of brain sections demonstrated a diffuse surface gradient and widespread perivascular signal. Representative coronal sections for (A) sdAb and (B) IgG. Intrathecal sdAb resulted in a large, diffuse surface gradient, particularly on the ventral surface, and numerous PV profiles throughout the section including deep brain regions (e.g., deep cortex and striatum). sdAb also spread along periventricular white matter (*). Intrathecal IgG resulted

in a small gradient at the brain surface, as well as widespread PV signal, though far less than sdAb. Fluorescent signal above a certain threshold (shown in black) was detected throughout the entire section area (outlined in red) using Fiji for (C) sdAb and (D) IgG (number of profiles for the representative images shown: sdAb, 1153; IgG, 843). (E) The percent area with antibody signal was then rigorously quantified (Fiji) for dorsal (d) and ventral (v) halves of multiple 100 μm sections, centered at three different bregma levels (+1.5 mm, 8 sections per animal; -2.5 mm, 7 sections per animal; -5.5 mm, 3-4 sections per animal), for sdAb (N=5 animals; e.g., for section shown in (C), dorsal and ventral percent areas were 9.06% and 23.9%, respectively) and IgG (N=5-6 animals; e.g., for section shown in (D), dorsal and ventral percent areas were 1.04% and 2.67%, respectively). Summary data (circles indicate individual sections analyzed, columns indicate individual animals, and bars indicate mean ± s.e.m.) showed percent slice area accessed by the sdAb was significantly greater compared to IgG for all six dorsal and ventral regions examined ($p<0.001$). (F) Surface gradients at the brain-CSF interface along lines normal to the section surface (yellow) were next assessed for consistency with size-dependent, Fickian diffusion from the CSF into the brain (as described in (Wolak et al., 2015)); lines were analyzed at a ventral location for sdAb and at dorsal and ventral locations for IgG (as shown). (G) The raw surface gradient data was fit to the diffusion equation (Wolak et al., 2015) to estimate a brain surface diffusion coefficient after intrathecal infusion (D^*_{infus}; data shown: sdAb, $D^*_{\text{infus}} = 3.33 \times 10^{-7}$ cm^2/s; IgG dorsal, $D^*_{\text{infus}} = 0.23 \times 10^{-7}$ cm^2/s; IgG ventral, $D^*_{\text{infus}} = 0.34 \times 10^{-7}$ cm^2/s). (H) Summary data (mean ± s.e.m.) for parenchymal diffusion measurements from intrathecal surface gradient profiles (D^*_{infus}) or from point source injections in the somatosensory cortex using integrative optical imaging (D^*_{IOI}; see Fig. 4 for details). Differences between sdAb D^*_{infus} (N=4 animals, n=30 measurements) and D^*_{IOI} (N=4, n=19) were not significant (n.s.; p=0.62). However, dorsal IgG D^*_{infus} (N=5, n=34) was significantly lower than ventral IgG D^*_{infus} (N=5, n=50) and both IgG D^*_{infus} were significantly lower than IgG D^*_{IOI} (value reported in (Wolak et al., 2015)). (Sagittal schematic adapted from (Swanson, 1998); scale bars: 1 mm.)

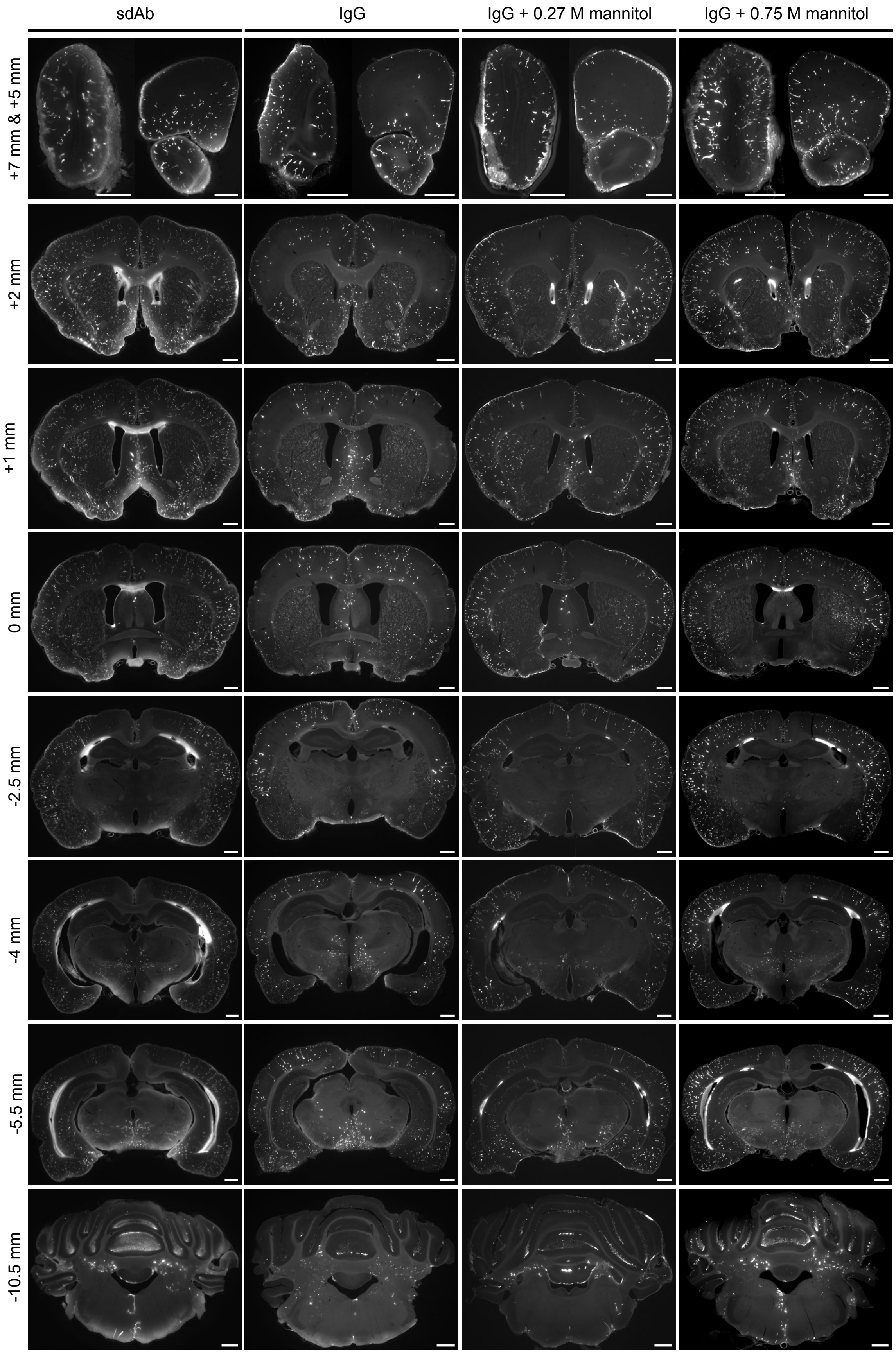
sdAb
IgG
IgG + 0.27 M mannitol
IgG + 0.75 M mannitol
+7 mm & +5 mm
+2 mm
+1 mm
0 mm
-2.5 mm
-4 mm
-5.5 mm
-10.5 mm

Figure 8. Coronal brain sections demonstrated widespread, size-dependent perivascular signal throughout the rat brain. Widespread PV signal was evident from the most anterior sections (e.g., olfactory bulb) to the most posterior sections examined (e.g., cerebellum and brainstem). Section levels are indicated to denote the approximate coronal levels anterior or posterior to bregma, according to reference (Paxinos & Watson, 2007). Choroid plexus-associated signal was evident in all ventricles for sdAb infusions and for infusions of IgG only when co-infused with mannitol (dose-dependent). Note that perivascular signal in the cortex exhibited more variability than most other brain areas. See text for additional details. Scale bars = 1 mm.

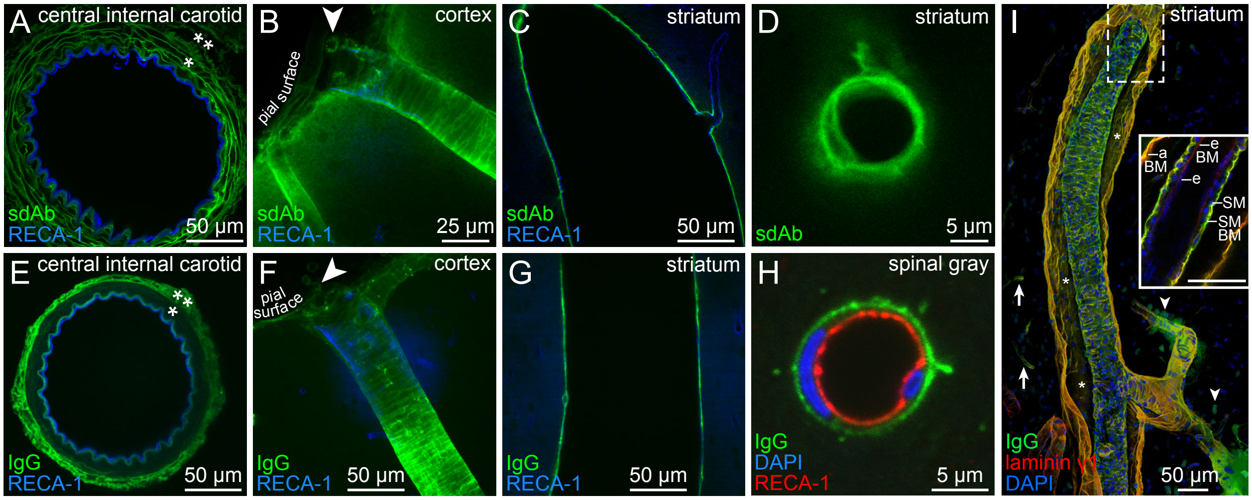

Figure 9. Confocal microscopy of sdAb and IgG in the perivascular space demonstrated distribution along vessels of all caliber and a size-dependent association with the smooth muscle basement membrane compartment. (A and E) Leptomeningeal arteries on the brain surface (vascular endothelium labeled with RECA-1) revealed a size-dependent access to the arterial wall (see Fig. 1B). The smaller sdAb (A) distributed throughout the outer connective tissue space (**) and the tunica media (*). (E) IgG distributed throughout the outer connective tissue PVS but penetration of the tunica media appeared restricted. Representative images of putative penetrating cortical arterioles showed sdAb (B) and IgG (F) distributed along the pial surface and around the borders of circumferentially arranged smooth muscle cells (presumably in the basement membrane). Punctate sdAb and IgG signal was present in subarachnoid cells at the cortical surface (e.g., macrophages, arrowheads). Antibody signal was also present longitudinally along many vessels (likely association with perivascular collagen). Based on size and morphology, sdAb and IgG were also found to be present in the PVS of numerous putative venules (C and G; representative examples) and microvessels (D and H; representative examples); often, a line of antibody signal could be seen extending away from microvessels, likely due to basement membrane extending into the ECS between astrocytic endfeet (Peters et al., 1991). (I) IgG association with perivascular/vascular basement membranes (BM; endothelial, smooth muscle, and astrocyte) was revealed by lamininγ 1 (pan-laminin) staining. An arteriole in the striatum demonstrated a particularly large, presumably fluid-filled PVS compartment (*), although its exaggerated size and lack of IgG signal was likely

due to tissue processing and washout; co-localization of IgG with the astrocyte BM and smooth muscle BM of the arterial wall (and other fixable elements) was noticeably evident. A longitudinal cross-section (inset; scale bar 50 µm) revealed IgG did not extend as far as the innermost endothelial BM because no co-localization was evident (e: endothelial cell; e BM: endothelial basement membrane (BM); a BM: astrocyte BM; SM: smooth muscle cell; SM BM: smooth muscle BM). IgG was also visible around microvessels (arrows) and a few, scattered brain cells in nearby regions (arrowheads).

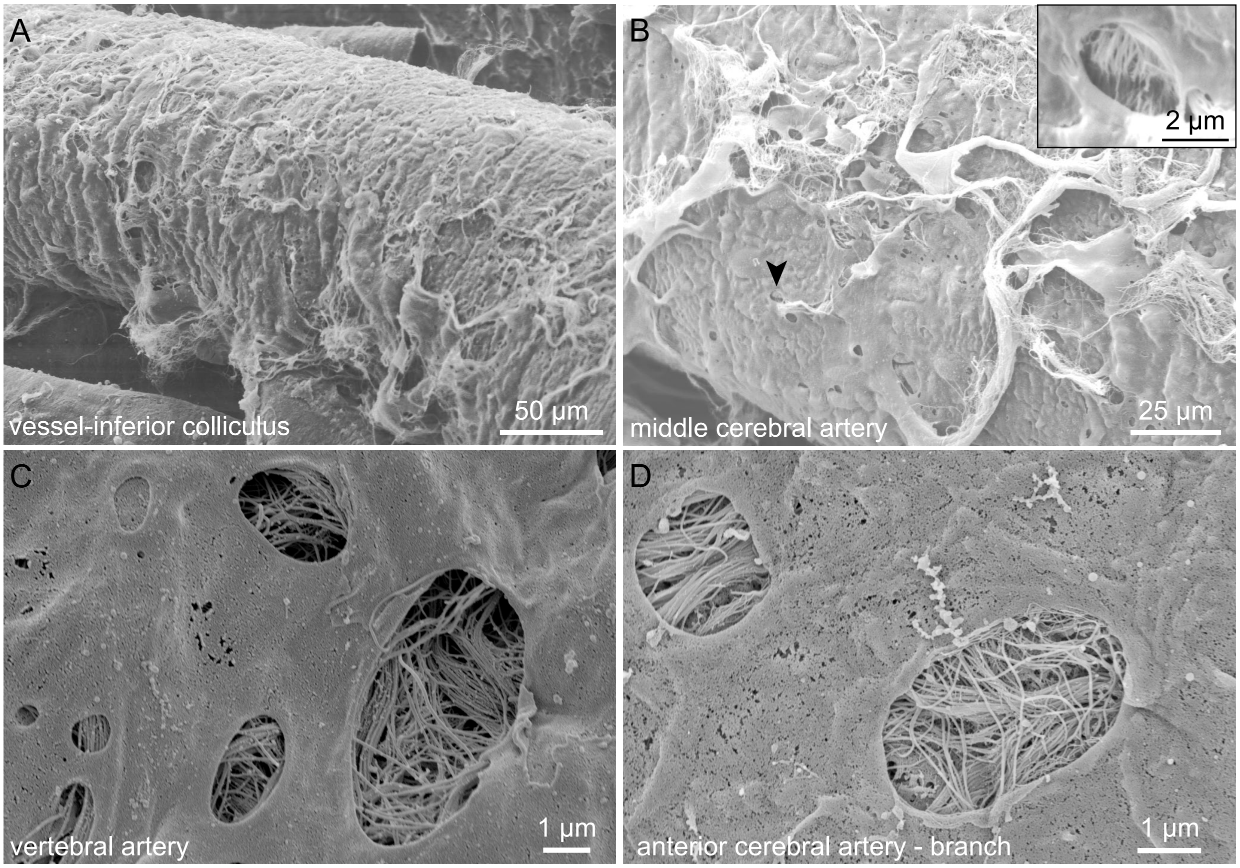

Figure 10. Stomata are present on leptomeningeal sheaths of blood vessels in the subarachnoid space. Scanning electron microscopy of vessels on the brain surface of untreated rats (*N*=4) demonstrated numerous micron-sized stomata. (A) A large vessel on the surface of the inferior colliculus was marked with many stomata, which appear as small dark circles/ovals. (B) The middle cerebral artery, close to its branch point from the circle of Willis. Fibrous connective tissue was visible through most stomata (area indicated by arrowhead, shown in inset). Magnified images of stomata on the surfaces of the vertebral artery (C) or anterior cerebral artery branch (D) exhibited smooth, slightly thickened rims with noticeably dense, underlying perivascular connective tissue.

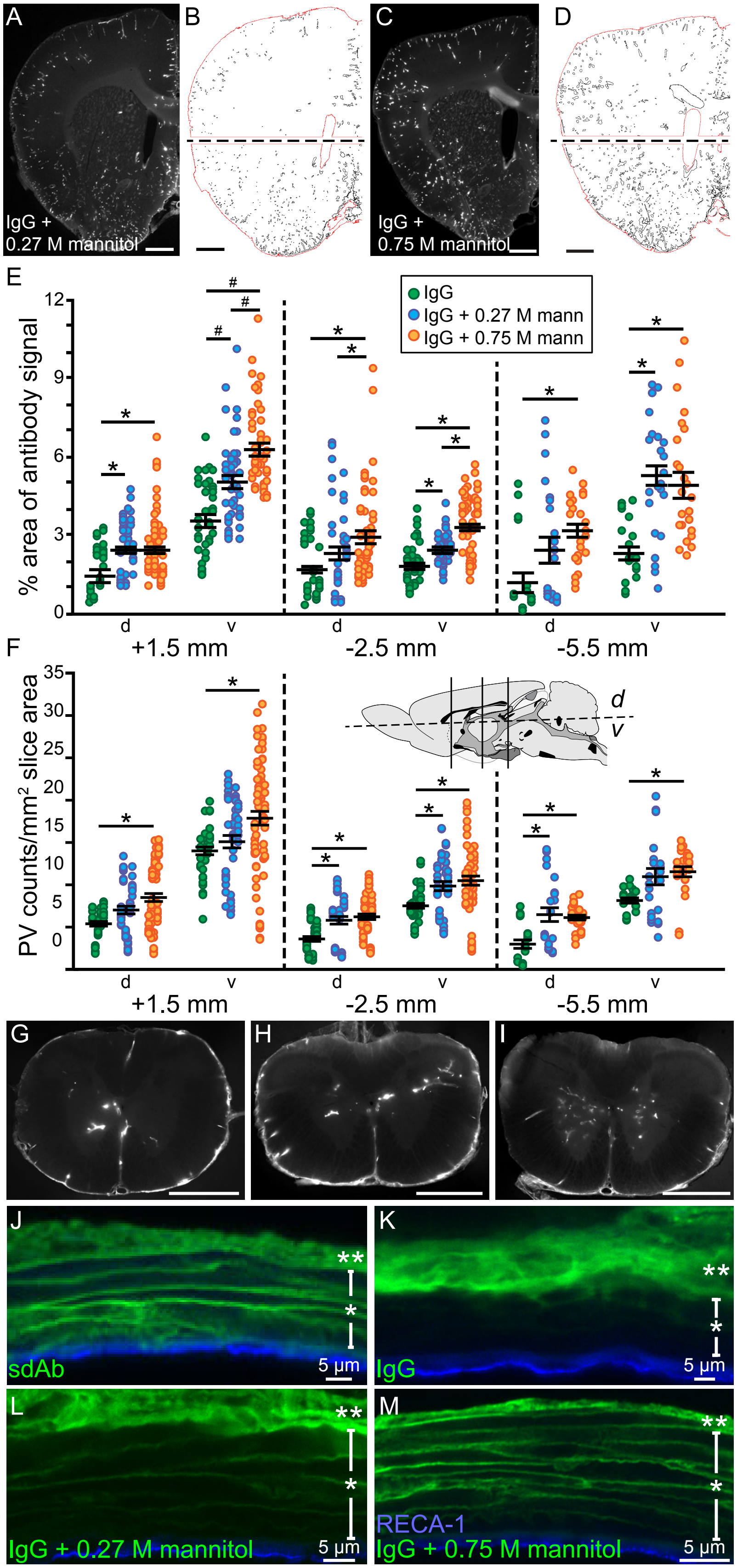
A
IgG +
0.27 M mannitol
B
C
IgG +
0.75 M mannitol
D
E
% area of antibody signal
12
9
6
3
0
IgG
IgG + 0.27 M mann
IgG + 0.75 M mann
*
#
d
v
+1.5 mm
-2.5 mm
-5.5 mm
F
PV counts/mm² slice area
35
30
25
20
15
10
5
0
d
v
d
v
+1.5 mm
-2.5 mm
-5.5 mm
G
H
I
J
**
*
sdAb
5 μm
K
IgG
5 μm
L
IgG + 0.27 M mannitol
5 μm
M
RECA-1
IgG + 0.75 M mannitol
5 μm

Figure 11. Co-infusion of mannitol enhanced IgG area of distribution in a dose-dependent manner. *Ex vivo* fluorescence images showed increased IgG perivascular (PV) distribution throughout brain sections with co-infusion of 0.27 M mannitol (A and B) and greatly increased PV distribution and periventricular white matter IgG signal with co-infusion of 0.75 M mannitol (C and D). Fluorescent signal above a certain threshold (shown in black) was detected throughout the entire section area (outlined in red) using Fiji for (B) IgG co-infused with 0.27 M mannitol and (D) IgG co-infused with 0.75 M mannitol. (E) Percent area with antibody signal or (F) number of PV profiles normalized by the whole slice area (in mm^2) was quantified (Fiji) for dorsal (d) and ventral (v) halves of multiple 100 μm sections, centered at three different bregma levels (+1.5 mm, 8 sections per animal; -2.5 mm, 7 sections per animal; -5.5 mm, 3-4 sections per animal), for IgG with 0.27 M mannitol (*N*=6 animals; e.g., for section shown in (B), dorsal and ventral percent areas were 0.948% and 3.55%, respectively; dorsal and ventral PV counts per slice area were 6.20 PV/mm^2 and 17.7 PV/mm^2, respectively) and IgG with 0.75 M mannitol (*N*=7-9 animals; e.g., for section shown in (D), dorsal and ventral percent areas were 5.43% and 7.90%, respectively; dorsal and ventral PV counts per slice area were 12.4 PV/mm^2 and 26.7 PV/mm^2, respectively). For IgG infusion (*N*=5-6 animals) the section shown in Fig. 7D had dorsal and ventral PV counts per slice area of 6.57 PV/mm^2 and 14.2 PV/mm^2, respectively. Summary data in (E) (circles indicate individual sections analyzed, columns indicate individual animals, and bars indicate mean ± s.e.m.) for percent slice area accessed by IgG are indicated with significance as follows: (*) Kruskal-Wallis one-way ANOVA on ranks, Dunn's post hoc test (p<0.05); (#) one-way ANOVA, Bonferroni t-test (p<0.001). Summary data in (F) (circles indicate individual sections analyzed, columns indicate individual animals, and bars indicate mean ± s.e.m.) for PV counts per slice area demonstrated that co-infusion of IgG with 0.27 M mannitol significantly increased the number of PV counts per mm^2 in 3 out of 6 brain regions compared to IgG alone. Co-infusion of 0.75 M mannitol significantly increased the number of PV counts per mm2 in all dorsal and ventral brain regions for all three coronal levels compared to IgG; (*) indicates Kruskal-Wallis one-way ANOVA on ranks with Dunn's post hoc, p<0.05. Also see Table 2. Sagittal schematic adapted from (Swanson, 1998). (G) *Ex vivo* fluorescence of upper

cervical spinal cord cross-sections. PV IgG signal was predominantly in the spinal gray matter and exhibited a dose-dependent increase with co-infusion of (H) 0.27 M mannitol or (I) or 0.75 M mannitol. (J-M) Confocal microscopy of the wall of the (leptomeningeal) internal carotid artery after antibody infusion (infused antibody, green), stained for rat endothelial cell antigen-1 (RECA-1) to indicate the vascular endothelial cell layer associated with the tunica intima (blue). (J) sdAb distributed in the outer connective tissue space (**) and throughout the entire tunica media (*) in the smooth muscle basement membrane but (K) IgG was essentially absent from this layer. (L) Co-infusion of 0.27 M mannitol slightly increased IgG access, and (M) co-infusion of 0.75 M mannitol often substantially increased IgG access to the smooth muscle layer, sometimes to a level of appearance similar to that exhibited by sdAb (J). Scale bars (A-D) = 1 mm.

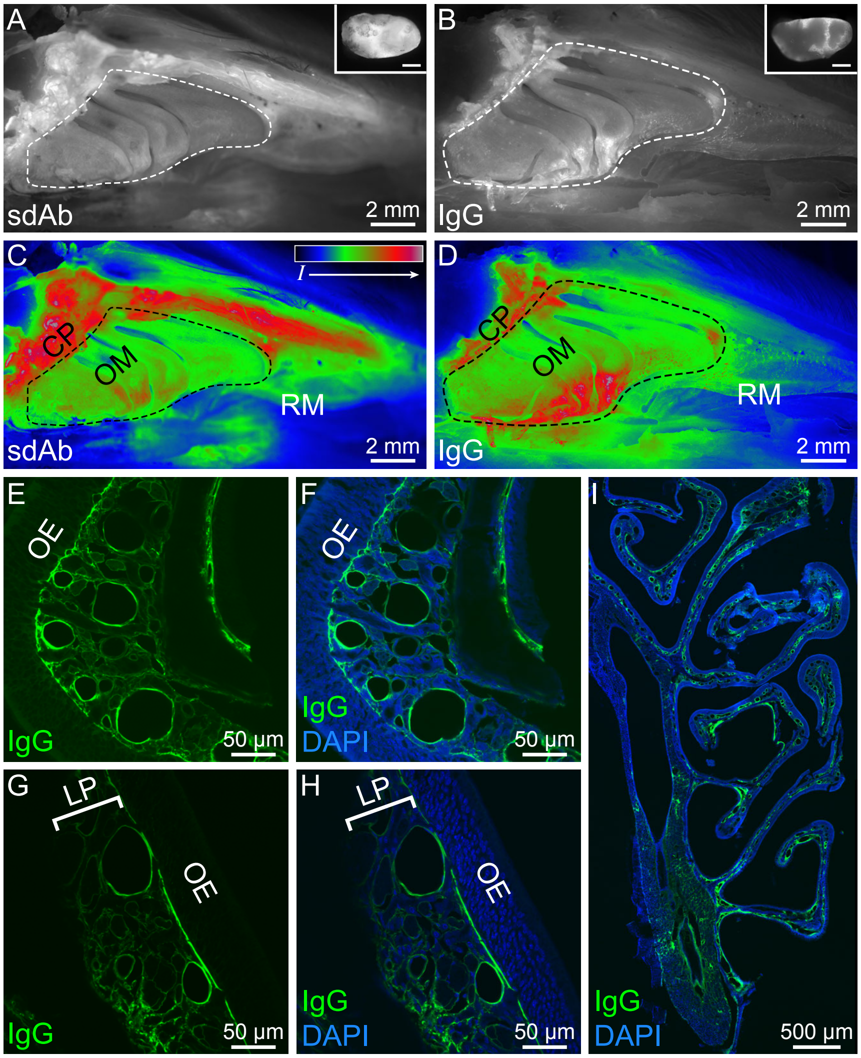

Figure 12. Antibody drainage to the nasal mucosa and deep cervical lymph nodes following intracisternal infusion. *Ex vivo* fluorescence imaging of the lateral walls of the nasal passages for (A) sdAb and (B) IgG revealed highest antibody signal at the cribriform plate (CP) region and in the ethmoturbinate region comprising the olfactory mucosa (OM), with less signal in the more rostrally located nasal respiratory mucosa (RM). Both sdAb and IgG were also present in deep cervical lymph nodes (inset, A and B; scale bars 1 mm) on both left and right sides for all animals. (C and D) A and B, pseudocolored for fluorescence intensity (I), demonstrated that most sdAb (C) or IgG (D) signal was associated with the cribriform plate and olfactory region, while little was present in the respiratory region. (E-I) Confocal imaging of coronal sections showed IgG (green) was present throughout the lamina propria of the olfactory mucosa, with no IgG present in the olfactory epithelium.

The role of brain barriers in fluid movement in the CNS – is there a ‘glymphatic’ system?

N. Joan Abbott[1], **Michelle E Pizzo[2,3]**, Jane E Preston[1], Damir Janigro[4,5] and Robert G Thorne[2,3,6,7,8]

[1]Institute of Pharmaceutical Science, Faculty of Life Sciences and Medicine, King's College London, UK; [2]Division of Pharmaceutical Sciences, University of Wisconsin-Madison School of Pharmacy, Madison, WI, USA; [3]Clinical Neuroengineering Training Program, University of Wisconsin-Madison, Madison, WI, USA; [4] Flocel Inc., Cleveland, OH, USA; [5]Department of Physiology, Case Western Reserve University, Cleveland, OH, USA; [6]Neuroscience Training Program, [7]Cellular and Molecular Pathology Graduate Training Program, [8]Institute for Clinical and Translational Research, University of Wisconsin-Madison, Madison, WI, USA

Reproduced with permission:
Abbott NJ, **Pizzo ME**, Preston JE, Janigro D & Thorne RG (2018). The role of brain barriers in fluid movement in the CNS: is there a ‘glymphatic’ system? Acta Neuropathol 135, 387–407.

Abstract

Brain fluids are rigidly regulated to provide stable environments for neuronal function, e.g. low K^+, Ca^{2+} and protein to optimise signalling and minimise neurotoxicity. At the same time, neuronal and astroglial waste must be promptly removed. The interstitial fluid (ISF) of the brain tissue and the cerebrospinal fluid (CSF) bathing the CNS are integral to this homeostasis and the idea of a glia-lymph or 'glymphatic' system for waste clearance from brain has developed over the last 5 years. This links bulk (convective) flow of CSF into brain along the outside of penetrating arteries, glia-mediated convective transport of fluid and solutes through the brain extracellular space (ECS) involving the aquaporin-4 (AQP4) water channel, and finally delivery of fluid to venules for clearance along peri-venous spaces. However, recent evidence favours important amendments to the 'glymphatic' hypothesis, particularly concerning the role of glia and transfer of solutes within the ECS. This review discusses studies which question the role of AQP4 in ISF flow and the lack of evidence for its ability to transport solutes; summarizes attributes of brain ECS that strongly favour the diffusion of small and large molecules without ISF flow; discusses work on hydraulic conductivity and the nature of the extracellular matrix which may impede fluid movement; and reconsiders the roles of the perivascular space (PVS) in CSF-ISF exchange and drainage. We also consider the extent to which CSF-ISF exchange is possible and desirable, the impact of neuropathology on fluid drainage, and why using CSF as a proxy measure of brain components or drug delivery is problematic. We propose that new work and key historical studies both support the concept of a perivascular fluid system whereby CSF enters the brain via PVS convective flow or dispersion along larger calibre arteries/arterioles, diffusion predominantly regulates CSF/ISF exchange at the level of the neurovascular unit associated with CNS microvessels, and, finally, a mixture of CSF/ISF/waste products is normally cleared along the PVS of venules/veins as well as

other pathways; such a system may or may not constitute a true ‘circulation’ but, at the least, suggests a comprehensive re-evaluation of the previously proposed ‘glymphatic’ concepts in favour of a new system better taking into account basic cerebrovascular physiology and fluid transport considerations.

Introduction

The brain is the most important regulatory site in the body, coordinating the input from sensory endings in all organs and the appropriate motor output in response, taking into account learning and memory, and allowing for running repairs to maintain active function. The neurons responsible for this coordination and their synaptic interconnections use transmembrane ionic gradients and movements to generate essential potential changes, including action potentials that propagate along axons, and synaptic potentials generated in post-synaptic membranes by transmitters released from the presynaptic neuron. Generation of the ionic currents responsible requires an extremely stable ionic microenvironment (Abbott, 2013). Homeostasis of the neural microenvironment depends on the effective separation of this environment from the blood, while allowing efficient exchange of essential gases, nutrients and waste products of metabolism, and efficient removal of larger waste products and cell debris. The housing of the delicate brain tissue within the skull provides some mechanical protection from trauma, but ‘buffer zones’ allowing the brain to float in a suitable fluid are also needed. The modern mammalian brain achieves all of these by compartmentalisation that allows dynamic exchange across key interfaces.

The surface of the brain is protected by three layers of ‘meninges’, the tough outer dura, then the ‘leptomeninges’ formed by the arachnoid layer and the pia (Davson & Segal, 1995). The mammalian central nervous system is immersed in cerebrospinal fluid (CSF), a complex secretion primarily from circulating plasma, divided unequally between ventricular sites inside the brain (the connected lateral, third, and fourth ventricles) and extraventricular sites outside the brain and spinal cord (the subarachnoid spaces that typically contain most of the CSF) (Davson & Segal, 1995; Thorne, 2014; Pizzo & Thorne, 2017). Interstitial fluid (ISF) fills the narrow 40-60 nm wide extracellular space (ECS) between neurons and glia (Thorne & Nicholson, 2006; Syková & Nicholson, 2008). While ISF is often regarded as similar in composition to CSF, this may be strictly correct only at ventricular and pial brain/spinal cord surface interfaces because (i) diffusion increasingly limits exchange with distance from these interfaces and (ii) a number of proteins and polysaccharides, e.g., extracellular matrix, are bound to cells and other ECS constituents and therefore not available for free exchange with the relatively cell-free CSF (Syková & Nicholson, 2008; Wolak & Thorne, 2013).

History of CSF generation and flow

Ancient views on the role of CSF have ranged from symptoms of disease, to the seat of the soul or spirit. The ethereal spirit was thought to be formed in the brain and processed to a *liquor vitalis*, flowing to the rest of the body along nerves and spinal cord (Galenus of Pergamon 130-201 AD, in (Bauer, 1993)). What is astounding to us now is that the brain itself was thought to have little value, beyond acting as a conduit for CSF and maintaining the fluid. This idea became so culturally embedded, despite reservations by scientists such as Vesalius in the 16th century, that Shakespeare writes “ a foolish … spirit, …full of … objects, ideas, apprehensions, …begot in the ventricles of memory, nourished in the womb of the pia mater” when describing his school master in ‘Love’s Labour’s Lost’ (Bauer, 1993).

Centuries of anatomists including Cotugno (1764), Magendie (1842) and von Luschka (1870), (Deisenhammer, 2015) demonstrated the connections between the lateral ventricles and subarachnoid space, the latter two giving their names to the anatomical foramina connecting these spaces. Although they could not then discern the direction of CSF flow, important progress was made. However, it was not until 1891 when Quincke developed lumbar puncture to sample CSF from living subjects (McConnell, 1994), that the modern study of CSF dynamics, production and composition began, opening the way to new tools for diagnosis of brain diseases and treatment progress.

In the early 20th century, experimental physiologists took this further, identifying a location for CSF secretion as the choroid plexuses (CPs) and the source of fluid as choroidal blood. By removing one lateral ventricle CP in the dog and blocking outflow via the foramina of Monro and the aqueduct of Sylvius, Dandy in 1919 (Dandy, 1919) observed the ventricle containing the plexus expanded whilst the other decreased in size, concluding that the CP was actively secreting CSF. More direct evidence for choroidal blood as a source of the CSF was given by Welch in 1963 (Welch, 1963) who showed that the haematocrit of blood from the main choroidal vein was higher than in the anterior choroidal artery, suggesting loss of plasma volume as the blood passed through the plexus. The rate of CSF secretion has since been estimated for several mammalian species using a variety of techniques. Despite the obvious caveats when comparing rates between species, CSF secretion rate per unit weight of CP is quite comparable, between 0.2 – 0.6 µl/min/g (Davson *et al.*, 1987).

At the same time as Welch, Ames *et al.* (Ames *et al.*, 1965) observed freshly secreted CSF from exposed CPs which had been covered in oil. This method allowed newly secreted CSF collection and analysis, showing that its composition was similar to bulk CSF, but quite different from a simple plasma filtrate. For example, CSF has a higher Na^+ and Cl^- concentration compared to plasma, but is lower in K^+, Ca^{2+}, glucose, amino acids, urea (Davson, 1967). Notably, CSF has little protein, less than 0.5% of plasma levels (Cutler *et al.*, 1967). The relative paucity of complex molecules led to the idea of CSF acting as a 'sink' (Davson *et al.*, 1962) into which brain metabolites and waste products could flow down their concentration gradient and be removed with the normal drainage of CSF. Examples include metabolites of serotonin and histamine flowing from brain into CSF for disposal (Barkai *et al.*, 1972; Prell *et al.*, 1989).

Pulsatile flow of CSF

With the advent of modern imaging techniques, especially phase-contrast and real-time MRI, it is now possible to visualise CSF flow in the intact CNS and understand its circulation in more detail. These techniques are not without methodological issues (Brinker *et al.*, 2014), but the weight of evidence favours a second-to-second pulsatile movement of CSF through the ventricular system, which also changes throughout the day. Early MRI studies by Nilsson *et al.* (Nilsson *et al.*, 1992) observed pulsatile CSF flow through the cerebral aqueduct, and CSF velocity varied with cardiac cycle. During cardiac systole, CSF flowed approximately 8mm/sec toward the posterior brain (caudally), then gently back at 5mm/sec to the anterior brain (cranially) during cardiac diastole. Although the net direction of flow is toward the posterior brain, such pulsatility would act to mix CSF contents between ventricles and encourage the sink action of CSF (illustrative video can be seen at Wikimedia creative commons; (Dilmen, 2005)). Because peak CSF pulse velocity corresponds with the elevated systolic blood pressure during each heart beat, the increased volume and pressure of blood entering the brain tissue and plexuses is thought to cause transient tissue swelling, squeezing the ventricles and subarachnoid space (SAS), mixing and moving the bulk CSF toward drainage sites. Mathematical models developed by Linninger and colleagues to inform a mechanistic understanding of the relationship between vascular pulsation and CSF flow, correlate well with *in vivo* data from healthy humans and help explain in more detail the clinical observation that CSF flow reversal is seen first in the cisterns, then in the lateral ventricles during the cardiac cycle (Sweetman & Linninger, 2011). Their models predict vascular expansion following cardiac systole occurs first at the base of the brain, so reversing the flow of cisternal CSF, followed by dilation of arterioles in brain parenchyma, compressing both sub-arachnoid space and lateral ventricles and displacing fluid toward the spinal canal. Contributing to this rhythm, respiration adds to pulsatility, but at a lower frequency (Dreha-Kulaczewski *et al.*, 2015). Spector *et al.* (Spector *et al.*, 2015) suggest that during anaesthesia, with slower and shallower breathing, this mixing effect would be reduced.

Superimposed on these acute pulses is a circadian or diurnal rhythm. In children with hydrocephalus and an intrathecal catheter, circadian rhythms are seen in intracranial pressure, achieving twice the pressure during slow-wave sleep compared to the awake state (Di Rocco *et al.*, 1975). In adult volunteers (25-32 y), maximal CSF production was estimated as 42 ± 2 ml/h at 02:00 in the middle of the sleep cycle (range 35-48 ml/h *n*= 6), whereas the minimum was 12 ± 7 ml/h at 18:00 in the afternoon (Nilsson *et al.*, 1992). This gives a range of around 300 – 1000 ml CSF produced per day, depending on the time of day the measurements are made. A similar diurnal rhythmicity is also seen in rat CSF (Kervezee *et al.*, 2014) and, interestingly, there is a parallel change in BBB P-glycoprotein efflux transport function, which is increased during the waking period, suggesting a wider circadian control of brain barriers and fluids consistent with the majority of physiological functions.

Refinements in MRI and improved resolution have made CSF imaging an invaluable tool in diagnosis and treatment supervision and carefully designed studies have confirmed these early results. Overall, the net CSF flow in adults is through the ventricles to the basal subarachnoid spaces (Bateman & Brown, 2012; Spector *et al.*, 2015).

The need for CSF – brain ISF exchange

The exchange between CSF and ISF is the subject of intense and technically difficult investigation, either in the context of CSF as a route for drug delivery to brain, or to understand removal of waste products and pathological markers. But what might be the physiological purpose of this fluid exchange, beyond acting as a sink?

The requirement for molecular transfer between CSF and brain ISF can be illustrated by compounds which are required by the CNS, but do not significantly enter brain from the systemic circulation across the brain endothelium forming the blood-brain barrier (BBB). These fall into three categories based on the origin of the molecules.

Firstly, compounds synthesised by one region of the brain may require wider CNS distribution and use CSF pathways to achieve this, for example melatonin and vasopressin (Schwartz & Reppert, 1985; Seckl & Lightman, 1988; Reiter *et al.*, 2014). Melatonin, an antioxidant which also sets the body's circadian rhythm via the suprachiasmatic nucleus (SCN), requires CSF for its distribution from synthesis in the pineal gland to multiple CNS sites. Melatonin is secreted into the 3rd ventricle (3V) CSF, which is in direct contact with the pinealocytes; at night, during peak melatonin synthesis, the CSF concentration is 15 – 20x that of plasma (Legros *et al.*, 2014; Tan *et al.*, 2016). The hormone is transferred by CSF to the SCN, other hypothalamic regions, the hippocampus and choroid plexuses where there are high affinity MT1 receptors (Dubocovich *et al.*, 2005). Lateral ventricle (LV) melatonin concentrations have been reported to be far lower than 3V melatonin concentrations; this observation has been used in part to argue that 3V melatonin is not coming from recirculation via the plasma and choroid plexuses but rather through direct secretion into the pineal recess (Skinner & Malpaux, 1999; Tricoire *et al.*, 2002). Indeed, in sheep, brain melatonin concentration close to the 3rd ventricle walls and aqueduct of Sylvius is double that of plasma (Legros *et al.*, 2014), penetrating 8-10 mm into brain as the concentration gradually falls.

In a second category are compounds of the systemic circulation that primarily enter CNS across the CPs into CSF, for example vitamin C and folate (Spector, 2014; Spector & Johanson, 2014). Vitamin C crosses CPs via the sodium vitamin C transporter 2 (SVCT2, solute carrier family Slc23a1), which is absent at the BBB in health, although may be expressed after stroke (Gess *et al.*, 2011). Oxidized Vitamin C (≈ 10% of total Vitamin C) may use the GLUT1 transporter (Nualart, 2014), but there is little functional contribution in SVCT2 knockout mice, where CNS vitamin C is not detectable and mice die soon after birth (Sotiriou *et al.*, 2002). In wild-type animals, CSF and brain vitamin C is around 6x higher than plasma (200–400 µM and 30–60 µM respectively, (Nualart, 2014)).

Thirdly, many compounds are synthesised by CPs or leptomeninges in health or response to disease or trauma, and secreted into CSF for CNS use, for example transthyretin, IGF-II and NGF (Stylianopoulou *et al.*, 1988; Borlongan *et al.*, 2004; Chen *et al.*, 2005, 2008).

The extent to which molecules exchange between CSF and ISF depends on many factors, including their chemistry (mass, lipophilicity), the presence and direction of concentration gradients and the presence of cellular receptors or uptake mechanisms on tanycytes, astrocytes and neurons. However, it is clear that such exchange is an important part of CNS function and homeostasis.

Blood vessels and the perivascular space

Arteries in the subarachnoid space penetrate into the brain parenchyma, carrying with them a number of layers (Fig. 1). The arteries branch into arterioles and then capillaries, followed by transition into venules and veins and finally vascular return to the brain surface. At the capillary level, transverse sections show one or more endothelial cells lining the lumen and a number of associated cell types including pericytes and astrocyte foot processes (endfeet), together with their basal laminae, forming the neurovascular unit (NVU).

The perivascular spaces (PVS)[1] of cerebral blood vessels have in recent years been the subject of increasing research focus as pathways for CSF/ISF exchange (Abbott, 2004; Iliff *et al.*, 2012*a*,

---

[1] Definitions: ‘Peri’ is enclosing or surrounding (as in pericardial, perimeter); ‘Para’ has many, less specific meanings, along or beside, e.g. parathyroid – but this does not really apply to circumferential structures. In common terms, ‘para’ is alongside (as in paramedic) or relating to, not the structure enveloping something closely. So here we have chosen to use the term ‘perivascular’ for the small spaces surrounding vessels in which tracer can move, and this is also its most common usage for the BBB/NVU.

2013; Jessen *et al.*, 2015; Lochhead *et al.*, 2015; Benveniste *et al.*, 2017; Pizzo & Thorne, 2017; Pizzo *et al.*, 2018) but controversy exists over their precise role (Hladky & Barrand, 2014; Smith *et al.*, 2015, 2017; Jin *et al.*, 2016; Engelhardt *et al.*, 2017). Indeed, the glial components (astrocyte foot processes) that provide the outer boundary of the PVS within the parenchyma have been proposed to serve a special function for CNS clearance and waste turnover, forming the basis for a so-called 'glymphatic' circulation (Iliff *et al.*, 2012*a*; Nedergaard, 2013) that may potentially allow a more complete exchange of CSF and ISF at both superficial and deep sites spanning the entire neural axis. Such a PVS (Fig. 1a) may be identified on all larger cerebral blood vessels in both the subarachnoid spaces (leptomeningeal blood vessels) and within the parenchyma. Filled with a fluid in potential communication with both CSF and ISF but also containing connective tissue, scattered cells, and basement membranes (BM), the PVS is a real compartment within the vascular connective tissue space of the adventitia (Frederickson & Low, 1969; Jones, 1970; Krisch *et al.*, 1984; Zhang *et al.*, 1990; Sixt *et al.*, 2001; Wu *et al.*, 2009; Pizzo *et al.*, 2018) and possibly also the tunica media BM of large vessels (Carare *et al.*, 2008; Weller *et al.*, 2008; Pizzo *et al.*, 2018) as well as a potential compartment within the basal lamina of capillaries (Rennels *et al.*, 1985; Iliff *et al.*, 2012*a*; Pizzo *et al.*, 2018; Hannocks *et al.*, 2018). Potential routes of entry from the CSF into the PVS include specialized pores, termed stomata, recently demonstrated on the adventitial lining cells of leptomeningeal vessels in the SAS of the rat by scanning electron microscropy (Fig. 1b; (Pizzo *et al.*, 2018)), confirming earlier decades-old identification of such structures in cats (Zervas *et al.*, 1982); similar pores may also exist on the pia (Cloyd & Low, 1974; Reina *et al.*, 2004), providing an additional route into the PVS via the subpial space (discussed in (Pizzo *et al.*, 2018)). It has become increasingly clear that substances within the CSF may potentially access and distribute along the PVS to varying extents all throughout the cerebrovascular tree, e.g. large full length antibodies (immunoglobulin G) have been shown to access the PVS of arterioles (Fig. 1c), capillaries (Fig. 1d), and venules following intrathecal infusion in rats (Pizzo *et al.*, 2018). The demonstration that CSF-infused tracers can distribute perivascularly even along microvessels comprising the classical NVU has now led to a number of interesting questions regarding i) how such a perivascular distribution might accomplish CSF-ISF exchange, ii) the roles that astrocytes may play in regulating CSF-ISF exchange, and iii) the transport processes (e.g. diffusion, dispersion, or convection) governing fluid and tracer movement within the PVS and the surrounding brain ECS (Fig. 2). The PVS is unquestionably a site of great importance due to its involvement in disease processes affecting the NVU (e.g., cerebral amyloid angiopathy, present in > 90% of Alzheimer's disease brains and a major cause of intracerebral haemorrhage in the elderly; (Thal *et al.*, 2012; Iadecola, 2013; Greenberg *et al.*, 2014)), emerging roles in physiology (e.g., immune surveillance, central waste clearance and the proposed 'glymphatic' concepts; (Muldoon *et al.*, 2013; Nedergaard, 2013; Jessen *et al.*, 2015; Pizzo *et al.*, 2018)), and as a critical gatekeeper for widespread central drug delivery (Pizzo *et al.*, 2018).

Historical considerations: CSF/ISF exchange & flow along low-resistance pathways including the PVS

It was recognized over one century ago that CSF was primarily formed by the choroid plexuses in the ventricles of the brain, through which it flowed before reaching the cranial and spinal SAS (Cushing, 1914; Weed, 1914). Even then, it was thought that ISF secreted at the BBB may drain along perivascular spaces *out of the brain* and into the CSF to clear the brain of waste (Cushing, 1914; Weed, 1914), a concept revisited 60 years later by Helen Cserr to explain how the brain, lacking the classical lymphatics of the periphery, might accomplish efficient waste removal (Cserr, 1974; Cserr & Ostrach, 1974; Cserr & Patlak, 1992). Importantly, Cserr and colleagues (Cserr, 1974; Cserr & Ostrach, 1974; Cserr *et al.*, 1977, 1981, 1986) revived an earlier idea that a convective or bulk flow of ISF occurred along specialized pathways in the brain to communicate with and drain to the CSF. The key experiments involved the injection of small volumes (< 1 µL) of 2000 kDa blue dextran (Cserr & Ostrach, 1974) or 40 kDa horseradish peroxidase (Cserr *et al.*, 1977) into the caudate nucleus; although tracer profiles close to the injection site were interpreted as suggestive of short range diffusive transport in brain ECS, longer range transport seemingly inconsistent with diffusion was also observed along the perivascular spaces of blood vessels, along white matter tracts, and within the subependymal region and interpreted as having been produced by convective transport (bulk flow).

Subsequent studies showed that a variety of different radiolabelled tracers were cleared from the brain with similar rate constants, despite vast differences in molecular size and diffusion coefficient, again suggestive of a clearance process that was convective in nature (Cserr *et al.*, 1977, 1981). While others disagreed with the existence of these convective flow pathways for ISF-CSF exchange, arguing that diffusion through the brain ECS was solely responsible for drainage (Oldendorf & Davson, 1967; Davson & Segal, 1970), a general consensus emerged around the idea that ISF is largely produced by secretion of fluid across the capillaries (Cserr *et al.*, 1977; Abbott, 2004), albeit with some contribution from the CSF (Abbott, 2004), and that ISF is an important extra-choroidal source of CSF (Pollay & Curl, 1967; Milhorat, 1969). Later studies complementary to Cserr's original work also suggested preferential routes for ISF flow in the white matter (Rosenberg *et al.*, 1980), particularly in the presence of brain oedema (Kalimo *et al.*, 1986; Ohata *et al.*, 1990; Ohata & Marmarou, 1992), and in the perivascular spaces (Rennels *et al.*, 1985).

Experiments and discussion suggesting that CSF could potentially flow *into the brain* along the perivascular spaces began in the early 1900s with several groups making contributions (discussed in: (Woollam & Millen, 1954; Janzen, 1961)). Studies conducted by Weed (1914, (Weed, 1914)) implied that increased intracranial/infusion pressure was required to achieve perivascular distribution of CSF-administered tracer but subsequent work by Brierley (1950, (Brierley, 1950)) demonstrated perivascular distribution was possible with a physiological/minimal pressure increase. Later notable insights were provided by (i) Wagner (1974, (Wagner *et al.*, 1974)) and Rennels (1985, (Rennels *et al.*, 1985)), who showed that CSF-infused substances may be capable of reaching the PVS of capillaries, (ii) Rosenberg (1980, (Rosenberg *et al.*, 1980)) and Konsman (2000, (Konsman *et al.*, 2000)), who demonstrated the involvement of the white matter as a bulk flow pathway for CSF-infused substances, (iii) Fenstermacher and Patlak (1970 & 1975, (Levin *et al.*, 1970; Patlak & Fenstermacher, 1975)), Rosenberg (1980, (Rosenberg *et al.*, 1980)), Ghersi-Egea (1996, (Ghersi-Egea *et al.*, 1996*a*)), and Proescholdt (2000, (Proescholdt *et al.*, 2000)), who performed experiments where the penetration of CSF-infused tracers across the brain-CSF-interfaces appeared consistent with diffusive transport, and (iv) Krisch (1983 & 1984, (Krisch *et al.*, 1983, 1984)) and Ichimura (1991, (Ichimura *et al.*, 1991)), who demonstrated communication between the ECS, PVS, subpial space, and subarachnoid trabeculae core following CSF-infusion of tracer. It must be noted that the group of Weller and Carare have interpreted a number of their own more recent studies injecting tracers into the brain parenchyma as suggesting *outward* directed flow of ISF/solutes primarily confined to the capillary basal lamina and the smooth muscle basement membrane (tunica media) of arterioles/arteries (Carare *et al.*, 2008; Morris *et al.*, 2016), a process they have termed an ‘intramural periarterial drainage’ pathway (Diem *et al.*, 2017; Engelhardt *et al.*, 2017). Nevertheless, most experimental work and modelling to date has been interpreted as supporting some type of inward transport process from the CSF to the brain within the vascular connective tissue space of the tunica adventitia of arteries and arterioles (see (Abbott, 2004; Hladky & Barrand, 2014; Pizzo *et al.*, 2018) for more discussion).

The 1985 publication of Rennels *et al*. with CSF infusions of HRP stands out for both the speed at which the tracer distributed throughout the brain (taking as little as 10 min) and for the bold suggestion that a rapid 'paravascular' fluid *circulation* of CSF must exist along perivascular spaces comprising the entire vascular network (i.e., arteries → capillaries → veins) to account for it (Rennels *et al.*, 1985). While certain aspects of the Rennels work were questioned in the decade after their publication (Ichimura *et al.*, 1991), the past five years have witnessed a dramatically renewed interest in a possible *circulation* of CSF and CSF-borne tracers along perivascular spaces with relevance for CSF-ISF exchange, initially stimulated by new work from Nedergaard and colleagues (Iliff *et al.*, 2012*a*).

The 'glymphatic' system: original hypothesis & critical appraisal

In 2012, Iliff *et al*. reported findings based on intracisternal injections of fluorescently-labelled dextrans and ovalbumin in mice, real-time monitoring of tracer movement using *in vivo* two-photon microscopy via a closed cranial window preparation, and *ex vivo* confocal microscopy that suggested to them a brain-wide system of 'paravascular pathways' (Iliff *et al.*, 2012*a*). Live animal two-photon imaging was used to show that fluorescence from infused tracers first appeared along the PVS of arteries on the brain surface and their associated penetrating arterioles and only later along capillaries and draining venules. They observed that both a small (3 kDa) and very large (2000 kDa) dextran each appeared to be rapidly transported over great distances via the PVS (suggesting convective flow); however, only the smaller dextran appeared to efficiently leave the PVS to access the brain interstitium, interpreted as the result of 'sieving' by presumed narrow (~20 nm) gaps between astrocyte endfeet. When the same experiments were repeated in aquaporin-4 (AQP4) null mice, Iliff et al. reported that intracisternal ovalbumin (45 kDa) entry into the brain parenchyma was significantly diminished 30 min following a 5 min infusion (2 μL/min); furthermore, *in vivo* two-photon imaging showed that while 2000 kDa dextran access to penetrating arteriole PVS did not appear to be significantly altered in AQP4-null animals, penetration of 3 kDa dextran into the surrounding interstitium was dramatically reduced. Clearance of radiolabelled tracer substances out of the brain also tended to be reduced 1-2 hours after intrastriatal injection in AQP4-null animals.

Taking account of these results together with speculated roles for how perivascular AQP4 might be affecting tracer distribution, as these water channels are enriched on glial (astrocyte) endfeet (Nielsen *et al.*, 1997; Badaut *et al.*, 2002), Iliff et al. hypothesized three serial steps of a glial-lymphatic or 'glymphatic' system for waste clearance: (i) initial convective flow of subarachnoid CSF into the brain along peri-arterial spaces, (ii) AQP4-facilitated water and tracer flow from this peri-arterial space through the brain ECS ('transparenchymal' convection) resulting in directed transport of ISF toward venules/veins, and (iii) clearance out of the brain along peri-venous spaces (Iliff *et al.*, 2012*a*; Iliff & Nedergaard, 2013; Nedergaard, 2013; Nedergaard & Goldman, 2016).

A major critique of the 'glymphatic' hypothesis involves the proposed role of AQP4. Aquaporins are a large family of cell membrane channels containing ~0.5 nm pores (Gutiérrez *et al.*, 1995) that confer selective permeability to water and, in some cases, certain other small molecules;

AQP1, AQP4, AQP5, and AQP9 are present in rodent brain (Badaut *et al.*, 2002). AQP4 is particularly enriched in the brain at CSF-interfaces (Jung *et al.*, 1994), with polarized expression in astrocytes at the pial surface-facing glia limitans, in ventricle-facing ependymal cells, and, importantly, within perivascular endfeet that form the boundary between the parenchymal blood vessels and the neuropil (Nielsen *et al.*, 1997) (Fig. 2). It has been unclear by what precise mechanism(s) perivascular astrocytic AQP4 water channels might facilitate a transparenchymal flow of ISF and perivascular macromolecule tracers under normal conditions, as proposed in the 'glymphatic' concept, particularly because (i) directed-convection from the arterial PVS to the venule PVS through the neuropil interstitium would depend on a hydrostatic pressure/osmotic gradient that is difficult to envision (Smith *et al.*, 2015), (ii) AQP4 is incapable of transporting macromolecules, and (iii) much experimental work has suggested the high hydraulic resistance of the brain ECS would greatly restrict such a flow in favour of diffusion (Wolak & Thorne, 2013; Pizzo & Thorne, 2017; Holter *et al.*, 2017). Additionally, a transparenchymal flow of ISF, solutes, and waste would appear difficult to reconcile with the required homeostasis of the brain microenvironment for synaptic transmission. Aquaporins clearly do play diverse roles in brain water balance in health and disease (Badaut *et al.*, 2002; Hsu *et al.*, 2015) and such concepts have undoubtedly informed the 'glymphatic' hypothesis. Previous studies performed on AQP4-deficient mice have demonstrated that such animals exhibit an increased brain ECS volume fraction (Yao *et al.*, 2008), increased basal brain water content (Haj-Yasein *et al.*, 2011), and larger intracranial pressure elevations in response to induced vasogenic (non-cellular) oedema (Papadopoulos *et al.*, 2004), suggesting that AQP4 indeed plays critical roles in the transport of water between brain compartments as well as the formation and resolution of oedema. The key question for the ‘glymphatic’ concept is just what role astrocytic AQP4 may play in the circulation of fluid in perivascular compartments and how its deletion affects such circulation.

Verkman and colleagues have further argued that the proposed ‘glymphatic’ hypothesis and its reliance on AQP4 is implausible based on physiological grounds (Smith *et al.*, 2015) and recently reported on their own experimental work testing key aspects of the original Iliff *et al.* studies (Smith *et al.*, 2017). Interestingly, this new work (Smith *et al.*, 2017) emphasized that tracer movement in the brain parenchyma (outside of the perivascular spaces) was size-dependent and consistent with diffusion as the mechanism of transport, using a cisternal infusion paradigm in mice that was very similar to that employed by Iliff et al. (Iliff *et al.*, 2012*a*). A separate recent experimental study in rats (Pizzo *et al.*, 2018) has also confirmed the role of tracer size-dependent diffusive transport at the pial brain surface using a similar cisternal infusion paradigm to the Nedergaard group (Iliff *et al.*, 2013). Finally and perhaps most importantly, the Verkman group replicated many of the original Iliff *et al.* cisternal infusion experiments in AQP4-null animals and found no qualitative or quantitative differences in ovalbumin distribution between wild type and AQP4 null mice (or between wild type and AQP4 null rats)(Smith *et al.*, 2017). Further work will be required to resolve the precise role(s) that AQP4 water channels may or may not play with respect to tracer distribution in the perivascular and parenchymal compartments.

The role of brain capillaries in secreting a fluid suitable for the optimal function of neurons and glia was largely ignored in the early conception of the ‘glymphatic’ system. The evidence for origin of ISF as a secretion across the brain capillary endothelium is well established; *in vivo* studies show good regulation of brain ions in the face of large changes in plasma concentration, and the necessary ion channels and transporters are expressed at the BBB (Schielke & Betz, 1992; Abbott, 2004). Careful studies in primary cultured brain endothelial cells have provided a complex map of ion transporters and channels on apical and basal membranes, and the ways in which they could generate the required fluid flow (Hladky & Barrand, 2016). As the flow rate per unit area is low compared with choroid plexus secretion of CSF, it is not possible to demonstrate fluid production from segments of isolated brain capillary, but the net result is to supply local regions of the neuropil with fresh fluid of optimal composition for neural function. Interestingly, the brain endothelium shows down-regulation of the AQP1 highly expressed on non-brain endothelial cells (Dolman *et al.*, 2005), consistent with the need to limit the rate of fluid production in order to maximize local ionic homeostasis. If a large percentage of the ISF were provided from recirculated CSF as might be implied by the 'glymphatic' hypothesis, this would contain waste products from all the upstream sites exposed to that CSF, a much less suitable medium for optimal neural function.

Diffusion or flow of the ISF in the brain ECS?

A great many studies using a wide variety of tracer substances and multiple different *ex vivo*/*in vivo* methods have concluded that the local transport of small and large molecules through the brain ECS of the neuropil is predominantly diffusive in nature; such studies have included ventriculocisternal or subarachnoid-cisternal perfusion of radiolabelled tracers (Rall *et al.*, 1962; Levin *et al.*, 1970; Patlak & Fenstermacher, 1975), real-time iontophoresis of the small tetramethylammonium ion (Nicholson & Phillips, 1981), and integrative optical imaging (IOI) of pressure-injected fluorescently labelled molecules (Nicholson & Tao, 1993; Thorne *et al.*, 2004*a*; Thorne & Nicholson, 2006; Thorne *et al.*, 2008; Wolak *et al.*, 2015). Electron microscopy studies focused on neuropil ultrastructure have long indicated a brain ECS width of approximately 10-20 nm (Horstmann & Meves, 1959; Brightman & Reese, 1969; Van Harreveld, 1972; Peters *et al.*, 1991) and, importantly, that these narrow spaces could be accessed with tracers such as HRP (40 kDa) following intracerebroventricular injection (Brightman & Reese, 1969; Brightman, 2002).

More recently, Thorne and Nicholson used *in vivo* diffusion measurements to demonstrate that the ECS width in rat somatosensory cortex is substantially wider in living animals than these earlier EM-based estimates from processed, conventionally fixed tissue had indicated (Thorne & Nicholson, 2006). Integrative optical imaging of intraparenchymally-injected dextrans and quantum dots ranging from 3-35 nm in size showed that (i) transport in the neuropil of living animals could be adequately described by diffusion theory and (ii) modelling the brain ECS as cylindrical pores or as parallel planes and fitting such models (with the application of hydrodynamic theory for hindered diffusion) to experimental data led to ECS width estimates of approximately 40-60 nm (Thorne & Nicholson, 2006). Subsequent *in silico* modelling work based on expansion of actual tissue geometry from serial EM to match the established physiological brain ECS volume (20%; (Syková & Nicholson, 2008)) has mostly agreed well with the earlier IOI diffusion measurement-based estimates of brain ECS width (Kinney *et al.*, 2013). It has long been suggested that the reason diffusive transport is strongly favoured over flow in the brain ECS under most conditions is that the hydraulic resistance of such narrow spaces is too high for bulk flow to occur even in the presence of a significant pressure difference (Fenstermacher & Patlak, 1976; Wolak & Thorne, 2013; Holter *et al.*, 2017). Recent modelling studies of tracer movement through the ECS have continued to suggest that flow in the ECS (as suggested by the 'glymphatic' hypothesis) is unlikely (Jin *et al.*, 2016; Holter *et al.*, 2017).

There is currently much discussion regarding how the brain ECS as well as tracer transport from CSF into the brain may be affected by different brain states, i.e. awake versus sleeping versus anaesthetized conditions. Significant transport of a variety of different tracers into the brain from the CSF has now been demonstrated *in vivo* in rodents subjected to a wide variety of anaesthetics, including ketamine/xylazine (Iliff *et al.*, 2012*b*; Xie *et al.*, 2013), isoflurane (Iliff *et al.*, 2013), avertin (Smith *et al.*, 2017), and urethane (Pizzo *et al.*, 2018). It has been suggested by Nedergaard and colleagues that the influx of tracers such as 3 kDa dextran from the CSF to the brain is profoundly suppressed in awake mice compared to naturally sleeping or ketamine/xylazine anaesthetized mice (Xie *et al.*, 2013); reduced brain influx and circulation of CSF-infused tracer was further suggested to be the result of a significantly reduced brain ECS volume (and changes in ISF ionic composition (Ding *et al.*, 2016)) associated with the awake state (Xie *et al.*, 2013), a novel finding in itself that needs to be studied further and subjected to replication. Although interesting, decreased transport of substances from the CSF to the brain and a decreased brain ECS in awake animals has subsequently been challenged both conceptually (Hladky & Barrand, 2014) and experimentally (Gakuba *et al.*, 2018). Indeed, Gakuba and colleagues recently used MRI and other methods to show that isoflurane-, ketamine/xylazine-, and ketamine-anaesthetized mice actually exhibited reduced CSF-to-brain influx of intrathecally infused contrast agent (DOTA-Gd), Evans blue, and 775 Da indocyanine green dye as compared to the awake state (Gakuba *et al.*, 2018). More work will be needed to resolve the discrepancies between different groups and the effects that different methods and tracer substances may have on the findings.

A sieving effect of perivascular astrocyte endfeet?

It is tempting to speculate that transport from the perivascular space into the adjacent brain ECS may be restricted or regulated based on the size of the gaps between adjacent astrocyte endfeet bordering the perivascular space; indeed, Iliff *et al.* concluded that these gaps were likely responsible in some way for the sieving effect they observed between the distributions of small and large cisternally infused dextrans (discussed above; (Iliff *et al.*, 2012*a*)). Transmission EM measurements from conventionally prepared, aldehyde-fixed tissue have suggested such endfoot-endfoot clefts are approximately 20 nm wide (similar to conventional EM-based estimates of ECS width) (Mathiisen *et al.*, 2010). However, a more recent transmission EM study using cryofixation methods suggested astrocyte coverage of cerebral blood vessels was significantly less complete than previously shown (Korogod *et al.*, 2015), calling into question whether astrocyte endfoot sieving indeed occurs. The Korogod *et al.* figure for ECS volume in the relatively uniform brain parenchyma (~15% with cryopreservation cf ~2.5% with conventional fixation) is encouragingly closer to physiological measurements, so that in this case cryopreservation may well give a truer picture of the ECS than conventional fixation. However, it is harder to assess the data for perivascular coverage by astrocytes (~62% cf >90% with conventional fixation).

Fig. 3 provides a summary of the major junctions and adhesions that have been described for endothelial cells and astrocytes at the BBB (Huber *et al.*, 2001; Abbott *et al.*, 2006; Mehta & Malik, 2006; Barresi & Campbell, 2006; del Zoppo & Milner, 2006; Förster, 2008; Strbian *et al.*, 2009; Tietz & Engelhardt, 2015). Endothelial cell-astrocyte interactions occur in part through complex associations with the extracellular matrix (ECM) and basal lamina that are mediated by integrins, αβ heterodimeric receptors that bind extracellularly to laminins and fibronectin to link the ECM to the cytoskeleton, and dystroglycan, a complex of α and β subunits that binds to laminins, agrin, and perlecan to provide additional links of the ECM to the cytoskeleton. Many additional linkages between laminins, proteoglycans, fibronectin, type IV collagen, and other ECM

/ basal lamina constituents have also been described (Mehta & Malik, 2006; Barresi & Campbell, 2006; del Zoppo & Milner, 2006). In life, there is evidence that the astrocyte endfeet are strongly linked to the basal side of the endothelial cells by numerous such integrin-dystroglycan complexes, involving integrins in the endothelial basal cell membrane interacting with extracellular laminin and fibronectin, connecting collagen IV and proteoglycans in the extracellular space to dystroglycan inserted in the underlying astrocyte endfeet membrane. Similarly, it is proposed that the astrocytic layer forms an effective ‘second barrier’ surrounding the endothelial tube, with connexin 43 gap junctions linking adjacent astrocyte endfeet (Gaete *et al.*, 2014), and the whole complex being sufficiently tightly knit to restrict ready entry of leukocytes and mast cells to the brain parenchyma except in pathological conditions (Engelhardt *et al.*, 2016). It is also possible that matrix components of the basal lamina (e.g., specific laminin composition; (Sixt *et al.*, 2001)) may play a more important role than has been appreciated (Hannocks *et al.*, 2018), e.g., in restricting the entry of cells into the parenchyma after their migration across brain endothelial cells or the transfer of very large macromolecules (e.g., ~460 kDa ferritin; (Brightman, 2002)) from the ECS to the perivascular space for clearance.

While the close proximity of adjacent cells and the small size of the extracellular spaces in conventionally-fixed brain tissue would not seem to accurately reflect the living condition, it is possible that the organization of adjacent perivascular astrocyte foot processes is captured more effectively in aldehyde-preserved tissue than in the TEM images captured after cryopreservation, where ice crystals may disrupt the fragile cell:cell associations in the neurovascular unit and perivascular space. More research is needed to resolve this question. The conclusion is that it is important to bear in mind the physiology when interpreting microscopic images, especially those potentially subject to fixation/freezing artefacts.

It bears stressing that basement membranes may prove to play a critical role in the sieving of perivascularly located molecules attempting to enter the brain parenchyma (Brightman, 1968, 2002; Hannocks *et al.*, 2018); indeed, recent experimental work has demonstrated that intracisternally infused small single-domain antibodies (17 kDa; 4.5 nm apparent hydrodynamic diameter) more fully access perivascular basement membranes than similarly infused large full length immunoglobulin G antibodies (150 kDa; 10 nm) (Pizzo *et al.*, 2018). A recent molecular characterization of the PVS with respect to laminin composition and other markers by Sorokin and colleagues provides new, critical information for future work in this area (Hannocks *et al.*, 2018).

"ISF bulk flow"

Confusion has long been associated with what different groups have meant in suggesting or describing "ISF bulk flow". The pioneering work of Helen Cserr and a number of her contemporaries often made mention of "bulk flow of ISF" but careful reading reveals that this typically was intended to describe flow *principally limited to low-resistance pathways* such as the perivascular spaces and white matter tracts (Cserr *et al.*, 1977; Rosenberg *et al.*, 1980; Abbott, 2004) and not within the narrow and tortuous brain ECS. In summary, it seems increasingly likely that a great many studied macromolecule tracers as well as endogenous proteins in the CSF distribute into brain tissue via transport processes that may be adequately described by some combination of diffusion in the ECS and convection in the perivascular spaces (Wagner *et al.*, 1974; Rennels *et al.*, 1985; Ghersi-Egea *et al.*, 1996*a*; Proescholdt *et al.*, 2000; Pizzo *et al.*, 2018).

CSF and ISF compartmentalization & drainage pathways

CSF and ISF are generally considered to be similar in composition (Cserr & Patlak, 1992; Abbott, 2004; Hladky & Barrand, 2014; Thorne, 2014), with the exception that the ISF exists in an environment containing an abundant ECM that may play key roles in CSF/ISF transport and exchange (Syková & Nicholson, 2008; Thorne, 2014). The polyanionic nature and binding capacity of the ECM may significantly impact the diffusion of certain ions and other molecules in the brain ECS (e.g., confinement or binding of ions by perineuronal nets (Härtig *et al.*, 1999) or chondroitin sulphate proteoglycans (Hrabetová *et al.*, 2009), sequestration of growth factors (Taipale & Keski-Oja, 1997), and protein binding to heparan sulphate proteoglycans (Thorne *et al.*, 2008)). CSF-ISF exchange of molecules is therefore expected to be limited by (i) molecular size, (ii) ECM interactions, (iii) receptor binding, (iv) aggregation state (e.g., certain pathogenic proteins), (v) permeability characteristics (e.g., clearance across the BBB), (vi) distance from the brain-CSF interface, and likely other factors.

The precise drainage pathways for CSF and ISF out of the central compartment have also been the source of much recent interest. CSF drainage occurs directly into the blood via arachnoid villi or granulations into the venous sinuses of the dura mater and also into the lymphatic system via cranial and spinal nerves (Pizzo & Thorne, 2017). Drainage occurs along the olfactory nerves to the nasal mucosa to the cervical lymph nodes (Faber, 1937; Bradbury *et al.*, 1981; Bradbury & Westrop, 1983; Szentistványi *et al.*, 1984; Weller *et al.*, 1992; Kida *et al.*, 1993), and along spinal nerves to cervical, intercostal, and other lymph nodes (Koh *et al.*, 2005). An additional pathway for CSF/ISF drainage appears to occur within dural lymphatic vessels to the cervical lymph nodes (Aspelund *et al.*, 2015; Louveau *et al.*, 2015), but just how CSF enters the dural lymphatic vessels has not been well described.

Tracer studies suggest that the drainage of ISF and CSF from the brain is compartmentalized. For example, the transport and drainage of ISF-administered tracers has shown significant lateralization; brain-injected tracers appear to preferentially drain along perivascular spaces on the same side as the injection and into ipsilateral cervical lymph nodes (Bradbury *et al.*, 1981; Szentistványi *et al.*, 1984). By contrast, CSF-administered tracers drain into cervical lymph nodes on both sides (Szentistványi *et al.*, 1984; Kida *et al.*, 1993; Pizzo *et al.*, 2018). Studies of nose-to-brain transport further support some degree of separation between CSF and ISF (Thorne *et al.*, 2004*b*). Földi and colleagues have long proposed that drainage of ISF along the PVS is indeed compartmentalized from the CSF as it drains from the brain, possibly by the presence of the cells ensheathing the vessel in the subarachnoid space (Földi, 1996) (e.g., as described by (Alcolado *et al.*, 1988)). In addition to tracer studies, antigenic responses also appear to suggest a compartmentation of CSF and ISF (Galea *et al.*, 2007; Engelhardt *et al.*, 2017), as parenchymal tissue grafts and ISF antigens elicit more limited immune responses (e.g., (Shirai, 1921; Murphy & Sturm, 1922; Stevenson *et al.*, 1997)) than CSF administered tissue or antigen that usually results in a strong immune response (e.g., (Murphy & Sturm, 1922; Stevenson *et al.*, 1997)). In summary, a synthesis of the older descriptive work on ISF-CSF relationships and fluid turnover and clearance from the central compartment, together with more recent work incorporating more sophisticated molecular characterization of specific drainage pathways out of the CNS to venous blood and draining lymph nodes suggests there remain gaps in our understanding of the precise relationships, pathways, and their relative importance. Further work is clearly needed in this area.

Practical and Clinical Implications of ISF/CSF interaction

CSF sampling has inherent problems associated with studying the composition and dynamics of CSF which include: pharmacological effect of anaesthesia; confounding effects of circadian rhythm; inflammation during disease or surgical intervention; changed ventricular pressure after removing CSF or adding tracers into the enclosed ventricular system. All these will affect CSF flow and/or production, potentially influencing data obtained (these and other confounding factors are discussed in detail elsewhere (Spector *et al.*, 2015)). Sampling CSF multiple times is a particular problem when comparing healthy and diseased states, or young vs old. Removal of fluid and reduction in intracranial pressure alter CSF dynamics until the fluid can be replenished, and replacement rate is faster in the young or healthy (591 ml/day, human), compared to in older or pathological situations (294 ml/day) (Silverberg *et al.*, 2001; Rapoport *et al.*, 2004). As a result, biomarkers or drugs are expected to be concentrated in the smaller volume of fluid of the old or with certain diseases. For example, Slats *et al.* (Slats *et al.*, 2012) sampled 6 ml of patients' CSF every hour for 36 hours using indwelling L3-4 lumber puncture cannula. They noted total CSF protein and pathological tau increased over the study period in the Alzheimer's disease patients, but not in age-matched controls, suggesting an artefact in sampling from the frailer patients.

Another important issue is assessing CSF uptake of systemic drugs when plasma concentration is 10-100x greater than CSF or brain. Contamination of the CSF sample with whole blood or plasma must be ruled out, but microscopic inspection for erythrocytes cannot always rule out contamination because erythrocytes may lyse. Tests for haemoglobin are preferred because even a 1 in 100 contamination with blood could significantly affect drug determination (Chen *et al.*, 2006).

Using CSF as a proxy for brain drug levels is commonly used in both clinical and pre-clinical studies. However, the pitfalls are numerous and include the issues already mentioned above, as well as the fact that drug distribution in CSF depends on the chemistry of the compound and its interaction with uptake and efflux transporters at CNS/blood interfaces.

Doran *et al.* (Doran *et al.*, 2005) very helpfully studied a library of Pfizer's small molecule drugs <450Da, measuring both brain and CSF uptake in mice after systemic administration. Re-analysis of their data (Fig. 4) shows that brain penetration increases as drugs become more lipid soluble (increasing CLogD); conversely however, CSF penetration decreases as drugs become more lipid soluble. This is consistent with the aqueous CSF being less amenable to partitioning of lipid soluble drugs compared to brain, where drugs are exposed to lipid cell membranes into which they can partition.

For hydrophilic drugs with CLogD <1, CSF drug content may be predictive of brain levels because there is similar, modest distribution into both compartments and there is significant correlation between the two (p=0.023, R^2 =0.68, df=6). However, for highly brain penetrant lipophilic drugs with CLogD > 3, CSF uptake does not correlate with brain (p=0.148, R^2 =0.45, df=5) and brain levels are on average 9x those in CSF.

Drug interaction with efflux transporters may also play a role. In mice lacking P-glycoprotein (mdr1a$^{-/-}$/1b$^{-/-}$ knockout mice), there is even greater difference between brain and CSF distribution. This is mainly due to increased brain distribution in mdr1a$^{-/-}$/1b$^{-/-}$ mice since P-glycoprotein is not available to efflux the drug back to blood. For example, lipophilic drugs with CLogD >3 have brain levels on average 12x higher than CSF (compared to 9x CSF levels in wild-type mice). Even hydrophilic drugs' brain distribution is affected, increasing from 2x CSF levels in the wild-type mice, to 3x CSF levels in the mdr1a$^{-/-}$/1b$^{-/-}$ mice for drugs with CLogD <1. In general, brain and CSF uptake of P-glycoprotein substrates are closer to each other at any given CLogD in the wild-type mice.

Therefore, it cannot be assumed that the presence of any compound in CSF is a true reflection of its brain level, particularly for lipophilic drugs that evade efflux transport. Similar data are not available for large molecules or biologics and would presumably be different for drugs interacting strongly with other transport or efflux systems.

CNS pathologies and disturbances of brain fluids

Several pathologies of the cerebral microvasculature, including the associated cells of the neurovascular unit, and the perivascular space, have been mentioned briefly above. Here we focus on some additional brain pathologies with particular relevance to fluid drainage pathways and brain fluid flow.

Brain oedema is the accumulation of excess fluid in the brain, either in the intracellular (cytotoxic oedema) or extracellular compartments (vasogenic oedema) (Nag *et al.*, 2009), though these two types of fluid accumulation rarely occur independently (e.g., certain pathologies including diabetes, stroke, and traumatic brain injury may involve both vasogenic and cytotoxic oedema (Tasker & Acerini, 2014; Dreier *et al.*, 2017)). Cytotoxic (cellular) oedema can result from toxic agents (including many in common use such as dinitrophenol (weight loss agent), hexachlorophene (disinfectant), and organophosphates including insecticides (Chen, 2012)), ischaemic stroke, or hypoxia; in cytotoxic oedema, the BBB stays intact, but disturbance of cellular metabolism impairs ion transport in glial cell membranes, leading to cellular retention of sodium and water, and cell swelling especially in astrocytes in grey and white matter. Cytotoxic oedema may also be associated with a reduced ECS volume, further hindering diffusional transport of oedema fluid and solutes in the gray matter (Hossmann, 1976). Vasogenic oedema results from breakdown of the BBB, e.g. associated with trauma, hypertension, osmotic imbalance, brain cancer and brain inflammation (meningitis or encephalitis), allowing intravascular proteins and fluids into the parenchymal ECS. Several studies of vasogenic oedema models have demonstrated that bulk flow pathways, including white matter tracts and perivascular spaces, are important sites for oedema fluid movement and clearance (reviewed in (Pizzo & Thorne, 2017)). Aquaporin water channels clearly play a role in the resolution of edema; in particular, AQP4 has been suggested to regulate ECS water in the healthy and diseased brain due to its localized expression on astrocytes at brain-CSF and blood-brain interfaces and demonstrated alterations in disease states (Badaut *et al.*, 2014). Treatments based on mechanistic understanding may include intravascular mannitol and/or saline (osmotherapy), melatonin, and inhibitors of water channels (e.g., aquaporins) and ion cotransporters (Deng *et al.*, 2016; Winkler *et al.*, 2016). Finally, decompressive craniectomy may be required in extreme/acute cases (Brown & Wijdicks, 2017).

Prion diseases (or transmissible spongiform encephalopathies, TSE's) are a group of progressive neurodegenerative conditions, which unlike most infections which involve bacteria or viruses, involve misfolded protein (Griffoni *et al.*, 2003; Zabel & Reid, 2015). All known prion diseases in mammals affect brain structure, creating microscopic holes and hence a ‘spongy’ texture, with severe consequences for brain function. Prion diseases exist in both animals and humans. Scrapie, a disease affecting sheep and goats, was the first prion disease to be identified in the 1730s. In humans, the outbreak of Creutzfeldt-Jakob disease variant resulted from eating infected bovine-derived meat.

Prion-like spread of other CNS pathologies involving aggregated proteins is now recognised – for Amyloid-β (Alzheimer's disease), α-synuclein (Parkinson's disease) and mutant huntingtin (Huntington's disease) (Costanzo & Zurzolo, 2013; Borghammer, 2017), although the underlying mechanisms are not understood in detail (Holmes & Diamond, 2012; Huang *et al.*, 2015). Extracellular vesicles (EVs) released from one cell and capable of influencing another (a known method of cell:cell communication), are recognised to be involved in the protein transmission in some of these neuropathies (Krämer-Albers & Hill, 2016; Valdinocci *et al.*, 2017), and also in tumours (Choi *et al.*, 2017). It is clear that the health of CSF and ISF flow and drainage will influence the spread of such aggregated proteins.

Epilepsy, brain trauma, phosphorylated tau, and enlarged perivascular spaces

A recent analysis of abnormal phosphorylated tau (p-tau) deposition in samples from temporal cortex and adjacent white matter taken from patients with temporal lobe epilepsy (TLE) and chronic traumatic encephalopathy (CTE) has reported a similar pattern of pathological tau deposition in perivascular spaces in both conditions, suggesting similar underlying cerebrovascular pathology with abnormal perivascular p-tau accumulation as a potential mechanism (Puvenna *et al.*, 2016). Both TLE and CTE physiopathology involve neuronal death which likely initiates spillage of unbound tau protein into the extracellular space and, from there, to perivascular lining cells and perivascular spaces. Extracellular p-tau appeared to follow extracellular drainage pathways in the neuropil that led toward perivascular spaces bordering large

(>100 µm diameter) blood vessels; p-tau immunoreactivity was prominent within astroglial cells adjacent to blood vessels and frequently appeared clustered within the perivenous space. Importantly, aggregated p-tau was detected in brain tissue from both CTE and TLE, but little was observed in control brain. Since larger aggregates of p-tau would not be as free to move readily through the brain ECS by diffusion as unbound monomers, such aggregates likely become trapped within the tissue, particularly the tissue space bordering venules and large veins; this sequence of events would be expected to further impede the subsequent clearance of p-tau and other waste constituents over time. Interestingly, military personnel exposed to blast shockwaves (e.g., from explosive devices) also show a characteristic pattern of GFAP and p-tau immunoreactivity with prominent astroglial scarring at brain-fluid interfaces including the subpial region and perivascular spaces (Shively *et al.*, 2016). Perivascular accumulation of p-tau is also observed in Alzheimer's disease and has been demonstrated to be present in arteries/arterioles as well as veins in the parenchyma (Merlini *et al.*, 2016). Interestingly, perivascular amyloid beta deposits (cerebral amyloid angiopathy) within the tunica media of leptomeningeal arteries as well as cortical arteries, arterioles and capillaries are among the classic neuropathological hallmarks of Alzheimer's disease, while veins and venules rarely exhibit such deposits (Serrano-Pozo *et al.*, 2011*a*). Such characteristic amyloid beta accumulation in Alzheimer's disease has led some to suggest that this pathology results from failure of amyloid beta drainage out of the brain within the basement membranes of capillaries, arterioles and arteries (Preston *et al.*, 2003). However, it has also been suggested that this pattern of amyloid beta deposition could be due to abnormal perivascular amyloid beta entry and accumulation from the CSF into the brain (Ghersi-Egea *et al.*, 1996*b*; Pizzo *et al.*, 2018), consistent with reports that leptomeningeal arteries typically exhibit more cerebral amyloid angiopathy than penetrating cortical arteries (Serrano-Pozo *et al.*, 2011*b*). Indeed, it is now increasingly appreciated that structural alterations in draining venules and veins also may play a role in the pathology of Alzheimer's disease (Lai *et al.*, 2015), so the precise mechanisms at play in producing the perivascular pathology and amyloid deposition of Alzheimer's disease require further study .

Finally, it bears noting that an enlarged PVS has been identified (typically associated with larger caliber vessels such as perforating arterioles and venules) in a number of clinical MRI studies of patients with traumatic brain injuries (Inglese *et al.*, 2005), acute ischemic stroke (Doubal *et al.*, 2010), and multiple different types of mucopolysaccharidoses (Zafeiriou & Batzios, 2013; Matsubara *et al.*, 2017). Enlarged perivascular spaces might simplistically suggest either increased water secretion by the BBB, decreased clearance of CSF, increased resistance to the circulation/transport and/or drainage of perivascular fluid, or a combination of all of the above. The mechanism of increased production or decreased CSF absorption seems unlikely, at least in ageing-related small vessel ischemic disease where ventricular size is commonly normal, so it is tempting to speculate that some form of hindrance or impedance of perivascular fluid circulation/transport may underlie the enlarged PVS observed in this condition.

In summary*,* if cerebral regulation of fluid and waste elimination is disrupted, a dangerous cycle can emerge between impedance of waste clearance pathways and exacerbation of cerebral oedema or inflammation.

Conclusions

So, to return to the question – Does the 'glymphatic' system exist, in the form of AQP4-dependent convective flow pathways bathing neurons, synapses and glia in the parenchyma? It is becoming increasingly apparent that under normal conditions such flows likely do *not* exist in the neuropil of the grey matter. Rather than a 'glymphatic' system as originally proposed (Iliff *et al.*, 2012*a*; Nedergaard, 2013; Nedergaard & Goldman, 2016), the weight of the evidence now suggests the existence of a perivascular fluid system for the CNS, with convective flow or dispersion along the perivascular spaces of larger vessels and then diffusion predominantly regulating CSF/ISF exchange at the level of the neurovascular unit associated with CNS microvessels, as now proposed by several groups (Wolak & Thorne, 2013; Smith *et al.*, 2015, 2017; Jin *et al.*, 2016; Asgari *et al.*, 2016; Holter *et al.*, 2017; Pizzo *et al.*, 2018; Hannocks *et al.*, 2018). It remains possible that pericapillary convection occurs in the basal lamina in addition to diffusion to formally link up the arteriolar and venular perivascular fluid compartments and allow a fully convective circulation pathway (Pizzo *et al.*, 2018; Hannocks *et al.*, 2018); regardless, CSF/ISF exchange may at least partly occur through the neuropil of the grey matter at the capillary level by diffusion, as neurons and all the other constituents of the NVU are not located further than about 10-20 μm from the pericapillary spaces, a distance that has likely been optimized for the effective diffusion of glucose, oxygen, and countless other substances from the circulation (Abbott *et al.*, 2006; Wolak & Thorne, 2013).

In summary, the classical view of the system (pre-2012) together with recent studies, supports the evidence for diffusion (not bulk flow) from capillaries and throughout the interstitium, the optimal arrangement for homeostasis of the neuronal microenvironment. This acts together with a well-regulated system of convective flow channels where they are most needed and will least disturb neural function: a) in the vascular system supplying arteries and ultimately capillaries, and b) in the perivascular space around large arteries and arterioles, extending down to the capillary level, carrying flow of a small volume of CSF from the brain surface into the brain. The PVS around venules and veins would appear to collect fluid drainage from the interstitium and channel it out of the parenchyma, partly back to the CSF in the SAS but also to other sites; in addition, there is some seepage of fluid drainage across the ependyma into the ventricles. The net result is well-maintained homeostasis of the neural microenvironment, efficient (and sufficient) communication between CSF produced by the CP and the brain parenchyma, and efficient clearance of cell debris and waste products of metabolism which are too large to exit across the endothelium of the blood vessels. Clearly, much more work is needed to resolve current discrepancies surrounding many other aspects of the system, perhaps most notably the effect that different anaesthetics, natural sleep and wakefulness may have on convective and diffusive transport in the PVS and ECS, respectively. More sophisticated quantitative modelling of such transport is urgently needed and will likely play a larger role in the future to better clarify some of the discrepancies and to suggest new experiments that may help to resolve them.

In several pathologies, disturbances of any element of this system can result in brain fluid accumulation and oedema. In many cases the oedema is local and resolved by endogenous repair mechanisms; in more severe cases, medical/surgical intervention may be required. Recovery of brain function can involve adjustments in the vascular and brain fluid flow channels, and neuronal plasticity to compensate at least in part for damaged circuits. It is clear that maintaining some form of healthy perivascular fluid circulation and at least some degree of CSF/ISF exchange, as well as a healthy cardiovascular system, are important in preserving effective CNS function into old age.

References

Abbott NJ (2004). Evidence for bulk flow of brain interstitial fluid: significance for physiology and pathology. *Neurochem Int* **45,** 545–552.

Abbott NJ (2013). Blood-brain barrier structure and function and the challenges for CNS drug delivery. *J Inherit Metab Dis* **36,** 437–449.

Abbott NJ, Rönnbäck L & Hansson E (2006). Astrocyte-endothelial interactions at the blood-brain barrier. *Nat Rev Neurosci* **7,** 41–53.

Alcolado R, Weller RO, Parrish EP & Garrod D (1988). The cranial arachnoid and pia mater in man: anatomical and ultrastructural observations. *Neuropathol Appl Neurobiol* **14,** 1–17.

Ames A, Higashi K & Nesbett FB (1965). Relation of potassium concentration in choroidplexus fluid to that in plasma. *J Physiol* **181,** 506–515.

Asgari M, de Zélicourt D & Kurtcuoglu V (2016). Glymphatic solute transport does not require bulk flow. *Sci Rep* **6,** 38635.

Aspelund A, Antila S, Proulx ST, Karlsen TV, Karaman S, Detmar M, Wiig H & Alitalo K (2015). A dural lymphatic vascular system that drains brain interstitial fluid and macromolecules. *J Exp Med* **212,** 991–999.

Badaut J, Fukuda AM, Jullienne A & Petry KG (2014). Aquaporin and brain diseases. *Biochim Biophys Acta - Gen Subj* **1840,** 1554–1565.

Badaut J, Lasbennes F, Magistretti PJ & Regli L (2002). Aquaporins in brain: distribution, physiology, and pathophysiology. *J Cereb Blood Flow Metab* **22,** 367–378.

Barkai A, Glusman M & Rapport MM (1972). Serotonin turnover in the intact cat brain. *J Pharmacol Exp Ther* **181,** 28–35.

Barresi R & Campbell KP (2006). Dystroglycan: from biosynthesis to pathogenesis of human disease. *J Cell Sci* **119,** 199–207.

Bateman GA & Brown KM (2012). The measurement of CSF flow through the aqueduct in normal and hydrocephalic children: from where does it come, to where does it go? *Childs Nerv Syst* **28,** 55–63.

Bauer HJ (1993). The Quincke centennial lecture. In *CNS barriers and modern diagnostics*, ed. Felgenhauer K, Holzgraefe M PH, pp. XXVII–XXXII. VCH, Weinheim.

Benveniste H, Lee H & Volkow ND (2017). The Glymphatic Pathway. *Neurosci*107385841769103.

Borghammer P (2017). How does parkinson's disease begin? Perspectives on neuroanatomical pathways, prions, and histology. *Mov Disord*; DOI: 10.1002/mds.27138.

Borlongan C V, Skinner SJM, Geaney M, Vasconcellos A V, Elliott RB & Emerich DF (2004). Intracerebral transplantation of porcine choroid plexus provides structural and functional neuroprotection in a rodent model of stroke. *Stroke* **35,** 2206–2210.

Bradbury MW, Cserr HF & Westrop RJ (1981). Drainage of cerebral interstitial fluid into deep cervical lymph of the rabbit. *Am J Physiol* **240,** F329-36.

Bradbury MW & Westrop RJ (1983). Factors influencing exit of substances from cerebrospinal fluid into deep cervical lymph of the rabbit. *J Physiol* **339,** 519–534.

Brierley JB (1950). The penetration of particulate matter from the cerebrospinal fluid into the spinal ganglia, peripheral nerves, and perivascular spaces of the central nervous system. *J Neurol Neurosurg Psychiatry* **13,** 203–215.

Brightman MW (1968). The intracerebral movement of proteins injected into blood and cerebrospinal fluid of mice. *Prog Brain Res* **29,** 19–40.

Brightman MW (2002). The brain's interstitial clefts and their glial walls. *J Neurocytol* **31,** 595–603.

Brightman MW & Reese TS (1969). Junctions between intimately apposed cell membranes in the vertebrate brain. *J*

Cell Biol **40,** 648–677.

Brinker T, Stopa E, Morrison J & Klinge P (2014). A new look at cerebrospinal fluid circulation. *Fluids Barriers CNS* **11,** 10.

Brown DA & Wijdicks EFM (2017). *Decompressive craniectomy in acute brain injury*, 1st edn. Elsevier B.V. Available at: http://linkinghub.elsevier.com/retrieve/pii/B9780444636003000167.

Carare RO, Bernardes-Silva M, Newman TA, Page AM, Nicoll JAR, Perry VH & Weller RO (2008). Solutes, but not cells, drain from the brain parenchyma along basement membranes of capillaries and arteries: significance for cerebral amyloid angiopathy and neuroimmunology. *Neuropathol Appl Neurobiol* **34,** 131–144.

Chen RL, Athauda SBP, Kassem NA, Zhang Y, Segal MB & Preston JE (2005). Decrease of transthyretin synthesis at the blood-cerebrospinal fluid barrier of old sheep. *J Gerontol A Biol Sci Med Sci* **60,** 852–858.

Chen RL, Kassem NA, Sadeghi M & Preston JE (2008). Insulin-like growth factor-II uptake into choroid plexus and brain of young and old sheep. *J Gerontol A Biol Sci Med Sci* **63,** 141–148.

Chen RL, Sage EA, Dunn MJ, Wait R & Preston JE (2006). Optimising ovine cerebrospinal fluid preparation for two-dimensional gel electrophoresis. *Proteomics* **6,** 3170–3175.

Chen Y (2012). Organophosphate-induced brain damage: mechanisms, neuropsychiatric and neurological consequences, and potential therapeutic strategies. *Neurotoxicology* **33,** 391–400.

Choi D, Lee TH, Spinelli C, Chennakrishnaiah S, D'Asti E & Rak J (2017). Extracellular vesicle communication pathways as regulatory targets of oncogenic transformation. *Semin Cell Dev Biol* **67,** 11–22.

Cloyd MW & Low FN (1974). Scanning electron microscopy of the subarachnoid space in the dog. I. Spinal cord levels. *J Comp Neurol* **153,** 325–368.

Costanzo M & Zurzolo C (2013). The cell biology of prion-like spread of protein aggregates: mechanisms and implication in neurodegeneration. *Biochem J* **452,** 1–17.

Cserr HF (1974). Relationship between cerebrospinal fluid and interstitial fluid of brain. *Fed Proc* **33,** 2075–2078.

Cserr HF, Cooper DN & Milhorat TH (1977). Flow of cerebral interstitial fluid as indicated by the removal of extracellular markers from rat caudate nucleus. *Exp Eye Res* **25 Suppl,** 461–473.

Cserr HF, Cooper DN, Suri PK & Patlak CS (1981). Efflux of radiolabeled polyethylene glycols and albumin from rat brain. *Am J Physiol* **240,** F319-28.

Cserr HF, Depasquale M, Patlak CS & Pullen RG (1986). Convection of cerebral interstitial fluid and its role in brain volume regulation. *Ann N Y Acad Sci* **481,** 123–134.

Cserr HF & Ostrach LH (1974). Bulk flow of interstitial fluid after intracranial injection of blue dextran 2000. *Exp Neurol* **45,** 50–60.

Cserr HF & Patlak CS (1992). Secretion and bulk flow of interstitial fluid. In *Physiology and Pharmacology of the Blood-Brain Barrier*, ed. Bradbury MW, Handbook of Experimental Pharmacology, pp. 245–261. Springer-Verlag, Berlin Heidelberg. Available at: http://link.springer.com/10.1007/978-3-642-76894-1.

Cushing H (1914). Studies on the Cerebro-Spinal Fluid : I. Introduction. *J Med Res* **31,** 1–19.

Cutler RW, Deuel RK & Barlow CF (1967). Albumin exchange between plasma and cerebrospinal fluid. *Arch Neurol* **17,** 261–270.

Dandy WE (1919). Experimental hydrocephalus. *Ann Surg* **70,** 129–142.

Davson H ed. (1967). *Physiology of the cerebrospinal fluid*. Churchill, London.

Davson H, Kleeman CR & Levin E (1962). Quantitative studies of the passage of different substances out of the cerebrospinal fluid. *J Physiol* **161,** 126–142.

Davson H & Segal MB (1970). The effects of some inhibitors and accelerators of sodium transport on the turnover of 22Na in the cerebrospinal fluid and the brain. *J Physiol* **209,** 131–153.

Davson H & Segal MB (1995). *Phyioslogy of the CSF and Blood-Brain Barriers*, 1st edn.ed. Davson H & Segal MB.

CRC Press, Inc, Boca Raton.

Davson H, Welch K & Segal MB (1987). *Physiology and pathophysiology of the cerebrospinal fluid*. Churchill Livingstone, Edinburgh.

Deisenhammer F (2015). The History of Cerebrospinal Fluid. In *Cerebrospinal Fluid in Clinical Neurology*, ed. Deisenhammer F, Sellebjerg F, Teunissen C & Tumani H, pp. 3–16. Springer International Publishing, Cham. Available at: http://link.springer.com/10.1007/978-3-319-01225-4_1.

Deng YY, Shen FC, Xie D, Han QP, Fang M, Chen CB & Zeng HK (2016). Progress in Drug Treatment of Cerebral Edema. *Mini Rev Med Chem* **16,** 917–925.

Diem AK, MacGregor Sharp M, Gatherer M, Bressloff NW, Carare RO & Richardson G (2017). Arterial Pulsations cannot Drive Intramural Periarterial Drainage: Significance for Aβ Drainage. *Front Neurosci* **11,** 475.

Dilmen N (2005). MRI showing pulsation of CSF. Available at: https://commons.wikimedia.org/wiki/File:NPH_MRI_272_GILD.gif [Accessed October 2, 2017].

Ding F, O'donnell J, Xu Q, Kang N, Goldman N & Nedergaard M (2016). Changes in the composition of brain interstitial ions control the sleep-wake cycle. *Science (80-)* **352,** 550–555.

Dolman D, Drndarski S, Abbott NJ & Rattray M (2005). Induction of aquaporin 1 but not aquaporin 4 messenger RNA in rat primary brain microvessel endothelial cells in culture. *J Neurochem* **93,** 825–833.

Doran A et al. (2005). The impact of P-glycoprotein on the disposition of drugs targeted for indications of the central nervous system: evaluation using the MDR1A/1B knockout mouse model. *Drug Metab Dispos* **33,** 165–174.

Doubal FN, MacLullich AMJ, Ferguson KJ, Dennis MS & Wardlaw JM (2010). Enlarged Perivascular Spaces on MRI Are a Feature of Cerebral Small Vessel Disease. *Stroke* **41,** 450–454.

Dreha-Kulaczewski S, Joseph AA, Merboldt K-D, Ludwig H-C, Gärtner J & Frahm J (2015). Inspiration is the major regulator of human CSF flow. *J Neurosci* **35,** 2485–2491.

Dreier JP, Lemale CL, Kola V, Friedman A & Schoknecht K (2017). Spreading depolarization is not an epiphenomenon but the principal mechanism of the cytotoxic edema in various gray matter structures of the brain during stroke. *Neuropharmacology*; DOI: 10.1016/j.neuropharm.2017.09.027.

Dubocovich ML, Hudson RL, Sumaya IC, Masana MI & Manna E (2005). Effect of MT1 melatonin receptor deletion on melatonin-mediated phase shift of circadian rhythms in the C57BL/6 mouse. *J Pineal Res* **39,** 113–120.

Engelhardt B, Carare RO, Bechmann I, Flügel A, Laman JD & Weller RO (2016). Vascular, glial, and lymphatic immune gateways of the central nervous system. *Acta Neuropathol* **132,** 317–338.

Engelhardt B, Vajkoczy P & Weller RO (2017). The movers and shapers in immune privilege of the CNS. *Nat Immunol* **18,** 123–131.

Faber WM (1937). The nasal mucosa and the subarachnoid space. *Am J Anat* **62,** 121–148.

Fenstermacher JD & Patlak CS (1976). The Movements of Water and Solutes in the Brains of Mammals. In *Dynamics of Brain Edema*, ed. Pappius HM & Feindel W, pp. 87–94. Springer Berlin Heidelberg.

Földi M (1996). The brain and the lymphatic system (I). *Lymphology* **29,** 1–9.

Förster C (2008). Tight junctions and the modulation of barrier function in disease. *Histochem Cell Biol* **130,** 55–70.

Frederickson RG & Low FN (1969). Blood vessels and tissue space associated with the brain of the rat. *Am J Anat* **125,** 123–145.

Gaete PS, Lillo MA & Figueroa XF (2014). Functional role of connexins and pannexins in the interaction between vascular and nervous system. *J Cell Physiol* **229,** 1336–1345.

Gakuba C, Gaberel T, Goursaud S, Bourges J, D Palma C, Quenault A, de Lizarrondo SM, Vivien D & Gauberti M (2018). General anesthesia inhibits the activity of the "glymphatic system." *Theranostics* **8,** 710–722.

Galea I, Bechmann I & Perry VH (2007). What is immune privilege (not)? *Trends Immunol* **28,** 12–18.

Gess B, Sevimli S, Strecker J-K, Young P & Schäbitz W-R (2011). Sodium-Dependent Vitamin C Transporter 2

(SVCT2) Expression and Activity in Brain Capillary Endothelial Cells after Transient Ischemia in Mice. *PLoS One* **6,** e17139.

Ghersi-Egea JF, Finnegan W, Chen JL, Fenstermacher JD & Hospital HF (1996*a*). Rapid distribution of intraventricularly administered sucrose into cerebrospinal fluid cisterns via subarachnoid velae in rat. *Neuroscience* **75,** 1271–1288.

Ghersi-Egea JF, Gorevic PD, Ghiso J, Frangione B, Patlak CS & Fenstermacher JD (1996*b*). Fate of cerebrospinal fluid-borne amyloid beta-peptide: rapid clearance into blood and appreciable accumulation by cerebral arteries. *J Neurochem* **67,** 880–883.

Greenberg SM, Al-Shahi Salman R, Biessels GJ, van Buchem M, Cordonnier C, Lee J, Montaner J, Schneider JA, Smith EE, Vernooij M & Werring DJ (2014). Outcome markers for clinical trials in cerebral amyloid angiopathy. *Lancet Neurol* **13,** 419–428.

Griffoni C, Toni M, Spisni E, Bianco M, Santi S, Riccio M & Tomasi V (2003). The cellular prion protein: biochemistry, topology, and physiologic functions. *Cell Biochem Biophys* **38,** 287–304.

Gutiérrez AM, González E, Echevarría M, Hernández CS & Whittembury G (1995). The proximal straight tubule (PST) basolateral cell membrane water channel: selectivity characteristics. *J Membr Biol* **143,** 189–197.

Haj-Yasein NN, Vindedal GF, Eilert-Olsen M, Gundersen GA, Skare Ø, Laake P, Klungland A, Thorén AE, Burkhardt JM, Ottersen OP & Nagelhus EA (2011). Glial-conditional deletion of aquaporin-4 (Aqp4) reduces blood-brain water uptake and confers barrier function on perivascular astrocyte endfeet. *Proc Natl Acad Sci U S A* **108,** 17815–17820.

Hannocks M-J, Pizzo ME, Huppert J, Deshpande T, Abbott NJ, Thorne RG & Sorokin L (2018). Molecular characterization of perivascular drainage pathways in the murine brain. *J Cereb Blood Flow Metab* **38,** 669–686.

Van Harreveld A (1972). The Extracellular Space in the Vertebrate Central Nervous System. In *The Structure and Function of Nervous Tissue*, ed. Bourne, pp. 447–511. Elsevier. Available at: http://dx.doi.org/10.1016/B978-0-12-119284-6.50015-4.

Härtig W, Derouiche A, Welt K, Brauer K, Grosche J, Mäder M, Reichenbach A & Brückner G (1999). Cortical neurons immunoreactive for the potassium channel Kv3.1b subunit are predominantly surrounded by perineuronal nets presumed as a buffering system for cations. *Brain Res* **842,** 15–29.

Hladky SB & Barrand MA (2014). Mechanisms of fluid movement into, through and out of the brain: evaluation of the evidence. *Fluids Barriers CNS* **11,** 26.

Hladky SB & Barrand MA (2016). Fluid and ion transfer across the blood-brain and blood-cerebrospinal fluid barriers; a comparative account of mechanisms and roles. *Fluids Barriers CNS* **13,** 19.

Holmes BB & Diamond MI (2012). Cellular mechanisms of protein aggregate propagation. *Curr Opin Neurol* **25,** 721–726.

Holter KE, Kehlet B, Devor A, Sejnowski TJ, Dale AM, Omholt SW, Ottersen OP, Nagelhus EA, Mardal K-A & Pettersen KH (2017). Interstitial solute transport in 3D reconstructed neuropil occurs by diffusion rather than bulk flow. *Proc Natl Acad Sci U S A* **114,** 9894–9899.

Horstmann E & Meves H (1959). Die Feinstruktur des molekularen Rindengraues und ihre physiologische Bedeutung. *Zeitschrift für Zellforsch und Mikroskopische Anat* **49,** 569–604.

Hossmann KA (1976). Development and Resolution of Ischemic Brain Swelling. In *Dynamics of Brain Edema*, ed. Pappius HM & Feindel W, pp. 219–227. Springer Berlin Heidelberg.

Hrabetová S, Masri D, Tao L, Xiao F & Nicholson C (2009). Calcium diffusion enhanced after cleavage of negatively charged components of brain extracellular matrix by chondroitinase ABC. *J Physiol* **587,** 4029–4049.

Hsu Y, Tran M & Linninger AA (2015). Dynamic regulation of aquaporin-4 water channels in neurological disorders. *Croat Med J* **56,** 401–421.

Huang W-J, Chen W-W & Zhang X (2015). Prions mediated neurodegenerative disorders. *Eur Rev Med Pharmacol*

Sci **19,** 4028–4034.

Huber JD, Egleton RD & Davis TP (2001). Molecular physiology and pathophysiology of tight junctions in the blood-brain barrier. *Trends Neurosci* **24,** 719–725.

Iadecola C (2013). The Pathobiology of Vascular Dementia. *Neuron* **80,** 844–866.

Ichimura T, Fraser PAA & Cserr HF (1991). Distribution of extracellular tracers in perivascular spaces of the rat brain. *Brain Res* **545,** 103–113.

Iliff JJ, Lee H, Yu M, Feng T, Logan J, Nedergaard M & Benveniste H (2013). Brain-wide pathway for waste clearance captured by contrast-enhanced MRI. *J Clin Invest* **123,** 1299–1309.

Iliff JJ & Nedergaard M (2013). Is there a cerebral lymphatic system? *Stroke* **44,** S93-5.

Iliff JJ, Wang M, Liao Y, Plogg BA, Peng W, Gundersen GA, Benveniste H, Vates GE, Deane R, Goldman SA, Nagelhus EA & Nedergaard M (2012*a*). A paravascular pathway facilitates CSF flow through the brain parenchyma and the clearance of interstitial solutes, including amyloid β. *Sci Transl Med* **4,** 147ra111.

Iliff JJ, Wang M, Liao Y, Plogg BA, Peng W, Gundersen GA, Benveniste H, Vates GE, Deane R, Goldman SA, Nagelhus EA & Nedergaard M (2012*b*). A paravascular pathway facilitates CSF flow through the brain parenchyma and the clearance of interstitial solutes, including amyloid ?? *Sci Transl Med*; DOI: 10.1126/scitranslmed.3003748.

Inglese M, Bomsztyk E, Gonen O, Mannon LJ, Grossman RI & Rusinek H (2005). Dilated perivascular spaces: Hallmarks of mild traumatic brain injury. *Am J Neuroradiol* **26,** 719–724.

Janzen W (1961). The relationship between the perivascular and the subarachnoidal space. *Psychiatr Neurol Neurochir* **64,** 37–45.

Jessen NA, Munk ASF, Lundgaard I & Nedergaard M (2015). The Glymphatic System: A Beginner's Guide. *Neurochem Res*1–17.

Jin B-J, Smith AJ & Verkman AS (2016). Spatial model of convective solute transport in brain extracellular space does not support a "glymphatic" mechanism. *J Gen Physiol* **148,** 489–501.

Jones EG (1970). On the mode of entry of blood vessels into the cerebral cortex. *J Anat* **106,** 507–520.

Jung JS, Bhat R V, Preston GM, Guggino WB, Baraban JM & Agre P (1994). Molecular characterization of an aquaporin cDNA from brain: candidate osmoreceptor and regulator of water balance. *Proc Natl Acad Sci USA* **91,** 13052–13056.

Kalimo H, Fredriksson K, Nordborg C, Auer RN, Olsson Y & Johansson B (1986). The spread of brain oedema in hypertensive brain injury. *Med Biol* **64,** 133–137.

Kervezee L, Hartman R, van den Berg D-J, Shimizu S, Emoto-Yamamoto Y, Meijer JH & de Lange ECM (2014). Diurnal Variation in P-glycoprotein-Mediated Transport and Cerebrospinal Fluid Turnover in the Brain. *AAPS J* **16,** 1029–1037.

Kida S, Pantazis A & Weller RO (1993). CSF drains directly from the subarachnoid space into nasal lymphatics in the rat. Anatomy, histology and immunological significance. *Neuropathol Appl Neurobiol* **19,** 480–488.

Kinney JP, Spacek J, Bartol TM, Bajaj CL, Harris KM & Sejnowski TJ (2013). Extracellular sheets and tunnels modulate glutamate diffusion in hippocampal neuropil. *J Comp Neurol* **521,** 448–464.

Koh L, Zakharov A & Johnston M (2005). Integration of the subarachnoid space and lymphatics: is it time to embrace a new concept of cerebrospinal fluid absorption? *Cerebrospinal Fluid Res* **2,** 6.

Konsman JP, Tridon V & Dantzer R (2000). Diffusion and action of intracerebroventricularly injected interleukin-1 in the CNS. *Neuroscience* **101,** 957–967.

Korogod N, Petersen CCH & Knott GW (2015). Ultrastructural analysis of adult mouse neocortex comparing aldehyde perfusion with cryo fixation. *Elife* **4,** 1–17.

Krämer-Albers E-M & Hill AF (2016). Extracellular vesicles: interneural shuttles of complex messages. *Curr Opin Neurobiol* **39,** 101–107.

Krisch B, Leonhardt H & Oksche A (1983). The meningeal compartments of the median eminence and the cortex. A comparative analysis in the rat. *Cell Tissue Res* **228,** 597–640.

Krisch B, Leonhardt H & Oksche A (1984). Compartments and perivascular arrangement of the meninges covering the cerebral cortex of the rat. *Cell Tissue Res* **238,** 459–474.

Lai AY, Dorr A, Thomason LAM, Koletar MM, Sled JG, Stefanovic B & McLaurin J (2015). Venular degeneration leads to vascular dysfunction in a transgenic model of Alzheimer's disease. *Brain* **138,** 1046–1058.

Legros C, Chesneau D, Boutin JA, Barc C & Malpaux B (2014). Melatonin from cerebrospinal fluid but not from blood reaches sheep cerebral tissues under physiological conditions. *J Neuroendocrinol* **26,** 151–163.

Levin VA, Fenstermacher JD & Patlak CS (1970). Sucrose and inulin space measurements of cerebral cortex in four mammalian species. *Am J Physiol* **219,** 1528–1533.

Lochhead JJ, Wolak DJ, Pizzo ME & Thorne RG (2015). Rapid transport within cerebral perivascular spaces underlies widespread tracer distribution in the brain after intranasal administration. *J Cereb blood flow Metab* **35,** 371–381.

Louveau A, Smirnov I, Keyes TJ, Eccles JD, Rouhani SJ, Peske JD, Derecki NC, Castle D, Mandell JW, Lee KS, Harris TH & Kipnis J (2015). Structural and functional features of central nervous system lymphatic vessels. *Nature* **523,** 337–341.

Mathiisen TM, Lehre KP, Danbolt NC & Ottersen OP (2010). The perivascular astroglial sheath provides a complete covering of the brain microvessels: An electron microscopic 3D reconstruction. *Glia* **58,** 1094–1103.

Matsubara Y, Miyazaki O, Kosuga M, Okuyama T & Nosaka S (2017). Cerebral magnetic resonance findings during enzyme replacement therapy in mucopolysaccharidosis. *Pediatr Radiol*1–11.

McConnell H (1994). Historical Perspective. In *Cerebrospinal Fluid in Neurology and Psychiatry*, ed. McConnell H & Bianchine JR, pp. 1–4. Springer US, Boston, MA. Available at: http://link.springer.com/10.1007/978-1-4899-3372-0_1.

Mehta D & Malik AB (2006). Signaling mechanisms regulating endothelial permeability. *Physiol Rev* **86,** 279–367.

Merlini M, Wanner D & Nitsch RM (2016). Tau pathology-dependent remodelling of cerebral arteries precedes Alzheimer???s disease-related microvascular cerebral amyloid angiopathy. *Acta Neuropathol* **131,** 737–752.

Milhorat TH (1969). Choroid plexus and cerebrospinal fluid production. *Science* **166,** 1514–1516.

Morris AWJ, Sharp MM, Albargothy NJ, Fernandes R, Hawkes CA, Verma A, Weller RO & Carare RO (2016). Vascular basement membranes as pathways for the passage of fluid into and out of the brain. *Acta Neuropathol*; DOI: 10.1007/s00401-016-1555-z.

Muldoon LL, Alvarez JI, Begley DJ, Boado RJ, del Zoppo GJ, Doolittle ND, Engelhardt B, Hallenbeck JM, Lonser RR, Ohlfest JR, Prat A, Scarpa M, Smeyne RJ, Drewes LR & Neuwelt E a (2013). Immunologic privilege in the central nervous system and the blood–brain barrier. *J Cereb Blood Flow Metab* **33,** 13–21.

Murphy JB & Sturm E (1922). Homoplastic and heteroplastic tumor grafts in the brain. *JAMA J Am Med Assoc* **79,** 2159–2160.

Nag S, Manias JL & Stewart DJ (2009). Pathology and new players in the pathogenesis of brain edema. *Acta Neuropathol* **118,** 197–217.

Nedergaard M (2013). Neuroscience. Garbage truck of the brain. *Science* **340,** 1529–1530.

Nedergaard M & Goldman SA (2016). Brain drain. *Sci Am* **314,** 44–49.

Nicholson C & Phillips JM (1981). Ion diffusion modified by tortuosity and volume fraction in the extracellular microenvironment of the rat cerebellum. *J Physiol* **321,** 225–257.

Nicholson C & Tao L (1993). Hindered diffusion of high molecular weight compounds in brain extracellular microenvironment measured with integrative optical imaging. *Biophys J* **65,** 2277–2290.

Nielsen S, Nagelhus EA, Amiry-Moghaddam M, Bourque C, Agre P & Ottersen OP (1997). Specialized membrane domains for water transport in glial cells: high-resolution immunogold cytochemistry of aquaporin-4 in rat brain.

J Neurosci **17,** 171–180.

Nilsson C, Ståhlberg F, Thomsen C, Henriksen O, Herning M & Owman C (1992). Circadian variation in human cerebrospinal fluid production measured by magnetic resonance imaging. *Am J Physiol* **262,** R20-4.

Nualart F (2014). Vitamin C Transporters, Recycling and the Bystander Effect in the Nervous System: SVCT2 versus Gluts. *J Stem Cell Res Ther*; DOI: 10.4172/2157-7633.1000209.

Ohata K & Marmarou A (1992). Clearance of brain edema and macromolecules through the cortical extracellular space. *J Neurosurg* **77,** 387–396.

Ohata K, Marmarou A & Povlishock JT (1990). An immunocytochemical study of protein clearance in brain infusion edema. *Acta Neuropathol* **81,** 162–177.

Oldendorf WH & Davson H (1967). Brain extracellular space and the sink action of cerebrospinal fluid. Measurement of rabbit brain extracellular space using sucrose labeled with carbon 14. *Arch Neurol* **17,** 196–205.

Papadopoulos MC, Manley GT, Krishna S & Verkman AS (2004). Aquaporin-4 facilitates reabsorption of excess fluid in vasogenic brain edema. *Faseb J* **18,** 1291–1293.

Patlak CS & Fenstermacher JD (1975). Measurements of dog blood-brain transfer constants by ventriculocisternal perfusion. *Am J Physiol* **229,** 877–884.

Peters A, Palay SSL & Webster H deF. (1991). *The fine structure of the nervous system: neurons and their supporting cells*, 3rd edn. Oxford University Press, New York. Available at: http://openurl.ingenta.com/content/xref?genre=article&issn=0963-6897&volume=20&issue=11&spage=1659.

Pizzo ME & Thorne RG (2017). The extracellular and perivascular spaces of the brain. In *Brain Edema: From Molecular Mechanisms to Clinical Practice*, 1st edn., ed. Badaut J & Plesnila N, pp. 103–128. Academic Press. Available at: https://www.elsevier.com/books/brain-edema/badaut/978-0-12-803196-4.

Pizzo ME, Wolak DJ, Kumar NN, Brunette E, Brunnquell CL, Hannocks M-J, Abbott NJ, Meyerand ME, Sorokin L, Stanimirovic DB & Thorne RG (2018). Intrathecal antibody distribution in the rat brain: surface diffusion, perivascular transport and osmotic enhancement of delivery. *J Physiol* **596,** 445–475.

Pollay M & Curl F (1967). Secretion of cerebrospinal fluid by the ventricular ependyma of the rabbit. *Am J Physiol* **213,** 1031–1038.

Prell GD, Khandelwal JK, Burns RS & Green JP (1989). Diurnal fluctuation in levels of histamine metabolites in cerebrospinal fluid of rhesus monkey. *Agents Actions* **26,** 279–286.

Preston SD, Steart P V., Wilkinson A, Nicoll J a R & Weller RO (2003). Capillary and arterial cerebral amyloid angiopathy in Alzheimer's disease: defining the perivascular route for the elimination of amyloid beta from the human brain. *Neuropathol Appl Neurobiol* **29,** 106–117.

Proescholdt MG, Hutto B, Brady LS & Herkenham M (2000). Studies of cerebrospinal fluid flow and penetration into brain following lateral ventricle and cisterna magna injections of the tracer [14C]inulin in rat. *Neuroscience* **95,** 577–592.

Puvenna V, Engeler M, Banjara M, Brennan C, Schreiber P, Dadas A, Bahrami A, Solanki J, Bandyopadhyay A, Morris JK, Bernick C, Ghosh C, Rapp E, Bazarian JJ & Janigro D (2016). Is phosphorylated tau unique to chronic traumatic encephalopathy? Phosphorylated tau in epileptic brain and chronic traumatic encephalopathy. *Brain Res* **1630,** 225–240.

Rall DP, Oppelt WW & Patlak CS (1962). Extracellular space of brain as determined by diffusion of inulin from the ventricular system. *Life Sci* **1,** 43–48.

Rapoport SI, Schapiro MB & May C (2004). Reduced brain delivery of homovanillic acid to cerebrospinal fluid during human aging. *Arch Neurol* **61,** 1721–1724.

Reina MA, De León Casasola ODL, Villanueva MC, López A, Machés F & De Andrés JA (2004). Ultrastructural findings in human spinal pia mater in relation to subarachnoid anesthesia. *Anesth Analg* **98,** 1479–1485.

Reiter RJ, Tan DX, Kim SJ & Cruz MHC (2014). Delivery of pineal melatonin to the brain and SCN: role of canaliculi, cerebrospinal fluid, tanycytes and Virchow–Robin perivascular spaces. *Brain Struct Funct* **219,** 1873–1887.

Rennels ML, Gregory TF, Blaumanis OR, Fujimoto K & Grady PA (1985). Evidence for a "paravascular" fluid circulation in the mammalian central nervous system, provided by the rapid distribution of tracer protein throughout the brain from the subarachnoid space. *Brain Res* **326,** 47–63.

Di Rocco C, McLone DG, Shimoji T & Raimondi a J (1975). Continuous intraventricular cerebrospinal fluid pressure recording in hydrocephalic children during wakefulness and sleep. *J Neurosurg* **42,** 683–689.

Rosenberg GA, Kyner WT & Estrada E (1980). Bulk flow of brain interstitial fluid under normal and hyperosmolar conditions. *Am J Physiol* **238,** F42–F49.

Schielke GP & Betz AL (1992). Electrolyte Transport. In *Physiology and Pharmacology of the Blood-Brain Barrier*, ed. Bradbury MWB, pp. 221–243. Springer-Verlag Berlin Heidelberg. Available at: http://www.springerlink.com/index/10.1007/978-3-642-76894-1_8.

Schwartz WJ & Reppert SM (1985). Neural regulation of the circadian vasopressin rhythm in cerebrospinal fluid: a pre-eminent role for the suprachiasmatic nuclei. *J Neurosci* **5,** 2771–2778.

Seckl J & Lightman S (1988). Cerebrospinal fluid neurohypophysial peptides in benign intracranial hypertension. *J Neurol Neurosurg Psychiatry* **51,** 1538–1541.

Serrano-Pozo A, Frosch MP, Masliah E & Hyman BT (2011*a*). Neuropathological alterations in Alzheimer disease. *Cold Spring Harb Perspect Med* **1,** a006189.

Serrano-Pozo A, Frosch MP, Masliah E & Hyman BT (2011*b*). Neuropathological alterations in Alzheimer disease. *Cold Spring Harb Perspect Med* **1,** a006189.

Shirai Y (1921). On the transplantation of the rat sarcoma in adult heterogeneous animals. *Japan Med World* **1,** 14–15.

Shively SB, Horkayne-Szakaly I, Jones R V., Kelly JP, Armstrong RC & Perl DP (2016). Characterisation of interface astroglial scarring in the human brain after blast exposure: a post-mortem case series. *Lancet Neurol* **15,** 944–953.

Silverberg GD, Heit G, Huhn S, Jaffe RA, Chang SD, Bronte-Stewart H, Rubenstein E, Possin K & Saul TA (2001). The cerebrospinal fluid production rate is reduced in dementia of the Alzheimer's type. *Neurology* **57,** 1763–1766.

Sixt M, Engelhardt B, Pausch F, Hallmann R, Wendler O & Sorokin LM (2001). Endothelial cell laminin isoforms, laminins 8 and 10, play decisive roles in T cell recruitment across the blood-brain barrier in experimental autoimmune encephalomyelitis. *J Cell Biol* **153,** 933–945.

Skinner DC & Malpaux B (1999). High melatonin concentrations in third ventricular cerebrospinal fluid are not due to Galen vein blood recirculating through the choroid plexus. *Endocrinology* **140,** 4399–4405.

Slats D, Claassen JAHR, Spies PE, Borm G, Besse KTC, van Aalst W, Tseng J, Sjögren MJC, Olde Rikkert MGM & Verbeek MM (2012). Hourly variability of cerebrospinal fluid biomarkers in Alzheimer's disease subjects and healthy older volunteers. *Neurobiol Aging* **33,** 831.e1-9.

Smith AJ, Jin B & Verkman AS (2015). Muddying the water in brain edema ? *Trends Neurosci*1–2.

Smith AJ, Yao X, Dix JA, Jin B & Verkman AS (2017). Test of the "glymphatic" hypothesis demonstrates diffusive and aquaporin-4-independent solute transport in rodent brain parenchyma. *Elife*; DOI: 10.7554/eLife.27679.

Sotiriou S, Gispert S, Cheng J, Wang Y, Chen A, Hoogstraten-Miller S, Miller GF, Kwon O, Levine M, Guttentag SH & Nussbaum RL (2002). Ascorbic-acid transporter Slc23a1 is essential for vitamin C transport into the brain and for perinatal survival. *Nat Med* **8,** 514–517.

Spector R (2014). Vitamin transport diseases of brain: Focus on folates, thiamine and riboflavin. *Brain Disord Ther* **3,** 120.

Spector R & Johanson CE (2014). The nexus of vitamin homeostasis and DNA synthesis and modification in mammalian brain. *Mol Brain* **7,** 3.

Spector R, Keep RF, Snodgrass SR, Smith QR & Johanson CE (2015). A balanced view of choroid plexus structure and function: Focus on adult humans. *Exp Neurol* **267,** 78–86.

Stevenson PG, Hawke S, Sloan DJ & Bangham CR (1997). The immunogenicity of intracerebral virus infection depends on anatomical site. *J Virol* **71,** 145–151.

Strbian D, Kovanen PT, Karjalainen-Lindsberg M-L, Tatlisumak T & Lindsberg PJ (2009). An emerging role of mast cells in cerebral ischemia and hemorrhage. *Ann Med* **41,** 438–450.

Stylianopoulou F, Herbert J, Soares MB & Efstratiadis A (1988). Expression of the insulin-like growth factor II gene in the choroid plexus and the leptomeninges of the adult rat central nervous system. *Proc Natl Acad Sci U S A* **85,** 141–145.

Sweetman B & Linninger AA (2011). Cerebrospinal fluid flow dynamics in the central nervous system. *Ann Biomed Eng* **39,** 484–496.

Syková E & Nicholson C (2008). Diffusion in brain extracellular space. *Physiol Rev* **88,** 1277–1340.

Szentistványi I, Patlak CS, Ellis RA & Cserr HF (1984). Drainage of interstitial fluid from different regions of rat brain. *Am J Physiol* **246,** 35–44.

Taipale J & Keski-Oja J (1997). Growth factors in the extracellular matrix. *FASEB J* **11,** 51–59.

Tan DX, Manchester LC & Reiter RJ (2016). CSF generation by pineal gland results in a robust melatonin circadian rhythm in the third ventricle as an unique light/dark signal. *Med Hypotheses* **86,** 3–9.

Tasker RC & Acerini CL (2014). Cerebral edema in children with diabetic ketoacidosis: vasogenic rather than cellular? *Pediatr Diabetes* **15,** 261–270.

Thal DR, Grinberg LT & Attems J (2012). Vascular dementia: Different forms of vessel disorders contribute to the development of dementia in the elderly brain. *Exp Gerontol* **47,** 816–824.

Thorne RG (2014). Primer on Central Nervous System Structure/Function and the Vasculature, Ventricular System, and Fluids of the BRain. In *Drug Delivery to the Brain: Physiological Concepts, Methodologies, and Approaches*, ed. Hammarlund-Udenaes M, de Lange E & Thorne RG, pp. 685–707. Springer-Verlag, New York.

Thorne RG, Hrabetová S & Nicholson C (2004*a*). Diffusion of epidermal growth factor in rat brain extracellular space measured by integrative optical imaging. *J Neurophysiol* **92,** 3471–3481.

Thorne RG, Lakkaraju A, Rodriguez-Boulan E & Nicholson C (2008). In vivo diffusion of lactoferrin in brain extracellular space is regulated by interactions with heparan sulfate. *Proc Natl Acad Sci USA* **105,** 8416–8421.

Thorne RG & Nicholson C (2006). In vivo diffusion analysis with quantum dots and dextrans predicts the width of brain extracellular space. *Proc Natl Acad Sci USA* **103,** 5567–5572.

Thorne RG, Pronk GJ, Padmanabhan V & Frey WH (2004*b*). Delivery of insulin-like growth factor-I to the rat brain and spinal cord along olfactory and trigeminal pathways following intranasal administration. *Neuroscience* **127,** 481–496.

Tietz S & Engelhardt B (2015). Brain barriers: Crosstalk between complex tight junctions and adherens junctions. *J Cell Biol* **209,** 493–506.

Tricoire H, Locatelli A, Chemineau P & Malpaux B (2002). Melatonin enters the cerebrospinal fluid through the pineal recess. *Endocrinology* **143,** 84–90.

Valdinocci D, Radford RAW, Siow SM, Chung RS & Pountney DL (2017). Potential Modes of Intercellular α-Synuclein Transmission. *Int J Mol Sci*; DOI: 10.3390/ijms18020469.

Wagner HJ, Pilgrim C & Brandl J (1974). Penetration and removal of horseradish peroxidase injected into the cerebrospinal fluid: Role of cerebral perivascular spaces, endothelium and microglia. *Acta Neuropathol* **27,** 299–315.

Weed L (1914). Studies on Cerebro-Spinal Fluid. No. IV : The dual Source of Cerebro-Spinal Fluid. *J Med Res* **31,** 93–118.

Welch K (1963). Secretion of cerebrospinal fluid by choroid plexus of the rabbit. *Am J Physiol* **205,** 617–624.

Weller RO, Kida S & Zhang ET (1992). Pathways of fluid drainage from the brain--morphological aspects and immunological significance in rat and man. *Brain Pathol* **2,** 277–284.

Weller RO, Subash M, Preston SD, Mazanti I & Carare RO (2008). Perivascular drainage of amyloid-beta peptides from the brain and its failure in cerebral amyloid angiopathy and Alzheimer's disease. *Brain Pathol* **18,** 253–266.

Winkler EA, Minter D, Yue JK & Manley GT (2016). Cerebral Edema in Traumatic Brain Injury: Pathophysiology and Prospective Therapeutic Targets. *Neurosurg Clin N Am* **27,** 473–488.

Wolak DJ, Pizzo ME & Thorne RG (2015). Probing the extracellular diffusion of antibodies in brain using in vivo integrative optical imaging and ex vivo fluorescence imaging. *J Control Release* **197,** 78–86.

Wolak DJ & Thorne RG (2013). Diffusion of macromolecules in the brain: implications for drug delivery. *Mol Pharm* **10,** 1492–1504.

Woollam DHM & Millen JW (1954). Perivascular spaces of the mammalian central nervous system. *Biol Rev* **29,** 251–283.

Wu C, Ivars F, Anderson P, Hallmann R, Vestweber D, Nilsson P, Robenek H, Tryggvason K, Song J, Korpos E, Loser K, Beissert S, Georges-Labouesse E & Sorokin LM (2009). Endothelial basement membrane laminin alpha5 selectively inhibits T lymphocyte extravasation into the brain. *Nat Med* **15,** 519–527.

Xie L, Kang H, Xu Q, Chen MJ, Liao Y, Thiyagarajan M, O'Donnell J, Christensen DJ, Nicholson C, Iliff JJ, Takano T, Deane R & Nedergaard M (2013). Sleep drives metabolite clearance from the adult brain. *Science* **342,** 373–377.

Yao X, Hrabetova S, Nicholson C & Manley GT (2008). Aquaporin-4-Deficient Mice Have Increased Extracellular Space without Tortuosity Change. *J Neurosci* **28,** 5460–5464.

Zabel MD & Reid C (2015). A brief history of prions. *Pathog Dis* **73,** ftv087.

Zafeiriou DI & Batzios SP (2013). Brain and spinal MR imaging findings in mucopolysaccharidoses: A review. *Am J Neuroradiol* **34,** 5–13.

Zervas NT, Liszczak TM, Mayberg MR & Black PM (1982). Cerebrospinal fluid may nourish cerebral vessels through pathways in the adventitia that may be analogous to systemic vasa vasorum. *J Neurosurg* **56,** 475–481.

Zhang ET, Inman CB & Weller RO (1990). Interrelationships of the pia mater and the perivascular (Virchow-Robin) spaces in the human cerebrum. *J Anat* **170,** 111–123.

del Zoppo GJ & Milner R (2006). Integrin-matrix interactions in the cerebral microvasculature. *Arterioscler Thromb Vasc Biol* **26,** 1966–1975.

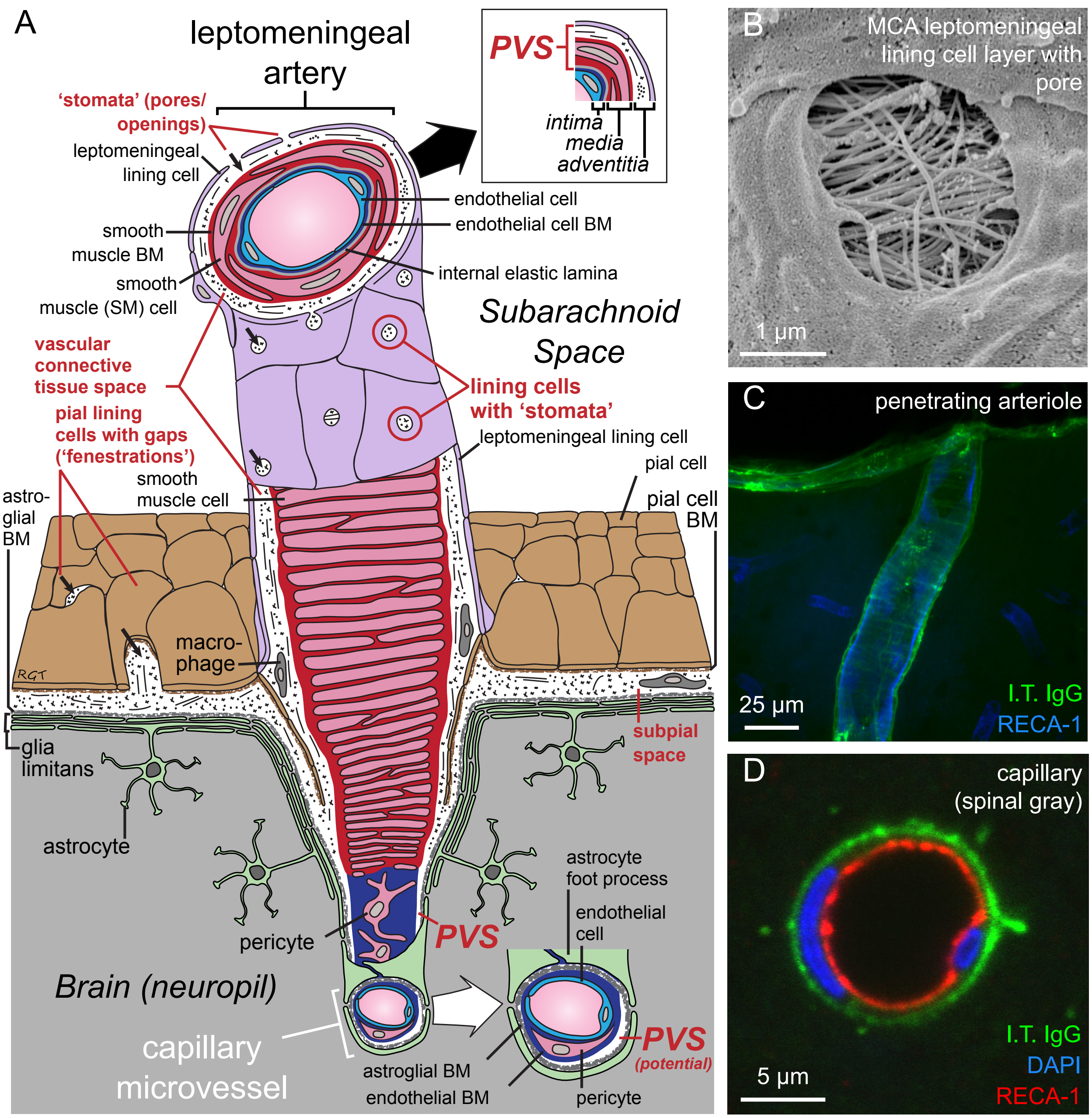

Figure 1. The perivascular space (PVS). (A) Schematic depicting a leptomeningeal artery in the subarachnoid space as it penetrates into the brain parenchyma (neuropil), with a gradually thinning smooth muscle cell layer (tunica media) and narrowing lumen diameter. Smooth muscle cells become sparser as vessel size decreases, with capillary microvessels characterized by a small lumen, pericytes and a basal lamina originating mainly from capillary endothelial cells and astrocytes. Key locations of potential CSF and ISF exchange are labelled with red text: (i) stomata / pores present on the CSF-facing leptomeningeal lining cells that have been identified

on the outer surfaces of arteries in the subarachnoid space, (ii) fenestrations / gaps / clefts on the CSF-facing pial lining cells of the brain surface, and (iii) the PVS, a fluid compartment within the outer walls of blood vessels that includes the vascular connective tissue space of the arterial/arteriolar adventitia, the basement membrane (BM) surrounding smooth muscle cells in the tunica media, and potentially extends all the way down to a pericapillary fluid space between astroglial and endothelial BM of microvessels. Veins/venules are not depicted. (B) Scanning electron micrographs show the existence of numerous pores/openings termed 'stomata' on the outer leptomeningeal sheaths of blood vessels in the subarachnoid space. Shown: Middle cerebral artery (MCA) leptomeningeal surface (rat) exhibiting a micron-sized pore with noticeably dense, underlying perivascular fibres in the vascular connective tissue space (see (Pizzo et al., 2018)). (C-D) Fluorescently labelled non-targeted immunoglobulin G (IgG) antibodies intrathecally (I.T.) infused at a low flow rate (80 μL applied cisternally over 50 min) reveal prominent perivascular signal along all vessel types in the rat, including cortical penetrating arterioles and numerous microvessels (shown). RECA-1, rat endothelial cell antigen-1 (endothelial cell marker) (D adapted from (Pizzo et al., 2018)).

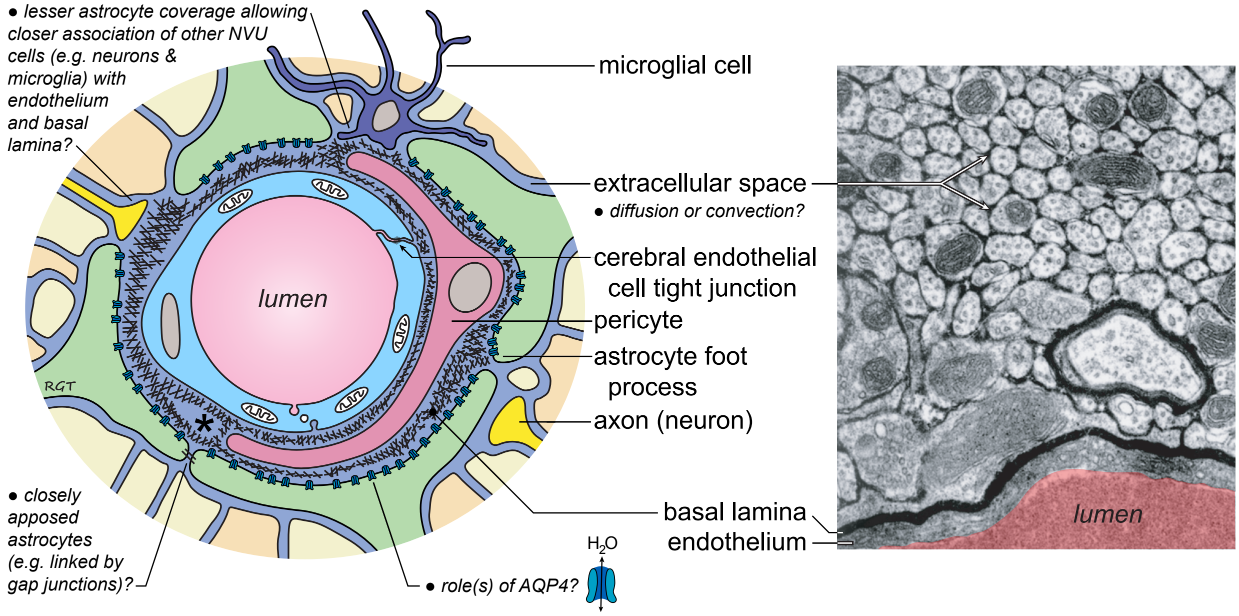

Figure 2. The neurovascular unit (NVU). The NVU refers to the monolayer of brain endothelial cells making up CNS blood vessels (and smooth muscle cells for larger calibre vessels), their associated neurons, and the numerous non-neuronal cells (e.g., pericytes, astrocytes, and microglia), extracellular matrix and basement membranes that surround them; our understanding of the NVU and the details of the extensive coupling, association, and regulation that exists between NVU components remains a highly active area of investigation. Key questions (bulleted text) include the degree of astrocyte coverage (e.g., are adjacent astrocyte foot processes nearly always closely situated or do larger gaps exist to allow more intimate association of neurons, microglia and other cells with the endothelial cell and its associated extracellular matrix?), the roles subserved by aquaporin-4 (AQP4) water channels highly expressed on astrocytic endfeet, the normal mode of fluid/tracer transport in the extracellular space, and whether a pericapillary fluid space normally exists in the basal lamina (indicated with an asterisk). See text for discussion. The transmission electron micrograph (right) illustrates the extensive distribution of 40 kDa horseradish peroxidase through the extracellular space and the basal lamina of a cerebral blood vessel following intraventricular administration (adapted from (Brightman, 2002) with permission).

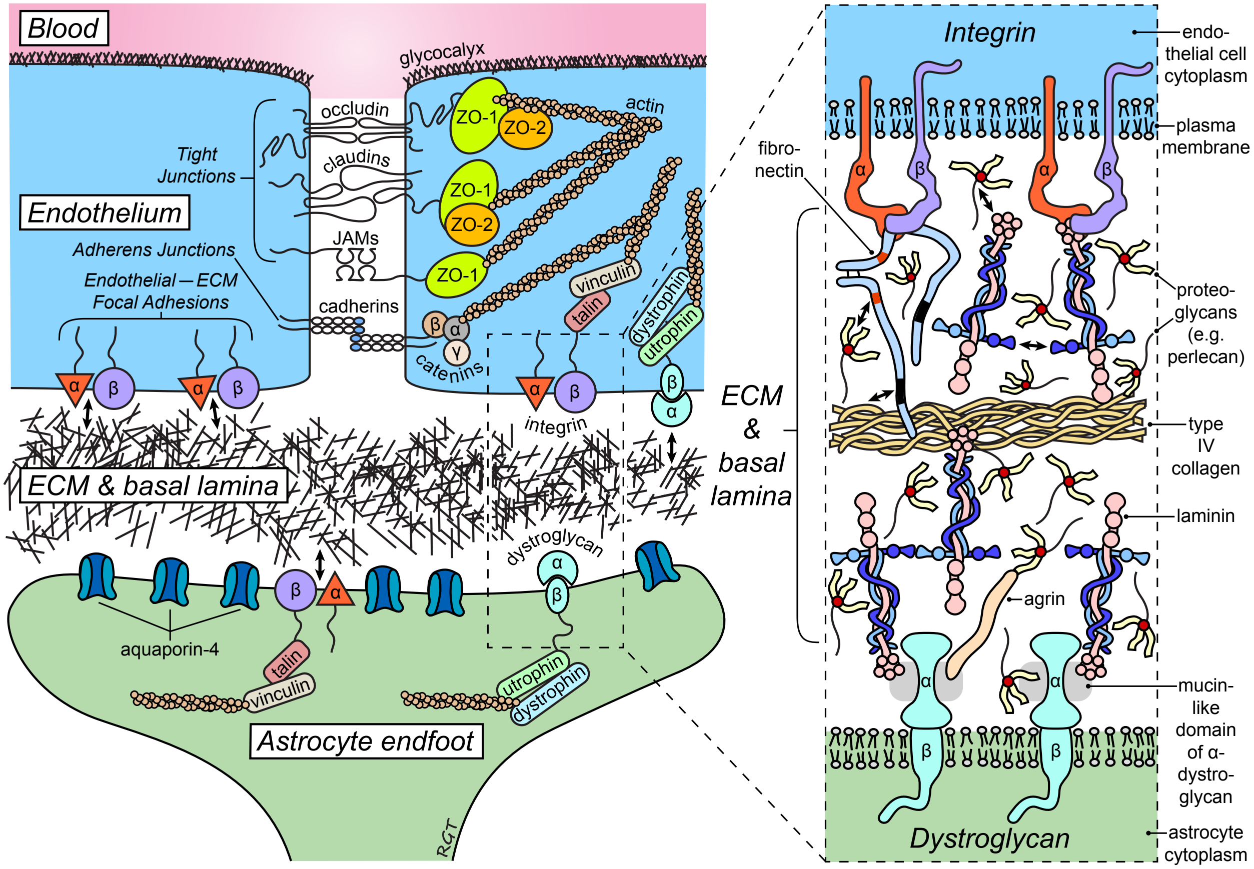

Figure 3. Junctions and adhesions of the blood-brain barrier (BBB) and cerebral microvessel basal lamina. Several different tight junction proteins restrict and regulate paracellular diffusion as well as the diffusion of membrane components between the luminal and abluminal compartments of polarized endothelial cells; these include occludin, claudins-3, -5, and -12, zonula occludens-1 (ZO-1) and -2 (ZO-2), and various junctional adhesion molecules (JAMs), all of which also participate in complex linkages with the actin cytoskeleton that allow endothelial cells to sense and respond to internal and external forces. Adherens junctions consisting of vascular endothelial cadherins and associated intracellular scaffold proteins such as the catenins regulate cell-cell contacts and tensile forces through additional linkages with the actin cytoskeleton. Interactions of endothelial cells (and astrocytes) with components of the extracellular matrix (ECM) and basal lamina are facilitated by integrins, αβ heterodimeric receptors that bind extracellularly to laminins and fibronectin to link the ECM to the cytoskeleton, and dystroglycan, a complex of α and β subunits that binds to laminins, agrin, and perlecan to provide additional links of the ECM to

the cytoskeleton. Numerous additional linkages within the ECM and basal lamina occur between laminins, proteoglycans, fibronectin, and type IV collagen (arrows), among others. Adapted from (Huber et al., 2001; Barresi & Campbell, 2006; del Zoppo & Milner, 2006; Strbian et al., 2009) with additional information incorporated from (Abbott et al., 2006; Mehta & Malik, 2006; Förster, 2008; Tietz & Engelhardt, 2015).

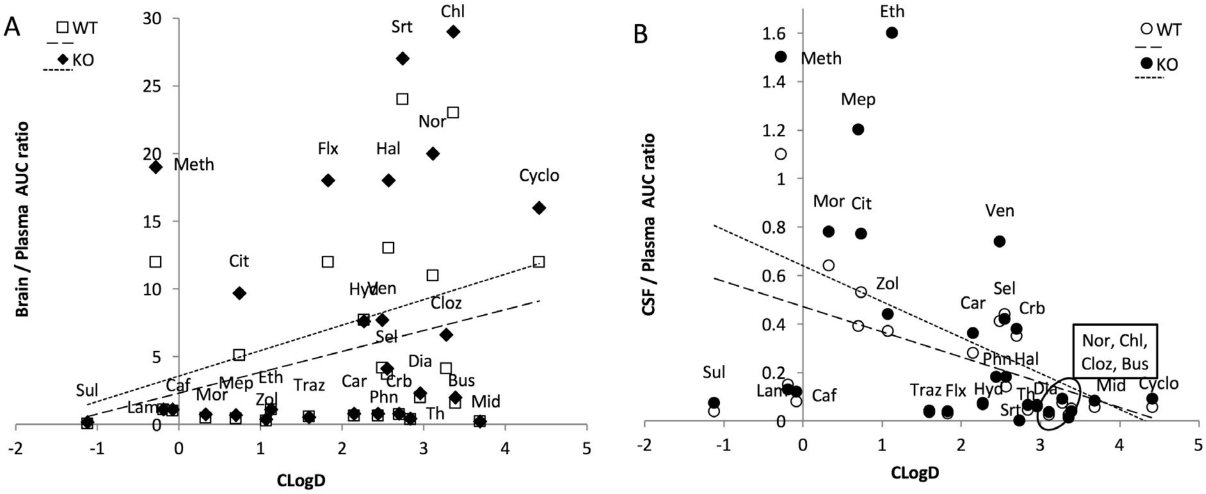

Figure 4. Brain/plasma (a) and CSF/plasma (b) AUC ratios for CNS-active agents plotted against their CLogD values, in Female FVB (WT) and mdr1a$^{-/-}$ /1b$^{-/-}$ (KO) mice. Re-analysis of data from Doran *et al.* (Doran *et al.*, 2005). Mice were administered with 3 mg/kg drug s.c. (5 mg/kg caffeine) then brain, CSF and plasma taken at 0.5, 1, 2.5, or 5 h post-dose. Drug analysis was by HPLC/mass spectrometry, yielding the area under the curve (AUC). For this analysis, drugs with weak P-glycoprotein interaction (brain uptake KO : WT ratio <2), were selected from the original data set of 33 compounds, *n* = 5 mice per genotype per time point. The inverse correlation between CSF/plasma ratio and drug lipid solubility CLogD (b) shows the most lipid soluble drugs had the smallest distribution in CSF in both WT and KO mice (p<0.05). Lines represent linear regression analysis for (a) Brain/plasma; WT open squares, R^2 0.01, *p*=0.109; KO filled diamonds, R^2 0.09, *p*= 0.138 (b) CSF/plasma; WT open circles, R^2 0.158, *p*=0.040. KO filled circles, R^2 0.206, *p*=0.017 (df=26). Key: Bus Buspirone, Caf Caffeine, Car Carisoprodol, Chl Chlorpromazine, Cit Citalopram, Cloz Clozapine, Crb Carbamazepine, Cyclo Cyclobenzaprine, Dia Diazepam, Eth Ethosuximide, Flx Fluoxetine, Hal Haloperidol, Hyd Hydroxyzine, Lam Lamotrigine, Mep Meprobamate, Meth Methylphenidate, Mid Midazolam, Mor Morphine, Nor Nortriptyline, Phn Phenytoin, Sel Selegiline, Srt Sertraline, Sul Sulpiride, Th Thiopental, Traz Trazodone, Ven Venlafaxin, Zol Zolpidem.

CHAPTER 4
Perivascular access of intrathecal antibodies to the rat brain is receptor-mediated and is reduced in a model of glioma

Michelle E. Pizzo[1,2], Brynna Wilken-Resman[1], Gretchen Greene[1], Paul A Clark[3], John S Kuo[3-5], Robert G Thorne[6-8]
[1]School of Pharmacy, Division of Pharmaceutical Sciences, [2]Clinical Neuroengineering Training Program, [3]Department of Neurological Surgery; University of Wisconsin-Madison, Madison, Wisconsin, USA, [4]Carbone Cancer Center, [5]Center for Stem Cell and Regenerative Medicine; University of Wisconsin School of Medicine and Public Health, Madison, Wisconsin, USA; [6]Neuroscience Training Program; [7]Cellular and Molecular Pathology Graduate Program; [8]Institute for Clinical and Translational Research; University of Wisconsin-Madison

Abstract

Antibody-based therapeutics are being administered into the cerebrospinal fluid (CSF) for the treatment of central nervous system cancers in humans, despite a scarcity of data describing or demonstrating how these large macromolecules exchange with the brain tissue or how the presence of brain tumors impacts CSF-brain exchange. In the present study we investigated the transport of an intracisternally-infused, species-matched rat immunoglobulin G (IgG) into and out of the rat central nervous system. Coronal brain sections revealed superficial penetration at the brain-CSF interface that was characteristic of diffusion as well as remarkable access of rat IgG to the cerebral perivascular spaces. We hypothesized this widespread perivascular access may indicate a receptor-mediated shuttling of IgG into the perivascular spaces across leptomeningeal cells. We showed the perivascular entry of rat IgG could be competed off by a co-infusion of excess unlabeled rat IgG, which reduced the number of perivascular profiles by 2-3 fold across different brain regions, providing supporting evidence for receptor-mediated transport of IgG into the perivascular space. Infusion of rat IgG into tumor-bearing nude rats after implantation of human glioma cells revealed an absence of IgG within the tumor and up to a 5-fold reduction in the number of perivascular spaces accessed. This data provides critical new information regarding the importance of IgG species/receptor-binding capacity and highlights the severe impact that brain tumors have on the delivery and distribution of intrathecal antibodies within the central nervous system.

Introduction

A number of clinical trials are underway administering antibody therapeutics into the cerebrospinal fluid (CSF) for the treatment of central nervous system (CNS) cancer, particularly leptomeningeal disease and CNS lymphoma (clinicalstrials.gov; see Prologue Tables 1 and 2). However, preclinical work describing the precise CSF-to-brain distribution mechanisms and patterns, or the distribution expected in much larger human brains, is scarce (Pizzo *et al.*, 2018). Our recent study suggested that CSF-to-brain transport of non-targeted single-domain (4.5 nm) and full-length species-mismatched goat (10 nm) antibodies occurred via diffusion into the brain at brain-CSF interfaces and rapid transport along cerebral perivascular spaces. Prior experimental (Rall *et al.*, 1962; Levin *et al.*, 1970; Patlak & Fenstermacher, 1975; Nicholson & Phillips, 1981; Nicholson & Tao, 1993; Thorne *et al.*, 2004; Thorne & Nicholson, 2006; Thorne *et al.*, 2008; Wolak *et al.*, 2015*a*) and modeling (Jin *et al.*, 2016; Holter *et al.*, 2017) studies also suggested that transport within the brain's extracellular spaces was consistent with size-dependent Fickian diffusion, including at brain-CSF interfaces (Levin *et al.*, 1970; Patlak & Fenstermacher, 1975; Pizzo *et al.*, 2018) where molecules in the CSF can move directly into the neuropil. However, transport *within* cerebral perivascular spaces is relatively size-independent and occurs far more rapidly than can be explained by diffusion, suggesting it involves convective transport/bulk flow (reviewed in (Abbott, 2004)) or the recently proposed mechanism of dispersion/bulk mixing with no net directional flow (Asgari *et al.*, 2016). The perivascular space referred to here (Pizzo *et al.*, 2018; Hannocks *et al.*, 2018) is a mostly fluid space i) between the blood vessel wall and ensheathing leptomeningeal fibroblasts or ii) between the blood vessel wall and brain parenchyma (delineated by the perivascular glia limitans, formed by astrocyte end feet and their basement membrane); it also contains connective tissue (e.g., collagen) and perivascular macrophages and is analogous to the vessel tunica adventitia (see (Pizzo *et al.*, 2018)). It is possible that transport involves both this fluid space as well as surrounding basement membranes (Carare *et al.*, 2008; Morris *et al.*, 2016), which have recently been characterized (Hannocks *et al.*, 2018).

The perivascular transport pathway has been suggested to involve i) size-dependent entry into perivascular spaces from the CSF (Pizzo *et al.*, 2018), potentially via stomata in leptomeningeal fibroblasts that ensheath subarachnoid blood vessels (Zervas *et al.*, 1982; Pizzo *et al.*, 2018), intercellular gaps between leptomeningeal cells (Frederickson & Low, 1969; Jones, 1970; Cloyd & Low, 1974; Oda & Nakanishi, 1984), or openings in the pia mater (Frederickson & Low, 1969; Jones, 1970; Cloyd & Low, 1974) followed by ii) rapid, relatively size-independent transport along perivascular spaces via convection or dispersion (Abbott, 2004; Asgari *et al.*, 2016) to the level of the capillaries (Hannocks *et al.*, 2017; Pizzo *et al.*, 2018). Thus, we hypothesize that the ability of macromolecules in the CSF to access and rapidly distribute throughout the perivascular spaces, and subsequently diffuse into the brain parenchyma, will govern if therapeutic brain levels are achievable using CSF administration. However, there are a number of understudied factors that may impact perivascular/CNS transport including antibody binding to endogenous receptors and the presence of CNS tumors.

Immunoglobulin G (IgG) antibodies are produced by B lymphocytes and are composed of two antigen-binding fragments (Fab) and a crystallizable fragment (Fc)(See Prologue Fig. 1). The Fab domains impart the bivalent, selective, and potent binding affinity for antigens and the Fc domain imparts binding to Fc receptors (Woof & Burton, 2004; Holliger & Hudson, 2005; Abbas *et al.*, 2015). IgG binding to Fcγ receptors on the cell surface (at physiological pH) to modulate effector functions, e.g., stimulation of phagocytosis by macrophages, activation of neutrophils, or natural killer cell-mediated antibody dependent cell toxicity (Ravetch & Bolland, 2001). The neonatal Fc receptor, FcRn, is involved in IgG recycling (e.g., IgG is rescued by FcRn in endothelial cells gives IgG its characteristically long systemic half-life) and IgG transcytosis (e.g., IgG is transported across syncytiotrophoblasts from maternal circulation to fetal circulation to confer immunity). FcRn binds IgG at an acidic pH (<6.5), i.e., in mucus layers or in the acidified endosome (Roopenian & Akilesh, 2007). Previous reports have described CNS expression of Fcγ receptors on leptomeningeal cells, perivascular cells (macrophages), and choroid plexus cells (stromal (macrophages) and epithelial) (Nyland, 1982; Peress *et al.*, 1989) and expression of FcRn on brain endothelial cells and choroid plexus epithelial cells (Schlachetzki *et al.*, 2002; Latvala *et al.*, 2017) but their precise localization in the brain and comprehensive functions are still unclear. The distribution of these receptors at CSF interfaces suggests a physiological role at these sites (Peress *et al.*, 1989). It is currently poorly understood how antibody binding to endogenous receptors in the brain could impact CSF-to-brain distribution, but this critical information could help guide antibody engineering and delivery strategies in pre-clinical and clinical studies.

Pathological changes in the brain are also likely to impact circulation of CSF and perivascular transport of CSF-borne molecules, as has been suggested in Alzheimer's disease/cerebral amyloid angiopathy (Hawkes *et al.*, 2011; Arbel-Ornath *et al.*, 2013), traumatic brain injury (Iliff *et al.*, 2014), stroke (Arbel-Ornath *et al.*, 2013); altered transport is also observed with different apolipoprotein E isoforms (Hawkes *et al.*, 2012) and with aging (Hawkes *et al.*, 2013; Kress *et al.*, 2014). However, the effect of brain tumors on the distribution of macromolecules from the CSF into the brain has not yet been studied, despite its clear relevance for ongoing clinical trials. It is likely that changes to the central compartment with CNS cancer—structural changes in the meninges or perivascular spaces, altered pressure differentials, blood-brain barrier disruption, and/or altered receptor expression—could induce vastly different CSF-to-brain macromolecule distributions; understanding potential causes for altered distribution may allow for significantly improved delivery strategies.

In the present study, we investigated the distribution of intrathecally-administered, fluorescently-labeled rat IgG in the normal rat brain or in a model of primary brain cancer using qualitative and quantitative *ex vivo* florescence microscopy techniques. Rat IgG showed surprisingly exceptional access to the cerebral perivascular spaces, despite the somewhat limited access of an identically-sized goat IgG to the perivascular spaces using the same infusion paradigm (Pizzo *et al.*, 2018). We hypothesized that endogenous Fc receptor expression at leptomeningeal sites shuttles IgG from the CSF into the perivascular spaces, likely for the purpose of immune surveillance; this was supported by competition experiments which showed an excess of unlabeled IgG could impede labeled IgG from accessing perivascular spaces. Intrathecal infusion of rat IgG into tumor-bearing nude rats intracranially-implanted with human U87 malignant glioma cells showed a lack of IgG delivery to the tumor and a significant reduction in perivascular space access, even at distant sites from the tumor. These results highlight the importance of understanding mechanisms of CNS transport for macromolecules, reveal the impact of antibody-receptor interactions, and demonstrate how pathology can disrupt macromolecule drug delivery.

Materials and Methods

Animal use

Experiments were carried out at the University of Wisconsin-Madison in accordance with the National Institutes of Health Guide for the Care and Use of Laboratory Animals (2011) and local Institutional Animal Care and Use Committee regulations. Rats were housed in a climate-controlled room under a 12:12 h light/dark cycle and had access to food and water *ad libitum*. Every effort was made to minimize pain and distress of the animals. Female Sprague-Dawley rats (180-240 g; approximately 9-14 weeks of age; Harlan/Envigo, Indianapolis, IN) were used for normal animal experiments and male athymic nude rats (200-300 g, approximately 2 months of age, Hsd:RH-*Foxn1*^{rnu}; Envigo, Indianapolis, IN) were used for glioma studies.

U87 cell culture

Standard serum conditions were used to maintain the U87 glioma cell line (growth medium: DMEM, 10% fetal bovine serum, 1% antibiotics), maintained in cell culture incubator at 37°C and 5% CO_2. Cells were passaged upon approximately 70% confluency using Accutase (Clark *et al.*, 2012; Zorniak *et al.*, 2012).

Glioma cell implantation

Orthotopic brain xenografts were initiated as previously described (Clark *et al.*, 2012; Zorniak *et al.*, 2012). Briefly, U87 glioma cells were enzymatically dissociated to single cells and 10^6 cells were suspended in 5 μL of growth medium. Nude rats were anesthetized with isoflurane and placed in a stereotaxic frame in the flat skull position. The skull was exposed by a midline cranial incision and a burr hole drilled in the skull without disrupting the dura; the dura was then punctured so as not to deflect the injection needle. Using a 5 μL Hamilton syringe with a 26 GA needle, glioma cells were stereotactically implanted into the right striatum at 1 μl/min at the following coordinates referenced from bregma: 0 mm antero-posterior, +3.5 mm medio-lateral, and -4.5 mm dorso-ventral. The needle was left in place in the brain for 3 minutes before being slowly withdrawn and the burr hole then sealed with cyanoacrylate. The skin was then sutured closed and the wound site injected with lidocaine/bupinorphine and a topical triple antibiotic ointment was applied. Animals were returned to their home cage and monitored until recovered from anesthesia. Intrathecal infusions were performed on tumor-bearing rats 12-14 days post injection (*N*=5 animals of lesser weight; divided between treatment groups) or 20-26 days post injection (*N*=2; animals of greater weight when injected, one from each treatment group), when neurological symptoms were observed (tumor cells implanted into slightly smaller rats progressed more quickly).

Intracisternal infusions

Normal or glioma-implanted rats were anesthetized to a surgical plane with urethane (1.2 g/kg, i.p., supplemented to effect with 0.375 g/kg urethane i.p.) and atropine (0.1 mg/kg s.c.) was administered to reduce bronchial secretions. Rats were placed on a homeothermic blanket (Harvard Apparatus, Holliston, MA) to maintain body temperature at 37°C and positioned in a stereotaxic frame in the flat skull position (prone). Rats were prepared surgically as described previously (Wolak *et al.*, 2015*a*; Pizzo *et al.*, 2018). The infusion setup consisted of a ~1.5 cm piece of polyetheretherketone (PEEK) tubing (PlasticsOne, Roanoke, VA) sealed inside PE-10 tubing connected to a Hamilton syringe, which was controlled by an infusion pump (Quintessential Stereotaxic Injector, Stoelting, Wood Dale, IL); the tubing was filled with infusate prior to insertion. The dura overlying the cisterna magna was exposed by a midline neck incision and retraction of the subcutaneous tissue. A 30 GA dental needle was used to puncture the dura and the PEEK cannula immediately inserted 1 mm into the cisterna magna (30° from the horizontal) and sealed to the dura with cyanoacrylate.

Eighty microliters of antibody solution was infused over 50 minutes at a rate of 1.6 µL/min, a rate that has been demonstrated not to significantly increase intracranial pressure (Yang *et al.*, 2013; Bedussi *et al.*, 2017). Rats were repositioned supine and the abdominal aorta cannulated immediately after the infusion. Thirty-minutes after completion of the infusion, 0.5 mL of blood was drawn via the abdominal aorta cannula then the animal was immediately perfused with 50 mL ice cold 0.01 M phosphate buffered saline (PBS) at a rate of 15 mL/min followed by 450 mL of 4% paraformaldehyde (PFA) in 0.1 M phosphate buffer, euthanizing the animal by exsanguination.

Infused antibody solutions

All rats received the same amount of fluorescently-labeled, normal pooled polyclonal rat IgG (AlexaFluor488 conjugated ChromPure rat IgG, 012-540-003; Jackson ImmunoResearch Laboratories, Inc., West Grove, PA) in a total infusate volume of 80 µL. Rat IgG was reconstituted with water as instructed to a concentration of 2 mg/mL (13.3 µM); the IgG solution contained 15 mg/mL bovine serum albumin (BSA) for stability, warranting removal before infusion as it was desirable to maintain similar osmotic pressure as previous studies (Pizzo *et al.*, 2018). Additionally, while albumin and IgG binding to FcRn have been suggested to be non-competitive (Chaudhury *et al.*, 2006), removal of BSA also ensured interaction of IgG with endogenous receptors was not impacted. BSA was removed from the IgG by adding the reconstituted solution to an Amicon Ultra-0.5 mL centrifugal filter (100 kDa molecular weight cutoff, Millipore, Billerica, MA) with 0.01 M PBS to achieve a total volume of 0.5 mL; the column was spun for 10 min at 14,000 *g* from a volume of 0.5 mL three times followed by a recovery spin for 2 min at 1,000 *g*. The concentration of the IgG solution was determined using a microplate reader (FLUOstar Omega; BMG Labtech, Ortenberg, Germany) and comparison with a standard curve, and the final concentration adjusted to 2 mg/mL IgG without BSA. Labeled IgG in a 20:1 molar excess of unconjugated IgG (ChromPure rat IgG, 012-000-003; Jackson ImmunoResearch Laboratories, Inc.) or labeled IgG in 0.75 M mannitol (in 0.01 M PBS) was similarly prepared by adding unlabeled IgG/0.01 M PBS or 0.75 M mannitol to the column to achieve the 0.5 mL total volume per spin; the concentration of the filtrate was determined, and the final concentration of labeled IgG adjusted to 2 mg/mL using 0.01 M PBS or 0.75 M mannitol.

Plasma levels

Blood drawn from the abdominal aorta cannula was added to a tube with heparin immediately after collection and kept on ice until centrifugation at 3,000 *g* for 10 min followed by centrifugation of the supernatant (plasma) at 10,000 *g* for 10 min. The final supernatant was removed and the IgG concentration in the plasma determined using a microplate reader (FLUOstar Omega; BMG Labtech) and comparison with a standard curve. Intrathecal saline-infused or untreated rats (*N*=7) were used as controls; *N*=2 untreated nude rats also showed similar control plasma fluorescence to normal untreated Sprague-Dawley rats.

Ex vivo fluorescence imaging

All dissected tissues (whole brain and spinal cord, nasal passages, cervical lymph nodes, dorsal dura mater) were imaged immediately using an MVX10 Macroview microscope (Olympus, Tokyo, Japan) equipped with an Orca-flash 2.8 CMOS camera (Hamamatsu, Hamamatsu City, Japan) and a X-Cite 120Q illuminator (Lumen Dynamics Group, Inc.,Mississauga, Ontario, Canada) using the appropriate filter set (Chroma, U-M49002XL or U-M49008XL, Bellows Falls, VT, USA), as described previously (Pizzo *et al.*, 2018). Images were taken in overlapping sections for the whole brain, spinal cord, nasal passages, and dura; the images were manually aligned and autoblended into a single image using Photoshop CC (Adobe Systems, San Jose, CA). The whole brain and dura were placed in 0.01 M PBS overnight and the whole brains sectioned (100 µm, coronal) the following day using a vibratome (VT1000S; Leica Microsystems, Wetzlar, Germany). Whole coronal sections were imaged immediately after sectioning by placing brain sections on a wet petri dish and some sections reserved for immunohistochemistry (IHC). The spinal cord, nasal passages, and lymph nodes were placed in 30% sucrose in 0.01 M PBS at 4°C after dissection and the following day coated in optimal cutting temperature compound (Tissue-Tek, Sakura Finetek USA, Inc., Torrance, CA) and frozen in isopentane on dry ice. Tissue was kept at -20°C until being sectioned (25 µm) on a cryostat (CM1950; Leica Microsystems).

Immunohistochemistry and confocal microscopy

All steps were performed at room temperature unless otherwise specific. Free-floating coronal brain sections and the dorsal dura mater were blocked for 2 hours in blocking buffer containing 5% serum or 10% BSA prepared in 0.01 M PBS with 0.3% triton X-100 (PBST). Sections were then washed for 15 min three times in PBST, incubated with primary antibodies in blocking buffer overnight at 4°C, washed three times in PBST for 15 min, incubated with secondary antibodies in blocking buffer for 2 hours, washed in PBST for 15 min, incubated with 4’,6-diamidino-2-phenylindole (DAPI) in PBST (2 µg/mL) for 20 minutes, then washed for 15 min 3 times in PBST, and finally mounted onto slides using Prolong Diamond Antifade (Life Technologies, Carlsbad, CA). A Cy3-conjugated mouse-anti-alpha smooth muscle actin antibody (1:500, C6198; Sigma-Aldrich, St. Louis, MO) was blocked and prepared in 10% BSA in PBST and was not combined with any other primary/secondary antibodies. Blocking buffer was 5% serum from the secondary antibody host (or 2.5%/2.5% serum from each secondary host species) for all unconjugated antibodies. Additional unconjugated primary antibodies included: mouse-anti-rat endothelial cell antigen-1 (RECA-1; 1:1000, ab9774; Abcam, Cambridge, MA), chicken-anti-glial fibrillary acidic protein (GFAP; 1:1000, NBP1-05198, Novus Biologicals, Littleton, CO), goat-anti-Iba-1 (1:100, NB100-1028; Novus Biologicals), mouse-anti-laminin gamma 1 (1:500, mab2139; R&D systems, Minneapolis, MN), mouse-anti-human nuclei (1:250-1:500, mab1281; EMD Millipore, Burlington, MA), mouse-anti-Cd11b (1:500, CBL1512; EMD Millipore), sheep-anti-Lyve-1 (1:1000, AF7939; R&D Systems), and rabbit-anti-Fc gamma receptor IIb (Fcgr2b, 1:250, bs-6031R; Bioss, Woburn, MA). Secondary antibodies included (all used at 1:500 dilution): donkey-anti-sheep 594 (A11016, Life Technologies), pre-adsorbed goat-anti-mouse 647 (ab150119, Abcam), goat-anti-chicken 594 (ab150172, Abcam), donkey-anti-goat 546 or 594 (A11056 or A11058, Life Technologies), or goat-anti-rabbit 594 (A11012, Life Technologies). Staining of sections without primary (control) showed the highly-cross adsorbed goat-anti-mouse 647 (A21236, Life Technologies) secondary antibody had substantial binding to endogenous/administered rat IgG and thus sections utilizing mouse primary antibodies detected with this secondary were not included. Staining for endogenous rat IgG in glioma brain sections was performed at room temperature by incubation in blocking buffer (5% goat serum in PBST) for 2 hours, incubation with goat-anti-rat 594 (SAB4600111, Sigma-Aldrich or goat-anti-rat 594, A11007, Life Technologies) or the goat-anti-mouse 647 (Life Technologies) mentioned above for 2 hours (1:250-1:500 dilution), 15 min PBST wash, 20 min DAPI incubation, and 3 PBST washes for 15 min each before mounting. Cryosections of spinal cord, lymph nodes, and nasal passages were stained on slides by outlining the sections with a hydrophobic pen and following the above protocol. Confocal imaging was performed using a FV1000 confocal microscope (Olympus) using FLUOVIEW (Olympus) or an A1R confocal microscope (Nikon, Tokyo, Japan) with NIS Elements (Nikon).

Diffusion measurements at the brain surface following intrathecal infusion of rat IgG

Images of coronal brain sections obtained using the Olympus MVX10 were analyzed using Fiji (Schindelin *et al.*, 2012) according to previously described methods (Wolak *et al.*, 2015*a*; Pizzo *et al.*, 2018). Briefly, the fluorescence intensity gradient along a line (~80 µm wide and ~200-500 µm deep) drawn normal to the ventral brain surface was fitted to the appropriate diffusion equations (Wolak *et al.*, 2015*a*). This provided an estimate of the effective diffusion coefficient for rat IgG following intrathecal infusion (D^*_{infus}) at the ventral brain surface. Four lines were analyzed per coronal section; four sections were analyzed per animal at coronal levels of approximately 1.5 mm anterior to bregma (± 0.5 mm) or 3 mm posterior to bregma (± 0.5 mm) from bregma (Paxinos & Watson, 2007) totaling 16 sections per animal. For one of the four rat IgG-infused animals, the difference between the maximum intensity and the minimum intensity (background) along the line was less than 500 arbitrary units so this animal was not included in the average diffusion coefficient. Average (and minimum) R^2 values were 0.94 (0.86) and 0.96 (0.89) for sections 1.5 mm anterior and 3 mm posterior to bregma, respectively.

Quantification of perivascular signal

Images of coronal brain sections were analyzed using Fiji (Schindelin *et al.*, 2012) similar to previously described methods (Pizzo *et al.*, 2018). Briefly, the coronal section was outlined using the wand tool (excluding the ventricular areas), the section was divided into dorsal and ventral halves, and the area of the dorsal/ventral halves measured. The horizontal dorsal/ventral division line was placed at approximately half the vertical distance from the dorsal–ventral extent of the lateral ventricles (LVs) for sections 1.5 mm anterior to bregma or at bregma (0mm), and just inferior to the dorsal hippocampus and dorsal third ventricle for sections 2.5 mm posterior to bregma. Next, a threshold was set for all sections from each individual animal to distinguish background autofluorescence (due to white matter) from the antibody signal and the 'Analyze Particles' command used to count and characterize i) the percent area of the dorsal/ventral half section that was positive for antibody signal and ii) the number of perivascular profiles within the dorsal/ventral half section (which could be normalized by the section area providing number of perivascular profiles per mm^2). For glioma rats, the coronal sections were further divided into ipsilateral and contralateral hemispheres along the midline, resulting in four quadrants analyzed per section, providing quantification relative to the general tumor quadrant (dorsal/ipsilateral). Re-analysis of rat IgG section in quadrants showed no differences from halves as both are normalized by area (not shown). There were no restrictions set on analyzed particle characteristics except that profiles must be two pixels or greater.

Scanning electron microscopy

In four tumor-bearing nude rats a portion of the brainstem/spinal cord containing part of the basilar artery and the vertebral arteries was carefully dissected from the whole brain by two coronal cuts following IgG (*N*=2) or IgG + 0.75 M mannitol (*N*=2) infusion and perfusion/fixation with PBS and 4% PFA described above. The tissue blocks were post-fixed overnight at 4°C in 2% PFA + 2.5% glutaraldehyde in 0.1 M PBS then washed in PBS the following day and prepared as described previously (Pizzo *et al.*, 2018). Briefly, tissue blocks were dehydrated at room temperature in increasing levels of ethanol, dried using a CO_2 critical point dryer (Tousimis, Sandri 780A, Rockville, MD, USA) and sputter coated with approximately 3-5 nm of 60:40 gold:palladium using an Auto ConductVac IV (SeeVac, Pittsburgh, PA, USA). Imaging was performed using an LEO 1530 field emission scanning EM (3 kV; Zeiss) at magnifications between approximately 60X and 120,000X.

Statistical Analysis

All statistical analyses were performed using SigmaPlot software (Systat Software Inc., San Jose, CA) and all values reported are mean ± SEM based on N animals and n individual measurements. Comparisons between only two treatment groups utilized a Student's two-tailed t test to determine statistical differences, with p values listed in the text. Group comparisons of three or more treatment groups utilized a Kruskal-Wallis one-way ANOVA on ranks ($p < 0.001$) as at least one group did not pass the normality test or equal variance test; post hoc pair-wise comparisons were made using Dunn's method ($p < 0.05$).

Results

Distribution of intrathecal rat IgG in the normal rat brain and spinal cord

Normal female Sprague-Dawley rats received an 80 µL intracisternal infusion of fluorescently-labeled rat IgG in the prone position (as described previously, (Pizzo *et al.*, 2018) over 50 min at a rate of 1.6 µL/min. This infusion rate is approximately half the CSF production rate in rats (Davson & Segal, 1995), and the infusion rate/duration has demonstrated no significant change in intracranial pressure in rats (Yang *et al.*, 2013; Bedussi *et al.*, 2017) nor evidence of retrograde flow into the ventricles (Pizzo *et al.*, 2018). Rats were perfused/fixed and the brain and spinal cord dissected and immediately imaged. Infusion of rat IgG (N=4) showed widespread distribution on the dorsal (Fig. 1*A*) and ventral (Fig. 1*B*) brain surfaces, predominantly associated with major surface vessels (e.g., circle of Willis and caudal rhinal vein), CSF cisterns (e.g., olfactofrontal, quadrigeminal), and some nerves (e.g., hypoglossal and trochlear). Punctate signal was associated with the perivascular spaces of penetrating vessels perpendicular to the brain surface. Similarly, the surface of the spinal cord showed IgG signal from the cervical region to the cauda equina that was predominantly associated with surface arteries and dorsal and ventral nerve roots (Fig. 1 *E* and *F*). Rat IgG was also intrathecally infused into rats in the presence of a 20:1 molar excess of unlabeled rat IgG to probe if labeled-IgG binding to endogenous receptors could be disrupted by competition from an excess of unlabeled IgG, potentially altering the distribution patterns. IgG was still associated with major surface arteries of the brain (Fig. 1 *C* and *D*) and spinal cord (Fig. 1 *G* and *H*), but showed less apparent signal around nerves, essentially no punctate perivascular signal associated with penetrating vessels, and revealed a very different pattern of signal associated with more tortuously-shaped vessels on the surface.

Imaging of coronal brain sections revealed a steep gradient at the surface of the brain facing the CSF as well as extensive access of rat IgG to the parenchymal perivascular spaces (Fig. 2*A-I*). The fluorescence profile at the ventral brain surface was extracted using Fiji and fit to the appropriate diffusion equation (an analytical solution to Fick's second law) to estimate a diffusion coefficient in the brain following intrathecal infusion (D^*_{infus}) as described previously (Wolak *et al.*, 2015*b*; Pizzo *et al.*, 2018); four gradients per section and four sections per animal were analyzed at two coronal levels (1 mm anterior to bregma and 3 mm posterior to bregma) which were not significantly different (Student's two-tailed t-test, p=0.06) so resulting diffusion coefficients were averaged. An excellent fit of the raw data to the diffusion equation suggested agreement of this transport with Fickian diffusion. The resulting D^*_{infus} was $2.5 \pm 0.1 \times 10^{-8}$ cm^2/s (N=3, n=96). A Student's two-tailed t-test showed a significant difference between rat IgG D^*_{infus} and the previously reported D^*_{infus} for goat IgG ($D^*_{\mathrm{infus}} = 3.4 \times 10^{-8}$ cm^2/s, p=0.004; (Pizzo *et al.*, 2018)), likely due to greater rapid, reversible binding of rat IgG to endogenous receptors in the brain (hindering transport and producing a lower D^*) compared to goat IgG.

The perivascular distribution of rat IgG was remarkably widespread (Fig. 2*A-I*). Rat IgG appeared to track along nearly the entire length of the vessel profile in many cases (e.g., in the cortex), continuing along many smaller branches. Interestingly, a few brain regions show lesser perivascular signal including the medial striatum (e.g., Fig. 2*C*) and large portions of the thalamus (e.g., Fig. 2 *E* and *F*) and brainstem (e.g., Fig. 2*H*). Perivascular signal in the upper cervical spinal cord was also limited to the anterior spinal artery in the anterior median fissure, a few penetrating profiles in the white matter, and a few profiles in the spinal gray matter. Diffuse signal was also prominent in the periventricular white matter around the lateral ventricle (in 3 of 4 animals), which has been previously described for a single-domain antibody and goat IgG under some conditions (Pizzo *et al.*, 2018). This precise origin of this signal is unknown but has been postulated to be associated with: connection/transition of the perivascular space with the choroid plexus/stroma, connections between the subarachnoid space and ventricles via velae or the choroidal fissure, and the potential for white matter to transport molecules by bulk flow (Cserr *et al.*, 1977; Szentistványi *et al.*, 1984; Ichimura *et al.*, 1991) (see discussion in (Pizzo *et al.*, 2018)). The phenomenal access of rat IgG to the perivascular spaces needed to be reconciled with the size-dependent perivascular access reported previously, where goat IgG showed a substantially lesser access to the perivascular space than what was observed here for the identically-sized rat IgG (Pizzo *et al.*, 2018). We hypothesized that rat IgG binding to endogenous Fc receptors in the brain could be partly responsible for rat IgG entry into the perivascular spaces, perhaps to allow IgG to survey for antigens in the perivascular space. To test this hypothesis, a competition experiment was designed to prevent labeled rat IgG from interacting with endogenous receptors by flooding the receptors with an excess of unlabeled rat IgG (see Prologue Fig 4). Thus, an identical amount of labeled rat IgG was prepared in a 20:1 molar excess of unlabeled rat IgG and infused intrathecally into normal rats (XIgG). Images of coronal sections revealed a strikingly different distribution of rat IgG with excess IgG (Fig. 2*J-R*), showing an apparent reduction in the number perivascular profiles accessed and greater IgG signal at the brain surface (periventricular white matter signal occurred in 4/5 animals, similar to rat IgG alone). Indeed, the perivascular distribution of rat IgG with excess IgG appeared quite similar to intrathecally-infused goat IgG (Pizzo *et al.*, 2018). A method was developed to quantify the perivascular signal from brain section images using Fiji to delineate the section outline, threshold signal from background, and analyze the 'particles' or perivascular profiles to facilitate comparison between treatment groups (Fig. 3*A-L*; see (Pizzo *et al.*, 2018)). Coronal sections (6-8 per coronal level per animal) were divided into dorsal and ventral halves based on anatomical landmarks to provide a simple division that would allow some regional differences to be distinguished (Fig. 3*A-L*). Quantification of the percent area of antibody signal (Fig. 3*M*; Table 1) overall showed little difference between IgG alone and IgG with excess (Kruskal-Wallis one-way analysis of variance on ranks with Dunn's method post hoc pairwise comparison); this lack of quantitative distinction is at least partly attributed to the numerous but small perivascular profiles of rat IgG alone, which contribute a smaller area, and the relatively high accumulation of surface signal following infusion of rat IgG with excess IgG. However, quantification of the number of perivascular profiles per mm^2 (Fig. 3*N*, Table 1) demonstrated a significantly reduced number of perivascular profiles for rat IgG with excess (Kruskal-Wallis one-way analysis of variance on ranks with Dunn's method post hoc pairwise comparison) both dorsally and ventrally in sections at all three coronal levels (1.5 mm anterior to bregma, at bregma (0mm), and 2.5 mm posterior to bregma). A previous study from our laboratory demonstrated size-dependent entry from the CSF into the perivascular spaces potentially caused by putative sieving by leptomeningeal lining cells; co-infusion of mannitol with goat IgG was thought to manipulate this barrier (see Prologue Fig. 3) to improve perivascular access for goat IgG (Pizzo *et al.*, 2018). Here, we also co-infused rat IgG with 0.75 M mannitol intrathecally, but observed no apparent differences in perivascular access, as may be expected for a molecule that already possesses and incredible ability to enter the perivascular space (Fig. S1).

Table 1. Summary of antibody signal quantification from *ex vivo* fluorescence imaging of brain sections.

	% Area with antibody signal (*N*,*n*)[a]		
Infused Antibody	+ 1.5 mm	0 mm	-2.5 mm
IgG			
dorsal	5.03 ± 0.17 (4,32)	3.16 ± (4,24) 0.12	5.49 ± 0.62 (4,28)
ventral	6.66 ± 0.37 (4,32)	4.07 ± (4,24) 0.39	2.99 ± 0.24 (4,28)
IgG + excess			
dorsal	4.53 ± 0.27 (5,40)	4.24 ± (5,30) 0.34	4.48 ± 0.26 (5,35)
ventral	6.95 ± 0.62 (5,40)	6.02 ± (5,30) 0.40	4.26 ± 0.28 (5,35)
	Number of PV profiles per mm^2 slice area (*N*,*n*)[a]		
Infused Antibody	+ 1.5 mm	0 mm	-2.5 mm
IgG			
dorsal	13.99 ± 0.72 (4,32)	12.19 ± (4,24) 0.72	10.26 ± 0.58 (4,28)
ventral	19.56 ± 0.61 (4,32)	16.88 ± (4,24) 0.76	11.21 ± 0.44 (4,28)
IgG + excess			
dorsal	4.50 ± 0.29 (5,40)	4.34 ± (5,30) 0.34	4.56 ± 0.26 (5,35)
ventral	8.46 ± 0.57 (5,40)	6.96 ± (5,30) 0.63	5.60 ± 0.46 (5,35)

[a]Antibody signal above a background threshold was quantified using Fiji to measure the percent area with antibody signal within dorsal or ventral halves of brain slices (1.5 mm anterior to bregma, 0 mm (at bregma), or 2.5 mm posterior to bregma) and the number of perivascular profiles normalized by slice area (mm^2). Values represent mean ± s.e.m.; *N* animal experiments and *n* brain sections per treatment group.

Confocal imaging of intrathecal rat IgG in the normal rat brain perivascular spaces

Representative coronal sections were stained using immunohistochemistry to examine infused rat IgG localization relative to other cellular markers including endothelial cells (rat endothelial cell antigen-1, RECA-1), vascular smooth muscle cells (alpha smooth muscle actin, αSMA), and astrocytes (glial fibrillary acidic protein, GFAP). Rat IgG signal was present around leptomeningeal arteries on the brain surface (e.g., the central internal carotid artery, Fig. 4*A*) in what has been described as the subarachnoid perivascular space/vascular connective tissue space/adventitia (Pizzo *et al.*, 2018); rat IgG appeared to be restricted from entering the tunica media to access the smooth muscle basement membrane between smooth muscle cells. Large veins on the brain surface, which were lacking significant smooth muscle and had a large diameter and relatively thin vascular wall, were also associated with rat IgG (Fig. 4*B*). Rat IgG was able to access parenchymal perivascular spaces along putative arterioles (Fig.4 *C* and *E*), microvessels (Fig. 4*D*), and venules (Fig. 4*E*); IgG appeared to integrate into the arteriole smooth muscle basement membrane between smooth muscle cells creating a circumferential banding pattern while signal along veins/venules appeared to have more a more longitudinally-arranged pattern. Rat IgG appeared in putative subarachnoid and perivascular macrophages (Fig. 4 *B* and arrowhead in *C*; also see Fig. S2) and was diffusely present along the pial surface (Fig. 4*F*). Rat IgG infused with an excess of unlabeled IgG was also present along perivascular spaces associated with leptomeningeal arteries (also failing to access the tunica media, Fig. 4*G*), arterioles (Fig. 4*H*, showing similar banding patterns), and venules (Fig. 4*I*). However, there were differences in the appearance of this perivascular signal—distinct 'holes' absent of signal were visible (particularly evident in Fig. 4. *I* (inset), *J3*, and *K3* single channel images), some areas of signal were very patchy and inconsistent (e.g., Fig. 4*K*), and most notably the signal on the pial surface was strikingly sporadic and irregular (Fig. 4 *L* compared with *F*).

Drainage pathways for intrathecal rat IgG

Previous studies have identified several drainage pathways for central molecules, including clearance via arachnoid granulations/villi to the dural sinuses and systemic circulation (Weller *et al.*, 1992; Davson & Segal, 1995), clearance via perivascular/perineural/lymphatic pathways to the nasal mucosa and cervical lymph nodes (Faber, 1937; Bradbury & Westrop, 1983; Weller *et al.*, 1992; Cserr & Knopf, 1992; Kida *et al.*, 1993; Koh *et al.*, 2005), clearance along other cranial and spinal nerves to the lymphatics (reviewed in (Koh *et al.*, 2005)), and clearance via lymphatic vessels in the dura around cranial nerves (Aspelund *et al.*, 2015) and other not fully elucidated dural lymphatic pathways to reach cervical lymph nodes (Kida *et al.*, 1993; Furukawa *et al.*, 2008; Aspelund *et al.*, 2015; Louveau *et al.*, 2015). Similar to intrathecally-infused goat IgG (Pizzo *et al.*, 2018), rat IgG appeared to utilize the olfactory drainage pathway with particularly prominent signal around the ventral olfactory bulbs (Fig. 1*B*) and olfactory nerve layer (Fig. 2*A* and *J*). Drainage predominantly reached the olfactory mucosa (with little signal in the respiratory mucosa) and both the superficial and deep cervical lymph nodes following IgG infusion (Fig. 5 *A*, *A inset*, and *B*) or infusion of IgG with excess unlabeled IgG (Fig. 5 *C, C inset*, and *D*), which appeared similar. Confocal imaging revealed that IgG was localized to the olfactory mucosa lamina propria, appeared to stop abruptly within the basal lamina (not reaching into the epithelium), and was associated with vessels (putative blood vessels or lymphatic vessels) and nerve bundles (Fig. 5*F*).

Cranial and spinal nerves showed IgG signal (Fig. 1 *B*, *E*, and *F*) potentially associated with dural lymphatic vessels or perineural drainage pathways. IgG in the dorsal dura mater was diffusely associated with the superior sagittal and transverse sinuses (Fig. 5*E*), likely due to clearance via arachnoid villi, with additional signal present around vessels, particularly in the dura over the dorsal and lateral cortex (Fig. 5*E* inset). Confocal imaging of the dural vessels (Fig. 5 *H* and *I*) with lymphatic vessel endothelial hyaluronan receptor 1 (Lyve-1) to label lymphatic endothelial cells (macrophages also stain positive for Lyve-1; see Fig. S2) did not reveal significant co-localization of IgG and Lyve-1 in what appeared to be vessels. In many cases it appeared Lyve-1 cells (putative macrophages) were adjacent to vessels where IgG was present (Fig. 5*H*, green arrows in *I*) without co-localization, but some co-localization of IgG with Lyve-1 cells was also observed (Fig. 5*I* yellow arrows); it is possible that some of these cells are part of lymphatic vessels and not individual cells, but this will require further investigation. As the dural blood vessels do not possess a tight endothelial barrier (Nabeshima *et al.*, 1975), movement of IgG between the dural sinuses, blood vessels, and interstitium are possible and may explain some of the dural distribution of IgG, in addition to the potential for substances in the dura (e.g., drained via arachnoid villi) to reach dural lymphatic vessels. Plasma concentration of rat IgG was measured by fluorescence detection using a microplate reader and comparison with a standard curve (Table 2). IgG concentration was 19.8 ± 0.4 nM (*N*=4, *n*=17) or 14.9 ± 1.3 nM (*N*=5, *n*=21) following infusion of rat IgG alone or with an excess of unlabeled IgG, respectively, demonstrating a slight but significant decrease in clearance to the blood in the presence of competition by unlabeled IgG (Student's two-tailed t-test, *p*=0.0016).

Table 2. Plasma levels of IgG in normal and glioma rats following intrathecal rat IgG infusion.

Infusate	**Measured plasma concentration of IgG (nM)**[a]	***N* animals (*n* measurements)**
rat IgG[a]	19.8 ± 0.4	4 (17)
rat IgG + excess[b]	14.9 ± 1.3	5 (21)
rat IgG (U87)[a]	7.6 ± 0.8	3 (13)
rat IgG + 0.75 M mann (U87)[a]	16.7 ± 1.3	4 (17)

[a]Estimated concentration of intrathecally-infused rat IgG in the CSF was approximately 4.3 µM, assuming 80 µL of 13.3 µM rat IgG administered into 250 µL of subarachnoid CSF (with instantaneous mixing). [b]Estimated total concentration of intrathecally-infused rat IgG with a 20:1 molar excess of unlabeled rat IgG in the CSF was approximately 90.5 µM, assuming 80 µL of 280 µM rat IgG administered into 250 µL of subarachnoid CSF (with instantaneous mixing). Total CSF volumes in the rat range ~150–300 µL (Davson & Segal, 1995; Fenstermacher *et al.*, 1999; Preston, 2001).

Distribution of intrathecal rat IgG in the rat brain and spinal cord of a primary rat model of glioma

Characterization of the CSF-to-brain distribution pathways in normal animals aids in understanding the physiological routes for exchange. However, it is highly likely that the presence of pathology can impact distribution along these routes, thus, it is critical to elucidate these differences for the sake of ongoing clinical trials. Therefore, we characterized the distribution of rat IgG in a primary rat model of glioma. Human U87 malignant glioma cells were injected into the right striatum in male athymic nude rats; approximately two weeks after implantation rats were intrathecally-infused with rat IgG. Distribution of IgG on the whole brain surface did not appear different from IgG distribution in normal animals; in some animals the tumor reached the cortical surface and showed slight abnormalities in the vasculature with lesser IgG signal (not shown). Coronal sections demonstrated a consistent and complete lack of IgG signal in the tumor (Fig. 6), and perivascular signal in the normal ipsilateral and contralateral brain regions was reduced but variable between animals (Fig. 6, compare columns one and two). Our previous study showed that intrathecal co-infusion of mannitol with goat IgG improved access of goat IgG into the perivascular spaces, putatively due to osmotic alteration of the lining cells that may govern perivascular entry (Pizzo *et al.*, 2018). Here, we intrathecally co-infused 0.75 M mannitol in 0.01 M PBS with rat IgG in tumor-bearing rats to probe if a physical barrier might be contributing to reduced perivascular access. Imaging of brain sections (Fig. 6) revealed a similar variability in perivascular access between animals as with rat IgG alone in glioma rats and no apparent delivery improvement with co-infusion of mannitol. Quantification of IgG from images of coronal brain sections (Fig. 7; Table 3) was performed by dividing the dorsal/ventral halves medially to determine differences between dorsal/ventral/ipsilateral/contralateral quadrants relative to the general tumor area (which was primarily in the dorsal/ipsilateral quadrant). IgG signal in brain sections showed a significant reduction in percent area of IgG signal between normal and glioma rats both ipsilaterally and contralaterally for approximately 9 of the 12 measured regions, with lesser differences in percent area of signal in more posterior (further from the tumor) ventral brain regions (Kruskal-Wallis one-way analysis of variance on ranks with Dunn's method post hoc pairwise comparison). However, the number of perivascular profiles per mm^2 revealed significantly fewer perivascular profiles in glioma animals compared to rat IgG in normal animals for all 12 regions, with no significant differences between IgG or IgG with mannitol in glioma rats (Kruskal-Wallis one-way analysis of variance on ranks with Dunn's method post hoc pairwise comparison).

Immunohistochemistry of representative coronal sections (Fig. 8) showed rat IgG localization and tumor characteristics using markers for human nuclei (HuNu, to detect implanted human tumor cells), astrocytes (GFAP), endothelial cells (RECA-1), ionized calcium-binding adapter molecule 1 (Iba-1, to detect microglia and macrophages), Fcγ receptor IIb (FcγRIIb, to label cells expressing this inhibiting Fc receptor), and laminin γ1 (to label all basement membranes). Characteristics of the tumors include: i) evident staining for human nuclei, as expected (Fig. 8 *A* and *H*), ii) low expression of GFAP within the tumor (as demonstrated previously (Restrepo *et al.*, 2011; Silver *et al.*, 2013)) but a strong astrocytic border between the tumor and surrounding normal brain (Fig. 8 *A*, *B3*, *D*, and *E*), iii) highly vascularized tumors with vessels that appeared slightly larger than vessels in the normal brain with some exceptionally large vessels within or around the tumor (Fig. 8*B4*), iv) high expression of Iba-1 within the tumor—the Iba-1 positive cells had a more rounded morphology similar to macrophages within the tumor, as compared with the typical microglial staining observed in surrounding normal brain (Fig. 8 *C3*), v) increased expression of FcγRIIb on

Table 3. Summary of antibody signal quantification from *ex vivo* fluorescence imaging of brain sections in glioma rats.

	% Area with antibody signal (*N*, *n*)[a]		
Infused Antibody	+ 1.5 mm	0 mm	-2.5 mm
IgG (U87 rats)			
dorsal contra	1.34 ± 0.11 (3,24)	1.74 ± 0.18 (3,18)	2.51 ± 0.48 (3,21)
dorsal ipsi	0.98 ± 0.10 (3,24)	0.49 ± 0.04 (3,18)	1.18 ± 0.09 (3,21)
ventral contra	4.00 ± 0.37 (3,24)	5.42 ± 0.44 (3,18)	4.38 ± 0.51 (3,21)
ventral ipsi	3.35 ± 0.35 (3,24)	3.51 ± 0.13 (3,18)	3.44 ± 0.41 (3,21)
IgG + 0.75 M mannitol (U87 rats)			
dorsal contra	1.36 ± 0.11 (4,32)	1.24 ± 0.21 (4,24)	1.29 ± 0.25 (4,28)
dorsal ipsi	0.48 ± 0.05 (4,32)	0.37 ± 0.05 (4,24)	0.69 ± 0.09 (4,28)
ventral contra	3.17 ± 0.32 (4,32)	3.43 ± 0.26 (4,24)	2.40 ± 0.22 (4,28)
ventral ipsi	2.22 ± 0.23 (4,32)	2.06 ± 0.14 (4,24)	1.94 ± 0.15 (4,28)
	Number of PV profiles per mm2 slice area (*N*, *n*)[a]		
Infused Antibody	+ 1.5 mm	0 mm	-2.5 mm
IgG (U87 rats)			
dorsal contra	4.90 ± 0.36 (3,24)	5.26 ± 0.49 (3,18)	3.97 ± 0.22 (3,21)
dorsal ipsi	2.69 ± 0.14 (3,24)	2.40 ± 0.21 (3,18)	2.93 ± 0.18 (3,21)
ventral contra	10.78 ± 0.70 (3,24)	10.27 ± 0.92 (3,18)	8.30 ± 0.25 (3,21)
ventral ipsi	8.83 ± 0.54 (3,24)	7.15 ± 0.77 (3,18)	7.05 ± 0.66 (3,21)
IgG + 0.75 M mannitol (U87 rats)			
dorsal contra	5.13 ± 0.47 (4,32)	4.93 ± 0.52 (4,24)	3.11 ± 0.31 (4,28)
dorsal ipsi	2.38 ± 0.25 (4,32)	1.88 ± 0.20 (4,24)	2.13 ± 0.21 (4,28)
ventral contra	14.34 ± 0.80 (4,32)	13.09 ± 0.65 (4,24)	8.51 ± 0.36 (4,28)
ventral ipsi	8.40 ± 0.43 (4,32)	6.97 ± 0.43 (4,24)	6.90 ± 0.42 (4,28)

[a] Antibody signal above a background threshold was quantified using Fiji to measure the percent area with antibody signal within dorsal/ventral/ipsilateral/contralaterl quadrants of brain slices (1.5 mm anterior to bregma, 0 mm (at bregma), or 2.5 mm posterior to bregma) and the number of perivascular profiles normalized by slice area (mm^2). Values represent mean ± s.e.m.; *N* animal experiments and *n* brain sections per treatment group.

cells within the tumor, quite possibly associated with the high number of Iba-1 positive cells (Fig. 8 *F* and *G*), and vi) strong expression of the basement membrane marker laminin γ1, which overshadowed laminin expression associated with the normal vasculature in the brain (Fig. 8*I*). In two nude rats with implanted U87 cells, the tumors had grown so large that insertion of the intracisternal cannula was not possible due to obstruction of the cisterna magna by the cerebellum. These untreated glioma rats, in addition to two IgG-infused glioma rats, were utilized to gauge blood-brain barrier integrity to endogenous, circulating rat IgG. Brain sections were stained using a fluorophore conjugated anti-rat IgG antibody, which revealed IgG throughout the entire tumor region with perhaps slight spillover into peri-tumoral edematous areas.

Evidence for leptomeningeal stomata in athymic nude rats

We previously demonstrated the presence of stomata, or pores, in leptomeningeal cells that ensheath leptomeningeal blood vessels on the brain surface using scanning electron microscopy in normal Sprague-Dawley rats (Pizzo *et al.*, 2018), which had previously been shown in cats (Zervas *et al.*, 1982). We hypothesized these pores may be a site of perivascular entry from the CSF, as leptomeningeal fibroblasts separate the perivascular/vascular connective tissue space of leptomeningeal vessels from the CSF. In the present study, we also confirmed the presence of numerous micron-sized stomata on leptomeningeal cells covering the basilar and vertebral arteries on the brain surface in athymic male nude rats following intrathecal infusion of rat IgG (N=2) or rat IgG with 0.75 M mannitol (N=2; Fig. 9).

Discussion

The key findings of this study were: i) transport of species-matched rat IgG antibodies in the brain extracellular space at brain-CSF interfaces was consistent with Fickian diffusion, ii) species-matched rat IgG readily accessed the parenchymal perivascular spaces, at least in part via a receptor-mediated process, iii) intrathecal IgG showed no delivery to a primary brain tumor in rats, and iv) the presence of a primary brain tumor significantly reduced perivascular transport throughout the brain.

Comparison of intrathecally-administered IgG antibodies

The results of the current study share important similarities and differences from our previous study of intrathecally-infused species-mismatched goat IgG in rats (Pizzo *et al.*, 2018). This allows us to make a powerful comparison that can probe transport differences between size-related outcomes and binding-related outcomes as well as speculate potential physiological roles of endogenous IgG circulating in the CSF based on its localization in the brain. First, both goat and rat IgG appeared to move into the narrow, brain extracellular spaces at the pial surface in a manner that is consistent with Fickian diffusion, as evidenced by an excellent fit of the raw data to the diffusion equation. The diffusion coefficient for rat IgG was slightly lower than for goat IgG following intrathecal infusion despite their essentially identical molecular weight and hydrodynamic diameter; this most likely reflects the enhanced species-specific ability of rat IgG to rapidly and reversibly bind to endogenous receptors (i.e., Fcγ receptors) while traversing the brain extracellular spaces. These results are in agreement with previous experimental (Rall *et al.*, 1962; Levin *et al.*, 1970; Patlak & Fenstermacher, 1975; Nicholson & Phillips, 1981; Nicholson & Tao, 1993; Thorne *et al.*, 2004; Thorne & Nicholson, 2006; Thorne *et al.*, 2008; Wolak *et al.*, 2015*a*) and modeling (Jin *et al.*, 2016; Holter *et al.*, 2017) studies which suggest that transport of molecules (from small tetramethyl ammonium ions to large quantum dots) within the narrow, 40-60 nm wide (Thorne & Nicholson, 2006) brain extracellular spaces are consistent with diffusion (as discussed in (Abbott *et al.*, 2018; Pizzo *et al.*, 2018)). This is in contrast to part of the 'glymphatic' hypothesis which suggests a convective/bulk flow occurs in the neuropil facilitated by aquaporin-4 water channels localized to perivascular astrocyte end feet (Iliff *et al.*, 2012; Nedergaard, 2013). Second, while rat IgG accessed significantly more perivascular spaces compared to goat IgG (Student's two-tailed t-test, all $p<0.001$ for percent area and number of perivascular profiles per mm^2 at coronal sections 1.5 mm anterior and 2.5 mm posterior to bregma), their distribution once within the perivascular spaces shared some patterns. Neither IgG had substantial access to the tunica media of large leptomeningeal arteries, possibly suggesting a lack of IgG access to amyloid beta (discussed in (Pizzo *et al.*, 2018)) which can accumulate in the tunica media in cerebral amyloid angiopathy and appears to be out of reach from both systemically- or centrally-delivered antibodies (Koenigsknecht-Talboo *et al.*, 2008). Rat and goat IgG both also distributed along vessels of all caliber, including arteries and arterioles (which exhibited circumferential banding patterns, presumably associated with the outer smooth muscle basement membrane), veins and venules, as well as microvessels smaller than 8 μm in diameter. As supported by this study and hypothesized elsewhere (Hannocks *et al.*, 2017; Abbott *et al.*, 2018; Pizzo *et al.*, 2018), the ability of CSF macromolecules of various sizes to reach the level of the capillary and the apparently distinct astrocyte and endothelial/pericyte basement membranes at the level of the capillary (Hannocks *et al.*, 2017) appear to suggest that a pericapillary space (or potential space) exists that is capable of quickly transporting large macromolecules. This has led us to postulate a possible 'perivascular fluid system' (Abbott *et al.*, 2018) which allows rapid convective or dispersive transport along the entire vascular network (arteries/arterioles-capillaries-venules/veins) in the brain. Third, rat IgG and goat IgG appear to utilize the similar drainage pathways, resulting in high antibody signal in the olfactory mucosa lamina propria and cervical lymph nodes; while rat IgG was also present in the dura it appeared to often be associated with larger blood vessels rather than associated with Lyve-1 cells which could indicate lymphatic vessels. It is possible that a shorter/longer distribution time may indicate differences in the kinetics along various drainage routes. Thus, the olfactory drainage pathway is at least an important pathway for CSF clearance with implications for drainage of CNS antigens (Bradbury & Westrop, 1983; Kida *et al.*, 1993; Knopf *et al.*, 1995; Engelhardt *et al.*, 2017).

There were also obvious differences between the parenchymal brain distribution of rat IgG and goat IgG (Pizzo *et al.*, 2018) from the CSF; first and foremost, rat IgG displayed an astonishingly greater access to the perivascular spaces than goat IgG (rat IgG percent area was 1.7-3.5 fold greater and number per mm^2 was 1.4-2.9 fold greater than goat IgG at coronal sections 1.5 mm anterior and 2.5 mm posterior to bregma). This did not appear to negate our hypothesis (which is supported by our additional unpublished observations) that access to the perivascular space is size-dependent (Pizzo *et al.*, 2018), but rather suggested that rat IgG possessed a unique mechanism to readily enter the perivascular space. One possible mechanism could be greater hinge length/flexibility (Roux *et al.*, 1997; Woof & Burton, 2004; Vidarsson *et al.*, 2014) for rat IgG which may allow it more conformational flexibility to fit through tighter spaces, but did not seemed sufficient to entirely account for the dramatic difference. Species-specific variations in potential glycosylation patterns also seemed insufficient to explain the difference. Thus, a receptor-mediated shuttling of IgG from the CSF into the perivascular space seemed most likely. There is clear physiological reason for this mechanism—IgG is the principal antibody in the extracellular fluid, responsible for encountering and binding to antigens to induce engulfment by phagocytes or activation of the complement system (Abbas *et al.*, 2015). Indeed, the cerebral perivascular spaces have demonstrated high levels of complement proteins (Broadwell & Sofroniew, 1993) and contain numerous phagocytic cells (perivascular macrophages; (Bechmann *et al.*, 2001)), and are also considered an important route for CNS surveillance by immune cells (Fabry *et al.*, 2008; Ransohoff & Engelhardt, 2012; Engelhardt *et al.*, 2017). Interestingly and notably, it does not appear that IgG easily escapes the perivascular spaces to diffuse into the neuropil (e.g., see Fig. 4); this implies the astrocyte basement membrane may pose a significant barrier to IgG, constraining it to the perivascular space (Hannocks *et al.*, 2017). This may indicate CNS surveillance occurs predominantly within the CSF and perivascular compartments unless there is a breach in the basement membrane. We then tested the CSF-to-perivascular IgG receptor-mediated transport hypothesis using a competition experiment—a 20:1 molar excess of unlabeled IgG with the same amount of labeled IgG as prior experiments was co-infused intrathecally and showed that the excess unlabeled IgG prevented a significant amount of labeled IgG from entering the perivascular spaces (a 2-3-fold decrease in number of perivascular profiles per mm^2 across different brain regions). The resulting distribution of IgG with excess appeared somewhat similar to the goat IgG (Pizzo *et al.*, 2018); however, goat IgG actually accessed a significantly greater number of perivascular profiles per mm^2 compared to rat IgG with an excess of unlabeled (Student's two-tailed t-test, all $p<0.05$ at coronal sections 1.5 mm anterior and 2.5 mm posterior to bregma) which may indicate that even goat IgG was to some extent able to utilize the Fc receptor-mediated pathway, despite species differences. This might also suggest that other 10 nm sized-molecules may have more limited perivascular entry compared to goat IgG. Additionally, the anatomical regions/specific vascular territories where infused rat IgG with excess unlabeled IgG and goat IgG were present showed similarities (e.g., both consistently accessed the perivascular space of lenticulostriate vessels). This suggested to us at least two 'types' of perivascular spaces in the brain—perivascular spaces that are more easily accessed, even by large substances in the CSF, and perivascular spaces that more difficult to access. More accessible perivascular spaces may be larger in size, have fewer obstructions, and/or have greater driving forces for entry and transport; this category generally includes the perivascular spaces of large penetrating lenticulostriate vessels and other penetrating vessels from the ventral brain surface. On the other hand, difficult to access perivascular spaces may be smaller in size, be more obstructed, and/or have weaker entry/transport driving forces; this category may include perivascular spaces of the dorsal cortex or dorsal thalamus. Co-infusion of intrathecal mannitol improved goat IgG access to these perivascular spaces, but intrathecal mannitol did not appear to improve access for rat IgG access—this is likely because rat IgG already accessed these spaces very well.

Altogether, this data suggests a receptor-mediated entry of IgG into the perivascular space, presumably by an Fc receptor. One Fc receptor in particular, FcRn, is known to play a role in recycling of IgG in endothelial cells and transcytosis of IgG at other sites in the body (see reviews (Roopenian & Akilesh, 2007; Knudsen Sand *et al.*, 2015; Pyzik *et al.*, 2015)). Prior studies have demonstrated expression of Fc receptors in the brain leptomeninges (Nyland, 1982; Peress *et al.*, 1989) and our own unpublished observations), precisely where we have hypothesized possible perivascular entry (Pizzo *et al.*, 2018). Thus, we postulate that IgG is transported by FcRn and potentially other Fc receptors from the CSF into the perivascular spaces. It is important to note that FcRn only has affinity for IgG in an acidic environment (e.g., the mucosa or acidified endosome; (Jones & Waldmann, 1972; Rodewald, 1976)), thus FcRn is not expected to aid in internalization of IgG. FcRn is only capable of binding and transcytosing IgG once it has reached the acidified endosome. IgG must therefore rely on nonspecific cellular uptake mechanisms (e.g., pinocytosis) or specific uptake mechanisms (e.g., binding to a protein or receptor on the cell surface) (Simister *et al.*, 1996; Kristoffersen & Matre, 1996; Leach *et al.*, 1996; Firan *et al.*, 2001). This hypothesized process may be similar to the FcRn-dependent transport of IgG across the syncytiotrophoblasts between two compartments at physiological pH (Simister *et al.*, 1996).

Overall, this distribution has incredibly important implications for the expected distribution of species-matched or species-mismatched antibodies in both pre-clinical and clinical studies, i.e., distribution of a non-human(ized) antibody in clinical trials may have a worse than expected distribution in the human brain. Direct visualization of administered antibodies in humans is no simple task, so a negative trial outcome may never even be attributed to a delivery problem. However, if a similar mechanism of enhanced perivascular entry for IgG exists in humans it provides an exciting opportunity to enhance the distribution and brain delivery of IgG and Fc-fusion proteins, for instance an Fc domain-fused enzyme for treatment of neuropathic lysosomal storage disorders.

A second less apparent difference between rat IgG and goat IgG (Pizzo *et al.*, 2018) was access to the spinal perivascular spaces—while subtle, it appeared that goat IgG actually had greater perivascular access (particularly to the spinal gray matter) but rat IgG was mostly excluded from spinal perivascular spaces. A recent study found no apparent ultrastructural differences between the spinal perivascular spaces (Lam *et al.*, 2017) and previously reported cerebral perivascular spaces. Specific reasons for poor rat IgG entry into spinal perivascular spaces are not obvious, but it is clear is that the spinal cord may not utilize the same receptor-mediated IgG shuttling into the spinal perivascular spaces we showed for the brain, which likely has interesting physiological explanations and important clinical implications.

Third, rat IgG showed a slightly but significantly lower plasma concentration after infusion compared to goat IgG (Student's two-tailed t-test, $p<0.05$). While the differences are small and could possibly be attributed to error in the standard curve or detection method, one might speculate that there may be Fc receptor-mediated mechanisms for prolonging IgG half-life in the CSF. Rat

IgG may also simply have a lower availability to drain out of the CNS because more rat IgG enters the brain tissue along perivascular spaces, leaving less in the CSF to drain into the blood. On the other hand, infusion of rat IgG with excess unlabeled rat IgG showed a slight but significantly reduced plasma concentration compared to IgG infusion alone (1.3-fold), which could suggest a receptor-mediated *efflux* of IgG from the CSF. Fc receptor-mediated clearance from the central compartment has been suggested by some studies (Bergman *et al.*, 1998; Schlachetzki *et al.*, 2002; Deane *et al.*, 2005; Cooper *et al.*, 2013) but refuted by others (Garg & Balthasar, 2009; Abuqayyas & Balthasar, 2013; Chen *et al.*, 2014), likely highlighting the complicated nature of these studies and the role of Fc receptors.

The impact of primary brain tumors on the intrathecal distribution of rat IgG in the brain

The number of clinical trials ongoing in children and adults utilizing CSF-administered antibodies and other larger proteins is surprising considering the paucity of preclinical data describing CNS distribution in animal models (healthy or diseased) or predicted distributions in larger human brains. In the present study we reported significantly reduced brain distribution of rat IgG following intrathecal infusion in athymic nude rats implanted with human U87 malignant glioma cells. No intrathecally-infused IgG was present within the tumor and perivascular transport was reduced on both ipsilateral and contralateral hemispheres and at sites several millimeters from the tumor. Co-infusion of mannitol intrathecally did not provide any delivery benefit. While there clearly an overall decrease in delivery in tumor-bearing animals, there was also some variability—certain glioma animals had a relatively ‘good’ distribution compared to other glioma animals. There was no apparent correlation between distribution and tumor size (i.e., some animals with large tumors had better distribution than other animals with smaller tumors), time post-implantation (i.e., animals implanted on the same day and intrathecally infused on the same day showed differences in the distribution), or tumor contact with CSF spaces (i.e., if the tumor contacted the ventricles or subarachnoid space). Interestingly, there was one correlative factor—two glioma animals with a strikingly 'poor' distribution (Fig. 6, second and fourth columns) from the rat IgG group or rat IgG with mannitol groups also had substantially lower levels of IgG in the plasma compared to the average for their treatment group (see Fig. 6 legend). There were no obvious reasons for these differences in terms of surgery or animal condition. Perhaps the differences reflect different states of Fc receptor expression and function, which appear to be involved in perivascular transport and potentially IgG efflux from the central compartment. Alternatively, these animals may have significantly altered CSF dynamics (e.g., reduced production rate or stagnation) which would likely impact brain delivery and clearance from the central compartment.

Several possible factors may have contributed to the lack of rat IgG transport to the brain tumor a well as reduced transport into the brain distant from the tumor, including: altered pressure gradients, disruption of Fc receptor-mediated transport, and additional physical barriers. First, a lack of signal in the tumor itself may be due in part to changes in the pressure differential in the brain. Elsewhere in the body, it has been demonstrated that tumor interstitial pressure is high compared to surrounding tissue, attributed in part to high permeability of tumor vasculature and a lack of functional lymphatic drainage of the interstitium (Baxter & Jain, 1989; Ferretti *et al.*, 2009; Stylianopoulos *et al.*, 2013). In the intracranial compartment, brain tumor interstitial pressure has been demonstrated to be elevated compared to the interstitial pressure of the normal cortex (with some dependence on tumor size), presumably driven by the same mechanisms of high vascular permeability and poor lymphatic drainage (Boucher *et al.*, 1997). Thus, for some tumors, the outwardly-directed pressure gradient would be to push fluid away from the tumor toward the CSF, opposing transport of CSF-borne IgG into the tumor. Intrathecal mannitol might even be expected to worsen tumor delivery by creating an osmotic gradient that encouraged fluid movement from the circulation/tumor toward the hyperosmolar CSF, opposing transport of IgG from CSF to brain/tumor. Indeed, systemic treatment of rodents with furosemide showed reduced pressure in both the tumor and the normal brain; however, in some cases the pressure gradient between the tumor/brain was maintained (Boucher *et al.*, 1997), which may still hinder CSF-to-brain delivery, and systemic mannitol would be expected to show similar results. In the present study, lower plasma concentration of IgG in glioma animals compared to normal animals also supports the idea that IgG is unable to *reach* the tumor, rather than suggesting that intrathecal IgG enters the tumor and then sinks into systemic circulation. Increased intracranial pressure caused by the mass effect of the growing brain tumor (Wasserstrom *et al.*, 1982; Boucher *et al.*, 1997) may induce compensatory mechanisms to balance intracranial pressure, potentially including altered CSF production, circulation, and/or drainage as well as changes in cerebral blood flow, which may impact transport within the CSF and perivascular spaces. Again, alterations in intracranial pressure are likely to disrupt the perivascular transport if it is convective (driven by a pressure gradient) in nature.

Second, it was evident that the blood-tumor barrier was permeable to systemic IgG and allowed IgG to distribute throughout the tumor and potentially into the CSF compartment. Systemic IgG may have thus competed with intrathecal IgG for Fc receptor-mediated perivascular access. However, infusion of IgG with excess unlabeled IgG in normal animals revealed a uniquely different pattern of IgG distribution, particularly at the pial surface but also in the perivascular spaces. Confocal imaging in glioma animals did not show these abnormalities, perhaps suggesting no significant competition. Competition for potentially receptor-mediated clearance pathways (as demonstrated by lower plasma concentration of IgG when IgG was infused with an excess of unlabeled IgG) contribute to the 2.6-fold lower plasma concentration of IgG in glioma animals compared to normal animals (though may not be sufficient to explain the large difference). Data from humans showed that approximately 59% or 46% of brain tumor patients showed elevated IgG levels depending on whether the tumor was protruding into the ventricles or not, with average CSF levels of IgG elevated nearly 6-fold in all patients with brain tumors (average CSF IgG concentration: 0.153 μM or 0.873 μM IgG, in normal controls and brain tumor patients, respectively; (Rao & Böker, 1987), suggesting competition is certainly possible. Additionally, expression of Fc receptors could be altered (as demonstrated here for FcγRIIb) so that receptor-mediated transport into the perivascular is reduced; even if receptor-mediated transport is functional the drivers of perivascular transport may be disrupted (e.g., altered pressure gradients) thus the distribution may still be severely impacted.

Third, physical barriers may also contribute to poor delivery into the tumor and within the tumor. The astrocytic border around the tumor may hinder diffusion between the surrounding brain and the tumor and the increased laminin basement membrane in the tumor could make diffusion within the tumor more difficult; indeed, measurements of the extracellular space in excised human brain tumors have shown increased extracellular space volume but also increased tortuosity (a measure of hindrance of molecule movement) within the tumor in part attributed to increased extracellular matrix (Vargová *et al.*, 2003). *In vivo*, however, factors such as vascular permeability have been suggested to cause an outwardly-directed convection in the tumor interstitium (Baxter & Jain, 1989). Perivascular transport may also be physically obstructed by cancer cells in the ‘perivascular niche’ (Calabrese *et al.*, 2007; Gilbertson & Rich, 2007; Winkler, 2017). In 1938 Scherer (Scherer,

1938) described specific preferential pathways (now known as Scherer's secondary structures) for the invasion of glioma cells in the brain along perivascular spaces, the subpial space, nerves, and white matter tracts—remarkably, the very same pathways thought to be involved in rapid CSF transport (Cserr *et al.*, 1977; Szentistványi *et al.*, 1984; Ichimura *et al.*, 1991). Numerous additional studies have demonstrated via both *ex vivo* and *in vivo* imaging methods that tumor cells utilize the perivascular spaces for migration and vascular co-option using rodent/human cell lines and patient-derived tumor cells in models of primary and metastatic brain cancer, as well as in genetically engineering models with *de novo* brain tumor formation (Olson *et al.*, 1974; Nagano *et al.*, 1993; Holash *et al.*, 1999; Farin *et al.*, 2006; Winkler *et al.*, 2009; Baker *et al.*, 2014; Watkins *et al.*, 2014). The CSF and its communication with the perivascular space has even been suggested as a way for tumor cells to disseminate to distant brain sites (Thorsen & Tysnes, 1997); indeed, it has been demonstrated that human leptomeningeal tumors involve many of the areas we visualize CSF tracers accessing—the perivascular spaces, CSF cisterns, subpial space, and cranial and spinal nerve roots (Olson *et al.*, 1974), and these routes could also play a role in the development of extracranial metastases (e.g., (Rickert, 2003)). However, it is unlikely that perivascular obstruction plays a significant role in our study because U87 tumors tend to grow in a single large mass without the infiltrative borders typical of glioblastoma and no tumor cells were detected with the human nuclei marker outside of the main mass.

Conclusions

We feel the data provided herein is critical for interpretation of preclinical and clinical pharmacodynamic response and for future guidance to improve drug delivery strategies. It also made it clear that it is vital to understand how pathological changes in the brain are likely to impact intrathecal delivery to predict the likelihood of success.

References

Abbas AK, Lichtman AH & Pillai S (2015). *Cellular and Molecular Immunology*, 8th edn.ed. Abbas AK, Lichtman AH & Pillai S. Elsevier Saunders, Philadelphia.

Abbott NJ (2004). Evidence for bulk flow of brain interstitial fluid: significance for physiology and pathology. *Neurochem Int* **45,** 545–552.

Abbott NJ, Pizzo ME, Preston JE, Janigro D & Thorne RG (2018). The role of brain barriers in fluid movement in the CNS: is there a 'glymphatic' system? *Acta Neuropathol* **135,** 387–407.

Abuqayyas L & Balthasar JP (2013). Investigation of the role of FcγR and FcRn in mAb distribution to the brain. *Mol Pharm* **10,** 1505–1513.

Arbel-Ornath M, Hudry E, Eikermann-Haerter K, Hou S, Gregory JL, Zhao L, Betensky R a., Frosch MP, Greenberg SM & Bacskai BJ (2013). Interstitial fluid drainage is impaired in ischemic stroke and Alzheimer's disease mouse models. *Acta Neuropathol* **126,** 353–364.

Asgari M, de Zélicourt D & Kurtcuoglu V (2016). Glymphatic solute transport does not require bulk flow. *Sci Rep* **6,** 38635.

Aspelund A, Antila S, Proulx ST, Karlsen TV, Karaman S, Detmar M, Wiig H & Alitalo K (2015). A dural lymphatic vascular system that drains brain interstitial fluid and macromolecules. *J Exp Med* **212,** 991–999.

Baker GJ, Yadav VN, Motsch S, Koschmann C, Calinescu A-A, Mineharu Y, Camelo-Piragua SI, Orringer D, Bannykh S, Nichols WS, deCarvalho AC, Mikkelsen T, Castro MG & Lowenstein PR (2014). Mechanisms of Glioma Formation: Iterative Perivascular Glioma Growth and Invasion Leads to Tumor Progression, VEGF-Independent Vascularization, and Resistance to Antiangiogenic Therapy. *Neoplasia* **16,** 543–561.

Baxter LT & Jain RK (1989). Transport of fluid and macromolecules in tumors. I. Role of interstitial pressure and convection. *Microvasc Res* **37,** 77–104.

Bechmann I, Priller J, Kovac A, Böntert M, Wehner T, Klett FF, Bohsung J, Stuschke M, Dirnagl U & Nitsch R (2001). Immune surveillance of mouse brain perivascular spaces by blood-borne macrophages. *Eur J Neurosci* **14,** 1651–1658.

Bedussi B, van der Wel NN, de Vos J, van Veen H, Siebes M, VanBavel E & Bakker EN (2017). Paravascular channels, cisterns, and the subarachnoid space in the rat brain: A single compartment with preferential pathways. *J Cereb Blood Flow Metab* **37,** 1374–1385.

Bergman I, Burckart GJ, Pohl CR, Venkataramanan R, Barmada MA, Griffin JA & Cheung NK (1998). Pharmacokinetics of IgG and IgM anti-ganglioside antibodies in rats and monkeys after intrathecal administration. *J Pharmacol Exp Ther* **284,** 111–115.

Boucher Y, Salehil H, Witwerl B, Harsh G & Jain R (1997). Interstitial fluid pressure in intracranial tumours in patients and in rodents. *Br Joumal Cancer* **75,** 829–836.

Bradbury MW & Westrop RJ (1983). Factors influencing exit of substances from cerebrospinal fluid into deep cervical lymph of the rabbit. *J Physiol* **339,** 519–534.

Broadwell RD & Sofroniew M V (1993). Serum proteins bypass the blood-brain fluid barriers for extracellular entry to the central nervous system. *Exp Neurol* **120,** 245–263.

Calabrese C, Poppleton H, Kocak M, Hogg TL, Fuller C, Hamner B, Oh EY, Gaber MW, Finklestein D, Allen M, Frank A, Bayazitov IT, Zakharenko SS, Gajjar A, Davidoff A & Gilbertson RJ (2007). A perivascular niche for brain tumor stem cells. *Cancer Cell* **11,** 69–82.

Carare RO, Bernardes-Silva M, Newman TA, Page AM, Nicoll JAR, Perry VH & Weller RO (2008). Solutes, but not cells, drain from the brain parenchyma along basement membranes of capillaries and arteries: significance for cerebral amyloid angiopathy and neuroimmunology. *Neuropathol Appl Neurobiol* **34,** 131–144.

Chaudhury C, Brooks CL, Carter DC, Robinson JM & Anderson CL (2006). Albumin Binding to FcRn : Distinct from the FcRn − IgG Interaction. *Biochemistry* **45,** 4983–4990.

Chen N, Wang W, Fauty S, Fang Y, Hamuro L, Hussain A & Prueksaritanont T (2014). The effect of the neonatal Fc receptor on human IgG biodistribution in mice. **6,** 1–7.

Clark PA, Iida M, Treisman DM, Kalluri H, Ezhilan S, Zorniak M, Wheeler DL & Kuo JS (2012). Activation of Multiple ERBB Family Receptors Mediates Glioblastoma Cancer Stem-like Cell Resistance to EGFR-Targeted Inhibition. *Neoplasia* **14,** 420-IN13.

Cloyd MW & Low FN (1974). Scanning electron microscopy of the subarachnoid space in the dog. I. Spinal cord levels. *J Comp Neurol* **153,** 325–368.

Cooper PR, Ciambrone GJ, Kliwinski CM, Maze E, Johnson L, Li Q, Feng Y & Hornby PJ (2013). Efflux of monoclonal antibodies from rat brain by neonatal Fc receptor, FcRn. *Brain Res* **1534,** 13–21.

Cserr HF, Cooper DN & Milhorat TH (1977). Flow of cerebral interstitial fluid as indicated by the removal of extracellular markers from rat caudate nucleus. *Exp Eye Res* **25 Suppl,** 461–473.

Cserr HF & Knopf PM (1992). Cervical lymphatics, the blood-brain barrier and the immunoreactivity of the brain: a new view. *Immunol Today* **13,** 507–512.

Davson H & Segal MB (1995). *Phyioslogy of the CSF and Blood-Brain Barriers*, 1st edn.ed. Davson H & Segal MB. CRC Press, Inc, Boca Raton.

Deane R, Sagare A, Hamm K, Parisi M, LaRue B, Guo H, Wu Z, Holtzman DM & Zlokovic B V (2005). IgG-assisted age-dependent clearance of Alzheimer's amyloid beta peptide by the blood-brain barrier neonatal Fc receptor. *J Neurosci* **25,** 11495–11503.

Engelhardt B, Vajkoczy P & Weller RO (2017). The movers and shapers in immune privilege of the CNS. *Nat Immunol* **18,** 123–131.

Faber WM (1937). The nasal mucosa and the subarachnoid space. *Am J Anat* **62,** 121–148.

Fabry Z, Schreiber H a., Harris MG & Sandor M (2008). Sensing the microenvironment of the central nervous system: immune cells in the central nervous system and their pharmacological manipulation. *Curr Opin Pharmacol* **8,** 496–507.

Farin A, Suzuki SO, Weiker M, Goldman JE, Bruce JN & Canoll P (2006). Transplanted glioma cells migrate and proliferate on host brain vasculature: a dynamic analysis. *Glia* **53,** 799–808.

Fenstermacher JD, Nagaraja TN, Wei L & Ghersi-Egea J-F (1999). Surprises and peculiarities in the distribution of material from cerebrospinal fluid to brain tissues and blood. In *Brain Barrier Systems: Alfred Benzon Symposium*, pp. 494–505. Munksgaard, Copenhagen.

Ferretti S, Allegrini PR, Becquet MM & McSheehy PM (2009). Tumor interstitial fluid pressure as an early-response marker for anticancer therapeutics. *Neoplasia* **11,** 874–881.

Firan M, Bawdon R, Radu C, Ober RJ, Eaken D, Antohe F, Ghetie V & Ward ES (2001). The MHC class I-related receptor, FcRn, plays an essential role in the maternofetal transfer of γ-globulin in humans. *Int Immunol* **13,** 993–1002.

Frederickson RG & Low FN (1969). Blood vessels and tissue space associated with the brain of the rat. *Am J Anat* **125,** 123–145.

Furukawa M, Shimoda H, Kajiwara T, Kato S & Yanagisawa S (2008). Topographic study on nerve-associated lymphatic vessels in the murine craniofacial region by immunohistochemistry and electron microscopy. *Biomed Res* **29,** 289–296.

Garg A & Balthasar JP (2009). Investigation of the influence of FcRn on the distribution of IgG to the brain. *AAPS J* **11,** 553–557.

Gilbertson RJ & Rich JN (2007). Making a tumour's bed: glioblastoma stem cells and the vascular niche. *Nat Rev Cancer* **7,** 733–736.

Hannocks M-J, Pizzo ME, Huppert J, Deshpande T, Abbott NJ, Thorne RG & Sorokin L (2018). Molecular characterization of perivascular drainage pathways in the murine brain. *J Cereb Blood Flow Metab* **38,** 669–686.

Hannocks M-J, Pizzo ME, Huppert J, Despande T, Abbott NJ, Thorne RG & Sorokin L (2017). Molecular characterization of perivascular drainage pathways in the murine brain. *J Cereb Blood Flow Metab*.

Hawkes CA, Gatherer M, Sharp MM, Dorr A, Yuen HM, Kalaria R, Weller RO & Carare RO (2013). Regional differences in the morphological and functional effects of aging on cerebral basement membranes and perivascular drainage of amyloid-β from the mouse brain. *Aging Cell* **12,** 224–236.

Hawkes CA, Härtig W, Kacza J, Schliebs R, Weller RO, Nicoll JAR & Carare RO (2011). Perivascular drainage of solutes is impaired in the ageing mouse brain and in the presence of cerebral amyloid angiopathy. *Acta Neuropathol* **121,** 431–443.

Hawkes CA, Sullivan PM, Hands S, Weller RO, Nicoll JAR & Carare RO (2012). Disruption of arterial perivascular drainage of amyloid-β from the brains of mice expressing the human APOE ε4 allele. *PLoS One* **7,** e41636.

Holash J, Maisonpierre PC, Compton D, Boland P, Alexander CR, Zagzag D, Yancopoulos GD & Wiegand SJ (1999). Vessel cooption, regression, and growth in tumors mediated by angiopoietins and VEGF. *Science* **284,** 1994–1998.

Holliger P & Hudson PJ (2005). Engineered antibody fragments and the rise of single domains. *Nat Biotechnol* **23,** 1126–1136.

Holter KE, Kehlet B, Devor A, Sejnowski TJ, Dale AM, Omholt SW, Ottersen OP, Nagelhus EA, Mardal K-A & Pettersen KH (2017). Interstitial solute transport in 3D reconstructed neuropil occurs by diffusion rather than bulk flow. *Proc Natl Acad Sci U S A* **114,** 9894–9899.

Ichimura T, Fraser PAA & Cserr HF (1991). Distribution of extracellular tracers in perivascular spaces of the rat brain. *Brain Res* **545,** 103–113.

Iliff JJ, Chen MJ, Plog BA, Zeppenfeld DM, Soltero M, Yang L, Singh I, Deane R & Nedergaard M (2014). Impairment of Glymphatic Pathway Function Promotes Tau Pathology after Traumatic Brain Injury. *J Neurosci* **34,** 16180–16193.

Iliff JJ, Wang M, Liao Y, Plogg BA, Peng W, Gundersen GA, Benveniste H, Vates GE, Deane R, Goldman SA, Nagelhus EA & Nedergaard M (2012). A paravascular pathway facilitates CSF flow through the brain parenchyma and the clearance of interstitial solutes, including amyloid ?? *Sci Transl Med*; DOI: 10.1126/scitranslmed.3003748.

Jin B-J, Smith AJ & Verkman AS (2016). Spatial model of convective solute transport in brain extracellular space does not support a "glymphatic" mechanism. *J Gen Physiol* **148,** 489–501.

Jones EA & Waldmann TA (1972). The mechanism of intestinal uptake and transcellular transport of IgG in the neonatal rat. *J Clin Invest* **51,** 2916–2927.

Jones EG (1970). On the mode of entry of blood vessels into the cerebral cortex. *J Anat* **106,** 507–520.

Kida S, Pantazis A & Weller RO (1993). CSF drains directly from the subarachnoid space into nasal lymphatics in the rat. Anatomy, histology and immunological significance. *Neuropathol Appl Neurobiol* **19,** 480–488.

Knopf PM, Cserr HF, Nolan SC, Wu TY & Harling-Berg CJ (1995). Physiology and immunology of lymphatic drainage of interstitial and cerebrospinal fluid from the brain. *Neuropathol Appl Neurobiol* **21,** 175–180.

Knudsen Sand KM, Bern M, Nilsen J, Noordzij HT, Sandlie I & Andersen JT (2015). Unraveling the interaction between FcRn and albumin: Opportunities for design of albumin-based therapeutics. *Front Immunol*; DOI: 10.3389/fimmu.2014.00682.

Koenigsknecht-Talboo J, Meyer-Luehmann M, Parsadanian M, Garcia-Alloza M, Finn MB, Hyman BT, Bacskai BJ & Holtzman DM (2008). Rapid microglial response around amyloid pathology after systemic anti-Abeta antibody administration in PDAPP mice. *J Neurosci* **28,** 14156–14164.

Koh L, Zakharov A & Johnston M (2005). Integration of the subarachnoid space and lymphatics: is it time to embrace a new concept of cerebrospinal fluid absorption? *Cerebrospinal Fluid Res* **2,** 6.

Kress BT, Iliff JJ, Xia M, Wang M, Wei Bs HS, Zeppenfeld D, Xie L, Hongyi Kang BS, Xu Q, Liew JA, Plog BA, Ding F, PhD RD & Nedergaard M (2014). Impairment of paravascular clearance pathways in the aging brain.

Ann Neurol **76,** 845–861.

Kristoffersen EK & Matre R (1996). Co-localization of the neonatal Fc gamma receptor and IgG in human placental term syncytiotrophoblasts. *Eur J Immunol* **26,** 1668–1671.

Lam MA, Hemley SJ, Najafi E, Vella NGF, Bilston LE & Stoodley MA (2017). The ultrastructure of spinal cord perivascular spaces: Implications for the circulation of cerebrospinal fluid. *Sci Rep* **7,** 12924.

Latvala S, Jacobsen B, Otteneder MB, Herrmann A & Kronenberg S (2017). Distribution of FcRn Across Species and Tissues. *J Histochem Cytochem* **65,** 321–333.

Leach JL, Sedmak DD, Osborne JM, Rahill B, Lairmore MD & Anderson CL (1996). Isolation from human placenta of the IgG transporter, FcRn, and localization to the syncytiotrophoblast: implications for maternal-fetal antibody transport. *J Immunol* **157,** 3317–3322.

Levin VA, Fenstermacher JD & Patlak CS (1970). Sucrose and inulin space measurements of cerebral cortex in four mammalian species. *Am J Physiol* **219,** 1528–1533.

Louveau A, Smirnov I, Keyes TJ, Eccles JD, Rouhani SJ, Peske JD, Derecki NC, Castle D, Mandell JW, Lee KS, Harris TH & Kipnis J (2015). Structural and functional features of central nervous system lymphatic vessels. *Nature* **523,** 337–341.

Morris AWJ, Sharp MM, Albargothy NJ, Fernandes R, Hawkes CA, Verma A, Weller RO & Carare RO (2016). Vascular basement membranes as pathways for the passage of fluid into and out of the brain. *Acta Neuropathol*; DOI: 10.1007/s00401-016-1555-z.

Nabeshima S, Reese TS, Landis DM & Brightman MW (1975). Junctions in the meninges and marginal glia. *J Comp Neurol* **164,** 127–169.

Nagano N, Sasaki H, Aoyagi M & Hirakawa K (1993). Invasion of experimental rat brain tumor: early morphological changes following microinjection of C6 glioma cells. *Acta Neuropathol* **86,** 117–125.

Nedergaard M (2013). Garbage truck of the brain. *Science (80-)* **340,** 1529–1530.

Nicholson C & Phillips JM (1981). Ion diffusion modified by tortuosity and volume fraction in the extracellular microenvironment of the rat cerebellum. *J Physiol* **321,** 225–257.

Nicholson C & Tao L (1993). Hindered diffusion of high molecular weight compounds in brain extracellular microenvironment measured with integrative optical imaging. *Biophys J* **65,** 2277–2290.

Nyland H (1982). Properties of Fc gamma receptors in the human central nervous system. *Acta Pathol Microbiol Immunol Scand C* **90,** 171–177.

Oda Y & Nakanishi I (1984). Ultrastructure of the mouse leptomeninx. *J Comp Neurol* **225,** 448–457.

Olson ME, Chernik NL & Posner JB (1974). Infiltration of the leptomeninges by systemic cancer. A clinical and pathologic study. *Arch Neurol* **30,** 122–137.

Patlak CS & Fenstermacher JD (1975). Measurements of dog blood-brain transfer constants by ventriculocisternal perfusion. *Am J Physiol* **229,** 877–884.

Paxinos G & Watson C (2007). *The Rat Brain in Stereotaxic Coordinates*, 6th edn. Academic Press, London. Available at: papers2://publication/uuid/ABC971ED-EB36-4DA4-8BB6-02C64513013F.

Peress NS, Siegelman J, Fleit HB, Fanger MW & Perillo E (1989). Monoclonal antibodies identify three IgG Fc receptors in normal human central nervous system. *Clin Immunol Immunopathol* **53,** 268–280.

Pizzo ME, Wolak DJ, Kumar NN, Brunette E, Brunnquell CL, Hannocks M-J, Abbott NJ, Meyerand ME, Sorokin L, Stanimirovic DB & Thorne RG (2018). Intrathecal antibody distribution in the rat brain: surface diffusion, perivascular transport and osmotic enhancement of delivery. *J Physiol* **596,** 445–475.

Preston JE (2001). Ageing choroid plexus-cerebrospinal fluid system. *Microsc Res Tech* **52,** 31–37.

Pyzik M, Rath T, Lencer WI, Baker K & Blumberg RS (2015). FcRn: The Architect Behind the Immune and Nonimmune Functions of IgG and Albumin. *J Immunol* **194,** 4595–4603.

Rall DP, Oppelt WW & Patlak CS (1962). Extracellular space of brain as determined by diffusion of inulin from the ventricular system. *Life Sci* **1,** 43–48.

Ransohoff RM & Engelhardt B (2012). The anatomical and cellular basis of immune surveillance in the central nervous system. *Nat Rev Immunol* **12,** 623–635.

Rao ML & Böker DK (1987). Cerebrospinal fluid and serum levels of albumin, IgG, IgA and IgM in patients with intracranial tumors and lumbar disc herniation. *Eur Neurol* **26,** 241–245.

Ravetch J V & Bolland S (2001). IgG Fc receptors. *Annu Rev Immunol* **19,** 275–290.

Restrepo A, Smith CA, Agnihotri S, Shekarforoush M, Kongkham PN, Seol HJ, Northcott P & Rutka JT (2011). Epigenetic regulation of glial fibrillary acidic protein by DNA methylation in human malignant gliomas. *Neuro Oncol* **13,** 42–50.

Rickert CH (2003). Extraneural metastases of paediatric brain tumours. *Acta Neuropathol* **105,** 309–327.

Rodewald R (1976). pH-dependent binding of immunoglobulins to intestinal cells of the neonatal rat. *J Cell Biol* **71,** 666–669.

Roopenian DC & Akilesh S (2007). FcRn: the neonatal Fc receptor comes of age. *Nat Rev Immunol* **7,** 715–725.

Roux KH, Strelets L & Michaelsen TE (1997). Flexibility of human IgG subclasses. *J Immunol* **159,** 3372–3382.

Scherer HJ (1938). Structural development in gliomas. *Am J Cancer* **34,** 333–351.

Schindelin J, Arganda-Carreras I, Frise E, Kaynig V, Longair M, Pietzsch T, Preibisch S, Rueden C, Saalfeld S, Schmid B, Tinevez J-Y, White DJ, Hartenstein V, Eliceiri K, Tomancak P & Cardona A (2012). Fiji: an open-source platform for biological-image analysis. *Nat Methods* **9,** 676–682.

Schlachetzki F, Zhu C & Pardridge WM (2002). Expression of the neonatal Fc receptor (FcRn) at the blood-brain barrier. *J Neurochem* **81,** 203–206.

Silver DJ, Siebzehnrubl FA, Schildts MJ, Yachnis AT, Smith GM, Smith AA, Scheffler B, Reynolds BA, Silver J & Steindler DA (2013). Chondroitin Sulfate Proteoglycans Potently Inhibit Invasion and Serve as a Central Organizer of the Brain Tumor Microenvironment. *J Neurosci* **33,** 15603–15617.

Simister NE, Story CM, Chen HL & Hunt JS (1996). An IgG-transporting Fc receptor expressed in the syncytiotrophoblast of human placenta. *Eur J Immunol* **26,** 1527–1531.

Stylianopoulos T, Martin JD, Snuderl M, Mpekris F, Jain SR & Jain RK (2013). Coevolution of solid stress and interstitial fluid pressure in tumors during progression: implications for vascular collapse. *Cancer Res* **73,** 3833–3841.

Szentistványi I, Patlak CS, Ellis RA & Cserr HF (1984). Drainage of interstitial fluid from different regions of rat brain. *Am J Physiol* **246,** 35–44.

Thorne RG, Hrabetová S & Nicholson C (2004). Diffusion of epidermal growth factor in rat brain extracellular space measured by integrative optical imaging. *J Neurophysiol* **92,** 3471–3481.

Thorne RG, Lakkaraju A, Rodriguez-Boulan E & Nicholson C (2008). In vivo diffusion of lactoferrin in brain extracellular space is regulated by interactions with heparan sulfate. *Proc Natl Acad Sci USA* **105,** 8416–8421.

Thorne RG & Nicholson C (2006). In vivo diffusion analysis with quantum dots and dextrans predicts the width of brain extracellular space. *Proc Natl Acad Sci USA* **103,** 5567–5572.

Thorsen F & Tysnes BB (1997). Brain tumor cell invasion, anatomical and biological considerations. *Anticancer Res* **17,** 4121–4126.

Vargová L, Homola A, Zámecník J, Tichý M, Benes V & Syková E (2003). Diffusion parameters of the extracellular space in human gliomas. *Glia* **42,** 77–88.

Vidarsson G, Dekkers G & Rispens T (2014). IgG subclasses and allotypes: From structure to effector functions. *Front Immunol*; DOI: 10.3389/fimmu.2014.00520.

Wasserstrom WR, Glass JP & Posner JB (1982). Diagnosis and treatment of leptomeningeal metastases from solid tumors: experience with 90 patients. *Cancer* **49,** 759–772.

Watkins S, Robel S, Kimbrough IF, Robert SM, Ellis-Davies G & Sontheimer H (2014). Disruption of astrocyte-vascular coupling and the blood-brain barrier by invading glioma cells. *Nat Commun* **5,** 4196.

Weller RO, Kida S & Zhang ET (1992). Pathways of fluid drainage from the brain--morphological aspects and immunological significance in rat and man. *Brain Pathol* **2,** 277–284.

Winkler F (2017). Hostile takeover: how tumours hijack pre-existing vascular environments to thrive. *J Pathol* **242,** 267–272.

Winkler F, Kienast Y, Fuhrmann M, Von Baumgarten L, Burgold S, Mitteregger G, Kretzschmar H & Herms J (2009). Imaging glioma cell invasion in vivo reveals mechanisms of dissemination and peritumoral angiogenesis. *Glia* **57,** 1306–1315.

Wolak DJ, Pizzo ME & Thorne RG (2015*a*). Probing the extracellular diffusion of antibodies in brain using in vivo integrative optical imaging and ex vivo fluorescence imaging. *J Control Release* **197,** 78–86.

Wolak DJ, Pizzo ME & Thorne RG (2015*b*). Probing the extracellular diffusion of antibodies in brain using in vivo integrative optical imaging and ex vivo fluorescence imaging. *J Control Release* **197,** 78–86.

Woof JM & Burton DR (2004). Human antibody–Fc receptor interactions illuminated by crystal structures. *Nat Rev Immunol* **4,** 89–99.

Yang L, Kress BT, Weber HJ, Thiyagarajan M, Wang B, Deane R, Benveniste H, Iliff JJ & Nedergaard M (2013). Evaluating glymphatic pathway function utilizing clinically relevant intrathecal infusion of CSF tracer. *J Transl Med* **11,** 107.

Zervas NT, Liszczak TM, Mayberg MR & Black PM (1982). Cerebrospinal fluid may nourish cerebral vessels through pathways in the adventitia that may be analogous to systemic vasa vasorum. *J Neurosurg* **56,** 475–481.

Zorniak M, Clark PA, Leeper HE, Tipping MD, Francis DM, Kozak KR, Salamat MS & Kuo JS (2012). Differential expression of 2′,3′-cyclic-nucleotide 3′-phosphodiesterase and neural lineage markers correlate with glioblastoma xenograft infiltration and patient survival. *Clin Cancer Res* **18,** 3628–3636.

Figure 1. Representative distribution of intrathecally-infused rat IgG on the surface of the brain and spinal cord. Ex vivo fluorescence imaging of rat IgG on the dorsal (A) and ventral (B) surfaces of the brain demonstrated association of IgG with major surface arteries (e.g., the middle cerebral artery, MCA; basilar artery, bas; and vertebral arteries; vert). High signal is also present at brain interfaces with CSF cisterns (e.g., olfactofrontal cistern, OFC; quadrigeminal cistern, QC) and around several cranial nerves/nerve roots (e.g., trochlear nerves, cranial nerve IV; hypoglossal nerves, cranial nerve VII). Widespread punctate signal is associated with perivascular spaces of penetrating vessels. Infusion of rat IgG with a 20:1 molar excess of unlabeled IgG (XIgG) shows signal in similar areas on the dorsal (C) and ventral (D) brain surface, including at interfaces with CSF cisterns and in association with major surface arteries. However, the signal on the

surface shows a very different pattern of signal, outlining numerous tortuously-shaped vessels on the surface (e.g., area around basilar artery) and demonstrating far fewer penetrating profiles. The dorsal (E) and ventral (F) surfaces of the spinal cord after rat IgG infusion revealed perivascular signal associated with surface vessels and penetrating vessels along the entire length of the spinal cord, with marked signal around each spinal nerve root. The surface of the dorsal (G) and ventral (H) spinal cord following infusion of rat IgG with excess unlabeled IgG showed similar distribution to the brain, with numerous tortuous vessels on the surface outlined by IgG signal and few penetrating profiles; signal around nerve roots was present but somewhat less apparent.

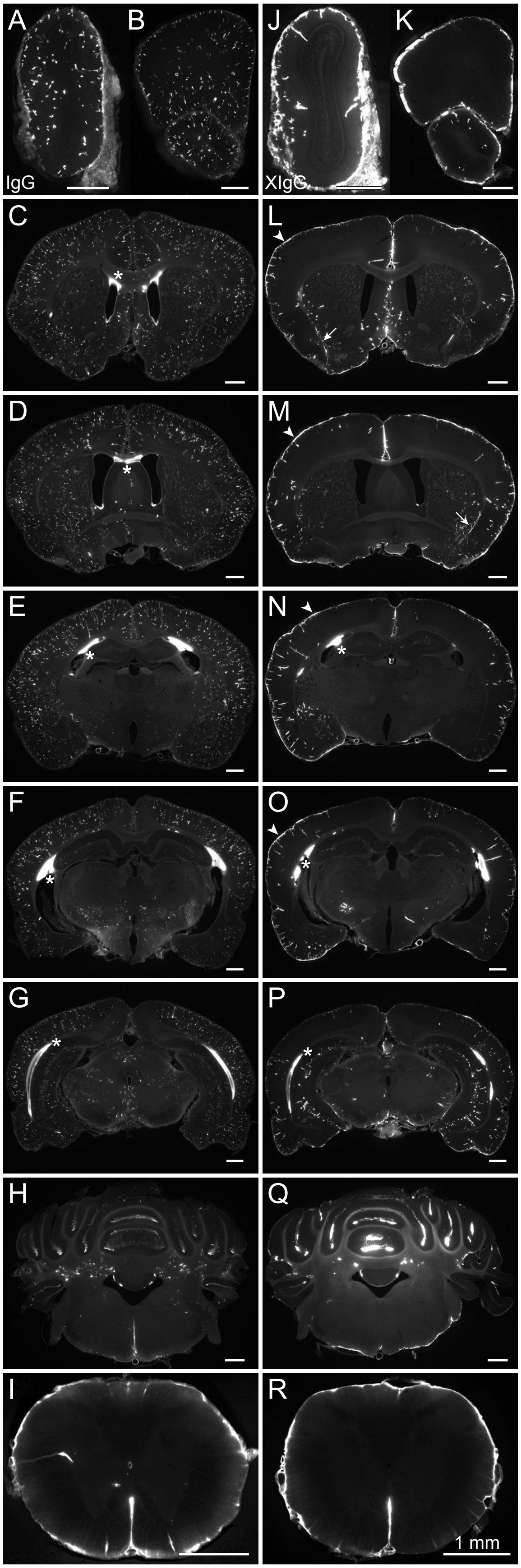

Figure 2. Representative ex vivo fluorescence imaging of intrathecally-infused rat IgG signal in coronal brain sections. (A-I) 100 µm sections of the brain after rat IgG infusion revealed widespread signal throughout most regions of the brain. (A) Olfactory bulbs showed signal associated with the olfactory nerve layer, and the olfactory bulbs and olfactory tract/frontal cortex had numerous perivascular profiles. (C-G) Perivascular signal was prominent in many brain regions including the cortex, lateral striatum, hypothalamus, and hippocampus; perivascular signal in the medial striatum and anterior thalamus was rare. Periventricular signal in the white matter adjacent to the lateral ventricles occurred in 3 of 4 animals (asterisks). (H) Signal in the cerebellum was predominantly in the interfolial spaces and within the deep cerebellar nuclei, while signal in the brainstem was generally scarce except along penetrating vessels of the putative basilar artery. (I) The spinal cord showed rare perivascular profiles, either penetrating from the surface to cross the white matter or along vessels in the spinal gray matter. (J-R) Rat IgG signal with infusion of a 20:1 molar excess of unlabeled rat IgG (XIgG) revealed striking differences in perivascular distribution—an accumulation of labeled rat IgG at the brain surface

was evident (arrowheads) and overall reduction in perivascular spaces accessed (particularly evident in the cortex and parts of the striatum and hypothalamus). Periventricular white matter was present in 4 of 5 animals, and certain brain areas maintained perivascular signal even with an excess of unlabeled IgG (e.g., anterior/medial areas like the diagonal band/medial septal nucleus, lenticulostriate vessels in striatum (arrows), and ventral brain areas like amygdala) relative to infusion of rat IgG alone. See (Pizzo et al., 2018) for additional discussion on potential origins of perivascular signal regional variability and periventricular white matter signal.

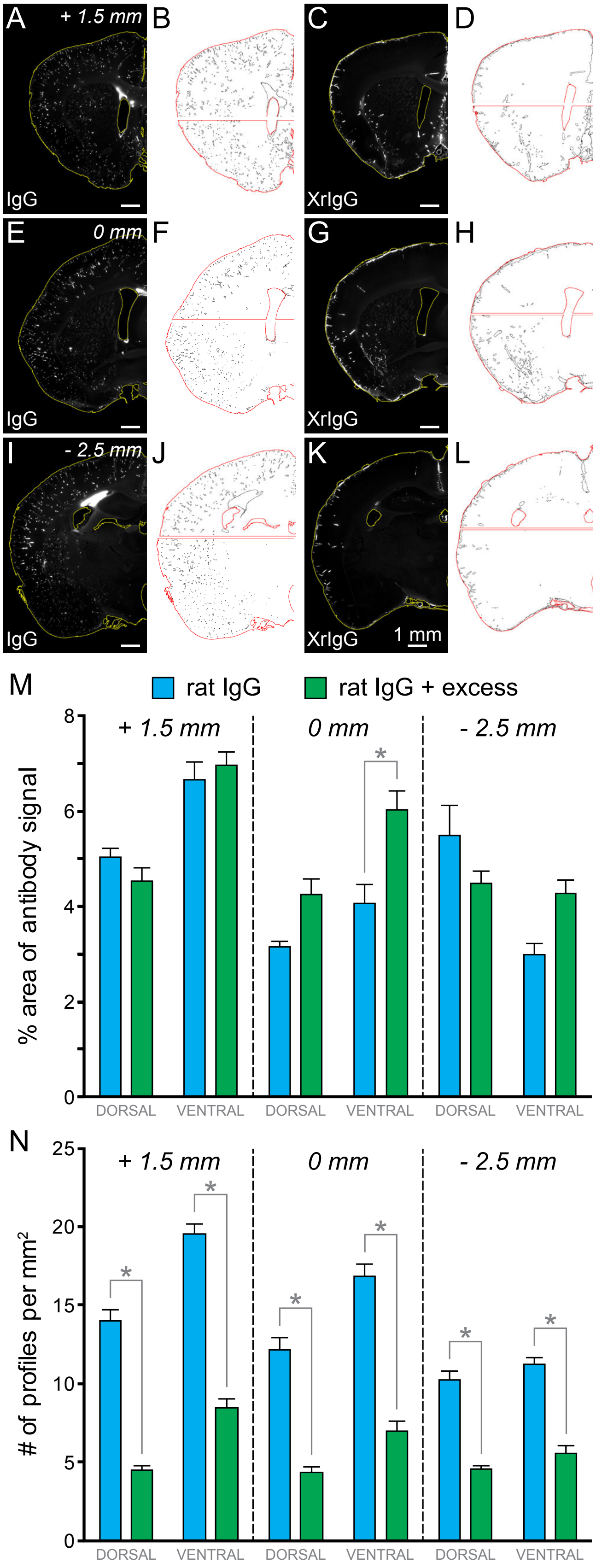

Figure 3. Quantification of perivascular fluorescent signal in coronal brain section images using Fiji. The whole coronal brain section was outlined (yellow or red) to determine the area of the section (with ventricular areas excluded). Each section was divided into a dorsal half and a ventral half by a horizontal line (described below). Fluorescent signal above a certain threshold (background autofluorescence from white matter) was detected within the section. (A-L) Eight sections per animal were analyzed approximately 1.5 mm anterior to bregma (± 1 mm) with the horizontal dorsal/ventral division line at approximately half the dorsal-ventral extent of the lateral ventricles. (E-H) Six sections per animal were analyzed at bregma (0 mm; ±0.5 mm) with the horizontal dorsal/ventral division line at approximately half the dorsal-ventral extent of the lateral ventricles. (I-L) Seven sections per animal were analyzed approximately 2.5 mm posterior to bregma (± 1 mm) with the horizontal dorsal/ventral division line placed just below the dorsal hippocampus and dorsal third ventricle. The percent area for the individual images were as follows:

(A-B) 5.7% dorsal, 3.6% ventral, (C-D) 4.2% dorsal, 6.3% ventral, (E-F) 2.6% dorsal, 1.5% ventral, (G-H) 5.0% dorsal, 6.1% ventral, (I-J) 5.5% dorsal, 1.2% ventral, (K-L) 5.5% dorsal, 3.7% ventral. The number of perivascular profiles per mm2 for the individual images were as follows: (A-B) 16.3 dorsal, 19.1 ventral, (C-D) 2.6 dorsal, 9.4 ventral, (E-F) 10.7 dorsal, 13.2 ventral, (G-H) 2.4 dorsal, 6.9 ventral, (I-J) 11.6 dorsal, 10.5 ventral, (K-L) 3.6 dorsal, 4.1 ventral. (M) Summary of the number of perivascular spaces per mm2 following intrathecal infusion of rat IgG (blue) or rat IgG with an excess of unlabeled IgG (green). The percent area of signal was not different between rat IgG versus rat IgG with excess for 5 of 6 brain regions. (N) Summary of the percent area of antibody signal following intrathecal infusion of rat IgG (blue) or rat IgG with an excess of unlabeled IgG (green). The number of perivascular spaces per mm2 was significantly greater for all 6 brain regions compared to rat IgG with an excess of unlabeled IgG. See Table 1 for details. (*) Denotes Kruskal-Wallis one-way analysis of variance on ranks ($p<0.001$) with Dunn's method post hoc pairwise comparison, $p<0.05$. $N=4$ animals for rat IgG and $N=5$ animals for rat IgG with excess.

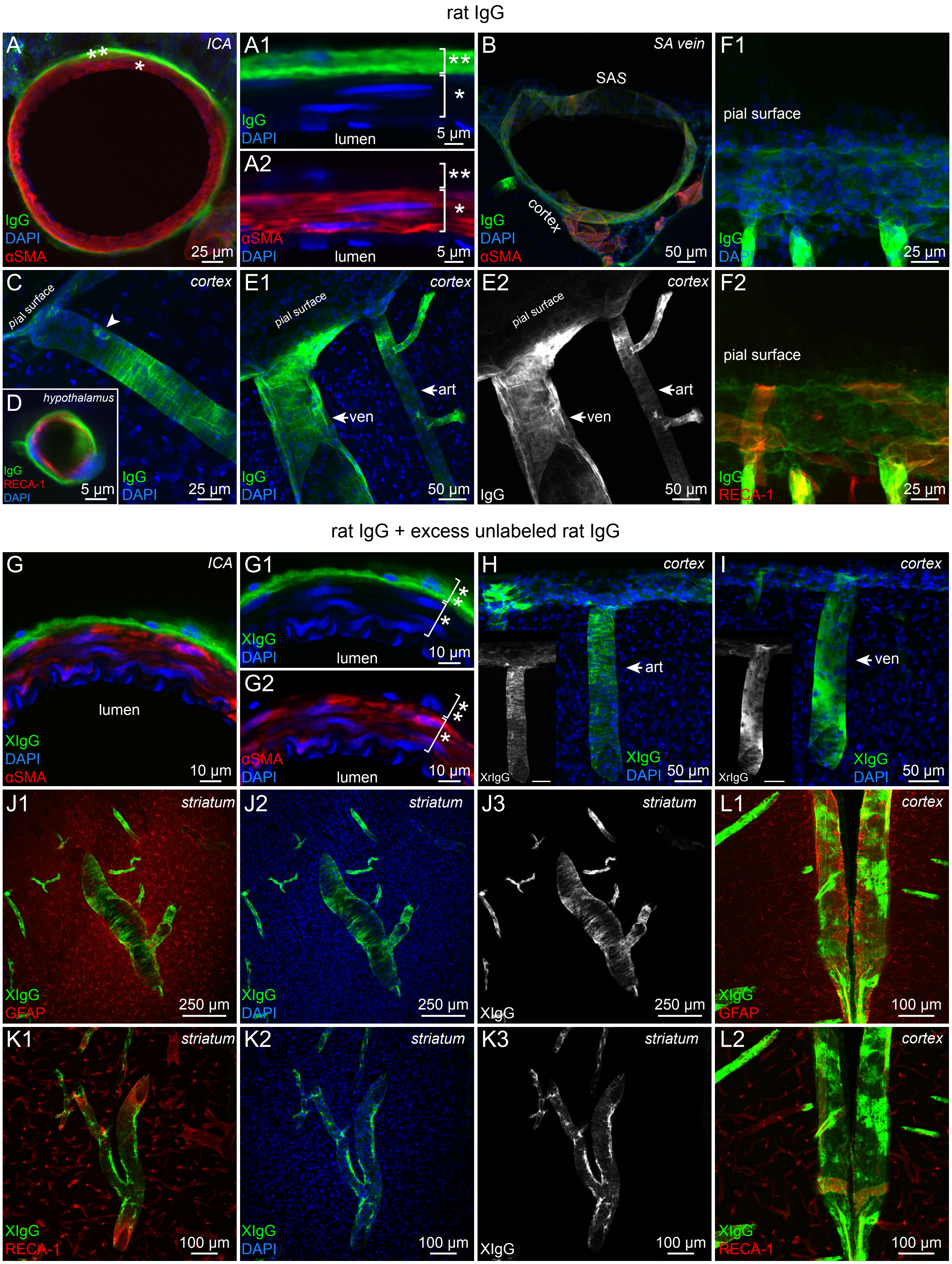
rat IgG
A
ICA
**
*
IgG
DAPI
αSMA
25 µm
A1
**
*
IgG
DAPI
lumen
5 µm
A2
**
*
αSMA
DAPI
lumen
5 µm
B
SA vein
SAS
cortex
IgG
DAPI
αSMA
50 µm
F1
pial surface
IgG
DAPI
25 µm
C
cortex
pial surface
D
hypothalamus
IgG
RECA-1
DAPI
5 µm
IgG
DAPI
25 µm
E1
cortex
pial surface
art
ven
IgG
DAPI
50 µm
E2
cortex
pial surface
art
ven
IgG
50 µm
F2
pial surface
IgG
RECA-1
25 µm
rat IgG + excess unlabeled rat IgG
G
ICA
lumen
XIgG
DAPI
αSMA
10 µm
G1
**
*
XIgG
DAPI
lumen
10 µm
G2
**
*
αSMA
DAPI
lumen
10 µm
H
cortex
art
XrIgG
XIgG
DAPI
50 µm
I
cortex
ven
XrIgG
XIgG
DAPI
50 µm
J1
striatum
XIgG
GFAP
250 µm
J2
striatum
XIgG
DAPI
250 µm
J3
striatum
XIgG
250 µm
L1
cortex
XIgG
GFAP
100 µm
K1
striatum
XIgG
RECA-1
100 µm
K2
striatum
XIgG
DAPI
100 µm
K3
striatum
XIgG
100 µm
L2
cortex
XIgG
RECA-1
100 µm

Figure 4. Confocal imaging of intrathecally-infused rat IgG within perivascular spaces of all caliber of vessels and associated with the meninges. (A and G) Fluorescently-labeled rat IgG was localized around large leptomeningeal arteries on the brain surface including the internal carotid artery (ICA), shown here. Neither rat IgG (A1-A2) or rat IgG with excess IgG (XIgG; G1-G2) were able to access the tunica media (*) where smooth muscle cells were labeled with alpha smooth muscle actin (αSMA); IgG appeared to be constrained to the outer perivascular compartment/vascular connective tissue space/adventitia (**). (B) Rat IgG was also associated with large veins on the brain surface (based on size/morphology and lack of smooth muscle staining) as well as macrophages in the subarachnoid space (green cells between vein and parenchyma; see Fig. S2 for macrophage markers). Rat IgG around penetrating arterioles (C and H) in the cortex showed a characteristic circumferential banding pattern associated with the smooth muscle basement membrane, while signal around venules (E and I) did not show circumferential banding but often showed longitudinal signal, perhaps associated with longitudinally-arranged perivascular connective tissue. Signal was also often present around vessels smaller than 8 μm in diameter (e.g., D). Rat IgG infused with an excess of unlabeled IgG showed differences in the pattern of signal, including dark perivascular cell profiles devoid of IgG signal (most apparent in single channel images H (inset), I (inset), J3, and K3) as well as overall patchy/irregular perivascular signal (e.g., K). A striking difference in signal pattern was evident along the pial brain surface, where rat IgG infused with an excess of unlabeled IgG showed irregular bright and dark patches of signal (L), while rat IgG alone showed a consistent appearance at the surface (F).

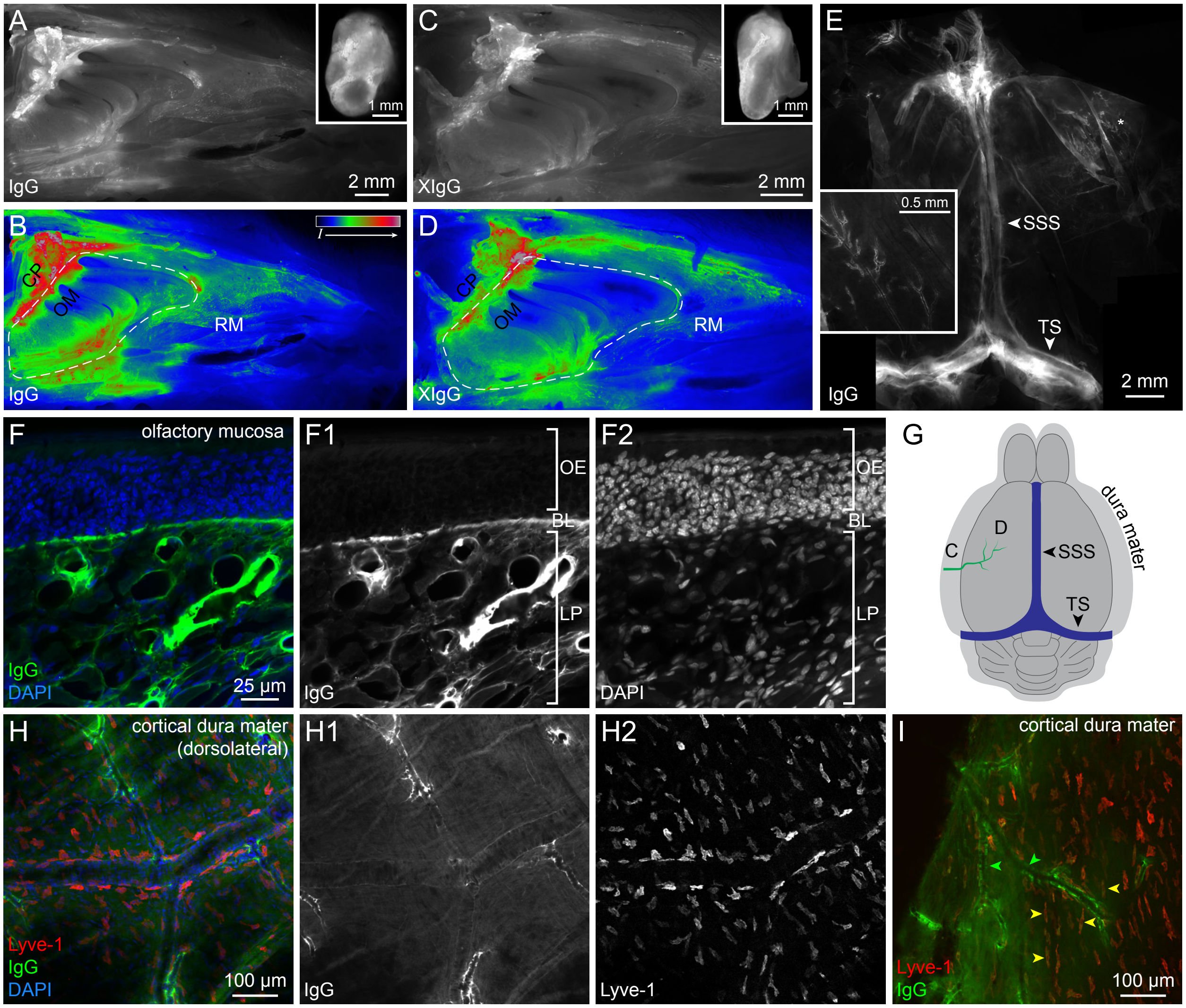

Figure 5. Drainage of intrathecally-infused rat IgG from the central compartment involves olfactory drainage pathways, cervical lymph nodes, and potentially the dura mater. Infusion of rat IgG (A) or rat IgG with an excess of IgG (XIgG; C) revealed similar drainage to the nasal mucosa, with the highest signal (see pseudocolored fluorescence intensity, B and D) at the cribriform plate (CP) and in the ethmoturbinate region of the olfactory mucosa (OM) and less signal in the respiratory mucosa (RM). (F) Confocal imaging demonstrated that rat IgG signal in the olfactory mucosa was within the lamina propria (LP) around putative blood/lymphatic vessels and nerve bundles, but signal stopped abruptly at the basal lamina (BL) and did not enter the olfactory epithelium (OE). (E) The dorsal dura mater showed rat IgG signal was prominent along the superior sagittal sinus (SSS) and transverse sinuses (TS; see schematic G); signal over the cortical dura (E inset) appeared

to be around vascular profiles and followed along branches. (H-I) Confocal imaging of the vascular profiles as designated in (G) with a marker of lymphatic endothelial cells and macrophages (Lyve-1) revealed little co-localization of rat IgG with Lyve-1 (e.g., H, and green arrowheads in I), with occasional co-localization in Lyve-1 positive cells (e.g., yellow arrowheads in I).

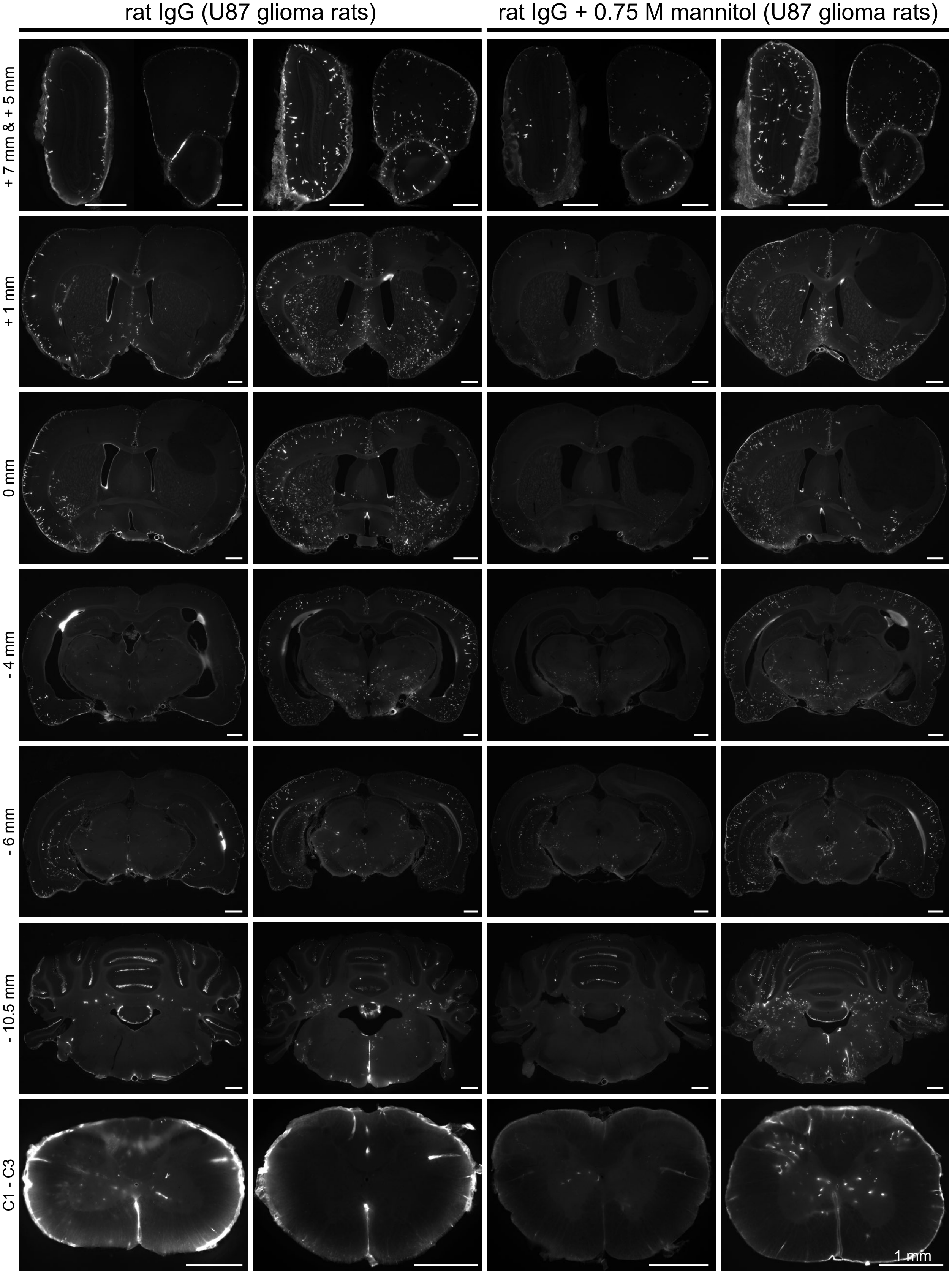
rat IgG (U87 glioma rats)
rat IgG + 0.75 M mannitol (U87 glioma rats)
+ 7 mm & + 5 mm
+ 1 mm
0 mm
- 4 mm
- 6 mm
- 10.5 mm
C1 - C3
1 mm

Figure 6. Perivascular distribution of intrathecally-infused rat IgG in a rat model of glioma. Human U87 malignant glioma cells were implanted into the right striatum in athymic nude rats prior to intrathecal infusion of rat IgG (first and second columns) or rat IgG prepared in 0.75 M mannitol (third and fourth columns). Intrathecal rat IgG signal was not present within the brain tumor in any animal, though occasionally rat IgG signal was present in perivascular spaces of the unaffected brain directly adjacent to the tumor (e.g., see 0 mm (bregma), column 2). Some animals (column 1 and 3) showed a particularly great reduction in IgG distribution throughout the brain across the entire neural axis (i.e., signal at sites very distant from the tumor had reduced perivascular signal, e.g., the olfactory bulbs). Some animals appeared less affected, with perivascular signal in similar brain regions as infused rat IgG in normal animals (e.g., cortex), except for the tumor. The variability did not appear to correlate with tumor size or the extension of the tumor to CSF interfaces (i.e., the pial surface or ventricular surface). Interestingly, the two glioma animals with the worst whole-brain distribution (column 1 and 3) had plasma concentrations that were a fraction of the average for their treatment group (i.e., plasma values for columns 1-4 were: 3.1 ± 0.06 nM (n=4), 9.9 ± 0.08 nM (n=5), 9.8 ± 0.08 nM (n=5), 16.6 ± 0.2 nM (n=4), while average values were 7.6 ± 0.8 nM (N=3) and 16.7 ± 1.3 nM (N=4) for rat IgG and rat IgG in 0.75 M mannitol, respectively; see Table 2).

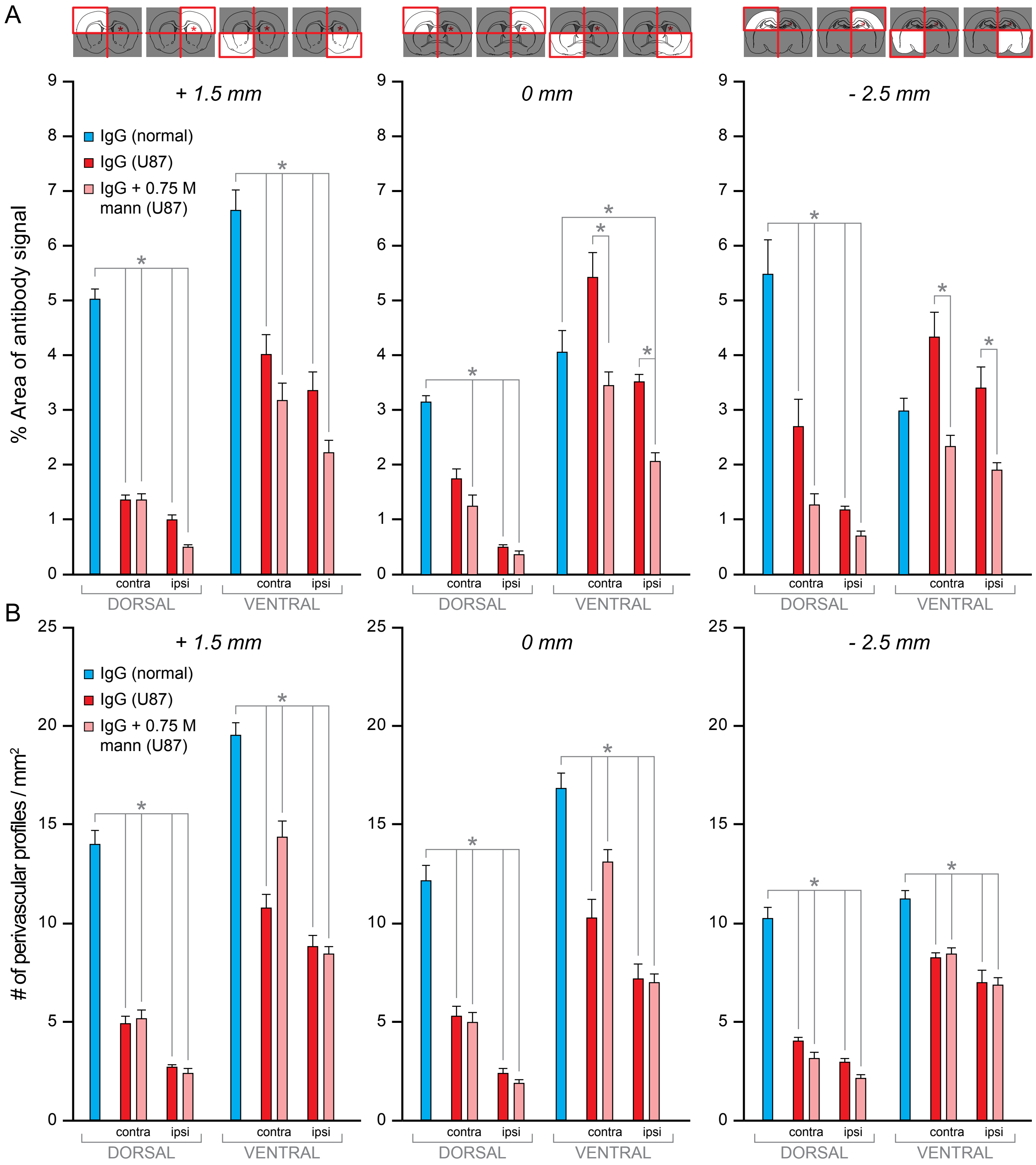

Figure 7. Quantification of perivascular fluorescent signal in coronal brain section images of tumor-bearing rats. Perivascular signal was quantified in the same manner for glioma animals as for normal animals (Fig. 3), except that brain sections were divided into dorsal/ventral halves (as before) and also additionally divided vertically along the midline. Thus four quadrants were

analyzed per section, providing quantification relative to the general tumor quadrant (dorsal/ipsilateral) as depicted in the coronal section schematics (adapted from (Paxinos & Watson, 2007). (A) Summary of the percent area of antibody signal following intrathecal infusion of rat IgG in normal rats (blue), rat IgG in glioma rats (red), or rat IgG in 0.75 M mannitol in glioma rats (light red). The percent area of signal was significantly lower in glioma animals for 9 of 12 analyzed quadrants as compared with normal animals. (B) Summary of the number of perivascular spaces per mm2 following intrathecal infusion of rat IgG in normal rats (blue), rat IgG in glioma rats (red), or rat IgG in 0.75 M mannitol in glioma rats (light red). The number of perivascular spaces per mm2 was significantly lower in glioma rats for all 12 brain regions compared to normal animals. See Table 3 for details. (*) Denotes Kruskal-Wallis one-way analysis of variance on ranks ($p<0.001$) with Dunn's method post hoc pairwise comparison, $p<0.05$. $N=4$ animals for rat IgG, $N=3$ animals for IgG in U87 rats, $N=4$ animals for IgG + 0.75 M mannitol in U87 rats.

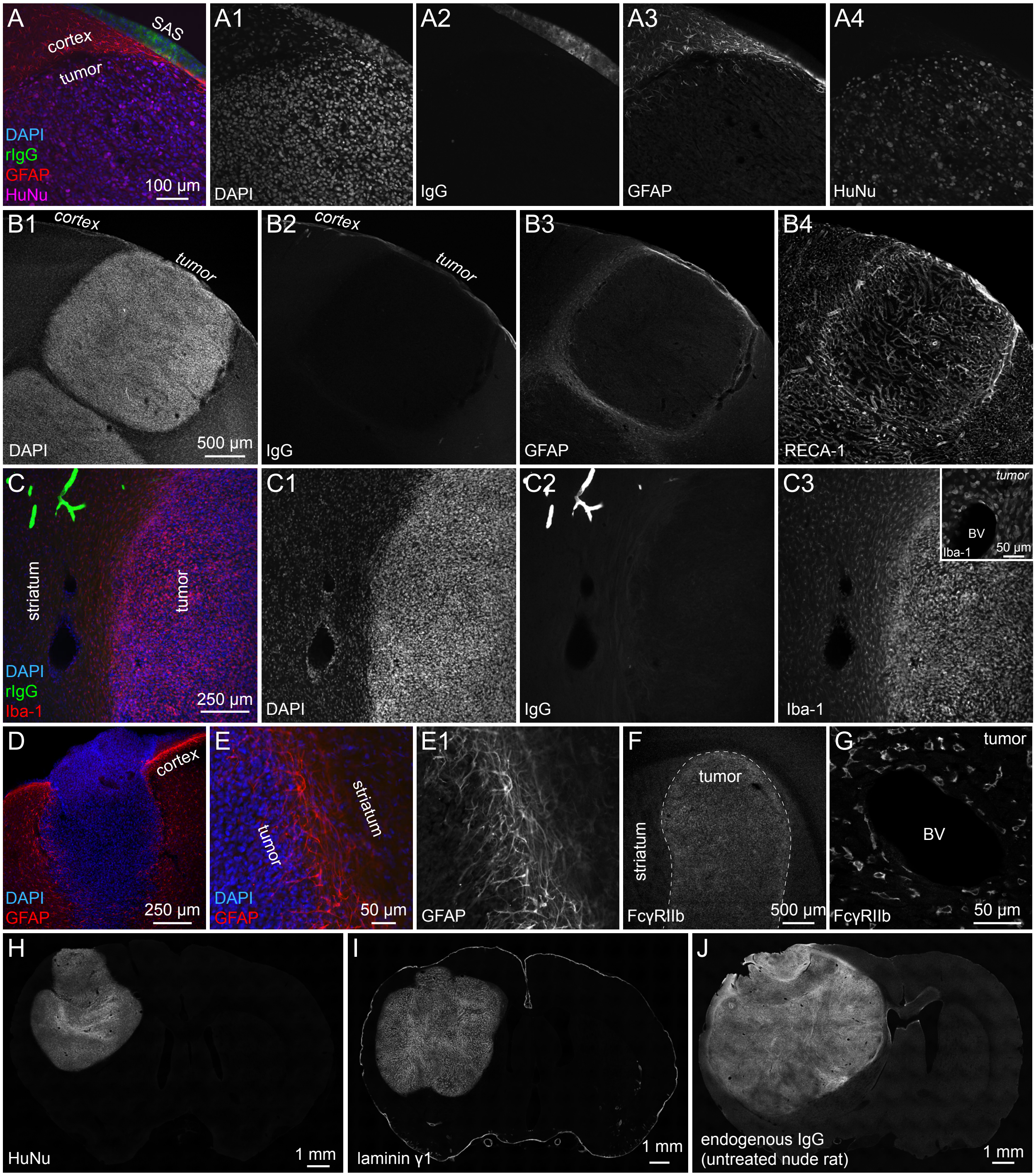

Figure 8. Confocal imaging of glioma rats. (A) A tumor in the cortex was labeled by a human nuclei antibody (HuNu; magenta; also in H) and showed imperceptible staining for the astrocyte marker glial fibrillary acidic protein (GFAP; red) within the tumor. Strong GFAP signal was present around the tumor border, separating the tumor from the adjacent normal cortex (also in D, E). Infused rat IgG (green) was absent from the tumor but was visible in the meninges

over the tumor and cortex. The tumor boundaries were also evident based on the density of the nuclear stain DAPI (blue). (B) Labeling of rat endothelial cell antigen-1 (RECA-1) demonstrated that the tumors are highly vascularized, as expected for U87, again with an astrocytic border around the tumor. (C) Numerous cells within the tumor were labeled by the microglial/macrophage marker Iba-1 (red; normal microglia morphology was apparent in adjacent normal tissue), with a more rounded/amoeboid morphology similar to macrophages. (F-G) The expression of the inhibitory Fc receptor (Fc gamma receptor IIb, FcγRIIb) was high in the tumor relative to the surrounding normal brain, and the cells expressing FcγRIIb had a similar morphology to the Iba-1 positive cells and were quite possibly in some of the same cells. (I) A pan-laminin (lamininγ1) antibody labeled all basement membranes, but signal around normal vasculature was overshadowed by extremely high signal associated with tumor vasculature; some basement membranes potentially associated with the meninges and glia limitans are evident at the pial surface. (J) A tumor-bearing rat that was not intrathecally infused was utilized to assess blood-brain barrier integrity. Endogenous rat IgG was detected by antibody labeling, revealing IgG (presumably from the systemic circulation) leaked across the permeable blood-tumor barrier and entered the tumor interstitium and likely peri-tumoral edematous areas as well, potentially also accessing the CSF at sites where the tumor reached the pial brain surface or the ventricular surfaces.

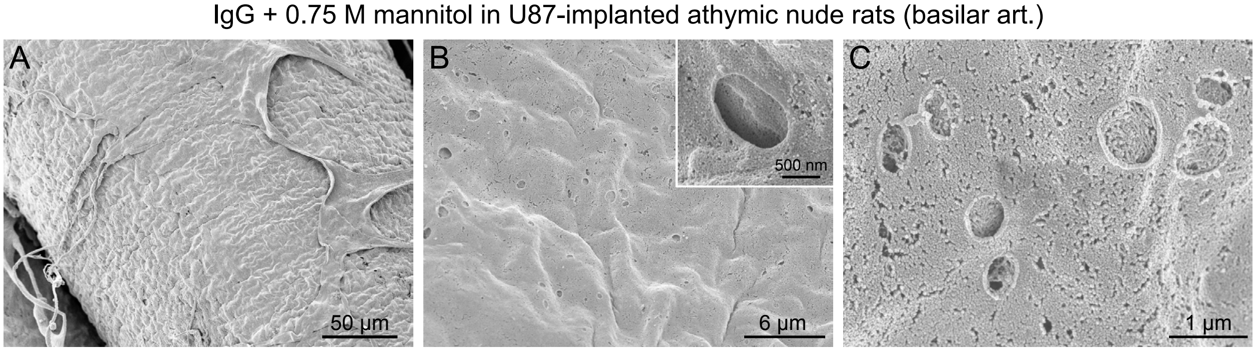

Figure 9. Stomata are present on leptomeningeal fibroblasts ensheathing subarachnoid blood vessels in athymic nude rats. In four glioma animals a portion of the brainstem containing the basilar and vertebral arteries was carefully dissected and processed for scanning electron microscopy. (A) Numerous micron-sized stomata, or pores, were present on the leptomeningeal fibroblasts ensheathing the basilar artery on the surface of the brain. (B-C) Close examination of the stomata reveals a smooth, thickened rim as well as underlying connective tissue (e.g., collagen) of the perivascular space/vascular connective tissue space. These leptomeningeal stomata have been previously shown using scanning electron microscopy in rats (Pizzo et al., 2018) and cats (Zervas et al., 1982).

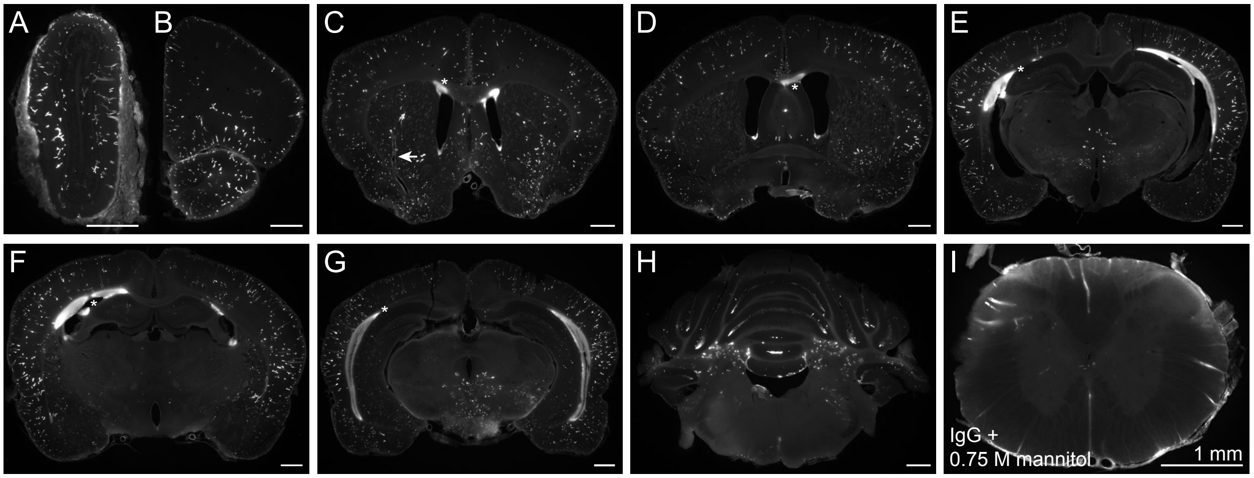

Figure S1. *Ex vivo* fluorescence imaging of intrathecally-infused rat IgG in 0.75 M mannitol in coronal brain sections. (A-I) Rat IgG was co-infused with 0.75 M mannitol into normal rats to determine if enhanced perivascular access could be achieved, as shown previously for goat IgG (Pizzo et al., 2018). Inclusion of hyperosmolar mannitol (*N*=1) did not show an obvious improvement, as might be expected for a molecule that already possesses remarkable access to the perivascular spaces.

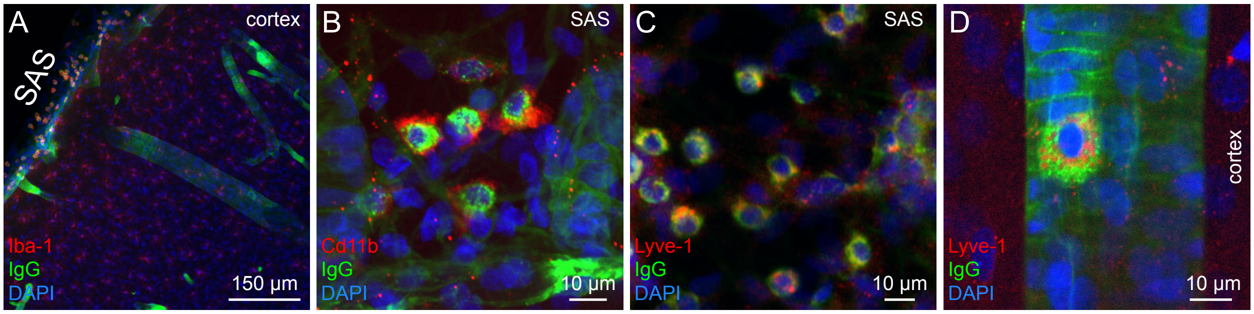

Figure S2. Characterization of rat IgG uptake by meningeal and perivascular cells. Immunohistochemistry was performed using three markers associated with macrophages (Iba-1, A, Cd11b, B, and Lyve-1, C). This revealed that intrathecal rat IgG is internalized by cells positive for all three markers and suggested that these cells were subarachnoid and perivascular macrophages.

CHAPTER 5

Endogenous immunoglobulin G (IgG) and albumin distribution in the rodent brain reveals striking differences: IgG is restricted to perivascular pathways and albumin is widespread

Michelle E. Pizzo[1,2] & Robert G. Thorne[1-5]
[1]School of Pharmacy, Division of Pharmaceutical Sciences; [2]Clinical Neuroengineering Training Program; [3]Neuroscience Training Program; [4]Cellular and Molecular Pathology Graduate Program; [5]Institute for Clinical and Translational Research; University of Wisconsin-Madison

Abstract

Albumin and IgG are abundant proteins in the serum and in the cerebrospinal fluid (CSF), albeit at <1% of serum concentrations. Surprisingly, the distribution of these proteins within the brain and spinal cord are not well-described but are certain to inform about the protein's origins and functions. Additionally, both albumin and IgG bind to the neonatal Fc receptor (FcRn) which is involved in both recycling of these proteins and has been implicated in transcytosis of IgG across barriers elsewhere in the body. We recently suggested that IgG transport from the CSF into the perivascular spaces of the brain utilizes receptor-mediated entry, perhaps FcRn, leading us to probe whether endogenous IgG can also enter and utilize the perivascular spaces, perhaps to carry out its role as a main contributor to humoral immunity. Indeed, we showed in rats that endogenous IgG was present in perivascular spaces throughout the brain without apparent entry into the brain parenchyma, while albumin was distributed widely and appeared intracellular. This suggests either nonspecific mechanisms of transport (e.g., size-dependent diffusion) and/or specific mechanisms of transport (e.g., receptor-mediated transcytosis) produce distinct patterns of distribution for these serum-derived proteins in the brain; likely reflecting their physiological functions.

Introduction

Albumin and immunoglobulin G (IgG) antibody are two of the most abundant proteins in the body, with serum concentrations of approximately 43 g/L and 10 g/L, respectively (albumin normal range: 28-54 g/L; IgG normal range: 5-17 g/L; (Ganrot & Laurell, 1974; Tibbling *et al.*, 1977; Reiber, 1980; Rao & Böker, 1987)). As large hydrophilic macromolecules such as these cannot cross the blood-brain barrier (BBB) or blood-CSF barriers (BCSFBs) in large amount by passive diffusion, their concentration in the central nervous system (CNS) is substantially less. However, they are still among the most abundant proteins in the cerebrospinal fluid at concentrations of approximately 240 mg/L and 22 mg/L, respectively (albumin normal range: 144-336 mg/L; IgG normal range: 7.4-39.4 mg/L; (Ganrot & Laurell, 1974; Tibbling *et al.*, 1977; Reiber, 1980; Rao & Böker, 1987)). Detailed distribution of these prevalent proteins within the brain and spinal cord are lacking but could provide valuable information regarding protein origin and function.

Albumin is a 66.5 kDa heart-shaped single polypeptide with a hydrodynamic diameter of 7.4 nm (Tao & Nicholson, 1996) folding into three homologous domains, each with two subdomains (DIA, DIB, DIIA, DIIB, DIIIA, and DIIIB; (Dockal *et al.*, 1999)). Albumin is the predominant contributor for maintaining the osmotic pressure of the blood and demonstrates an incredible propensity as a carrier molecule for both endogenous and exogenous substances (Peters, 1975). Albumin possesses the highest number of sites for binding fatty acids (including seven common binding sites), plus two primary drug binding sites (in addition to several secondary drug binding sites), several metal binding sites, and sites for interaction with other proteins and receptors (Peters, 1975; Curry, 2009; Knudsen Sand *et al.*, 2015). Albumin is predominantly produced in the liver but is found in nearly every fluid and tissue of the body with approximately 37.5% in the vascular system and 62.5% located extravascularly (Peters, 1975). Albumin diffusion through endothelial fenestrations expected to be very limited due to albumin's size (Sarin, 2010), thus it is also suggested to utilize transcytotic pathways across the endothelial cell by vesicular transport (Milici *et al.*, 1987; Michel, 1996); albumin binding proteins/receptors (e.g., gp60 now known as albondin, and the related secreted protein, acidic and rich in cysteine, SPARC, and cubilin/megalin) likely assist in this process (Schnitzer & Oh, 1992; Merlot *et al.*, 2014). At least two of these albumin binding proteins, SPARC and glycophorin A, are expressed in the choroid plexus epithelial cells and have been suggested to play a role in albumin (and other serum protein) transport across this barrier (Liddelow *et al.*, 2012).

IgG is a 150 kDa Y-shaped protein, comprised of two heavy chains and two light chains connected by disulfide bonds (see (Woof & Burton, 2004; Holliger & Hudson, 2005; Abbas *et al.*, 2015)) with a hydrodynamic diameter of ~10 nm (Wolak *et al.*, 2015*a*). This Y-shape is created by two antigen binding fragments (Fab; 50 kDa each, consisting of one light chain and part of one heavy chain, each) and one crystallizable fragment (Fc) domain (heavy chains), connected by a hinge region (Woof & Burton, 2004; Holliger & Hudson, 2005; Abbas *et al.*, 2015). IgGs and other antibodies are produced and secreted by B lymphocytes and are an important component of the adaptive immune system (humoral immunity), with a primary role of binding to antigens to assist with their neutralization or elimination via activation of effector functions (Woof & Burton, 2004; Holliger & Hudson, 2005; Abbas *et al.*, 2015). Antibodies thus are found all throughout the body where they may encounter pathogens (with specific tissue distributions depending on antibody isotype; (Janeway *et al.*, 2001; Abbas *et al.*, 2015)). IgG often functions by binding to Fcγ receptors (e.g., Fcγ I, II, III; only IgG-antigen complex binds at high affinity) to induce effector functions including phagocytosis and immune cell activation (or inhibition) (Woof & Burton, 2004; Holliger & Hudson, 2005; Abbas *et al.*, 2015). Previous reports have described CNS expression of Fcγ receptors in leptomeningeal cells, arachnoid granulations, perivascular cells (macrophages), choroid plexus epithelial and stromal cells, and subependymal periventricular regions (Nyland, 1982; Peress *et al.*, 1989; Ulvestad *et al.*, 1994; Vedeler *et al.*, 1994). *In situ* hydridization and expression data for mice appears to support FcγRIIb localization at brain-CSF interfaces (Allen Institute for Brain Science, 2004).

Interestingly, a single receptor is capable of binding to both of these proteins, the neonatal Fc receptor (FcRn). FcRn is a heterodimeric protein consisting of a smaller β2-microglobulin subunit non-covalently associated with a larger subunit major histocompatibility complex (MHC) class I-like heavy chain, which contains three extracellular loops (α1, α2, and α3) and a transmembrane region (Simister & Mostov, 1989). The DIII domain of albumin (with contributions from DI (Sand *et al.*, 2014)) binds to a flexible loop in the FcRn α1 domain (regulated by a histidine residue on the α2 domain; (Andersen *et al.*, 2012)), and the junction between the IgG Fc domains CH2 and CH3 binds the α2 domain on FcRn (with additional involvement of the α1 domain and the β2 microglobulin; (Burmeister *et al.*, 1994)); as albumin and IgG bind opposite sides of FcRn's heavy chain, albumin and IgG binding to FcRn is thought to be non-competitive (Chaudhury *et al.*, 2006). FcRn has a pH dependent binding to both albumin and IgG and is only capable of binding either protein with high affinity at an acidic pH (approximately 6.0-6.5; (Jones & Waldmann, 1972; Rodewald, 1976; Chaudhury *et al.*, 2003, 2006). The binding stoichiometries of FcRn to albumin and IgG appear to be 1:1 (Chaudhury *et al.*, 2006) and 2:1 (Huber *et al.*, 1993; Burmeister *et al.*, 1994), respectively. Both albumin and IgG possess some degree of species-specificity, an important consideration for preclinical studies, particularly pharmacokinetic and pharmacodynamic studies. For example, human FcRn has weak/negligible binding for most other species of IgG (e.g., illuminating the reason for the low mouse IgG half-life in humans), while mouse FcRn shows strong binding for most other species of IgG, and even binds human IgG with greater affinity than mouse IgG (thus human IgG has a longer half-life in mice than mouse IgG)(Ober *et al.*, 2001; Andersen *et al.*, 2010). Albumin species differences have also been demonstrated, for example, human FcRn is capable of binding mouse albumin in addition to human albumin (Andersen *et al.*, 2010), as well as other species of albumin (Chaudhury *et al.*, 2006). See Roopenian *et al*. for a thorough review on FcRn structure, function, and potential role in therapies (Roopenian & Akilesh, 2007).

Expression of FcRn in vascular endothelial cells in the body has been shown to rescue albumin and IgG from degradation in the lysosome (Brambell, 1966; Chaudhury *et al.*, 2003), giving each protein their characteristically long half-lives in the blood of approximately 19 days for albumin (Peters, 1975) and 21-28 days for IgG (Abbas *et al.*, 2015). FcRn was first implicated in the maternal-to-fetal transfer of IgG from the mother's milk from the (acidic) neonatal intestinal mucosa to the fetal circulation (Halliday, 1955; Hemmings & Brambell, 1961; Brambell, 1969; Jones & Waldmann, 1972; Wallace & Rees, 1980). FcRn has also been recognized for its transcytotic role between compartments at physiological pH (7.4), including transport across placental syncytiotrophoblasts for the purpose of maternal-to-fetal transfer of IgG to confer passive immunity; how IgG reaches the acidified endosome to bind FcRn is not understood, but may involve specific (e.g., other Fc receptor- or protein-mediated uptake) or nonspecific (fluid-phase endocytosis) mechanisms (Simister *et al.*, 1996; Kristoffersen & Matre, 1996; Leach *et al.*, 1996; Firan *et al.*, 2001). Transcytosis of albumin by FcRn has not been demonstrated but is assumed to be likely (Knudsen Sand *et al.*, 2015). CNS expression of FcRn has only been reported for brain endothelial cells and choroid plexus epithelial cells (Schlachetzki *et al.*, 2002; Latvala *et al.*, 2017). *In situ* hybridization and expression data for mice suggests FcRn localization at brain-CSF interfaces (Allen Institute for Brain Science, 2004). Studies utilizing Fc receptor knockout animals or competition experiments have generated a debate in the literature as to whether FcRn in the CNS plays a significant role in IgG efflux from the central compartment (Bergman *et al.*, 1998;

Schlachetzki *et al.*, 2002; Deane *et al.*, 2005; Cooper *et al.*, 2013) or whether it plays no significant role (Garg & Balthasar, 2009; Abuqayyas & Balthasar, 2013; Chen *et al.*, 2014).

An in-depth investigation of the distribution of albumin and IgG in the brain and spinal cord using modern techniques is lacking. A prior study by Broadwell & Sofroniew (Broadwell & Sofroniew, 1993) immunostained for endogenous albumin, IgG, IgM, and complement C9 in rat brain sections. These serum proteins were detected all along the brain-CSF interfaces and penetrated to a small extent (albumin, IgM) or large extent (IgG, C9) into the perivascular spaces of penetrating vessels in the cortex. Circumventricular organs (CVOs) stained evidently for these serum proteins leading the authors to suggest that signal along the ventricular compartment was a result of spillover from the CVOs. A similar CSF- and CVO-associated distribution was also demonstrated for IgG and serum proteins in other studies (Kozlowski *et al.*, 1992; Schmidt-Kastner *et al.*, 1993). We also recently reported a receptor-mediated transport of intrathecally-administered antibodies from the CSF into the cerebral perivascular spaces in rats (see Chapter 4). This suggested to us that endogenous IgG, which is abundant in the CSF, may utilize these same receptor-mediated pathways to enter the perivascular spaces and perform a role in immune surveillance. Thus, in the present study we used immunohistochemistry and fluorescence microscopy to determine the distribution of endogenous albumin and IgG in the rat and mouse brain and spinal cord. IgG in the rat brain appeared mostly extracellularly and was generally restricted to circumventricular organs and the perivascular compartment, with an appearance similar to that of intrathecally administered IgG (see Chapter 4 and (Pizzo *et al.*, 2018). Preliminary albumin distribution in the rat was widespread and predominantly appeared to be intracellular throughout the parenchyma. The results suggested possible differences in albumin and IgG and entry into/distribution within the brain tissue. Preliminary results in mice showed albumin distribution in the mouse was similarly widespread through the parenchyma, but endogenous mouse IgG appeared to have a more limited access to the perivascular spaces compared to rat IgG but also showed a widely cellular localization in sharp contrast to rats. A lack of cellular IgG in rats may be the result of a lack of sensitivity in detection or due to species differences. These findings suggest that IgG likely predominantly enters the CNS via the CSF, circulating through the PVS in search of antigens; however, there may be species differences in the extent of this surveillance that are critically important considering the mouse is a widely used animal model.

Materials and Methods

Animal use

Experiments were carried out at the University of Wisconsin-Madison in accordance with the National Institutes of Health Guide for the Care and Use of Laboratory Animals (2011) and local Institutional Animal Care and Use Committee regulations. Female Sprague-Dawley rats (250-280 g; Envigo, Indianapolis, IN) or female C57/BL6 mice (approximately 20 g; Envigo) were housed in a climate-controlled room under a 12:12 h light/dark cycle. Rodents had access to food and water *ad libitum*. Every effort was made to minimize pain and distress of the animals. Rodents were anesthetized to a surgical plane with urethane (1.2 g/kg, i.p., supplemented to effect with 0.375 g/kg urethane i.p.) as determined by absence of a pedal reflex and placed on a homeothermic blanket (Harvard Apparatus, Holliston, MA) to maintain body temperature at 37°C. In rats, the abdominal aorta was surgically exposed and cannulated using an 18.5 GA cannula (Exel International, Los Angeles, CA) connected to a three-way stopcock filled with sterile saline. Rats were perfused with 50 mL ice cold 0.01 M phosphate buffered saline (PBS) followed by 450 mL

4% paraformaldehyde in 0.1 M PBS at a rate of 15 mL/min using a peristaltic pump (Minipuls 3, Gilson, Inc., Middleton, WI). Mice were transcardially perfused with 10 mL ice cold 0.01 M PBS followed by 50 mL of 4% paraformaldehyde at a rate of ~7.5 mL/min. The brain and upper cervical spinal cord were dissected and sectioned immediately using a vibratome (100 μm, coronal; VT1000S, Leica Microsystems, Wetzlar, Germany). Sections were placed in 0.01 M PBS overnight at 4°C for immunohistochemistry the following day.

Immunohistochemistry of rat brain sections

Immunohistochemistry (IHC) of free-floating coronal brain sections was performed at room temperature unless otherwise stated. Steps entailed: 2 hour incubation in blocking buffer containing 5% serum prepared in 0.01 M PBS with 0.3% triton X-100 (PBST), three 15 min washes in PBST, incubation with chicken-anti-albumin primary (1:250; NBP1-77027, Novus Biologicals, Littleton, CO) in blocking buffer overnight at 4°C, three 15 min washes in PBST, 2 hour incubation with secondary antibodies in blocking buffer, one 15 min wash in PBST, 20 min incubation with 4',6-diamidino-2-phenylindole (DAPI) in PBST (2 μg/mL), and three 15 min washes in PBST. Some mouse sections were also stained with rabbit-anti-Neun (a neuronal marker, 1:1000; ab177487, Abcam). Some rat sections were stained with only conjugated anti-rat IgG antibodies thus the overnight incubation in primary was skipped and all IHC steps performed in a single day. Secondary antibodies included goat-anti-chicken 594 (ab150172, Abcam), highly cross-adsorbed goat-anti-rabbit 488 (A11034, Life Technologies, Carlsbad, CA), goat-anti-rat IgG 594 (SAB4600111, Sigma-Aldrich or goat-anti-rat IgG 594, A11007, Life Technologies), or a highly cross-adsorbed goat-anti-mouse IgG 647 (A21236, Life Technologies) which was found to bind to rat IgG very well. Mouse brain sections were then mounted onto slides and coverslipped using Prolong Diamond Antifade (Life Technologies).

Imaging of coronal brain sections

Rat brain sections were imaged immediately after completion of IHC on a petri dish wet with 0.01 M PBS. Images were captured using an MVX10 Macroview microscope (Olympus, Tokyo, Japan) equipped with an Orca-flash 2.8 CMOS camera (Hamamatsu, Hamamatsu City, Japan) and a X-Cite 120Q illuminator (Lumen Dynamics Group, Inc.,Mississauga, Ontario, Canada) using the appropriate filter set (Chroma, U-M49002XL or U-M49008XL, Bellows Falls, VT, USA). Sections were then immediately mounted onto slides and coverslipped using Prolong Diamond Antifade (Life Technologies). Slides were imaged using an A1R confocal microscope (Nikon, Tokyo, Japan) with NIS Elements (Nikon).

Results

Predominantly perivascular distribution of IgG in the rat brain

Immunohistochemistry of untreated coronal rat brain sections (100 μm) for endogenous rat IgG (*N*=3) revealed a widespread distribution of IgG across the entire neural axis (see Fig. 1 for detailed description). IgG appeared to be mostly confined to the perivascular spaces but also showed apparent entry into the brain in circumventricular organs (e.g., subfornical organ, median eminence, and area postrema). IgG also showed relatively high signal at brain-CSF interfaces, in the choroid plexus, in some periventricular white matter regions, and associated with the meninges and some cranial nerves (showing a markedly similar pattern of distribution to previous reports of CSF-infused IgG (see Chapter 4 and (Pizzo *et al.*, 2018)). IgG in the upper cervical spinal cord showed some patterns of signal that may be associated with the perivascular spaces, but also showed some cellular and diffuse profiles; more caudal sections of the upper cervical spinal cord showed little endogenous IgG labeling.

Widespread, cellular distribution of albumin in the rat brain and spinal cord

Preliminary immunohistochemistry of untreated coronal rat brain sections (100 μm) for endogenous rat albumin (*N*=2) revealed a widespread distribution across the entire neural axis that was strikingly different than IgG distribution. Albumin exhibited a cellular profile in most areas of the brain including the olfactory bulbs, cortex, cerebellum, as well as the spinal cord (see Fig. 2 for detailed description). Relatively high albumin signal was also present at brain-CSF interfaces (i.e., the pial and ventricular surfaces), in the choroid plexus, and associated with the meninges, as might be expected for the most abundant protein in the CSF. Perhaps surprisingly, there was not evidently high signal in circumventricular organs compared to adjacent brain areas which may be due to the generally widespread brain distribution.

Confocal imaging of IgG and albumin localization in the rat brain

Confocal imaging of endogenous rat IgG signal with the nuclear stain DAPI demonstrated the specific localization of IgG in the brain (Fig. 3). IgG at the cortical surface appeared to be associated with the meninges and the perivascular space (or vascular connective tissue space) of large leptomeningeal arteries on the brain surface, without substantial penetration into the tunica media. The most anterior aspect of the lateral ventricles revealed diffuse (seemingly extracellular) periventricular signal in this densely cellular region, and the ependyma of the lateral ventricles a few millimeters posterior revealed high patches of signal in addition to low cellular signal along the CSF interface. IgG also penetrated into the parenchyma along the perivascular spaces of arterioles and showed the same circumferential banding pattern associated with the smooth muscle basement membrane following intrathecal infusion of IgG (see Chapter 4 and (Pizzo *et al.*, 2018)). Some IgG signal also appeared to be in the perivascular space around penetrating venules but did not reach very far into the brain along these vessels. Endogenous IgG was also present around microvessels (smaller than approximately 8 μm in diameter), suggesting that IgG accessed spaces around all caliber of vessels in the brain.

The preliminary albumin distribution was quite different from IgG distribution, further evidenced by confocal imaging of albumin and IgG labeled in the same sections (Fig. 4). Periventricular regions of the dorsal aspect of the lateral ventricles (anterior horn) showed consistent albumin distribution in densely packed cells throughout the region, while IgG distribution in this area occurred irregularly in patches and appeared more diffuse (perhaps extracellular). Albumin was also present in association with the meninges and cortical brain surface, with the highest signal in cellular profiles of the cortex, reminiscent of astrocyte and neuronal morphologies, but this must be confirmed with additional immunohistochemistry. Interestingly, albumin did not show a perivascular distribution like IgG, and the two endogenous proteins did not appear to co-localize in any areas. However, it is also possible that the sensitivity of the fluorescence methods utilized were not high enough to detect fully detect the distribution of these endogenous proteins, which are present at relatively low concentrations compared to the periphery.

Confocal imaging of endogenous mouse IgG and albumin

Preliminary studies also demonstrated the localization of endogenous IgG and albumin in the mouse brain (*N*=2). Endogenous albumin distribution in the mouse brain was similar to the rat brain, and demonstrated signal in the choroid plexus, at brain-CSF interfaces, in cellular profiles throughout the parenchyma, but absence of signal in perivascular spaces. Co-localization with the neuronal marker NeuN appeared to occur occasionally but albumin signal was also evident in cells negative for NeuN. Endogenous mouse IgG brain distribution showed some dissimilarities to endogenous rat IgG. Mouse IgG showed less apparent signal associated with circumventricular organs (while rat IgG showed very high signal in these areas) and illuminated cellular profiles throughout the brain (while rat IgG showed no cellular profiles). Generally, IgG did not appear to be present in the same cells as albumin, and the IgG cellular profile was reminiscent of microglia, but this must be confirmed with additional cellular markers. Mouse IgG was also present in the perivascular spaces of some vessels and showed some circumferential banding around arteriole smooth muscle cells, but the extent of perivascular distribution in mice seemed substantially lesser than in the rat.

Discussion

In the present study we revealed the strikingly different brain and spinal cord distribution of endogenous albumin and IgG, two abundant serum proteins. IgG appeared to be restricted to the circumventricular organs and perivascular spaces in the rat brain. This suggested significant barriers to IgG exit from the perivascular compartment (i.e., the astrocyte basement membrane), possibly indicating a physiological reason to prevent IgG from diffusing into the parenchyma. The IgG distribution in the present study showed similarities to previous reports (Kozlowski *et al.*, 1992; Schmidt-Kastner *et al.*, 1993; Broadwell & Sofroniew, 1993). In sharp contrast, preliminary studies demonstrated a widespread cellular distribution of endogenous albumin in the rat brain, suggesting it either had no significant barriers to widespread transport or it utilized specific mechanisms to achieve extensive distribution. Preliminary studies in the mouse brain showed a similar albumin distribution to rats, but mouse IgG showed sparse perivascular profiles in addition to widespread cellular profiles (which does agree with one previous study (Hazama *et al.*, 2005)). It is unclear if this discrepancy shows species differences in IgG brain distribution or if cellular IgG in rat brain sections is below the sensitivity of detection with our methods; this will require further investigation. The current study has provided critical new information regarding endogenous protein access and distribution to the brain tissue, which we speculate may have a number of important physiological purposes and functions, discussed below.

Distribution of endogenous IgG in the brain—localization, proposed functions, and mechanisms of entry

Endogenous IgG in the rat brain was present at expected locations including the CVOs and CSF-contacting surfaces, but also demonstrated extensive signal along numerous perivascular spaces. Interestingly, the pattern of perivascular signal was strikingly similar to intrathecally-administered antibodies in rats (see Chapter 4 and (Pizzo *et al.*, 2018)). The observation that endogenous and intrathecal antibodies access the same pathways for distribution indicates important key points. First, the extensive perivascular distribution of intrathecal antibodies (see Chapter 4 and (Pizzo *et al.*, 2018)) is highly unlikely to have been caused by increased pressure or other non-physiological drivers 'forcing' access to the perivascular space, as access of endogenous antibodies demonstrates the ability to enter this compartment under normal conditions. Second, high levels of endogenous IgG were present in similar areas to intrathecal goat IgG (Pizzo *et al.*, 2018) and did not show signal as extensively as intrathecal rat IgG. We suggest that this is a result of 'easy' to access perivascular spaces (which large molecules with minimal binding can access, e.g., goat IgG (Pizzo *et al.*, 2018) and nanoparticles (Chapter 6)) and more difficult to access perivascular spaces (which may require special circumstances for large macromolecules to access, e.g., osmotically enhanced entry of goat IgG (Pizzo *et al.*, 2018) or Fc receptor-mediated entry of rat IgG (see Chapter 4 for additional discussion)). As intrathecal rat IgG is likely to highlight the same receptor-mediated pathways available for endogenous IgG, it is possible that endogenous rat IgG was present much more extensively at lower levels than IHC could reliably detect.

Endogenous IgG signal appeared within the CVOs which are lacking BBB characteristics and are permeable to serum proteins. Despite this IgG was constrained in its diffusion from the CVOs and did not penetrate far into surrounding brain tissue, nor did it significantly or consistently label the ventricular surfaces. This suggests that bloodborne IgG encountered a barrier layer at this level; perhaps in part imposed by the tanycytes and other glial cells/basement membranes. Indeed, previous studies have suggested that a blood/CVO-CSF barrier is imposed by the tight junctions between the tanycytes which tightly regulate movement of molecules between the CVOs and ventricles (Mullier *et al.*, 2010; Langlet *et al.*, 2013). This contrasts the idea proposed by Broadwell and Sofroniew (Broadwell & Sofroniew, 1993), who suggested that the ventricular signal of endogenous serum proteins observed was likely caused by spillover from CVOs. One group has also demonstrated glial cells/basement membranes demarcate the borders of the CVOs and may contribute to different functional areas (Pócsai & Kálmán, 2014, 2015), also perhaps imposing some kind of brain/CVO barrier; indeed in our studies IgG has not appeared to be capable of easily crossing basement membranes.

Neither endogenous IgG (which had a relatively long circulation time; Figs. 3 and 4) nor exogenous intrathecal IgGs (which had a much shorter circulation time ((Pizzo *et al.*, 2018)

Chapter 4) appeared to diffuse out of the perivascular spaces, again indicating a barrier. We have previously hypothesized that the astrocyte basement membrane may pose a diffusional barrier to IgG escape from the perivascular space into the parenchyma due to the large size of IgG ((Hannocks *et al.*, 2018) and Chapter 4). This implies a physiological reason to contain IgG to the CSF and perivascular spaces for surveillance of antigens. Indeed, IgG likely circulates these pathways to encounter antigens and is then appropriately positioned to activate the complement system (complement C9 has been demonstrated in the perivascular space; (Broadwell & Sofroniew, 1993)) or induce phagocytosis by perivascular macrophages. Perhaps only when the basement membrane is breached (e.g., to allow parenchymal entry of extravasated immune cells (Agrawal *et al.*, 2006; Song *et al.*, 2015)) can IgG also enter the parenchyma in high amounts.

In general, proteins in the systemic circulation are almost entirely excluded from the CNS by the BBB and BCSFBs (Davson & Segal, 1995; Abbott *et al.*, 2006; Calias *et al.*, 2014). For example, Azzi *et al*. immunized rats against HRP to later detect autologous anti-HRP IgG entry into the CNS using transmission electron microscopy. They demonstrated that in the cortex and spinal cord (both gray and white matter) IgG was restricted from entering the endothelial cells or crossing tight junctions and essentially did not access the brain, while extracellular IgG was present in the dorsal root ganglion of the spinal cord by apparent passage across permeable vessels (Azzi *et al.*, 1990). A similar study by the same group demonstrated autologous anti-HRP IgG antibodies crossed the fenestrated capillaries of the choroid plexus into the stroma but did not cross the choroid epithelial cells in any manner (interestingly, they did speculate that connections between the choroid plexus stroma and perivascular drainage pathways from the brain may serve to eliminate the accumulated IgG from the stroma; (Fleury *et al.*, 1984)). Another study of the rat choroid plexus by Aleshire *et al*. also demonstrated that endogenous IgG immunolabeled for transmission electron microscopy failed to detect IgG within the choroid plexus epithelial cells (but they also failed to detect IgG within the stroma; (Aleshire *et al.*, 1985)).

However, serum proteins do appear in the CSF (albeit at substantially lower concentrations than in the serum (<1% for albumin and IgG)) suggesting some entry route(s) exist. A classical idea for serum protein entry into the CSF was via physical 'leaks' in the BCSFBs due to occasional absent tight junctions between epithelial cells, supported by a correlation between a molecule's hydrodynamic size and the CSF/serum concentration (Rapoport & Pettigrew, 1979; Davson & Segal, 1995). The BCSFB is implicated in these 'leaks' more so than the BBB because several studies have demonstrated higher permeability and lower electrical resistance for the choroid plexus (discussed in (Rapoport & Pettigrew, 1979; Davson & Segal, 1995)). The suggested 'leaks' for the size-dependent entry of serum molecules into the CSF (derived from best-fit transport models) were ~12 nm pores in the epithelial layer (i.e., 0.08% open junctions) and ~25 nm vesicular 'pores' which could be so rare they are not generally captured in transmission electron microscopy studies (Rapoport & Pettigrew, 1979). Additional proposed locations of potential 'functional leaks' from the blood into the CSF include the site of choroid attachment (i.e., tela choroidea) and the transition point between choroid plexus cells and the ependymal cells (Brightman, 1975; Rapoport & Pettigrew, 1979). CSF perfusion studies (Hochwald & Wallenstein, 1967*b*, 1967*a*) also suggested systemic albumin and IgG entered predominantly into the ventricles (presumably through the choroid plexus) with some contribution from other brain sites (there are indeed extrachoroidal sources of CSF (Pollay & Curl, 1967; Milhorat, 1969)); as expected based on a size-dependent process albumin showed greater entry into the CSF than IgG (Hochwald &

Wallenstein, 1967*b*, 1967*a*). However, increasing evidence supports a transcytotic pathway or 'leak' may also exist. Indeed, during development the blood-to-CSF transport of albumin is very high (greater than can be expected by passive mechanisms) and is species-specific suggesting a receptor-mediated process (Dziegielewska *et al.*, 1991).

CSF also demonstrates an increase in protein as it travels along the neural axis from the ventricles to cisterna manga to spinal subarachnoid space, thus, it has also been suggested that some of the serum proteins from the brain are added to the CSF as it flows through the system (Davson & Segal, 1995). Note, some proteins in the CSF are known to be brain-derived, but their localization/gradient in the CSF compartments (e.g., ventricular → lumbar) are distinct from CSF-derived proteins (Reiber, 2001)). Intra-CNS synthesis of all the serum proteins in the CSF also seems insufficient to account for all serum proteins and their quantities in CSF. Thus it is proposed that 'leaks' across the BBB into the brain account for some of the serum-derived proteins in CSF along the neural axis—but transport of serum proteins across the BBB has also been demonstrated to be highly restricted (Davson & Segal, 1995). For example, St-Amour *et al.* showed merely 0.009% of a systemically-injected dose of intravenous Ig (IVIG) reached the brain (cortex) and was largely associated with the microvasculature, but they also demonstrated this was saturable indicating a receptor-mediated process (St-Amour *et al.*, 2013). Villasenor *et al.* probed for the localization of endogenous mouse IgG in brain endothelial cells and demonstrated substantial vesicular transport of IgG in endothelial cells that was directed for degradation. This degradation appeared to be regulated by the pericyte and a mouse model depleted of pericytes revealed successful IgG transcytosis to the abluminal (brain) side (Villaseñor *et al.*, 2017). Additionally, IgG-producing B cells are present in the CNS (though very few) and may contribute to CSF levels;

B cells have been shown to increase in disease (e.g., multiple sclerosis (Stern *et al.*, 2014) and a number of other CNS disorders (Chu *et al.*, 1983)) thus intra-CNS synthesis is required to explain CSF levels of antibodies following CNS challenge (e.g., (Cserr *et al.*, 1992)).

Significance for immunohistochemistry

Immunostaining for endogenous serum proteins is commonly used to gauge blood-brain barrier disruption and permeability following treatment with blood-brain barrier opening substances (e.g., hyperosmolar solutions (Vorbrodt *et al.*, 1994)) and in CNS disease (e.g., brain tumors (Reis *et al.*, 2012)). It is rare that a study discusses significant background IgG/albumin staining in normal control animals, but it has occasionally been described and compared with the disease model of interest (e.g., stab injury or infarct; (Schmidt-Kastner *et al.*, 1993)). It is likely that in many other studies the detection methods were not sensitive enough or the imaging setting were optimized for strong signal increases in diseased brains, thus failing to demonstrate (visible) endogenous albumin or IgG in the normal brain.

Additionally, the importance of understanding how endogenous levels of IgG could impact immunohistochemistry (and species-cross reactivity) has been emphasized previously (Schmidt-Kastner *et al.*, 1993) and supported by this work, i.e., anti-mouse IgG secondary antibodies may bind to endogenous rat IgG present at basal levels or at elevated levels in situations where there is CNS inflammation or the BBB is disrupted. This unintended binding can cause critical misinterpretation of the results, particularly if increased levels of IgG or BBB disruption is not expected/realized. This misinterpretation can of course be avoided with proper control labeling of the tissue with secondary antibodies in the absence of the primary antibodies.

Significance for drug delivery and disease pathology

Previous reports of endogenous CSF/serum ratios range from 0.0005-0.0035 (Felgenhauer, 1974; Reiber, 1980; Banks *et al.*, 2002) and compare well with exogenous CSF/serum ratios (Banks *et al.*, 2002; Rubenstein *et al.*, 2003; Wang *et al.*, 2018). The results of the present work as well as prior studies of intrathecal IgG distribution (Chapter 4 and (Pizzo *et al.*, 2018)) inform us about *how* systemically-administered antibodies might distribute in the brain—and importantly, that *the distribution is limited within the brain*. Endogenous IgG and intrathecal IgG in the CSF do not appear to penetrate into the brain parenchyma from the perivascular spaces, which may hamper therapeutic delivery. The limited meningeal and perivascular distribution may help in certain disorders where these compartments are the target (e.g., leptomeningeal cancer or cerebral amyloid angiopathy), but would not be expected to provide widespread distribution for whole brain disorders (e.g., Alzheimer's disease or Huntington's disease). The distribution of CSF-borne antibodies in the brain is also of particular interest for CNS autoimmune diseases such as multiple sclerosis and neuromyelitis optica, where antibody localization may correspond with lesions and antibody antigens/targets (Asgari *et al.*, 2015). It is also possible that these surveillance pathways for IgG are disrupted in a number of disorders (e.g., brain cancer) and that normalization of this process could be beneficial. Conceivably, Fc-domain fusion-conjugates (smaller than full-length IgG) could provide enhanced perivascular entry (i.e., Fc receptor-mediated entry, Chapter 4) but be small enough to penetrate the astrocyte basement membrane and reach the parenchyma.

Distribution of endogenous albumin in the brain—mechanisms of entry and proposed functions

Endogenous albumin was widespread throughout the brain parenchyma and was predominantly localized within the intracellular compartment or at brain-CSF interfaces. This was in striking contrast to endogenous IgG, which showed a much more limited distribution. The dissimilarities in albumin and IgG localization in the brain are likely imparted by their size-difference (7.4 nm for albumin (Tao & Nicholson, 1996) versus 10 nm for IgG (Wolak *et al.*, 2015*b*)), unless an unknown mechanism is selectively and specifically transporting albumin within the brain tissue. This extensive distribution probably represents a physiological need for albumin throughout the parenchyma, e.g., as an acceptor for fatty acids transported across the BBB (Mitchell *et al.*, 2009). Interestingly, albumin has been also demonstrated to bind to amyloid beta (Algamal *et al.*, 2013) and led to the suggestion that albumin could regulate amyloid beta aggregation (Stanyon & Viles, 2012). Additionally, non-hepatic synthesis and subsequent secretion of albumin by microglial cells has been shown *in vitro*, and the expression of albumin was increased when microglial cells were activated by amyloid beta or lipopolysaccharide (Ahn *et al.*, 2008), with further implicated roles in neuronal cell death *in vivo* (Byun *et al.*, 2012).

Reported endogenous albumin CSF/serum ratios range from 0.0018-0.0074 (Ganrot & Laurell, 1974; Felgenhauer, 1974; Reiber, 1980). Several studies have demonstrated the BBB and BCSFB act as significant barriers to albumin as with IgG. For example, Vorbrodt *et al*. demonstrated the tightness of the BBB to endogenous albumin using immunodetection and transmission electron microscopy. Untreated animals showed almost no albumin present in the endothelial cells or brain, but administration of intraarterial hyperosmolar arabinose showed increased intracellular and paracellular transport of albumin into the endothelial cell and brain (Vorbrodt *et al.*, 1994). Virgintino *et al*. used transmission electron microscopy to immunolabel the glucose 1 transporter and endogenous albumin and demonstrated a functional blood-brain barrier which excluded albumin even in the fetus (Virgintino *et al.*, 2000). As discussed above, the route for serum albumin into the brain may involve size-dependent physical or transcytotic ‘leaks’ in the BBB or BCSFB. In support of the transcytotic mechanism, several recent studies have implicated a role for SPARC in the transport of albumin across the choroid plexus. Albumin and SPARC colocalized in choroid plexus epithelial cells and stained a few percent of epithelial cells in total (highlighting the rarity of this transport). In adults, some albumin positive cells were negative for SPARC, indicating another mechanism of albumin transport may also occur (Liddelow *et al.*, 2011). Further investigation demonstrated albumin and SPARC are in close proximity and likely interact, and also demonstrated a species-specific binding of murine SPARC with mouse albumin over human albumin and species-specific transport from blood to CSF (Liddelow *et al.*, 2014). Altogether, these results suggest a specific mechanism for albumin to cross the choroid plexus, perhaps in addition to other transport processes in the BCSFBs or BBB.

Significance for drug delivery

Albumin showed a strikingly widespread distribution throughout the brain, perhaps suggesting that albumin can diffuse throughout the brain tissue from its site(s) of entry (given its long half-life and substantial serum concentration), or that albumin uses specific mechanisms to move within the brain. Albumin did not appear to utilize perivascular spaces for transport, unless it so easily diffuses away from the perivascular spaces that it shows no accumulation in the perivascular space. Thus, it is possible that albumin-fusion therapeutics could also have an enhanced brain distribution if there are specific within-brain mechanisms of transport. However, the increased size of albumin-fusion drugs could counteract this process and slow diffusional transport. The entry of albumin into the CNS, in part due to specific mechanisms on choroid plexus epithelial cells to enter the CSF, is still so incredibly limited that CNS entry of albumin fusion drugs would be very small. Additionally, if albumin binding to FcRn is hindered by albumin fusion the half-life would be substantially impacted (and potentially FcRn mediated transport in the brain, if such occurs).

Preliminary studies of endogenous albumin and IgG in the mouse brain

While endogenous mouse albumin showed a similar widespread distribution to albumin as in the rat brain, endogenous mouse IgG showed a strikingly different distribution. Mouse IgG was still present in perivascular spaces of the brain (though seemingly far lesser than in rats) but additionally showed widespread cellular localization. The cellular profiles appeared similar to microglia (but staining was not performed to confirm). While it might seem intuitive for IgG to associate with microglia, it is not immediately apparent why IgG would be localized intracellularly, as it usually exerts its effector functions at the cell surface by binding to Fc receptors. A previous study showed similar staining of IgG in the brains of four out of six mouse strains but not rats and demonstrated an absence of IgG from microglia when the FcγIIb receptor was knocked out, suggesting the receptor is required for cellular uptake (Hazama *et al.*, 2005). One possibility is that such intracellular IgG is present in rat brains, but the detection method was not sensitive enough. Alternatively, it could represent entirely different management of IgG within the brains of these two species. This would have incredibly important implications for immune surveillance in the mouse brain and its use as an animal model.

Conclusions

The distinct distribution of endogenous albumin and IgG suggest vastly different functions within the CNS. Restricted perivascular IgG in the brain parenchyma suggested that IgG utilized the perivascular spaces for surveillance of antigens within brain and should be restricted to these surveillance pathways for physiological reasons. Widespread albumin signal, on the other hand, suggested it is needed by cells throughout the brain. IgG access to the perivascular pathways is suggested to be partly Fc receptor-mediated (presumably FcRn), thus it is possible that albumin binding to FcRn could also allow it to utilize this pathway followed by subsequent size-dependent diffusion out of the perivascular compartment or possibly other specific transport mechanisms. Despite the presence of the serum proteins in the CSF and brain, vast evidence suggests that albumin and IgG do not enter the CNS in substantial quantities, thus systemically administered albumin, IgG, or fusion therapeutics would not be expected to achieve substantial quantities in the brain. If the therapeutic is incredibly potent (e.g., antibodies) a therapeutic concentration could be achieved, but the disadvantages are that high doses are required and high systemic exposure may be undesirable; even once within the CNS IgG appeared to be unable to escape the perivascular compartment.

References

Abbas AK, Lichtman AH & Pillai S (2015). *Cellular and Molecular Immunology*, 8th edn.ed. Abbas AK, Lichtman AH & Pillai S. Elsevier Saunders, Philadelphia.

Abbott NJ, Rönnbäck L & Hansson E (2006). Astrocyte-endothelial interactions at the blood-brain barrier. *Nat Rev Neurosci* **7,** 41–53.

Abuqayyas L & Balthasar JP (2013). Investigation of the role of FcγR and FcRn in mAb distribution to the brain. *Mol Pharm* **10,** 1505–1513.

Agrawal S, Anderson P, Durbeej M, Van Rooijen N, Ivars F, Opdenakker G & Sorokin LM (2006). Dystroglycan is selectively cleaved at the parenchymal basement membrane at sites of leukocyte extravasation in experimental autoimmune encephalomyelitis. *J Cell Biol* **173,** 1007–1019.

Ahn SM, Byun K, Cho K, Kim JY, Yoo JS, Kim D, Paek SH, Kim SU, Simpson RJ & Lee B (2008). Human microglial cells synthesize albumin in brain. *PLoS One*; DOI: 10.1371/journal.pone.0002829.

Aleshire SL, Hajdu I, Bradley CA & Parl FF (1985). Choroid plexus as a barrier to immunoglobulin delivery into cerebrospinal fluid. *J Neurosurg* **63,** 593–597.

Algamal M, Milojevic J, Jafari N, Zhang W & Melacini G (2013). Mapping the interactions between the Alzheimer's Aβ-peptide and human serum albumin beyond domain resolution. *Biophys J* **105,** 1700–1709.

Allen Institute for Brain Science (2004). Allen Mouse Brain Atlas.

Andersen JT, Daba MB, Berntzen G, Michaelsen TE & Sandlie I (2010). Cross-species binding analyses of mouse and human neonatal Fc receptor show dramatic differences in immunoglobulin G and albumin binding. *J Biol Chem* **285,** 4826–4836.

Andersen JT, Dalhus B, Cameron J, Daba MB, Plumridge A, Evans L, Brennan SO, Gunnarsen KS, Bjørås M, Sleep D & Sandlie I (2012). Structure-based mutagenesis reveals the albumin-binding site of the neonatal Fc receptor. *Nat Commun* **3,** 610.

Asgari N, Berg CT, Mørch MT, Khorooshi R & Owens T (2015). Cerebrospinal fluid aquaporin-4-immunoglobulin G disrupts blood brain barrier. *Ann Clin Transl Neurol* **2,** 857–863.

Azzi G, Bernaudin J-F, Bouchaud C, Bellon B & Fleury-Feith J (1990). Permeability of the normal rat brain, spinal cord and dorsal root ganglia microcirculations to immunoglobulins G. *BiolCell* **68,** 31–36.

Banks WA, Terrell B, Farr SA, Robinson SM, Nonaka N & Morley JE (2002). Passage of amyloid beta protein antibody across the blood-brain barrier in a mouse model of Alzheimer's disease. *Peptides* **23,** 2223–2226.

Bergman I, Burckart GJ, Pohl CR, Venkataramanan R, Barmada MA, Griffin JA & Cheung NK (1998). Pharmacokinetics of IgG and IgM anti-ganglioside antibodies in rats and monkeys after intrathecal administration. *J Pharmacol Exp Ther* **284,** 111–115.

Brambell FW (1966). The transmission of immunity from mother to young and the catabolism of immunoglobulins. *Lancet* **2,** 1087–1093.

Brambell FW (1969). The transmission of immune globulins from the mother to the foetal and newborn young. *Proc Nutr Soc* **28,** 35–41.

Brightman MW (1975). Ultrastructural Characteristics of Adult Choroid Plexus: Relation to the Blood—Cerebrospinal Fluid Barrier to Proteins. In *The Choroid Plexus in Health and Disease*, ed. Netsky MG & Shuangshoti S, pp. 86–112. Elsevier Ltd.

Broadwell RD & Sofroniew M V (1993). Serum proteins bypass the blood-brain fluid barriers for extracellular entry to the central nervous system. *Exp Neurol* **120,** 245–263.

Burmeister WP, Huber AH & Bjorkman PJ (1994). Crystal structure of the complex of rat neonatal Fc receptor with Fc. *Nature* **372,** 379–383.

Byun K, Bayarsaikhan E, Kim D, Son M, Hong J, Jeong G-B, Paek SH, Won M-H & Lee B (2012). Activated microglial cells synthesize and secrete AGE-albumin. *Anat Cell Biol* **45,** 47–52.

Calias P, Banks WA, Begley D, Scarpa M & Dickson P (2014). Intrathecal delivery of protein therapeutics to the brain: A critical reassessment. *Pharmacol Ther* **144,** 114–122.

Chaudhury C, Brooks CL, Carter DC, Robinson JM & Anderson CL (2006). Albumin Binding to FcRn : Distinct from the FcRn − IgG Interaction. *Biochemistry* **45,** 4983–4990.

Chaudhury C, Mehnaz S, Robinson JM, Hayton WL, Pearl DK, Roopenian DC & Anderson CL (2003). The major histocompatibility complex-related Fc receptor for IgG (FcRn) binds albumin and prolongs its lifespan. *J Exp Med* **197,** 315–322.

Chen N, Wang W, Fauty S, Fang Y, Hamuro L, Hussain A & Prueksaritanont T (2014). The effect of the neonatal Fc receptor on human IgG biodistribution in mice. **6,** 1–7.

Chu AB, Sever JL, Madden DL, Iivanainen M, Leon M, Wallen W, Brooks BR, Lee YJ & Houff S (1983). Oligoclonal IgG bands in cerebrospinal fluid in various neurological diseases. *Ann Neurol* **13,** 434–439.

Cooper PR, Ciambrone GJ, Kliwinski CM, Maze E, Johnson L, Li Q, Feng Y & Hornby PJ (2013). Efflux of monoclonal antibodies from rat brain by neonatal Fc receptor, FcRn. *Brain Res* **1534,** 13–21.

Cserr HF, DePasquale M, Harling-Berg CJ, Park JT & Knopf PM (1992). Afferent and efferent arms of the humoral immune response to CSF-administered albumins in a rat model with normal blood-brain barrier permeability. *J Neuroimmunol* **41,** 195–202.

Curry S (2009). Lessons from the crystallographic analysis of small molecule binding to human serum albumin. *Drug Metab Pharmacokinet* **24,** 342–357.

Davson H & Segal MB (1995). *Phyioslogy of the CSF and Blood-Brain Barriers*, 1st edn.ed. Davson H & Segal MB. CRC Press, Inc, Boca Raton.

Deane R, Sagare A, Hamm K, Parisi M, LaRue B, Guo H, Wu Z, Holtzman DM & Zlokovic B V (2005). IgG-assisted age-dependent clearance of Alzheimer's amyloid beta peptide by the blood-brain barrier neonatal Fc receptor. *J Neurosci* **25,** 11495–11503.

Dockal M, Carter DC & Rüker F (1999). The three recombinant domains of human serum albumin. Structural characterization and ligand binding properties. *J Biol Chem* **274,** 29303–29310.

Dziegielewska KM, Habgood MD, Møllgård K, Stagaard M & Saunders NR (1991). Species-specific transfer of plasma albumin from blood into different cerebrospinal fluid compartments in the fetal sheep. *J Physiol* **439,** 215–237.

Felgenhauer K (1974). Protein size and cerebrospinal fluid composition. *Klin Wochenschr* **52,** 1158–1164.

Firan M, Bawdon R, Radu C, Ober RJ, Eaken D, Antohe F, Ghetie V & Ward ES (2001). The MHC class I-related receptor, FcRn, plays an essential role in the maternofetal transfer of γ-globulin in humans. *Int Immunol* **13,** 993–1002.

Fleury J, Bellon B, Bernaudin JF, Bouchaud C, Pinchon MC, Kuhn J & Poirier J (1984). Electron-microscopic immunohistochemical study of the localization of immunoglobulin G in the choroid plexus of the rat. *Cell Tissue Res* **238,** 177–182.

Ganrot K & Laurell CB (1974). Measurement of IgG and albumin content of cerebrospinal fluid, and its interpretation. *Clin Chem* **20,** 571–573.

Garg A & Balthasar JP (2009). Investigation of the influence of FcRn on the distribution of IgG to the brain. *AAPS J* **11,** 553–557.

Halliday R (1955). The absorption of antibodies from immune sera by the gut of the young rat. *Proc R Soc Lond B Biol Sci* **143,** 408–413.

Hannocks M-J, Pizzo ME, Huppert J, Deshpande T, Abbott NJ, Thorne RG & Sorokin L (2018). Molecular characterization of perivascular drainage pathways in the murine brain. *J Cereb Blood Flow Metab* **38,** 669–686.

Hazama GI, Yasuhara O, Morita H, Aimi Y, Tooyama I & Kimura H (2005). Mouse brain IgG-like immunoreactivity: Strain-specific occurrence in microglia and biochemical identification of IgG. *J Comp Neurol* **492,** 234–249.

Hemmings WA & Brambell FW (1961). Protein transfer across the foetal membranes. *Br Med Bull* **17,** 96–101.

Hochwald GM & Wallenstein M (1967*a*). Exchange of albumin between blood, cerebrospinal fluid, and brain in the cat. *Am J Physiol* **212,** 1199–1204.

Hochwald GM & Wallenstein MC (1967*b*). Exchange of γ-globulin between blood, cerebrospinal fluid and brain in the cat. *Exp Neurol* **19,** 115–126.

Holliger P & Hudson PJ (2005). Engineered antibody fragments and the rise of single domains. *Nat Biotechnol* **23,** 1126–1136.

Huber AH, Kelley RF, Gastinel LN & Bjorkman PJ (1993). Crystallization and stoichiometry of binding of a complex between a rat intestinal Fc receptor and Fc. *J Mol Biol* **230,** 1077–1083.

Janeway CAJ, Travers P, Walport M & Shlomchik MJ (2001). The distribution and functions of immunoglobulin isotypes. In *Immunobiology: The Immune System in Health and Disease*, ed. Janeway CAJ, Travers P, Walport M & Shlomchik MJ. Garland Science, New York.

Jones EA & Waldmann TA (1972). The mechanism of intestinal uptake and transcellular transport of IgG in the neonatal rat. *J Clin Invest* **51,** 2916–2927.

Knudsen Sand KM, Bern M, Nilsen J, Noordzij HT, Sandlie I & Andersen JT (2015). Unraveling the interaction between FcRn and albumin: Opportunities for design of albumin-based therapeutics. *Front Immunol*; DOI: 10.3389/fimmu.2014.00682.

Kozlowski GP, Sterzl I & Nilaver G (1992). Localization patterns for immunoglobulins and albumins in the brain suggest diverse mechanisms for their transport across the blood-brain barrier (BBB). *Prog Brain Res* **91,** 149–154.

Kristoffersen EK & Matre R (1996). Co-localization of the neonatal Fc gamma receptor and IgG in human placental term syncytiotrophoblasts. *Eur J Immunol* **26,** 1668–1671.

Langlet F, Mullier A, Bouret SG, Prevot V & Dehouck B (2013). Tanycyte-like cells form a blood-cerebrospinal fluid barrier in the circumventricular organs of the mouse brain. *J Comp Neurol* **521,** 3389–3405.

Latvala S, Jacobsen B, Otteneder MB, Herrmann A & Kronenberg S (2017). Distribution of FcRn Across Species and Tissues. *J Histochem Cytochem* **65,** 321–333.

Leach JL, Sedmak DD, Osborne JM, Rahill B, Lairmore MD & Anderson CL (1996). Isolation from human placenta of the IgG transporter, FcRn, and localization to the syncytiotrophoblast: implications for maternal-fetal antibody transport. *J Immunol* **157,** 3317–3322.

Liddelow SA, Dziegielewska KM, Møllgård K, Phoenix TN, Temple S, Vandeberg JL & Saunders NR (2011). SPARC/osteonectin, an endogenous mechanism for targeting albumin to the blood-cerebrospinal fluid interface during brain development. *Eur J Neurosci* **34,** 1062–1073.

Liddelow SA, Dziegielewska KM, Møllgård K, Whish SC, Noor NM, Wheaton BJ, Gehwolf R, Wagner A, Traweger A, Bauer H, Bauer HC & Saunders NR (2014). Cellular specificity of the blood-CSF barrier for albumin transfer across the choroid plexus epithelium. *PLoS One*; DOI: 10.1371/journal.pone.0106592.

Liddelow SA, Temple S, Møllgård K, Gehwolf R, Wagner A, Bauer H, Bauer HC, Phoenix TN, Dziegielewska KM & Saunders NR (2012). Molecular characterisation of transport mechanisms at the developing mouse blood-CSF interface: A transcriptome approach. *PLoS One*; DOI: 10.1371/journal.pone.0033554.

Merlot AM, Kalinowski DS & Richardson DR (2014). Unraveling the mysteries of serum albumin-more than just a serum protein. *Front Physiol*; DOI: 10.3389/fphys.2014.00299.

Michel CC (1996). Transport of macromolecules through microvascular walls. *Cardiovasc Res* **32,** 644–653.

Milhorat TH (1969). Choroid plexus and cerebrospinal fluid production. *Science* **166,** 1514–1516.

Milici AJ, Watrous NE, Stukenbrok H & Palade GE (1987). Transcytosis of albumin in capillary endothelium. *J Cell Biol* **105,** 2603–2612.

Mitchell RW, Edmundson CL, Miller DW & Hatch GM (2009). On the mechanism of oleate transport across human brain microvessel endothelial cells. *J Neurochem* **110,** 1049–1057.

Mullier A, Bouret SG, Prevot V & Dehouck B (2010). Differential distribution of tight junction proteins suggests a role for tanycytes in blood-hypothalamus barrier regulation in the adult mouse brain. *J Comp Neurol* **518,** 943–962.

Nyland H (1982). Properties of Fc gamma receptors in the human central nervous system. *Acta Pathol Microbiol Immunol Scand C* **90,** 171–177.

Ober RJ, Radu CG, Ghetie V & Ward ES (2001). Differences in promiscuity for antibody-FcRn interactions across species: implications for therapeutic antibodies. *Int Immunol* **13,** 1551–1559.

Peress NS, Siegelman J, Fleit HB, Fanger MW & Perillo E (1989). Monoclonal antibodies identify three IgG Fc receptors in normal human central nervous system. *Clin Immunol Immunopathol* **53,** 268–280.

Peters TJ (1975). Serum Albumin. In *The plasma proteins : structure, function, and genetic control. Volume I*, 2nd edn., pp. 133–181. Academic Press, New York.

Pizzo ME, Wolak DJ, Kumar NN, Brunette E, Brunnquell CL, Hannocks M-J, Abbott NJ, Meyerand ME, Sorokin L, Stanimirovic DB & Thorne RG (2018). Intrathecal antibody distribution in the rat brain: surface diffusion, perivascular transport and osmotic enhancement of delivery. *J Physiol* **596,** 445–475.

Pócsai K & Kálmán M (2014). Extracellular matrix components mark the territories of circumventricular organs. *Neurosci Lett* **566,** 36–41.

Pócsai K & Kálmán M (2015). Glial and perivascular structures in the subfornical organ: distinguishing the shell and core. *J Histochem Cytochem* **63,** 367–383.

Pollay M & Curl F (1967). Secretion of cerebrospinal fluid by the ventricular ependyma of the rabbit. *Am J Physiol* **213,** 1031–1038.

Rao ML & Böker DK (1987). Cerebrospinal fluid and serum levels of albumin, IgG, IgA and IgM in patients with intracranial tumors and lumbar disc herniation. *Eur Neurol* **26,** 241–245.

Rapoport SI & Pettigrew KD (1979). A heterogenous, pore-vesicle membrane model for protein transfer from blood to cerebrospinal fluid at the choroid plexus. *Microvasc Res* **18,** 105–119.

Reiber H (1980). The discrimination between different blood-CSF barrier dysfunctions and inflammatory reactions of the CNS by a recent evaluation graph for the protein profile of cerebrospinal fluid. *J Neurol* **224,** 89–99.

Reiber H (2001). Dynamics of brain-derived proteins in cerebrospinal fluid. *Clin Chim acta* **310,** 173–186.

Reis M, Czupalla CJ, Ziegler N, Devraj K, Zinke J, Seidel S, Heck R, Thom S, Macas J, Bockamp E, Fruttiger M, Taketo MM, Dimmeler S, Plate KH & Liebner S (2012). Endothelial Wnt/β-catenin signaling inhibits glioma angiogenesis and normalizes tumor blood vessels by inducing PDGF-B expression. *J Exp Med* **209,** 1611–1627.

Rodewald R (1976). pH-dependent binding of immunoglobulins to intestinal cells of the neonatal rat. *J Cell Biol* **71,** 666–669.

Roopenian DC & Akilesh S (2007). FcRn: the neonatal Fc receptor comes of age. *Nat Rev Immunol* **7,** 715–725.

Rubenstein JL, Combs D, Rosenberg J, Levy A, McDermott M, Damon L, Ignoffo R, Aldape K, Shen A, Lee D, Grillo-Lopez A & Shuman MA (2003). Rituximab therapy for CNS lymphomas: Targeting the leptomeningeal compartment. *Blood* **101,** 466–468.

Sand KMK, Bern M, Nilsen J, Dalhus B, Gunnarsen KS, Cameron J, Grevys A, Bunting K, Sandlie I & Andersen JT (2014). Interaction with both domain I and III of albumin is required for optimal pH-dependent binding to the neonatal Fc receptor (FcRn). *J Biol Chem* **289,** 34583–34594.

Sarin H (2010). Physiologic upper limits of pore size of different blood capillary types and another perspective on the dual pore theory of microvascular permeability. *J Angiogenes Res* **2,** 14.

Schlachetzki F, Zhu C & Pardridge WM (2002). Expression of the neonatal Fc receptor (FcRn) at the blood-brain barrier. *J Neurochem* **81,** 203–206.

Schmidt-Kastner R, Meller D, Bellander BM, Strömberg I, Olson L & Ingvar M (1993). A one-step immunohistochemical method for detection of blood-brain barrier disturbances for immunoglobulins in lesioned rat brain with special reference to false-positive labelling in immunohistochemistry. *J Neurosci Methods* **46,** 121–132.

Schnitzer JE & Oh P (1992). Antibodies to SPARC inhibit albumin binding to SPARC, gp60, and microvascular endothelium. *Am J Physiol* **263,** H1872-9.

Simister NE & Mostov KE (1989). An Fc receptor structurally related to MHC class I antigens. *Nature* **337,** 184–187.

Simister NE, Story CM, Chen HL & Hunt JS (1996). An IgG-transporting Fc receptor expressed in the syncytiotrophoblast of human placenta. *Eur J Immunol* **26,** 1527–1531.

Song J, Wu C, Korpos E, Zhang X, Agrawal SM, Wang Y, Faber C, Schäfers M, Körner H, Opdenakker G, Hallmann R & Sorokin L (2015). Focal MMP-2 and MMP-9 Activity at the Blood-Brain Barrier Promotes Chemokine-Induced Leukocyte Migration. *Cell Rep* **10,** 1040–1054.

St-Amour I, Paré I, Alata W, Coulombe K, Ringuette-Goulet C, Drouin-Ouellet J, Vandal M, Soulet D, Bazin R & Calon F (2013). Brain bioavailability of human intravenous immunoglobulin and its transport through the murine blood-brain barrier. *J Cereb Blood Flow Metab* **33,** 1983–1992.

Stanyon HF & Viles JH (2012). Human serum albumin can regulate amyloid-β peptide fiber growth in the brain interstitium: Implications for Alzheimer disease. *J Biol Chem* **287,** 28163–28168.

Stern JNH, Yaari G, Vander Heiden JA, Church G, Donahue WF, Hintzen RQ, Huttner AJ, Laman JD, Nagra RM, Nylander A, Pitt D, Ramanan S, Siddiqui BA, Vigneault F, Kleinstein SH, Hafler DA & O'Connor KC (2014). B cells populating the multiple sclerosis brain mature in the draining cervical lymph nodes. *Sci Transl Med*; DOI: 10.1126/scitranslmed.3008879.

Tao L & Nicholson C (1996). Diffusion of albumins in rat cortical slices and relevance to volume transmission. *Neuroscience* **75,** 839–847.

Tibbling G, Link H & Ohman S (1977). Principles of albumin and IgG analyses in neurological disorders. I. Establishment of reference values. *Scand J Clin Lab Invest* **37,** 385–390.

Ulvestad E, Williams K, Vedeler C, Antel J, Nyland H, M??rk S & Matre R (1994). Reactive microglia in multiple sclerosis lesions have an increased expression of receptors for the Fc part of IgG. *J Neurol Sci* **121,** 125–131.

Vedeler C, Ulvestad E, Grundt I, Conti G, Nyland H, Matre R & Pleasure D (1994). Fc receptor for IgG (FcR) on rat microglia. *J Neuroimmunol* **49,** 19–24.

Villaseñor R, Kuennecke B, Ozmen L, Ammann M, Kugler C, Grüninger F, Loetscher H, Freskgård P-O & Collin L (2017). Region-specific permeability of the blood–brain barrier upon pericyte loss. *J Cereb Blood Flow Metab*0271678X1769734.

Virgintino D, Robertson D, Benagiano V, Errede M, Bertossi M, Ambrosi G & Roncali L (2000). Immunogold cytochemistry of the blood-brain barrier glucose transporter GLUT1 and endogenous albumin in the developing human brain. *Brain Res Dev Brain Res* **123,** 95–101.

Vorbrodt AW, Dobrogowska DH, Tarnawski M & Lossinsky AS (1994). A quantitative immunocytochemical study of the osmotic opening of the blood-brain barrier to endogenous albumin. *J Neurocytol* **23,** 792–800.

Wallace KH & Rees AR (1980). Studies on the immunoglobulin-G Fc-fragment receptor from neonatal rat small intestine. *Biochem J* **188,** 9–16.

Wang Q, Delva L, Weinreb PH, Pepinsky RB, Graham D, Veizaj E, Cheung AE, Chen W, Nestorov I, Rohde E, Caputo R, Kuesters GM, Bohnert T & Gan L-S (2018). Monoclonal antibody exposure in rat and cynomolgus monkey cerebrospinal fluid following systemic administration. *Fluids Barriers CNS* **15,** 10.

Wolak DJ, Pizzo ME & Thorne RG (2015*a*). Probing the extracellular diffusion of antibodies in brain using in vivo integrative optical imaging and ex vivo fluorescence imaging. *J Control Release* **197,** 78–86.

Wolak DJ, Pizzo ME & Thorne RG (2015*b*). Probing the extracellular diffusion of antibodies in brain using in vivo integrative optical imaging and ex vivo fluorescence imaging. *J Control Release* **197,** 78–86.

Woof JM & Burton DR (2004). Human antibody–Fc receptor interactions illuminated by crystal structures. *Nat Rev Immunol* **4,** 89–99.

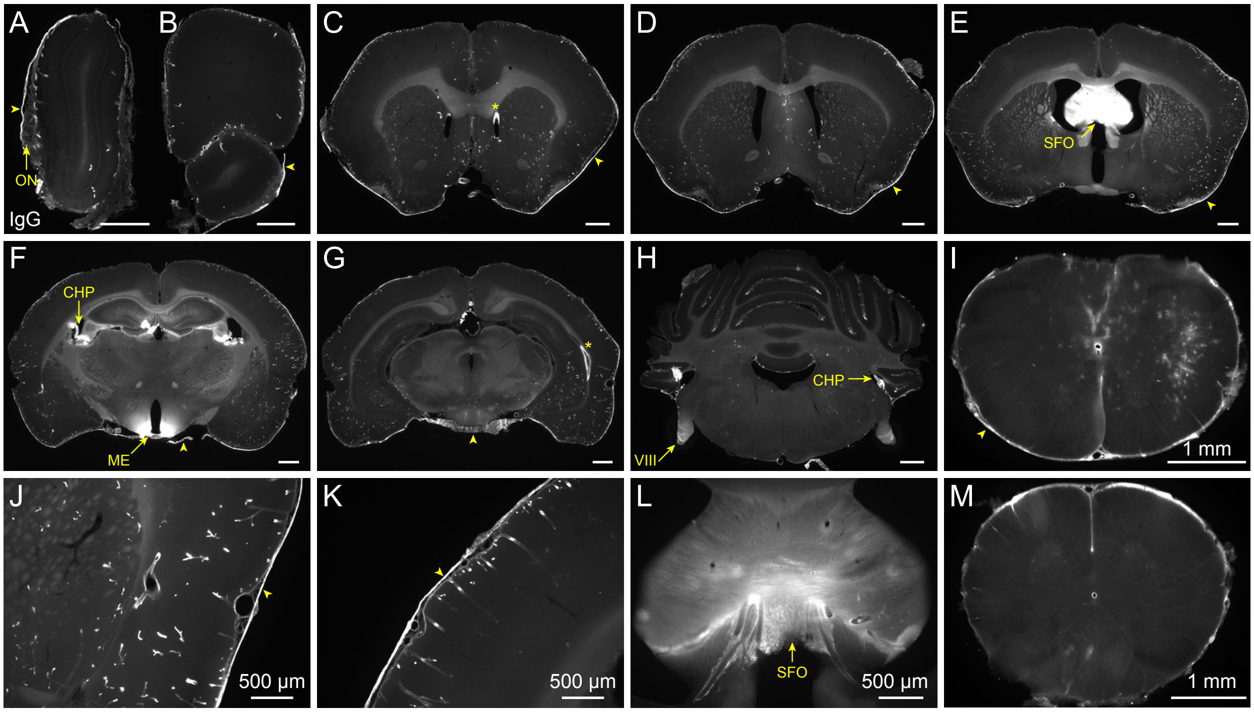

Figure 1. Detection of endogenous rat IgG revealed widespread distribution throughout the brain, predominantly associated with the meninges, perivascular spaces, and circumventricular organs. (A) IgG in the olfactory bulb was present between nerve bundles in the olfactory nerve layer (ON), in some perivascular spaces, and associated with the arachnoid (arrowhead). (C) Perivascular signal of IgG is widespread in both leptomeningeal and parenchymal vessels, though lesser in the cortex (some vessels show light staining; also see J and K), and the highest signal was present in association with the arachnoid (arrowhead) and around the dorsal aspect of the lateral ventricles (*). (E) IgG signal was evident in the septal nucleus and fimbria of the hippocampus adjacent to the subfornical organ (SFO; also see L), presumably due to spillover of systemic IgG into this circumventricular organ. (F) The median eminence (ME), another circumventricular organ, showed IgG signal presumably from the systemic circulation. The choroid plexuses (CHP) of the lateral and dorsal third ventricles also showed prominent endogenous IgG signal despite limited signal at the ependymal surface throughout the ventricular system. (H) IgG in the cerebellum was prominent at the folia surfaces, in the fourth ventricle choroid plexuses (CHP), and associated with the vestibulocochlear nerve (cranial nerve VIII). (I) The upper cervical spinal cord (C1-C3) revealed perivascular and diffuse IgG signal, but a more caudal section (M) showed sparse IgG signal aside from the meninges and pial surface.

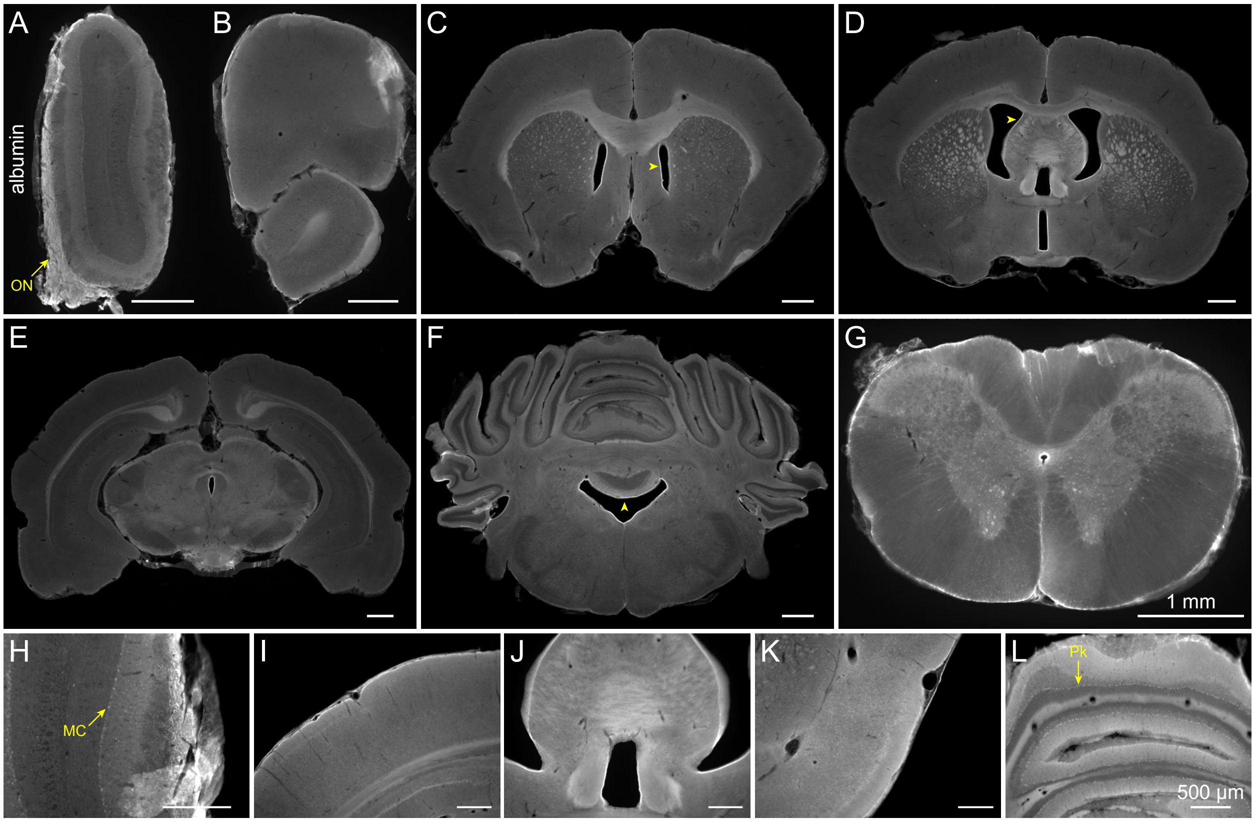

Figure 2. Preliminary detection of endogenous rat albumin revealed widespread cellular distribution throughout the brain and at brain-CSF interfaces. (A-G) Albumin showed signal across the CNS, including in the olfactory nerve layer (A and H) and at the brain/spinal cord pial and ventricular surfaces (C-G). Specific albumin signal associated with circumventricular organs was not apparent (in contrast to IgG), e.g., the subfornical organ (J). Albumin appeared to be present in mitral cells (in the olfactory bulbs, A and H), cell bodies likely including neurons in the cortex and striatum (I and K), in large spinal motor neurons (G), and Purkinje cells of the cerebellum (putatively based on size, location, and morphology).

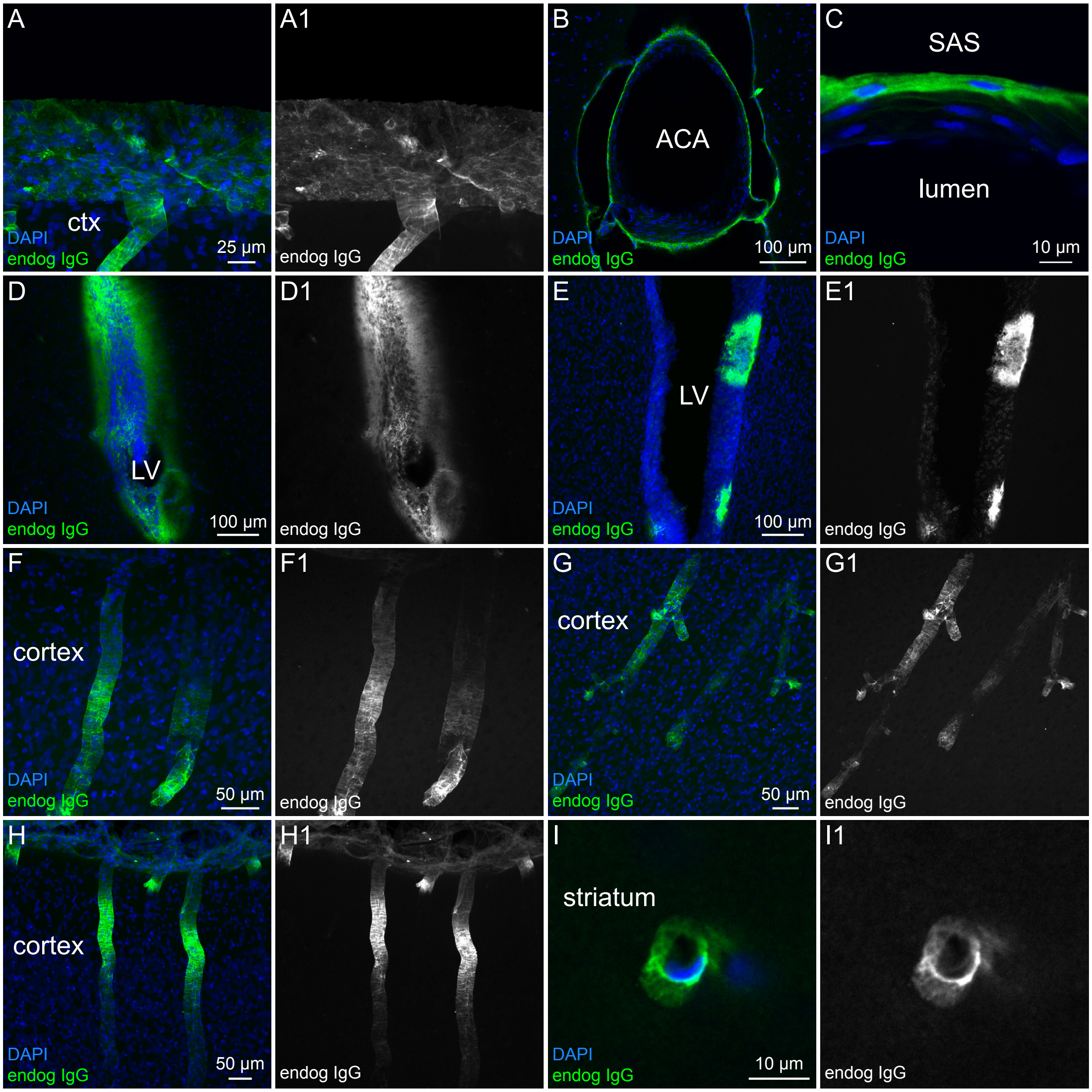

Figure 3. Confocal microscopy of endogenous IgG in the rat brain. (A) The cortical surface revealed IgG associated with the meninges as well as penetrating putative arterioles showing circumferential banding of IgG around smooth muscle cells. (B) IgG around the anterior cerebral artery (ACA) in the subarachnoid space at the ventral midline appeared to be associated with the perivascular space or vascular connective tissue space (C), while little signal penetrated into the tunica media. No signal was associated with endothelial cells or the lumen of the vessel. (D) The most anterior aspect of the lateral ventricle showed diffuse IgG signal around the ventricle (possibly extracellular)

but more posterior aspects of the lateral ventricle (E) showed high patches of IgG signal and low signal in scattered ependymal cells. (F-H) IgG signal was prominent in the perivascular spaces associated with arterioles (showing characteristic circumferential banding pattern), and also along some putative venules for a short distance into the brain (e.g., three short profiles penetrating in H). (I) Microvessels smaller than 8 μm also showed IgG signal in a potential pericapillary space.

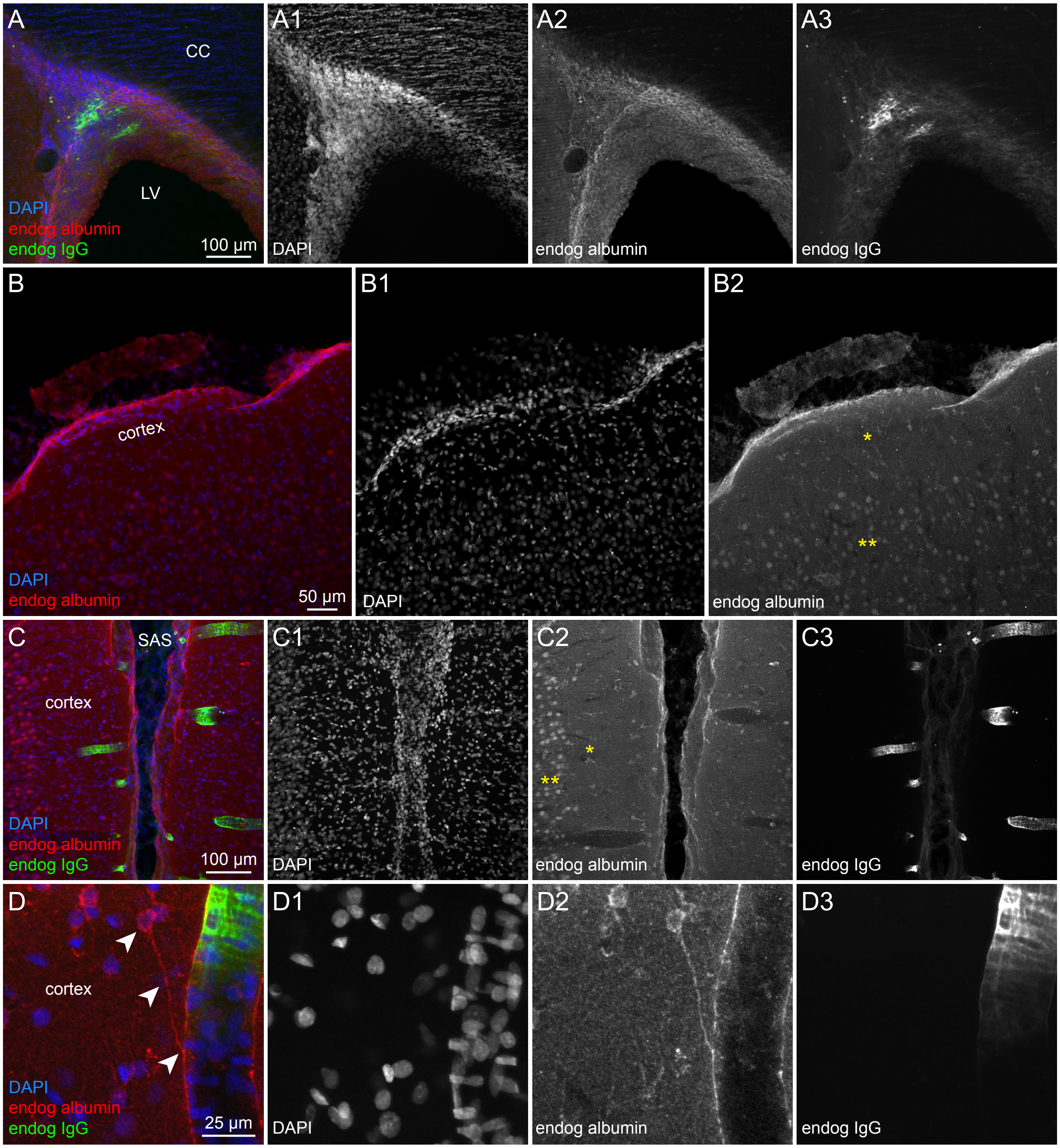

Figure 5. Confocal microscopy of endogenous albumin and IgG in the rat brain. (A) Albumin signal near the dorsal aspect of the lateral ventricle (LV) was regular and appeared cellular while IgG signal was sparse and diffuse in nature (possibly extracellular). Albumin in the striatum (left of LV) also showed cellular profiles but signal was faint in the white matter of the corpus callosum (CC). (B) Widespread albumin signal in the cortex was associated with cellular profiles (some cells showed extended processes toward the pial surface, reminiscent of astrocytes, and other cells

were rounded in deeper layers of the cortex, reminiscent of neuronal cell bodies). Prominent albumin signal was present at the pial surface with lower signal in the meninges overlying the cortex. (C) At the cortical midline albumin labeling also shows noticeable surface signal and similar cellular profiles; IgG is predominantly associated with the meninges and perivascular spaces. (D) IgG in a perivascular space reveals albumin present in a cell body with a process that reaches to contact the perivascular compartment. Overall, albumin and IgG did not appear to co-localize significantly in the rat brain except at the meningeal surfaces and in the choroid plexus.

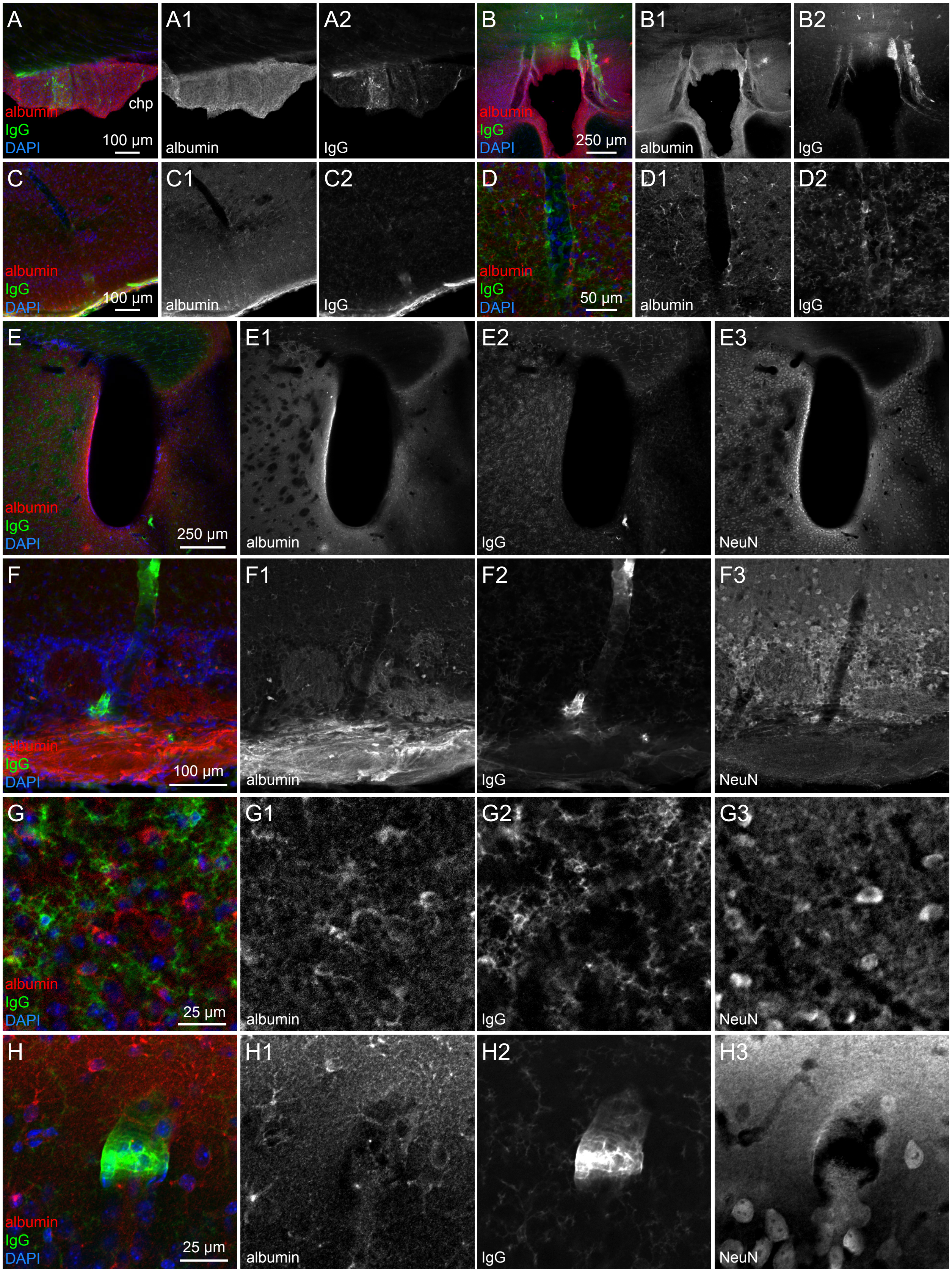
A
albumin
IgG
DAPI
chp
100 µm
A1
albumin
A2
IgG
B
albumin
IgG
DAPI
250 µm
B1
albumin
B2
IgG
C
albumin
IgG
DAPI
100 µm
C1
albumin
C2
IgG
D
albumin
IgG
DAPI
50 µm
D1
albumin
D2
IgG
E
albumin
IgG
DAPI
250 µm
E1
albumin
E2
IgG
E3
NeuN
F
albumin
IgG
DAPI
100 µm
F1
albumin
F2
IgG
F3
NeuN
G
albumin
IgG
DAPI
25 µm
G1
albumin
G2
IgG
G3
NeuN
H
albumin
IgG
DAPI
25 µm
H1
albumin
H2
IgG
H3
NeuN

Figure 6. Preliminary distribution of endogenous IgG and albumin in the mouse brain. (A) Albumin distributed consistently throughout the choroid plexus, but IgG distribution was patchy. (B) Albumin distribution around the subfornical organ was diffuse while IgG signal appeared around large vessels and faintly in cellular profiles. (C) The ventral cortex showed prominent albumin and IgG signal at the pial surface with distinct cellular profiles for both proteins. (D) Albumin and IgG both demonstrated an intracellular appearance surrounding a blood vessel but did not appear to colocalize. (E) In the striatum adjacent to the lateral ventricle albumin again showed cellular profiles (a few of which appeared to colocalize with NeuN (E3), while IgG showed sparse perivascular signal and widespread cellular labeling in both the striatum and corpus callosum. (F) Albumin was diffusely localized to the olfactory nerve layer at the edge of the olfactory bulb in addition to cellular signal, some of which appeared to colocalize with NeuN. IgG was present in a penetrating perivascular space and again in cellular profiles. (G) Albumin and IgG signal in the cortex demonstrated their distinct cellular profiles, with no apparent colocalization. Albumin may rarely colocalize with NeuN. (H) A blood vessel in the cortex showed perivascular IgG signal, surrounded by IgG and albumin positive cell profiles. Albumin was present in a cell that labeled positive for NeuN (far right). Overall, albumin and IgG appeared to be present in separate and distinct cells; cell morphology might suggest albumin in some neurons (as demonstrated with NeuN) and/or astrocytes, while IgG cell profiles appeared microglial. Additional labeling will be required to identify these cells.

CHAPTER 6

Dual-labeled nanoparticles allow for correlative *in vivo* magnetic resonance and *ex vivo* fluorescence imaging following intrathecal infusion in rats

Michelle E. Pizzo[1,2*], Guojun Chen[3,4*], Daniel J. Wolak[1,2*], Christina L. Brunnquell[5], M. Elizabeth Meyerand[2,5,6], Shaoqin Gong[3,4,6-7], Robert G. Thorne[1,2,8-10]
[1]School of Pharmacy, Division of Pharmaceutical Sciences, [2]Clinical Neuroengineering Training Program, [3]Department of Materials Science and Engineering, [4]Wisconsin Institute for Discovery, [5]Department of Medical Physics, [6]Department of Biomedical Engineering, [7]McPherson Eye Research Institute, [8]Neuroscience Training Program, [9]Cellular and Molecular Pathology Graduate Program, [10]Institute for Clinical and Translational Research, University of Wisconsin-Madison, Madison, WI
*These authors contributed equally to this work.

Abstract

A detailed description of the distribution of intrathecally administered nanoparticles from the cerebrospinal fluid into the brain is currently lacking. There is a need for cross-validation of *ex vivo* and *in vivo* techniques and findings. However, most studies have focused on comparison of 'similar' tracers for separate imaging modalities or labeling of the same substance with different labels for detection with various imaging techniques. It is therefore critical that multi-functional tracers are developed that allow for tracking of the exact same substance using multiple imaging techniques, ideally within the same animal. Here, we have developed a dual-labeled unimolecular nanoparticle for *in vivo* dynamic magnetic resonance imaging (MRI; via Gd label) and *ex vivo* high-resolution fluorescence imaging (via Cy3.5 label). The unimolecular nanoparticles were characterized using multiple techniques and the size determined utilizing transmission electron microscopy, dynamic light scattering, and integrative optical imaging, and were found to be approximately 13 nm in hydrodynamic diameter. Rats received low-flow intracisternal infusions of the nanoparticles during 3D T1-weighted dynamic MRI acquisition, which demonstrated the nanoparticles distributed throughout the CSF compartment in a rostral-to-caudal direction in the spinal subarachnoid space and a caudal-to-rostral direction in the cranial subarachnoid space, with entry into the brain parenchyma as well. *Ex vivo* fluorescence imaging of the whole brain and coronal brain sections revealed transport along the perivascular spaces of cerebral blood vessels. Nanoparticle entry into the parenchymal perivascular spaces was limited, likely due to large the nanoparticle size; nonetheless, transport was observed along all caliber of vessels including microvessels reconfirming the convective nature of this pathway.

Introduction

Movement of macromolecules throughout the brain remain poorly understood but are becoming better resolved using *ex vivo* detection methods (e.g., fluorescence, chromogenic substrates, gene-product detection, electron microscopy, radioactivity, mass spectrometry) and *in vivo* techniques (e.g., magnetic resonance imaging (MRI), positron emission tomography, bioluminescence, multi-photon microscopy). Limited work has been completed using identical probes that are labeled for one technique or the other to allow comparison (e.g., Gd-IgG vs fluor-IgG (Pizzo *et al.*, 2018)), but little to no work has been conducted using a single, identical, multi-functional probe to study brain distribution from the cerebrospinal fluid (CSF). To ensure that *ex vivo* data is reliable and valuable, it is necessary to demonstrate that it has relevance *in vivo*, but *in vivo* methods often lack some facet of resolution that can be clarified with *ex vivo* techniques. This necessitates novel, multi-functional probes (ideally with real-world utilities including drug delivery and diagnostics) capable of detection using a variety of methods.

Previous studies using either *ex vivo* (ventriculocisternal perfusion with radiolabeled tracers (Rall *et al.*, 1962; Levin *et al.*, 1970; Patlak & Fenstermacher, 1975), integrative optical imaging with acute slice preparation (Nicholson & Tao, 1993; Tao & Nicholson, 1996; Thorne *et al.*, 2004), fluorescence penetration following infusion (Wolak *et al.*, 2015*a*; Pizzo *et al.*, 2018)) or *in vivo* (real-time iontophoresis (Nicholson & Phillips, 1981), integrative optical imaging via open cranial window (Thorne & Nicholson, 2006; Thorne *et al.*, 2008), multi-photon fluorescence recovery after photobleaching (Binder *et al.*, 2004; Papadopoulos *et al.*, 2005*a*, 2005*b*)) techniques have suggested that small and large substances move through the brain extracellular spaces of the neuropil in a manner that is consistent with Fickian diffusion (see reviews (Syková & Nicholson, 2008; Wolak & Thorne, 2013)). However, pathways for convective or bulk flow have also been demonstrated along perivascular spaces of cerebral blood vessels and white matter tracts (Cserr *et al.*, 1977; Szentistványi *et al.*, 1984; Rennels *et al.*, 1985; Ichimura *et al.*, 1991), the former of which has been suggested to allow for communication between the CSF and the interstitial fluid (ISF) of the brain parenchyma to great depths (Rennels *et al.*, 1985; Iliff *et al.*, 2012). It has also been reported that *entry* into the perivascular spaces is size-dependent for proteins infused into the CSF (Pizzo *et al.*, 2018), which may restrict entry of larger endogenous or exogenous substances (e.g., nanoparticles) from readily accessing the perivascular spaces. Distribution of nanoparticles from the CSF into the brain (potentially for drug delivery or diagnostic purposes) and the mechanisms of transport have been sparsely studied.

To our knowledge, no studies have yet used a multi-functional probe to investigate CSF-to-brain distribution utilizing correlative *ex vivo* fluorescence imaging and *in vivo* dynamic MRI. Thus, here we characterized unimolecular nanoparticles conjugated to both a fluorescent dye (Cy3.5) and a MR contrast agent (Gd-DOTA) and then intrathecally infused the nanoparticles to reveal the distribution in the rat CNS using *in vivo* 3D dynamic MRI and *ex vivo* fluorescence microscopy. This allows for correlation of the results and validation of the methods with each technique contributing unique data (e.g., kinetic profiles versus high resolution distribution) and together guiding educated conclusions of the mechanisms and pathways of distribution.

Materials and Methods

Nanoparticle Materials

Poly(amidoamine)–NH_2 dendrimer (PAMAM-NH_2; ethylenediamine core; G5) was purchased from Sigma–Aldrich (St. Louis, MO). Methoxy–poly(ethylene glycol)–succinimidyl carboxymethyl ester (PEG–SCM; M_n = 2 kDa) was acquired from JenKem Technology (Allen, TX). *p*-SCN-Bn-DOTA was obtained from Macrocyclics, Inc. (Plano, TX). Cy3.5-NHS was purchased from Lumiprobe Corporation (Hallandale Beach, FL). All other reagents were purchased from Thermo Fisher Scientific (Waltham, MA) unless otherwise specified.

Synthesis of PAMAM-DOTA/Cy3.5/PEG

PAMAM-NH_2 (1 mg, 3.5×10^{-5} mmol) was first reacted with *p*-SCN-Bn-DOTA (0.95 mg, 1.4×10^{-3} mmol) and Cy3.5-NHS (0.1 mg, 1.4×10^{-4} mmol) in dimethylformamide (DMF; 3 mL) at room temperature in the dark for 12 h. PEG–SCM (3.15 mg, 3.15×10^{-3} mmol) was then added into the solution and the reaction was carried out for another 12 h. Thereafter, the resulting solution was dialyzed against deionized water for 48 h using a cellulose membrane (molecular weight cut-off, 15 kDa; Spectrum Laboratories, Inc., Rancho Dominguez, CA). The final product was dried by lyophilization (Labconco, Kansas City, MO).

Synthesis of PAMAM-Gd-DOTA/Cy3.5/PEG

PAMAM-DOTA/Cy3.5/PEG (4 mg) was dissolved in sodium acetate buffer solution (3 mL; 0.1 M; pH 7.0). $GdCl_3$ in a sodium acetate buffer solution (2 mL, 50 μg/mL) was added dropwise into the PAMAM-DOTA/Cy3.5/PEG solution. After stirring overnight, the resulting solution was dialyzed against DI water for 48 h using a cellulose membrane (molecular weight cut-off, 15 kDa) to remove unloaded Gd^{3+}. All above steps were performed at room temperature. The final product was dried by lyophilization. The lyophilized powder was stored at -20ºC until reconstituted for use. PAMAM-Gd-DOTA/Cy3.5/PEG can readily from unimolecular nanoparticles in an aqueous solution.

Characterization

The chemical structures and molecular weights of polymers were determined using ^{1}H NMR spectroscopy and gel permeation chromatography (GPC), respectively. The size and morphologies of the resulting nanoparticles were determined by dynamic light scattering (DLS, ZetaSizer Nano ZS90, Malvern Instrument; 0.05 mg/mL in DI water) and transmission electron microscopy (TEM, FEI Tecnai G2 F30 TWIN 300 KV, E.A. Fischione Instruments, Inc.). To prepare the TEM sample, a drop of copolymer solution (0.05 mg/ml) was deposited onto a 200 mesh copper grid coated with carbon, dried at room temperature, and negatively stained with 1 wt% of phosphotungstic acid for 30 s. The Gd^{3+} loading content was measured by inductively coupled plasma atomic emission spectroscopy (ICP-AES; Optima 2000 DV, PerkinElmer Inc.). The Cy3.5 content in the nanoparticles was determined by UV-Vis spectrometer (Varian Cary 300 Bio UV–Vis spectrophotometer, Agilent Technologies) at 590 nm.

Integrative optical imaging (IOI) diffusion measurements

Nanoparticles were prepared in 154 mM NaCl from a lyophilized powder at a concentration of 1 mg/mL, vortexed briefly, and centrifuged for 5 min at 12,000 × *g*. Nanoparticle diffusion was evaluated in free solution and in the rat neocortex *in vivo* (see below) using integrative optical imaging (IOI) as previously described (Thorne & Nicholson, 2006; Thorne *et al.*, 2008; Wolak *et al.*, 2015*b*). IOI is a well-characterized method that utilizes epifluorescent microscopy and quantitative image analysis to measure the diffusion of fluorescently-labeled molecules. After a brief pulse injection, successive images of the diffusion cloud were recorded at regular intervals of 4-8 s using a custom program in MatLab (The MathWorks) provided by C. Nicholson and L.

Tao (Nicholson & Tao, 1993). Image analysis was performed with a second MatLab program using the following expressions based on a point source approximation of Fick's Second Law:

$$I_i(r, \gamma_i) = E_i \exp\left[-(r / \gamma_i)^2\right] \qquad \text{(Equation 1)}$$

and

$$\gamma_i^2 = 4D(t_i + t_0) \qquad \text{(Equation 2)}$$

where I_i is the fluorescence intensity of the ith image at radial distance r from the source point, and E_i incorporates the defocused point spread function of the microscope objective (Tao & Nicholson, 1995). To account for deviation from the point source approximation, a time offset, t_0, was added to the measured time from injection, t_i. Eq. 1 was fit to the upper 90% of the fluorescence intensity curves using a nonlinear simplex algorithm, providing estimates of a parameter, γ^2, at a succession of t_i intervals. A linear regression plot of $\gamma^2/4$ versus t_i returned a slope equal to $D*$ (or D) based on Eq. 2. Analysis were performed using curves across six axes of the intensity clouds with the final value of $D*$ (or D) obtained from an average of four values (excluding the highest and lowest). Measurements of D were made at 37 ± 1°C using 0.3% NuSieve GTG agarose (FMC) in 154 mM NaCl and measurements of D^* were at a depth of 200 μm below the pial surface in the primary somatosensory cortex *in vivo* (see preparation below). D was further used to calculate the apparent hydrodynamic diameter (d_H) using the Stokes-Einstein equation [$d_H = (kT)/(3\pi\eta D)$, where k is Boltzmann's constant, T is absolute temperature, and η is the viscosity of water (6.9152×10^{-4} Pa·s at $T = 310$ K)] (Thorne *et al.*, 2004).

Animal use

Experiments were carried out at the University of Wisconsin-Madison in accordance with National Institutes of Health Guide for the Care and Use of Laboratory Animals (2011) and local

Institutional Animal Care and Use Committee regulations. Animals were housed in a climate-controlled room under a 12-hour light/dark cycle with *ad libitum* access to food and water. For all experiments Harlan Sprague-Dawley rats (female; 180-220 g, ~9-14 weeks of age; Harlan/Envigo, Indianapolis, IN) were anesthetized with urethane (1.2 g/kg i.p., to effect) and tracheotomized. Atropine sulfate (0.1 mg/kg every two hours; s.c.) was administered to diminish bronchial secretions. Following induction of anesthesia all animals were kept on a homeothermic blanket system (Harvard Apparatus, Holliston, MA) to maintain body temperature at 37ºC.

In vivo IOI surgical preparation

Animals were prepared for IOI as described previously (Thorne & Nicholson, 2006; Thorne *et al.*, 2008; Wolak *et al.*, 2015*b*). Briefly, anesthetized and tracheotomized rats were placed in a three-point head holder (Narishige, Amityville, NY). A custom fabricated chamber was fixed to the skull over the left parietal cortex and continuously superfused with artificial cerebrospinal fluid (ACSF; composition, mM: 124 NaCl, 3 KCl, 26 $NaHCO_3$, 1.25 NaH_2PO_4, 1.3 $MgCl_2$, 1.5 $CaCl_2$, and 10 D-glucose equilibrated with 95% O_2/5% CO_2; 300 ± 5 mOsm/kg osmolality determined using a freezing-point osmometer, Model 3250 Osmometer, Advanced Instruments, Norwood, MA) through the chamber ports at 2 ml/min (Minipuls 3, Gilson, Middleton, WI); ACSF was heated to 37 ± 1 °C using a solution in-line heater (TC-344B, Warner Instruments, Hamden, CT) and continuously superfused for the duration of experiments. An approximately 3 x 4 mm craniotomy performed over the primary somatosensory cortex and the dura was then carefully removed before animals were positioned under an BX61WI microscope (Olympus, Tokyo, Japan) for imaging after an equilibration period of at least 1 h.

Intracisternal cannula placement

Animals were prepared for intrathecal infusion as described previously (Wolak *et al.*, 2015*b*; Pizzo *et al.*, 2018). Briefly, anesthetized and tracheotomized rats were placed in a stereotaxic frame (Stoelting Co., Wood Dale, IL) in the flat skull position. A dorsal midline neck incision exposed the atlanto-occipital membrane overlying the cisterna magna. The atlanto-occipital membrane was retracted, a small durotomy made in the dura, a custom cannula made of 33 GA PEEK tubing (Plastics One Inc., Roanoke, VA) immediately inserted 1 mm into the cisterna magna at a 30-degree angle from the horizontal, and the tubing sealed to the dura with cyanoacrylate. The PEEK tubing was connected to PE-10 tubing and a Hamilton syringe controlled by an infusion pump (Quintessential stereotaxic injector, Stoelting), which was filled with infusate prior to insertion.

In vivo magnetic resonance imaging (MRI)

All MRI experiments were performed as described previously (Pizzo *et al.*, 2018) using an Agilent 4.7 T small animal MRI and VnmrJ software (Agilent Technologies Inc., Santa Clara, CA). Animals prepared as above (N=3) were carefully transferred from the stereotaxic frame to a transmitting/receiving volume coil after placement of the infusion cannula, maintaining animals in the prone position. Physiological parameters (i.e., heart rate, respiratory rate) were monitored and a warm air blower heater used to maintain the animal’s temperature to ensure animals were in good condition throughout the experiment. The unimolecular, gadolinium-DOTA dual-labeled nanoparticles were detected using isotropic 3D T1-weighted spoiled gradient echo scans with the following sequence parameters: TR = 9.5 ms, TE = 4.8 ms, flip angle = 20°, field of view = 60×30×30 mm, resolution = 256×128×128, averages = 4, voxel size = μm; each scan was 10 min 22 sec. A pre-infusion baseline scan was acquired then the following scan and the infusion of the nanoparticles (1.6 μL/min, 80 μL total) were started simultaneously. Animals were scanned continuously throughout the 50 min infusion and for approximately 60 min post-infusion.

Ex vivo fluorescence imaging

Animals were then removed from the coil, repositioned supine, and the abdominal aorta cannulated. At 100 minutes post-infusion the animals were perfused with 50 mL ice cold 0.01 M phosphate buffered saline (PBS) followed by 450 mL 10% paraformaldehyde (PFA) in 0.1 M phosphate buffer at a rate of 15 mL/min (*N*=2). The whole brain, cervical lymph nodes, and nasal passages were dissected and immediately imaged using an MVX10 Macroview microscope (Olympus) equipped with an Orca-flash 2.8 CMOS camera (Hamamatsu, Hamamatsu City, Japan) and X-Cite 120Q illuminator (Lumen Dynamics Group, Inc., Mississauga, Ontario, Canada) using the appropriate filter set (Chroma, U-M49008XL, Bellows Falls, VT). Images for large tissues were acquired at multiple depths of focus and in multiple overlapping sections; the former were first auto-blended in Photoshop CC (Adobe Systems, San Jose, CA) and the overlapping sections aligned then auto-blended. Brains were post-fixed overnight in 10% PFA at 4°C and lymph nodes placed in 20% sucrose in 0.01 M PBS overnight at 4°C. The following day brains were sectioned on a vibratome (Leica VT1000S) to 100 μm and the sections immediately imaged on a wet petri dish using the MVX10 (Olympus). Some sections were stained with 4',6-diamidino-2-phenylindole (DAPI; Life Technologies; 2 μg/mL in PBS with 0.1% triton X-100) for 20 minutes at room temperature followed by three five-minute washes in PBS; sections were mounted onto slides and coverslipped with Prolong Gold or Diamond Antifade (Life Technologies). Lymph nodes were covered in OCT (Tissue-Tek, Sakura, Torrance, CA), frozen in isopentane on dry ice, and stored at -20°C until sectioned on a cryostat (CM1950, Leica Microsystems, Wetzlar, Germany). Confocal imaging was performed using an FV1000 confocal microscope using FLUOVIEW software (Olympus) or an A1R confocal microscope with NIS Elements software (Nikon, Tokyo, Japan).

MRI Processing

MRI data was first registered using a rigid body registration by means of a custom Matlab (The MathWorks Inc.) program; subsequent quantification and dynamic visualization were performed using Fiji (Schindelin *et al.*, 2012). CSF and parenchymal brain regions of interest (ROIs) were manually outlined on raw MRI slices according to previous reports (Pizzo *et al.*, 2018), ensuring parenchymal brain areas did not include edges adjacent to CSF spaces to avoid signal contamination. The average pixel intensity for each ROI was measured for each MRI scan and the percent change from pre-infusion baseline for each ROI was averaged across all animals (N=3; negative values set to zero). Using Fiji for 3D dynamic visualization, the pre-infusion baseline images were subtracted from all subsequent scans with negative values set to zero and the extracranial tissue (e.g., tongue, neck) cropped. 4D videos and 3D still images were created using the 3D Viewer Plugin (volume, no resampling) (Schmid *et al.*, 2010).

Statistical analyses

A Student's two-tailed t-test was used for all two-way comparisons (p values listed in text). Statistical analyses were performed using SigmaPlot (Systat Software Inc., San Jose, CA); all values listed as mean ± s.e.m; N animals, n measurements.

Results

Dual-labeled nanoparticles

Novel dual-labeled nanoparticles (schematic in Fig. 1*A*) were created as multi-functional tracers to allow for novel, correlative *in vivo* MRI and *ex vivo* fluorescence experiments. The PAMAM-DOTA/Cy3.5/PEG polymer was synthesized as outlined in Fig. 1*B*. DOTA was conjugated onto PAMAM-NH_2 through a reaction between –SCN and –NH_2. Cy3.5 fluorophore was also conjugated onto the PAMAM dendrimer through amidization. Subsequently, the PAMAM-DOTA/Cy3.5 was functionalized with hydrophilic PEG segments via amidization. The chemical structure of PAMAM-DOTA/Cy3.5/PEG was confirmed by ^1H NMR; the characteristic peaks were labeled as shown in Fig. 2*A*. A significant increase in molecular weight determined by GPC (Table 1) also demonstrated the successful formation of PAMAM-DOTA/Cy3.5/PEG. An MRI contrast agent, Gd^{3+}, was then complexed with DOTA chelator to form PAMAM-Gd-DOTA/Cy3.5/PEG (Nwe *et al.*, 2010). The Gd^{3+} and Cy3.5 contents were measured by ICP-AEC and UV-vis spectroscopy, respectively. There were approximately 32 Gd^{3+} and approximately 3 Cy3.5 per PAMAM-Gd-DOTA/Cy3.5/PEG, as determined by ICP-AES and UV-Vis spectrophotometry, respectively.

The morphology of the PAMAM-Gd-DOTA/Cy3.5/PEG nanoparticles was first studied by TEM and DLS. The TEM image in Fig. *2B* shows spherical nanoparticles with a good dispersity. The average size observed by TEM was 8.6 ± 1.8 nm. The hydrodynamic diameter was measured by DLS, with an average size of 14.6 ± 1.7 nm (polydispersity index (PDI) = 0.12) (Fig. 2*C*). The zeta potential of the nanoparticles was determined to be approximately neutral (i.e., + 1.2 mV) by DLS as well.

Table 1. Summary of GPC analysis of PAMAM-DOTA/Cy3.5/PEG nanoparticles.

	M_n	**M_w**	**PDI**
PAMAM-NH_2	28,917	-	-
PAMAM-DOTA/Cy3.5/PEG	171,077	206,832	1.21

Integrative optical Imaging (IOI)

Integrative optical imaging (IOI) was utilized to determine the diffusion of the dual-labeled nanoparticles in free media or rat primary sensory cortex. Following a brief sub-nanoliter pressure injection fluorescent images were captured showing the diffusion cloud over time. The nanoparticles show a substantially faster spread away from the injection site in free media compared to cortex, as expected (Fig. 3*A*). The raw fluorescent profile along a line reveals a Gaussian-shaped curve that agrees well with the theoretical fit (Fig. 3*B*). IOI measurements for the nanoparticles (Table 2) yielded a free diffusion coefficient $D = 4.92 \pm 0.18 \times 10^{-7}$ cm^2/s ($n = 22$) and a hydrodynamic diameter of 13.35 ± 0.49 nm, in agreement with the results of TEM images and DLS measurements. Effective diffusion in brain ($D^* = 0.50 \pm 0.17 \times 10^{-7}$ cm^2/s ($n = 8$; $N = 3$ animals)) was 10-fold lower than in free medium with a with a tortuosity value ($\lambda = (D/D^*)^{1/2}$) of $\lambda = 3.13 \pm 0.57$, which was more hindered than predicted by the restricted diffusion (RD) model (Thorne & Nicholson, 2006) for a 13 nm inert object (predicted $\lambda = \sim 2.6\text{-}2.7$).

Table 2. Summary of integrative optical imaging (IOI) diffusion results.

	D (10^{-7} cm^2/s) (n)	**d_H (nm)**	**D^* (10^{-7} cm^2/s) (N, n)**	**$\lambda = (D/D^*)^{1/2}$**	**Predicted (RD model)**
PAMAM-DOTA/Cy3.5/PEG Nanoparticles	4.92 ± 0.18 (22)	13.35 ± 0.49	0.50 ± 0.17 (8, 3)	3.13 ± 0.57	2.62-2.71

All values reported as mean ± SEM; *N* animals, *n* measurements.

In vivo MRI and whole brain ex vivo fluorescence imaging

Nanoparticles were intracisternally infused for 50 min in rats, at a flow rate of 1.6 µL/min (Pizzo *et al.*, 2018), which has been demonstrated not to elevate intracranial pressure (Yang *et al.*, 2013; Bedussi *et al.*, 2017). 3D T1-weighted MRI scans were acquired throughout the infusion and for 60 min post-infusion (*N*=3). Image contrast enhancement associated with the infused nanoparticles in representative raw MRI slices (Fig. 4 *A-F* and *I-L*) showed nanoparticles initially distributed throughout CSF cisterns close to the infusion site (e.g., cisterna magna, interpeduncular cistern, ambient cistern) then flow in a rostral-to-caudal direction down the spinal SAS and in a caudal-to-rostral direction predominantly along the ventral SAS towards the olfactory nerves (Fig. 4 *A-F*), a known CSF efflux route (Faber, 1937; Bradbury *et al.*, 1981; Bradbury & Westrop, 1983; Szentistványi *et al.*, 1984; Zhang *et al.*, 1992; Kida *et al.*, 1993; Koh *et al.*, 2005). Sparse nanoparticle signal was present over the dorsal cortex or in the dorsal spinal SAS, as reported previously for gadolinium-labeled IgG (Pizzo *et al.*, 2018), possibly due to narrow SAS in these regions (Pease & Schultz, 1958; Morse & Low, 1972; Oda & Nakanishi, 1984). Quantification of the percent signal change from the pre-infusion baseline for several CSF or parenchymal regions of interest (ROIs) showed markedly different kinetics (e.g., time to peak change) (Fig. 4 *G* and *H*). CSF ROIs tended to show increasing nanoparticle signal during the infusion and a decline as or shortly after the infusion finished (though dorsal cranial cisterns (quadrigeminal and olfactofrontal) appeared to plateau for the ~70 min post-infusion distribution time); ROIs associated with potential nerve efflux routes, e.g., olfactory and trigeminal nerves, as well as parenchymal ROIs tended to progressively increase throughout the infusion and during the ~70 min post-infusion distribution time. Raw horizontal slices and 3D visualization revealed evident perivascular signal around major surface arteries associated with the circle of Willis within 20-30 minutes of the start of infusion, persisting after the infusion and extending further along the vessels (Fig. 4 *M-T*).

At 100 min post-infusion, two of the animals were transcardially perfused with PBS followed by 10% PFA, and the whole brains immediately removed for *ex vivo* imaging of the brain surface with fluorescence microscopy (Fig. 5). Preliminary *ex vivo* fluorescence revealed nanoparticle signal on the dorsal brain surface (Fig 5*A*) appeared to be associated with middle cerebral artery branches laterally, and possibly superficial superior cerebral veins branching laterally from the midline; signal was also prominent at brain surfaces adjacent to CSF cisterns including the olfactofrontal cistern, quadrigeminal cistern, and the cisterna magna (infusion site), as well as between the folia of the cerebellum. On the ventral brain surface (Fig. 5 *B-C*), particularly high signal was present around the basilar artery, circle of Willis, and lateral branches of the middle cerebral arteries, on the ventral aspects of the olfactory bulbs and ventral subarachnoid cisterns, and associated with the hypoglossal nerves (Fig. 5*D*). Punctate signal associated with perivascular nanoparticles around penetrating vessels appeared in close proximity to some large vessels with perivascular signal, but most other brain areas were devoid of punctate and diffuse surface signal. Perivascular signal also appeared around the caudal rhinal vein visible on the lateral surface of the brain (Fig. 5*E*). Dissection of the nasal passages (Fig. 5*F*) and cervical lymph nodes (Fig. 5 *G* and *I*), known CNS drainage pathways (Faber, 1937; Bradbury *et al.*, 1981; Bradbury & Westrop, 1983; Szentistványi *et al.*, 1984; Zhang *et al.*, 1992; Kida *et al.*, 1993; Koh *et al.*, 2005), revealed high signal was present within the cribriform plate and nasal mucosa, particularly in the olfactory region, as well as in the cervical lymph nodes (consistent with much past work (Bradbury *et al.*, 1981; Bradbury & Westrop, 1983; Szentistványi *et al.*, 1984)). Signal was present in at least some superficial lymph nodes (Fig. 5*G*) and all deep cervical lymph nodes (Fig. 5*I*) for all animals, but signal was always of higher intensity in deep cervical lymph nodes.

Ex vivo fluorescence in coronal brain sections and confocal microscopy of perivascular nanoparticles

The preliminary *ex vivo* fluorescence imaging of infused nanoparticles in coronal brain sections (*N*=2) revealed a limited distribution that spanned the entire neural axis, from the olfactory bulbs to the spinal cord (Fig. 6). Four general types of signal were observed: i) numerous perivascular profiles in both cortical and subcortical structures, ii) a small, diffuse gradient at the brain-subarachnoid interfaces, iii) periventricular signal in the white matter adjacent to the lateral ventricles, and iv) cranial and spinal nerve associated signal (e.g., optic chiasm, oculomotor nerve, cochlear nerve, and ventral spinal nerves, visible in Fig. 6 *E*, *H*, *I*, and *J*, respectively). Very high signal was observed at the brain surface relative to the diffuse signal in the parenchyma, possibly indicating nanoparticles associated within or entrapped by the leptomeninges. Nanoparticle signal in the spinal cord (Fig. 6*J*) was diffuse at the CSF interfaces (and high in spinal nerves) but also revealed that most perivascular signal was present within the spinal gray matter, which has a high relative vascularity compared to the spinal white matter (demonstrated in (Pizzo *et al.*, 2018)).

Confocal microscopy demonstrated that the perivascular nanoparticle signal was associated with vessels of all caliber, from arteries, to microvessels, to veins. For leptomeningeal arteries on the brain surface (Fig. 7 *A*-*C*) the nanoparticles were most prominent in the outer putative adventitial layer of the artery with lesser signal intercalated between smooth muscle cells, possibly associated with the smooth muscle basement membrane. Arterioles in the cortex and striatum also demonstrated perivascular nanoparticle signal, often appearing to surround smooth muscle cells creating a circumferential banding pattern (Fig. 7 *D-F*). Large, seemingly empty perivascular spaces are visible surrounding the arterioles, likely exaggerated due to tissue processing and fixation, but nonetheless allowing for the parenchyma-associated putative astrocyte basement membrane signal to be distinguished from signal associated with the arteriole wall. It is likely that these perivascular spaces were filled with fluid *in vivo*, as (i) nanoparticle signal is fixed to fiber-like structures within the space, possibly collagen, and (ii) perivascular macrophages appear to have taken up nanoparticles. Putative venules in the cortex also demonstrated perivascular nanoparticles, with a generally longitudinal arrangement of signal and a complete lack of smooth muscle banding visible for arterioles (Fig. 7 *G-I*). Nanoparticles were also present around numerous microvessels less than 10 μm in diameter (Fig. 7 *J-L*).

Discussion

These dual-labeled nanoparticles proved to be excellent tracers for *in vivo* dynamic 3D MRI and high-resolution *ex vivo* fluorescence techniques, allowing a direct comparison of the distribution within the same animal. Importantly, the combination of imaging techniques demonstrated that while the lower resolution MRI data might have suggested a relatively homogeneous distribution of nanoparticles throughout various brain regions of interest (e.g., cortex), the *ex vivo* fluorescence imaging revealed that the nanoparticles present in the brain parenchyma were almost entirely confined to the perivascular compartment.

Novel dual-labeled nanoparticles

Nanoparticles capable of dual fluorescence/MR imaging were readily formed by PAMAM-Gd-DOTA/Cy3.5/PEG in an aqueous solution. PAMAM-DOTA/Cy3.5/PEG polymers were synthesized by a simple one-pot reaction as shown in Fig. 1*B*. The reactions were also conveniently performed in a mild condition (e.g., room temperature and normal atmospheric pressure). DOTA has been demonstrated to be an excellent chelator for the MRI contrast agent, Gd^{3+}, since Gd-DOTA displays high relaxivity and stability and low toxicity (Magerstädt *et al.*, 1986; Bousquet *et al.*, 1988; Herborn *et al.*, 2007; Nwe *et al.*, 2010). Moreover, Gd-DOTA conjugated onto macromolecules, such as dendrimers, exhibits even higher relaxivity and thus better contrast enhancement effect with MRI (Wang *et al.*, 2003; Rudovský *et al.*, 2006; Nwe *et al.*, 2010). PAMAM dendrimer (G5) was chosen as the core macromolecule because such polymer is monodisperse and displays sufficient functional groups (128 $-NH_2$ groups) on its spherical surface for chemical modifications (e.g., Gd-DOTA, Cy3.5, and PEG conjugations) (Olson *et al.*, 2010). The Cy3.5 fluorophore conjugation proved to provide bright fluorescent signal for epifluorescence imaging and confocal microscopy. PEG functionalization can increase the water solubility as well as reduce nanoparticle opsonization with proteins. Since all the components are covalently linked, the resulting unimolecular nanoparticles are extremely stable both *in vitro* and *in vivo*, thus enabling excellent capability of dual fluorescence imaging and MRI. Moreover, in light of the good chemistry versatility of the unimolecular nanoparticles, other imaging modalities, such as radioisotopes for PET imaging, or small molecule payloads, can be incorporated into the nanoparticles to achieve their multifunctionalities.

Diffusion of nanoparticles in free media and in the rat brain in vivo

The size of the nanoparticles was characterized using TEM, DLS, and IOI, yielding comparable results (d= 9 nm, d_H= 14.6 nm, and d_H= 13.35, respectively). It is expected that DLS and IOI will provide a larger diameter than TEM because the IOI and DLS measure hydrodynamic size including the water shell in aqueous solution while TEM measures a dry diameter. DLS may suggest a higher size than IOI because of differences in salt concentration—DLS measurements were performed with nanoparticles in water, while IOI free diffusion measurements were performed in physiological saline; indeed DLS can provide inflated values of hydrodynamic diameter in lower salt environments as the electrical double layer is increased (Hackley & Clogston, 2011).

Previous studies suggest that transport within the brain parenchyma is strongly affected by the nanoparticle size and surface charge. Nanoparticles with a diameter close to the ECS width will experience steric hindrance and thus reduced transport and charged nanoparticles may be attracted to/repulsed by negatively-charged extracellular matrix (ECM) components (e.g., heparan sulfate proteoglycan) which could impact transport. The deviation of the measured IOI λ from the predicted value for an approximately 13 nm inert, spherical object is possibly explained by binding or charge effects as the effect of size is already accounted for by the RD model. It is expected that the PEG coating provides shielding to prevent potential interactions, but the amount or size of PEG may be insufficient to completely eliminate these interactions. Nanoparticle charge has been demonstrated as an important factor in determining brain distribution in studies injecting directly into the parenchyma. In general, studies have shown that neutrally-charged or negatively-charged nanoparticles have a greater distribution in the brain (following injection or CED) compared to positively-charged nanoparticles, even when considering size (MacKay *et al.*, 2005; Nance *et al.*, 2012; Kenny *et al.*, 2013; Arshad *et al.*, 2015). This is likely because attraction of positively-charged nanoparticles to negatively-charged ECM components hinders transport through the ECS. In the present study the nanoparticles are close to neutral, with only a very slight positive charge;

comparison with a study using similarly charged nanoparticles (+3-5 mV; 80 nm) demonstrated that CED infusion of these nearly neutral nanoparticles and slightly negatively-charged nanoparticles (-9 mV; ~80 nm) showed an identical distribution, while positively-charged nanoparticles (+70 mV; ~90 nm) showed a very restricted tissue penetration (MacKay *et al.*, 2005). As the nanoparticles in the present study are also substantially smaller in size, they are also expected to experience less hindrance from the negatively-charged 'walls' formed by the cells and ECM.

It is also important to consider the physical constraints to transport in the ECS. Nanoparticles for drug delivery or diagnostics must be sufficiently small enough that they are able to move through the brain ECS, which is on *average* 40-60 nm (Thorne & Nicholson, 2006). The nanoparticles used in the present study were approximately 13 nm in diameter, smaller than the average ECS width, and the present study showed considerable difficulty in small nanoparticles diffusing through the parenchyma or entering into the brain and perivascular spaces from the CSF. However, in many prior studies nanoparticles that are seemingly larger than the average ECS width have been administered into the brain and showed some distribution (MacKay *et al.*, 2005; Saito *et al.*, 2005; Nance *et al.*, 2012; Kenny *et al.*, 2013; Zhou *et al.*, 2013; Arshad *et al.*, 2015). Potential reasons for the distribution discrepancy include i) supraphysiological injection/infusion volumes and rates, ii) lesser-reported or investigated transport along low-resistance pathways, iii) heterogeneity in ECS width, and iv) dissolution of nanoparticles. First, much prior work used convection enhanced delivery (CED) to administer relatively large volumes into the parenchyma at relatively high flow rates. Initially it was suggested that the high infusion pressure of CED created a pressure gradient that forced the distribution of the infused substance *through the ECS of the neuropil* by convection

(Bobo *et al.*, 1994). However, as to the second point, it has been suggested that transport following CED infusion of micelles (~15 nm), AAV vectors (~20-25 nm), and liposomes (~65 nm) is predominantly along low-resistance perivascular pathways, not through the narrow ECS (Hadaczek *et al.*, 2006; Salegio *et al.*, 2014). Additionally, CED clearly does not reflect the ability of substances of such great size to distribute under physiological conditions, as was the goal of the present study. Third, electron microscopy studies have indicated a lack of ECS uniformity (Syková & Nicholson, 2008; Sosinsky *et al.*, 2008; Korogod *et al.*, 2015) suggesting that larger ECS widths may exist (e.g., at multicellular junctions (Kinney *et al.*, 2013)) that may be able to accommodate larger substances and explain some of the prior findings; however, the transport between these larger junctions would still be restricted by narrow connecting channels. Fourth, the distribution of some types of nanoparticles (e.g., liposomes (MacKay *et al.*, 2005; Saito *et al.*, 2005)) may not fully reflect the distribution of the large-sized particles *in vivo*, but may rather indicate the distribution of the incorporated tracers which have dissociated from intact nanoparticles or been released following nanoparticle disintegration.

Distribution of nanoparticles following intrathecal infusion

Here, we found excellent correlation between MRI and fluorescence imaging techniques following intrathecal infusion in rats: (i) CSF cisterns showed high nanoparticle signal in MRI *in vivo*, and *ex vivo* fluorescence showed highest surface signal at these brain-CSF interfaces, (ii) MRI showed increasing signal in the olfactory nerve region, and fluorescence demonstrated nanoparticles predominantly located in the olfactory mucosa of the nasal passages, (iii) the spinal cord showed a striking increase in nanoparticle signal in the internal spinal gray matter, where fluorescence revealed the nanoparticles predominantly in the spinal gray matter PVS. *Ex vivo* fluorescence also revealed limited penetration of the nanoparticles into the pial brain surface from the CSF, as expected of diffusion given their large size, but also revealed substantial transport of perivascular spaces of surface vessels and parenchymal vessels.

Confocal microscopy demonstrated that the infused nanoparticles were capable of being transported along the perivascular spaces of all types of vessels, including arteries/arterioles, veins/venules, and microvessels. Nanoparticles appeared to be associated with the vessel wall (putatively in the smooth muscle basement membrane) as well as the parenchymal wall (potentially associated with the astrocyte basement membrane); it is possible that the basement membranes present in these locations could be involved in transport, but they may also create a size-dependent barrier that these large nanoparticles are unable to easily cross. Nevertheless, the nanoparticles were able to continue along the PVS even to the level of the microvessel suggests that even at the capillary level a perivascular space may exist that is capable of rapid (relative to diffusion) transport (Pizzo *et al.*, 2018). However the basement membrane between the PVS and the brain parenchyma may pose a barrier to delivery for large therapeutics such as nanoparticles and gene therapy vectors (Hannocks *et al.*, 2018).

The more consistent presence of nanoparticles in the superficial cervical lymph nodes following nanoparticle infusion compared to IgG infusion (Pizzo *et al.*, 2018) may be due to the longer distribution time for the nanoparticles, or possibly some size-dependent pathway allowing nanoparticles easier access to the superficial cervical lymph nodes.

Brain distribution compared with other intrathecally delivered tracers

Coronal brain sections appeared to have fewer fluorescent perivascular profiles for the nanoparticles compared to a full-length goat IgG infused into rats using the same infusion rate/volume, despite the shorter distribution time for IgG (30 min post-infusion) and the longer distribution time for the nanoparticles (100 min post-infusion). This agrees with the hypothesis that there may be a size-dependent but permeable barrier between the CSF and the PVS, which may involve stomata or openings in the leptomeningeal cells lining blood vessels in the subarachnoid space (Pizzo *et al.*, 2018). The slight negative charge may have even attracted nanoparticles to these stomata, enhancing their perivascular entry despite their large hydrodynamic diameter.

These nanoparticles are similar in size to 70 kDa dextran (14-16 nm hydrodynamic diameter; (Syková & Nicholson, 2008)). Comparison with a much larger 500 kDa dextran administered using same infusion rate and volume in rats showed a somewhat similar distribution, however, the 500 kDa dextran appeared to access a great number of perivascular spaces, particularly of small vessels (Iliff *et al.*, 2013). It is likely that the nanoparticles are a more rigid assembly compared to dextrans, which are random-coil polymers and exhibit marked conformational flexibility (in addition to polydispersity), particularly for larger dextrans accessing confined environments (Xiao *et al.*, 2008). Thus while more flexible substances like dextrans may find it easier to cross between the CSF and PVS, large proteins (Pizzo *et al.*, 2018), nanoparticles, and gene therapy vectors may find diffusing across this barrier to be more challenging. Manipulation of the barrier between the CSF and PVS may allow for larger substances to gain access to the PVS, as hypothesized for intrathecal co-infusion of IgG with hyperosmolar mannitol (Pizzo *et al.*, 2018).

Previous studies have investigated the use of nanoparticles delivered via the CSF (Song *et al.*, 2010; Rungta *et al.*, 2013; Akita *et al.*, 2014, 2015), however, none provide detailed description or demonstration of delivery throughout various brain areas or specific pathways of distribution (i.e., perivascular spaces) as in the present study. Numerous studies have probed the use of nanoparticles for drug delivery via other CNS delivery routes including intraparenchymal injection/convection enhanced delivery (CED, e.g., (Hadaczek *et al.*, 2006; Salegio *et al.*, 2014)) or intranasal administration (e.g., (Harmon *et al.*, 2014)). In general, the results of these studies support the proposed mechanisms of distribution from the present study including diffusion in the neuropil and convective transport in the perivascular spaces. This highlights the critical need for knowledge of thorough *distribution* data following intrathecal administration to understand if delivery is achieved to the target areas, to understand the effects of nanoparticle size, charge, and binding, and to understand how delivery may translate to large human brains.

Delivery of multi-functional tracers

Multi-functional tracers have been of increasing interest for diagnostic and therapeutic purposes, as evidenced by numerous pre-clinical studies utilizing nanoparticles labeled for MRI and fluorescence molecular tomography (e.g., (Kircher *et al.*, 2003, 2012; Shibu *et al.*, 2013; Zhang *et al.*, 2013; Ni *et al.*, 2014; Shao *et al.*, 2015)). Most of these groups have used these nanoparticles to target brain tumors using systemic delivery routes, and generally rely on a leaky blood-tumor barrier or targeting moiety to enter the brain/tumor (Kircher *et al.*, 2003, 2012; Zhang *et al.*, 2013; Ni *et al.*, 2014; Shao *et al.*, 2015). However, our data would suggest that even though these nanoparticles are smaller (~10-30 nm) than the studies above and more similar to the size used in the present study (~13 nm), the distribution within the tumor and particularly to tumor boundaries (where the blood-brain barrier may be intact REF) may be hindered based on their size (note, many human brain tumors demonstrate increased tortuosity/hindrance (Vargová *et al.*, 2003)). Other studies prepared a single type of nanoparticles, each with a single label for various imaging modalities and correlated the distribution following administration (e.g., (Li *et al.*, 2014)).

However, caution should be taken in interpreting results of these experiments; even slight variation in size, charge, or binding capabilities may cause unanticipated discrepancies.

Conclusions

To our knowledge, this is the first detailed investigation of intrathecal dual-labeled nanoparticle distribution in the brain as demonstrated utilizing techniques that allow both high temporal (MRI) and spatial (epifluorescence / confocal imaging) resolution. Given the restricted brain distribution of our relatively small multi-functional probes, our results would suggest that larger, traditional nanoparticles would not sufficiently access the brain for the purpose of diagnostics or drug delivery using physiologically-relevant administration parameters. Use of multi-functionality nanoparticles in correlative studies that cross-validate transport processes and distribution (rather than co-administration of completely different tracers for various imaging modalities) and an emphasis on nanoparticle electrostatic/binding interactions and the physical barriers to delivery once inside the central compartment will be of utmost importance for design of clinically-useful nanoparticles.

References

Akita H, Nakatani T, Kuroki K, Maenaka K, Tange K, Nakai Y & Harashima H (2015). Effect of hydrophobic scaffold on the cellular uptake and gene transfection activities of DNA-encapsulating liposomal nanoparticles via intracerebroventricular administration. *Int J Pharm* **490,** 142–145.

Akita H, Tamaru M, Kajimoto K, Sato Y, Hatakeyama H, Harashima H & Nakatani T (2014). Application of apolipoprotein E-modified liposomal nanoparticles as a carrier for delivering DNA and nucleic acid in the brain. *Int J Nanomedicine*4267.

Arshad A, Yang B, Bienemann AS, Barua NU, Wyatt MJ, Woolley M, Johnson DE, Edler KJ & Gill SS (2015). Convection-Enhanced Delivery of Carboplatin PLGA Nanoparticles for the Treatment of Glioblastoma. *PLoS One* **10,** e0132266.

Bedussi B, van der Wel NN, de Vos J, van Veen H, Siebes M, VanBavel E & Bakker EN (2017). Paravascular channels, cisterns, and the subarachnoid space in the rat brain: A single compartment with preferential pathways. *J Cereb Blood Flow Metab* **37,** 1374–1385.

Binder DK, Papadopoulos MC, Haggie PM & Verkman AS (2004). In vivo measurement of brain extracellular space diffusion by cortical surface photobleaching. *J Neurosci* **24,** 8049–8056.

Bobo RH, Laske DW, Akbasak A, Morrison PF, Dedrick RL & Oldfield EH (1994). Convection-enhanced delivery of macromolecules in the brain. *Proc Natl Acad Sci U S A* **91,** 2076–2080.

Bousquet JC, Saini S, Stark DD, Hahn PF, Nigam M, Wittenberg J & Ferrucci JT (1988). Gd-DOTA: characterization of a new paramagnetic complex. *Radiology* **166,** 693–698.

Bradbury MW, Cserr HF & Westrop RJ (1981). Drainage of cerebral interstitial fluid into deep cervical lymph of the rabbit. *Am J Physiol* **240,** F329-36.

Bradbury MW & Westrop RJ (1983). Factors influencing exit of substances from cerebrospinal fluid into deep cervical lymph of the rabbit. *J Physiol* **339,** 519–534.

Cserr HF, Cooper DN & Milhorat TH (1977). Flow of cerebral interstitial fluid as indicated by the removal of extracellular markers from rat caudate nucleus. *Exp Eye Res* **25 Suppl,** 461–473.

Faber WM (1937). The nasal mucosa and the subarachnoid space. *Am J Anat* **62,** 121–148.

Hackley VA & Clogston JD (2011). Measuring the hydrodynamic size of nanoparticles in aqueous media using batch-mode dynamic light scattering. *Methods Mol Biol* **697,** 35–52.

Hadaczek P, Yamashita Y, Mirek H, Tamas L, Bohn MC, Noble C, Park JW & Bankiewicz K (2006). The "perivascular pump" driven by arterial pulsation is a powerful mechanism for the distribution of therapeutic molecules within the brain. *Mol Ther* **14,** 69–78.

Hannocks M-J, Pizzo ME, Huppert J, Deshpande T, Abbott NJ, Thorne RG & Sorokin L (2018). Molecular characterization of perivascular drainage pathways in the murine brain. *J Cereb Blood Flow Metab* **38,** 669–686.

Harmon BT, Aly AE, Padegimas L, Sesenoglu-Laird O, Cooper MJ & Waszczak BL (2014). Intranasal administration of plasmid DNA nanoparticles yields successful transfection and expression of a reporter protein in rat brain. *Gene Ther* **21,** 514–521.

Herborn CU, Honold E, Wolf M, Kemper J, Kinner S, Adam G & Barkhausen J (2007). Clinical safety and diagnostic value of the gadolinium chelate gadoterate meglumine (Gd-DOTA). *Invest Radiol* **42,** 58–62.

Ichimura T, Fraser PAA & Cserr HF (1991). Distribution of extracellular tracers in perivascular spaces of the rat brain. *Brain Res* **545,** 103–113.

Iliff JJ, Lee H, Yu M, Feng T, Logan J, Nedergaard M & Benveniste H (2013). Brain-wide pathway for waste clearance captured by contrast-enhanced MRI. *J Clin Invest* **123,** 1299–1309.

Iliff JJ, Wang M, Liao Y, Plogg BA, Peng W, Gundersen GA, Benveniste H, Vates GE, Deane R, Goldman SA, Nagelhus EA & Nedergaard M (2012). A paravascular pathway facilitates CSF flow through the brain parenchyma and the clearance of interstitial solutes, including amyloid β. *Sci Transl Med* **4,** 147ra111.

Kenny GD, Bienemann AS, Tagalakis AD, Pugh JA, Welser K, Campbell F, Tabor AB, Hailes HC, Gill SS, Lythgoe MF, McLeod CW, White EA & Hart SL (2013). Multifunctional receptor-targeted nanocomplexes for the delivery of therapeutic nucleic acids to the Brain. *Biomaterials* **34,** 9190–9200.

Kida S, Pantazis A & Weller RO (1993). CSF drains directly from the subarachnoid space into nasal lymphatics in the rat. Anatomy, histology and immunological significance. *Neuropathol Appl Neurobiol* **19,** 480–488.

Kinney JP, Spacek J, Bartol TM, Bajaj CL, Harris KM & Sejnowski TJ (2013). Extracellular sheets and tunnels modulate glutamate diffusion in hippocampal neuropil. *J Comp Neurol* **521,** 448–464.

Kircher MF, De La Zerda A, Jokerst J V., Zavaleta CL, Kempen PJ, Mittra E, Pitter K, Huang R, Campos C, Habte F, Sinclair R, Brennan CW, Mellinghoff IK, Holland EC & Gambhir SS (2012). A brain tumor molecular imaging strategy using a new triple-modality MRI-photoacoustic-Raman nanoparticle. *Nat Med* **18,** 829–834.

Kircher MF, Mahmood U, King RS, Kircher MF, Mahmood U, King RS, Weissleder R & Josephson L (2003). A Multimodal Nanoparticle for Preoperative Magnetic Resonance Imaging and Intraoperative Optical Brain Tumor Delineation Advances in Brief A Multimodal Nanoparticle for Preoperative Magnetic Resonance Imaging and Intraoperative Optical Brain Tumor Delinea. *Cancer Res* **63,** 8122–8125.

Koh L, Zakharov A & Johnston M (2005). Integration of the subarachnoid space and lymphatics: is it time to embrace a new concept of cerebrospinal fluid absorption? *Cerebrospinal Fluid Res* **2,** 6.

Korogod N, Petersen CCH & Knott GW (2015). Ultrastructural analysis of adult mouse neocortex comparing aldehyde perfusion with cryo fixation. *Elife* **4,** 1–17.

Levin VA, Fenstermacher JD & Patlak CS (1970). Sucrose and inulin space measurements of cerebral cortex in four mammalian species. *Am J Physiol* **219,** 1528–1533.

Li J, Cai P, Shalviri A, Henderson JT, He C, Foltz WD, Prasad P, Brodersen PM, Chen Y, Dacosta R, Rauth AM & Wu XY (2014). A multifunctional polymeric nanotheranostic system delivers doxorubicin and imaging agents across the blood-brain barrier targeting brain metastases of breast cancer. *ACS Nano* **8,** 9925–9940.

MacKay JA, Deen DF & Szoka FC (2005). Distribution in brain of liposomes after convection enhanced delivery; modulation by particle charge, particle diameter, and presence of steric coating. *Brain Res* **1035,** 139–153.

Magerstädt M, Gansow OA, Brechbiel MW, Colcher D, Baltzer L, Knop RH, Girton ME & Naegele M (1986). Gd(DOTA): An alternative to Gd(DTPA) as a T1,2 relaxation agent for NMR imaging or spectroscopy. *Magn Reson Med* **3,** 808–812.

Morse DE & Low FN (1972). The fine structure of the pia mater of the rat. *Am J Anat* **133,** 349–367.

Nance EA, Woodworth GF, Sailor KA, Shih T-Y, Xu Q, Swaminathan G, Xiang D, Eberhart C & Hanes J (2012). A dense poly(ethylene glycol) coating improves penetration of large polymeric nanoparticles within brain tissue. *Sci Transl Med* **4,** 149ra119.

Ni D, Zhang J, Bu W, Xing H, Han F, Xiao Q, Yao Z, Chen F, He Q, Liu J, Zhang S, Fan W, Zhou L, Peng W & Shi J (2014). Dual-targeting upconversion nanoprobes across the blood-brain barrier for magnetic resonance/fluorescence imaging of intracranial glioblastoma. *ACS Nano* **8,** 1231–1242.

Nicholson C & Phillips JM (1981). Ion diffusion modified by tortuosity and volume fraction in the extracellular microenvironment of the rat cerebellum. *J Physiol* **321,** 225–257.

Nicholson C & Tao L (1993). Hindered diffusion of high molecular weight compounds in brain extracellular microenvironment measured with integrative optical imaging. *Biophys J* **65,** 2277–2290.

Nwe K, Bernardo M, Regino CAS, Williams M & Brechbiel MW (2010). Comparison of MRI properties between derivatized DTPA and DOTA gadolinium-dendrimer conjugates. *Bioorg Med Chem* **18,** 5925–5931.

Oda Y & Nakanishi I (1984). Ultrastructure of the mouse leptomeninx. *J Comp Neurol* **225,** 448–457.

Olson ES, Jiang T, Aguilera TA, Nguyen QT, Ellies LG, Scadeng M & Tsien RY (2010). Activatable cell penetrating peptides linked to nanoparticles as dual probes for in vivo fluorescence and MR imaging of proteases. *Proc Natl Acad Sci U S A* **107,** 4311–4316.

Papadopoulos MC, Binder DK & Verkman AS (2005*a*). Enhanced macromolecular diffusion in brain extracellular space in mouse models of vasogenic edema measured by cortical surface photobleaching. *FASEB J* **19,** 425–427.

Papadopoulos MC, Kim JK & Verkman AS (2005*b*). Extracellular space diffusion in central nervous system: anisotropic diffusion measured by elliptical surface photobleaching. *Biophys J* **89,** 3660–3668.

Patlak CS & Fenstermacher JD (1975). Measurements of dog blood-brain transfer constants by ventriculocisternal perfusion. *Am J Physiol* **229,** 877–884.

Pease DC & Schultz RL (1958). Electron microscopy of rat cranial meninges. *Am J Anat* **102,** 301–321.

Pizzo ME, Wolak DJ, Kumar NN, Brunette E, Brunnquell CL, Hannocks M-J, Abbott NJ, Meyerand ME, Sorokin L, Stanimirovic DB & Thorne RG (2018). Intrathecal antibody distribution in the rat brain: surface diffusion, perivascular transport and osmotic enhancement of delivery. *J Physiol* **596,** 445–475.

Rall DP, Oppelt WW & Patlak CS (1962). Extracellular space of brain as determined by diffusion of inulin from the ventricular system. *Life Sci* **1,** 43–48.

Rennels ML, Gregory TF, Blaumanis OR, Fujimoto K & Grady PA (1985). Evidence for a "paravascular" fluid circulation in the mammalian central nervous system, provided by the rapid distribution of tracer protein throughout the brain from the subarachnoid space. *Brain Res* **326,** 47–63.

Rudovský J, Botta M, Hermann P, Hardcastle KI, Lukes I & Aime S (2006). PAMAM dendrimeric conjugates with a Gd-DOTA phosphinate derivative and their adducts with polyaminoacids: the interplay of global motion, internal rotation, and fast water exchange. *Bioconjug Chem* **17,** 975–987.

Rungta RL, Choi HB, Lin PJC, Ko RWY, Ashby D, Nair J, Manoharan M, Cullis PR & MacVicar BA (2013). Lipid nanoparticle delivery of sirna to silence neuronal gene expression in the brain. *Mol Ther - Nucleic Acids* **2,** 1–12.

Saito R, Krauze MT, Bringas JR, Noble C, McKnight TR, Jackson P, Wendland MF, Mamot C, Drummond DC, Kirpotin DB, Hong K, Berger MS, Park JW & Bankiewicz KS (2005). Gadolinium-loaded liposomes allow for real-time magnetic resonance imaging of convection-enhanced delivery in the primate brain. *Exp Neurol* **196,** 381–389.

Salegio EA, Streeter H, Dube N, Hadaczek P, Samaranch L, Kells AP, San Sebastian W, Zhai Y, Bringas J, Xu T, Forsayeth J & Bankiewicz KS (2014). Distribution of nanoparticles throughout the cerebral cortex of rodents and non-human primates: Implications for gene and drug therapy. *Front Neuroanat* **8,** 1–8.

Schindelin J, Arganda-Carreras I, Frise E, Kaynig V, Longair M, Pietzsch T, Preibisch S, Rueden C, Saalfeld S, Schmid B, Tinevez J-Y, White DJ, Hartenstein V, Eliceiri K, Tomancak P & Cardona A (2012). Fiji: an open-source platform for biological-image analysis. *Nat Methods* **9,** 676–682.

Schmid B, Schindelin J, Cardona A, Longair M & Heisenberg M (2010). A high-level 3D visualization API for Java and ImageJ. *BMC Bioinformatics* **11,** 274.

Shao C, Li S, Gu W, Gong N, Zhang J, Chen N, Shi X & Ye L (2015). Multifunctional Gadolinium-Doped Manganese Carbonate Nanoparticles for Targeted MR/Fluorescence Imaging of Tiny Brain Gliomas. *Anal Chem* **87,** 6251–6257.

Shibu ES, Ono K, Sugino S, Nishioka A, Yasuda A, Shigeri Y, Wakida SI, Sawada M & Biju V (2013). Photouncaging nanoparticles for MRI and fluorescence imaging in vitro and in vivo. *ACS Nano* **7,** 9851–9859.

Song HP, Yang JY, Lo SL, Wang Y, Fan WM, Tang XS, Xue JM & Wang S (2010). Gene transfer using self-assembled ternary complexes of cationic magnetic nanoparticles, plasmid DNA and cell-penetrating tat peptide. *Biomaterials* **31,** 769–778.

Sosinsky GE, Crum J, Jones YZ, Lanman J, Smarr B, Terada M, Martone ME, Deerinck TJ, Johnson JE & Ellisman MH (2008). The combination of chemical fixation procedures with high pressure freezing and freeze substitution preserves highly labile tissue ultrastructure for electron tomography applications. *J Struct Biol* **161,** 359–371.

Syková E & Nicholson C (2008). Diffusion in brain extracellular space. *Physiol Rev* **88,** 1277–1340.

Szentistványi I, Patlak CS, Ellis RA & Cserr HF (1984). Drainage of interstitial fluid from different regions of rat brain. *Am J Physiol* **246,** 35–44.

Tao L & Nicholson C (1995). The three-dimensional point spread functions of a microscope objective in image and object space. *J Microsc* **178,** 267–271.

Tao L & Nicholson C (1996). Diffusion of albumins in rat cortical slices and relevance to volume transmission. *Neuroscience* **75,** 839–847.

Thorne RG, Hrabetová S & Nicholson C (2004). Diffusion of epidermal growth factor in rat brain extracellular space measured by integrative optical imaging. *J Neurophysiol* **92,** 3471–3481.

Thorne RG, Lakkaraju A, Rodriguez-Boulan E & Nicholson C (2008). In vivo diffusion of lactoferrin in brain extracellular space is regulated by interactions with heparan sulfate. *Proc Natl Acad Sci USA* **105,** 8416–8421.

Thorne RG & Nicholson C (2006). In vivo diffusion analysis with quantum dots and dextrans predicts the width of brain extracellular space. *Proc Natl Acad Sci USA* **103,** 5567–5572.

Vargová L, Homola A, Zámecník J, Tichý M, Benes V & Syková E (2003). Diffusion parameters of the extracellular space in human gliomas. *Glia* **42,** 77–88.

Wang SJ, Brechbiel M & Wiener EC (2003). Characteristics of a new MRI contrast agent prepared from polypropyleneimine dendrimers, generation 2. *Invest Radiol* **38,** 662–668.

Wolak DJ, Pizzo ME & Thorne RG (2015*a*). Probing the extracellular diffusion of antibodies in brain using in vivo integrative optical imaging and ex vivo fluorescence imaging. *J Control Release* **197,** 78–86.

Wolak DJ, Pizzo ME & Thorne RG (2015*b*). Probing the extracellular diffusion of antibodies in brain using in vivo integrative optical imaging and ex vivo fluorescence imaging. *J Control Release* **197,** 78–86.

Wolak DJ & Thorne RG (2013). Diffusion of macromolecules in the brain: implications for drug delivery. *Mol Pharm* **10,** 1492–1504.

Xiao F, Nicholson C, Hrabe J & Hrabetová S (2008). Diffusion of flexible random-coil dextran polymers measured in anisotropic brain extracellular space by integrative optical imaging. *Biophys J* **95,** 1382–1392.

Yang L, Kress BT, Weber HJ, Thiyagarajan M, Wang B, Deane R, Benveniste H, Iliff JJ & Nedergaard M (2013). Evaluating glymphatic pathway function utilizing clinically relevant intrathecal infusion of CSF tracer. *J Transl Med* **11,** 107.

Zhang ET, Richards HK, Kida S & Weller RO (1992). Directional and compartmentalised drainage of interstitial fluid and cerebrospinal fluid from the rat brain. *Acta Neuropathol* **83,** 233–239.

Zhang Y, Zhang B, Liu F, Luo J & Bai J (2013). In vivo tomographic imaging with fluorescence and MRI using tumor-targeted dual-labeled nanoparticles. *Int J Nanomedicine* **9,** 33–41.

Zhou J, Patel TR, Sirianni RW, Strohbehn G, Zheng M-Q, Duong N, Schafbauer T, Huttner AJ, Huang Y, Carson RE, Zhang Y, Sullivan DJ, Piepmeier JM & Saltzman WM (2013). Highly penetrative, drug-loaded nanocarriers improve treatment of glioblastoma. *Proc Natl Acad Sci U S A* **110,** 11751–11756.

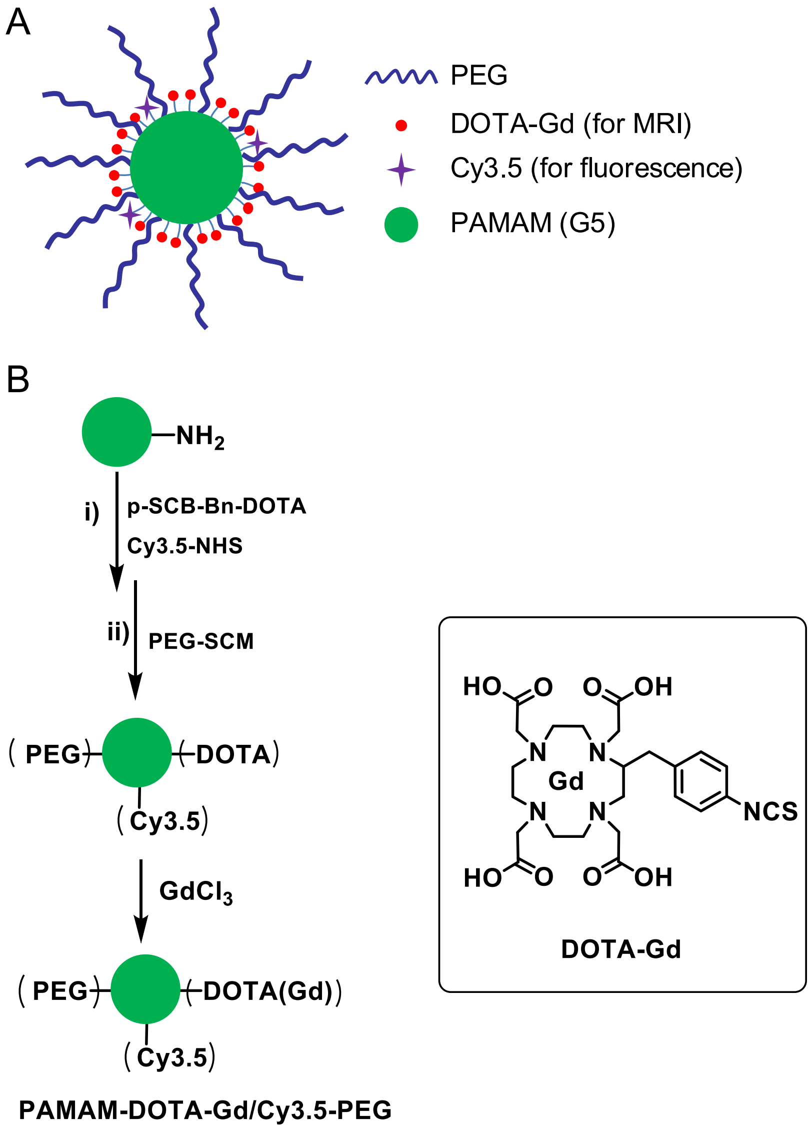

Figure 1. (A) An illustration of nanoparticles formed by PAMAM-Gd-DOTA/Cy3.5/PEG capable of dual fluorescence/MR imaging. (B) The synthetic scheme of PAMAM-Gd-DOTA/Cy3.5/PEG.

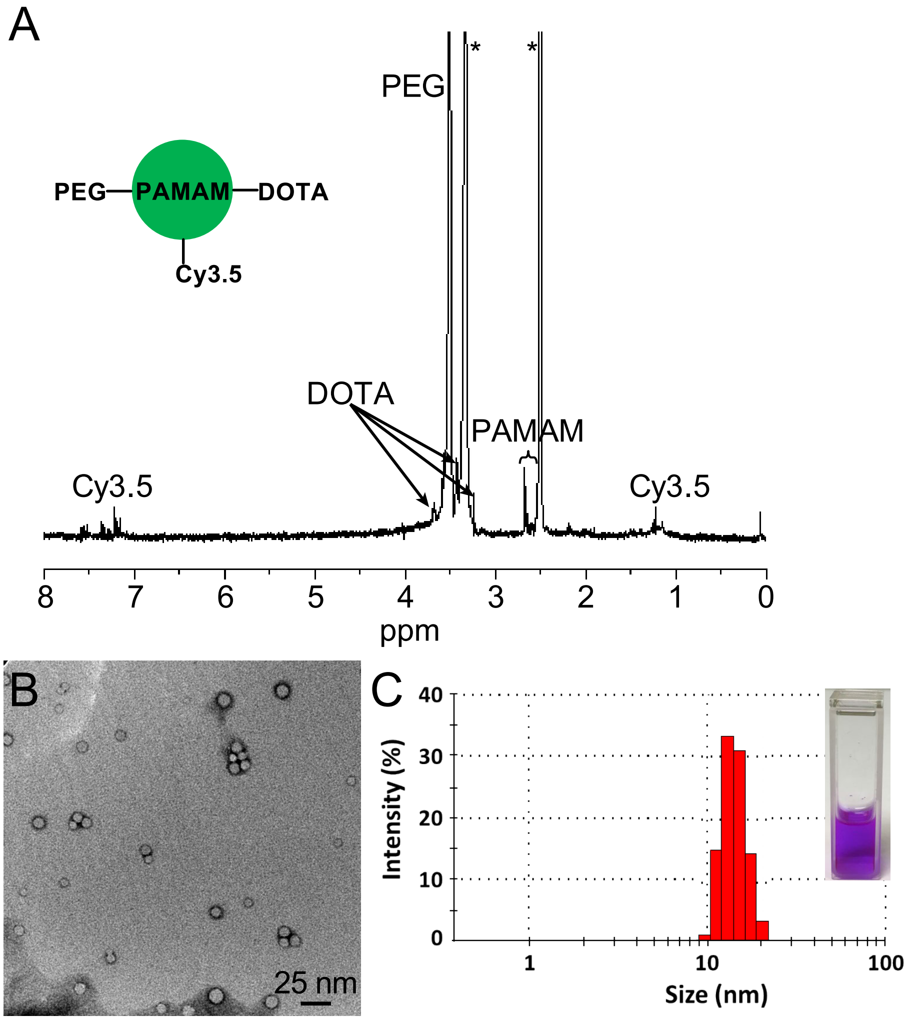

Figure 2. (A) ^{1}H NMR spectrum of PAMAM-DOTA/Cy3.5/PEG. (B) TEM images and (C) DLS analysis of the PAMAM-Gd-DOTA/Cy3.5/PEG nanoparticles demonstrated a relatively consistent spherical size.

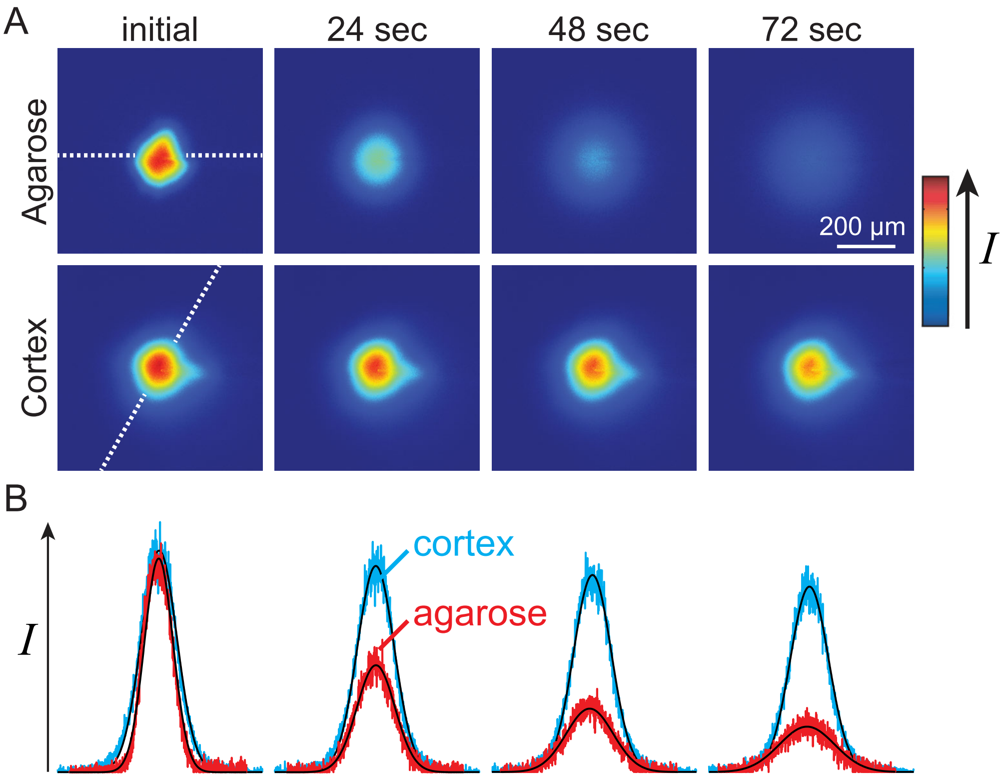

Figure 3. Nanoparticle diffusion is hindered in brain. (A) Representative images after injection of Cy3.5-NP into 0.3% agarose for *D* or into somatosensory cortex for *D**. (B) Fluorescence intensity data taken from A and fit to Fick's Second Law (white dashed lines; 0° in agarose and 60° in cortex). Data shown in color (agarose, red; cortex, green) matches curve fits (black) at each time point. Agarose curves flatten and broaden faster than cortex curves suggesting nanoparticle diffusion is hindered in brain compared to agarose. Values from these measurements return $D = 5.03 \times 10^{-7}$ cm^2/s and $D^* = 0.41 \times 10^{-7}$ cm^2/s.

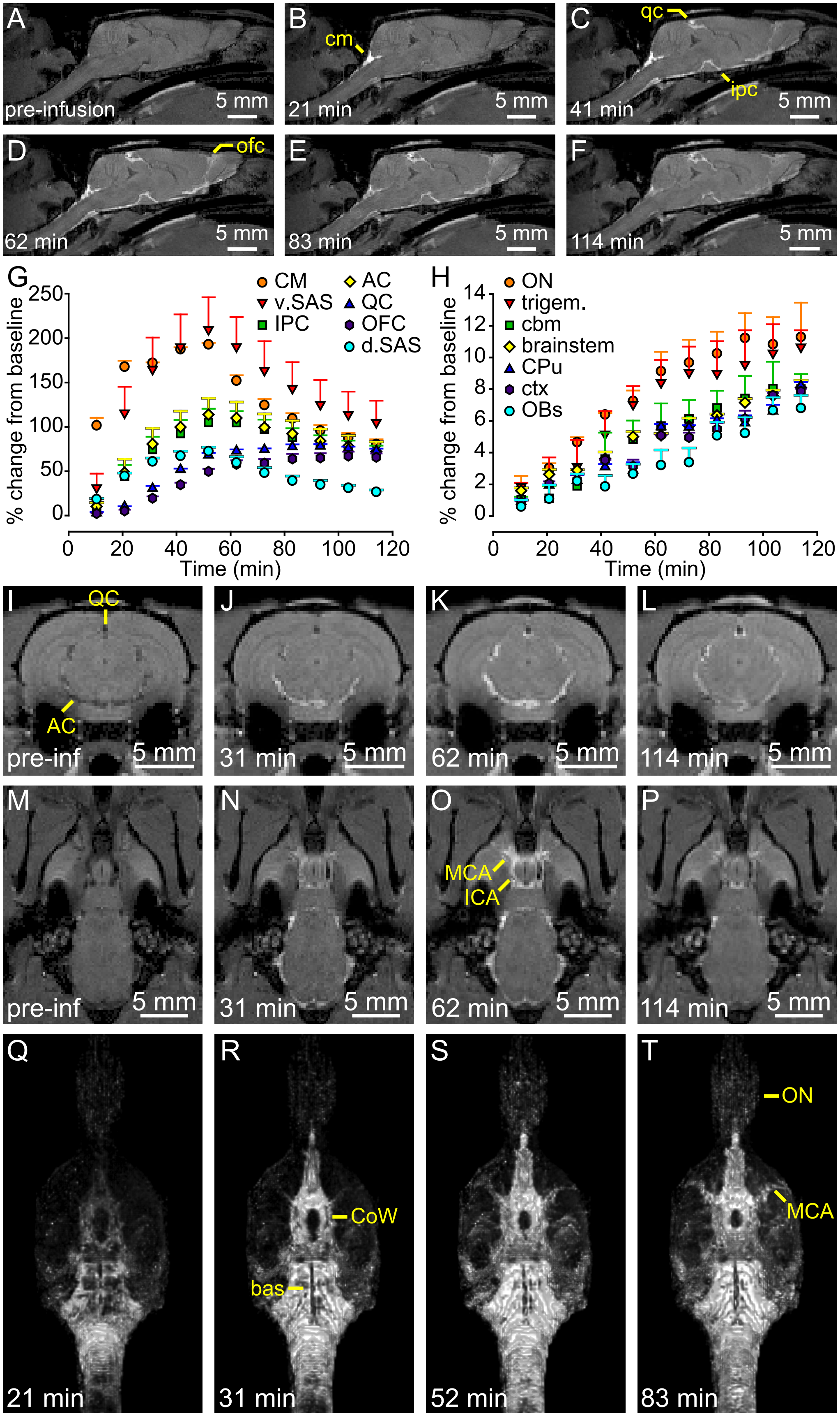
A
pre-infusion
5 mm
B
cm
21 min
5 mm
C
qc
ipc
41 min
5 mm
D
ofc
62 min
5 mm
E
83 min
5 mm
F
114 min
5 mm
G
% change from baseline
250
200
150
100
50
0
0
20
40
60
80
100
120
Time (min)
CM
v.SAS
IPC
AC
QC
OFC
d.SAS
H
% change from baseline
14
12
10
8
6
4
2
0
0
20
40
60
80
100
120
Time (min)
ON
trigem.
cbm
brainstem
CPu
ctx
OBs
I
QC
AC
pre-inf
5 mm
J
31 min
5 mm
K
62 min
5 mm
L
114 min
5 mm
M
pre-inf
5 mm
N
31 min
5 mm
O
MCA
ICA
62 min
5 mm
P
114 min
5 mm
Q
21 min
R
CoW
bas
31 min
S
52 min
T
ON
MCA
83 min

Figure 4. *In vivo* T1-weighted MRI of intracisternally-infused nanoparticles. (A-F) Representative mid-sagittal (~0.5 mm lateral to the midline) raw MRI slices (*N*=3) pre- intracisternal infusion (A), during the 50 minute infusion of dual-labeled nanoparticles (B,C) and for over one hour post-infusion (D-F). The percent change in signal intensity from the pre-infusion baseline was quantified for several CSF (G) and parenchymal (H) regions of interest from raw MRI sagittal or coronal slices (delineated according to (Pizzo et al., 2018)). Raw coronal MRI slices (I-L) and horizontal slices (M-P) also show cisternal and perivascular transport of the nanoparticles. (Q-T) Volume reconstruction of nanoparticle contrast enhancement with the pre-infusion baseline data subtracted over time; the ventral view reveals nanoparticle signal associated with the basilar artery, circle of Willis, and laterally branching middle cerebral arteries as well as drainage along the olfactory nerves. CM: cisterna magna; v. SAS: ventral spinal subarachnoid space; IPC: interpeduncular cistern; AC: ambient cistern; QC: quadrigeminal cistern; OFC: olfactofrontal cistern; d. SAS: dorsal spinal subarachnoid space; ON: olfactory nerves; trigem: trigeminal nerves; cbm: cerebellum; CPu: caudoputamen; ctx: cortex; OBs: olfactory bulbs.

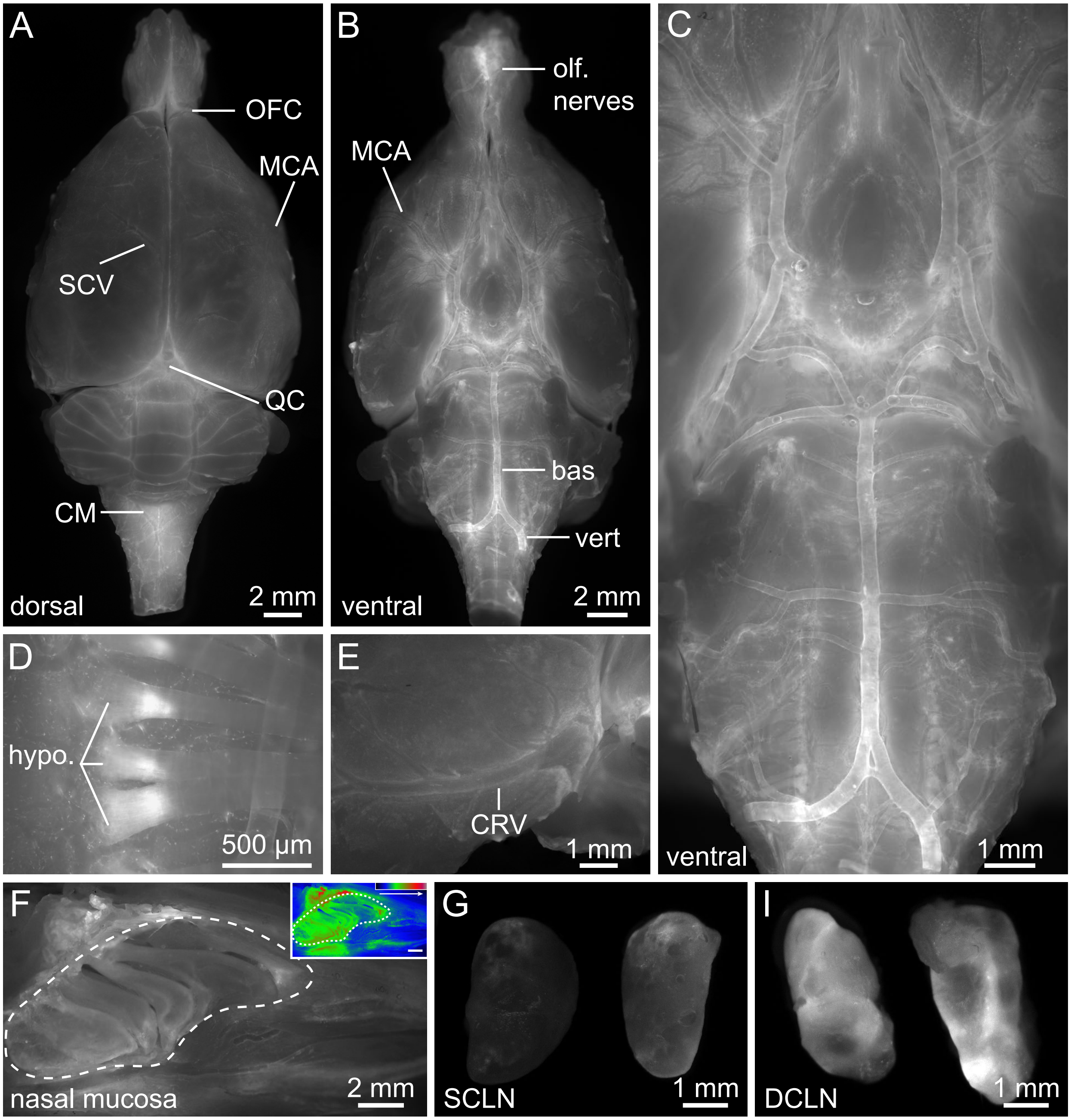

Figure 5. *Ex vivo* whole brain surface distribution of nanoparticles and olfactory drainage. Following intrathecal infusion of nanoparticles and MR imaging, two animals were perfused and fixed 100 minutes post-infusion for correlative *ex vivo* fluorescence of the dorsal (A) and ventral (B) whole brain. Perivascular signal was associated with major surface and some veins (C), correlating with Figure 4 Q-T, nerves (e.g., hypoglassal nerves; D), and veins (e.g., the caudal rhinal vein; E). A major drainage pathway for CSF-infused nanoparticles appeared to be via the

olfactory pathway, resulting in fluorescent signal predominantly associated with the olfactory mucosa of the nasal passages, and downstream signal in the superficial cervical lymph nodes (SCLN; G) and deep cervical lymph nodes (DCLN; I). OFC: olfactofrontal cistern; MCA: middle cerebral artery; SCV: superior cerebral veins; QC: quadrigeminal cistern; CM: cisterna magna; olf. nerves: olfactory nerves; bas: basilar artery; vert: vertebral arteries; hypo: hypoglossal nerves; CRV: caudal rhinal vein.

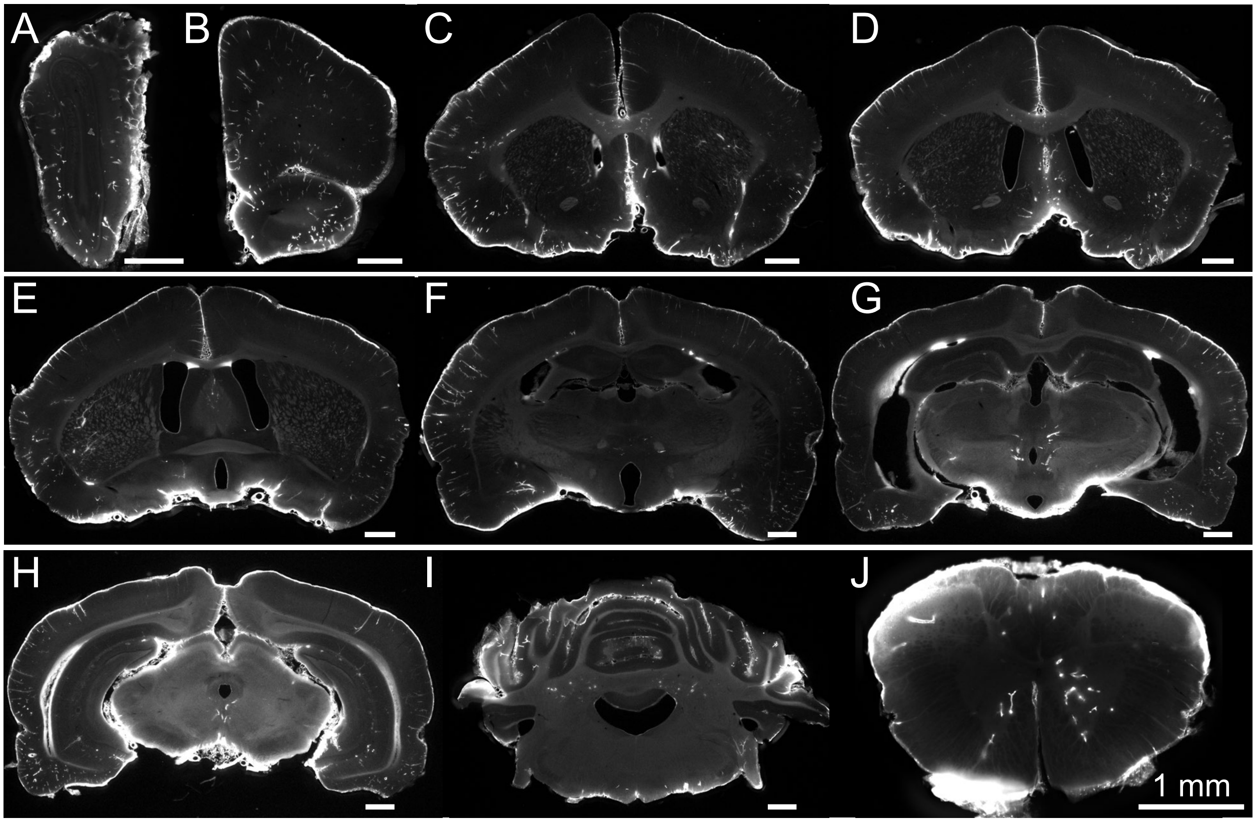

Figure 6. *Ex vivo* fluorescence imaging of coronal brain sections following intrathecal infusion and in vivo MR imaging. (A-J) Preliminary results showed fluorescent nanoparticle signal was evident in the brain, showing strong signal associated with the pial brain surface, periventricular white matter signal associated with the lateral ventricles, and scattered signal along perivascular spaces from the olfactory bulbs to the spinal cord (N=2).

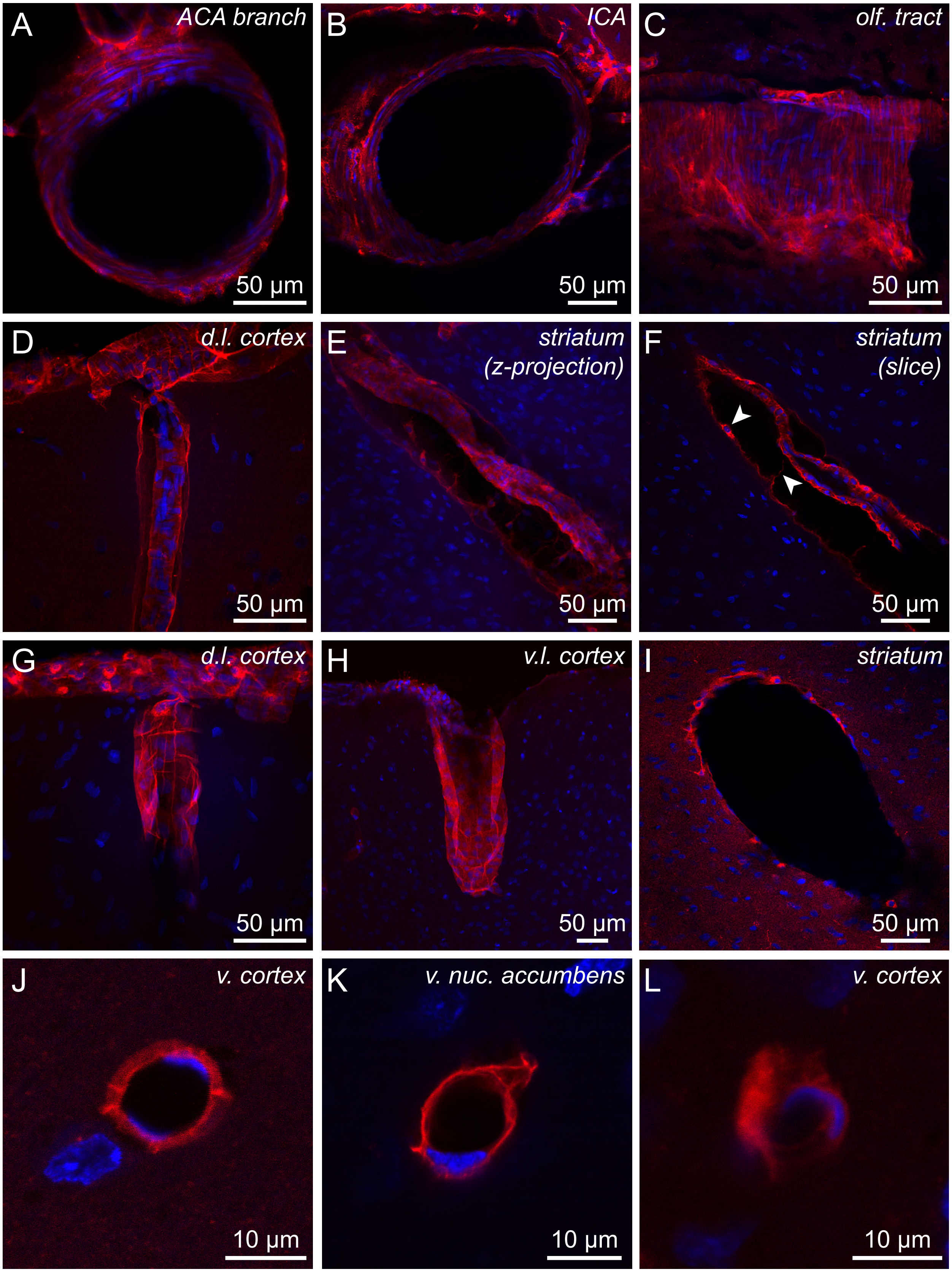
A
ACA branch
50 µm
B
ICA
50 µm
C
olf. tract
50 µm
D
d.l. cortex
50 µm
E
striatum
(z-projection)
50 µm
F
striatum
(slice)
50 µm
G
d.l. cortex
50 µm
H
v.l. cortex
50 µm
I
striatum
50 µm
J
v. cortex
10 µm
K
v. nuc. accumbens
10 µm
L
v. cortex
10 µm

Figure 7. Confocal microscopy of perivascular nanoparticles along the entire vascular tree. Representative coronal brain sections were stained with DAPI (to label all cell nuclei; blue) and confocal imaging performed to visualize perivascular nanoparticle signal (red; *N*=2). Nanoparticles were present around vessels of all caliber (based on size and morphology), including leptomeningeal arteries (A-C), putative parenchymal arterioles (D-F), putative parenchymal venules (G-I), and microvessels (J-L) less than 10 nm in diameter. ACA: anterior cerebral artery; ICA: central internal carotid artery; d.l.: dorsolateral; v.l.: ventrolateral.

Epilogue

Michelle Pizzo

These studies have provided critical new information regarding CSF-to-brain transport of large macromolecules, and likely shed light on the transport processes expected to govern therapeutic distribution in the brain. Key findings of this work suggest that CSF-to-brain macromolecule transport: i) is limited to superficial diffusion at brain-CSF interfaces, ii) is rapid and relatively size-independent along perivascular spaces in the brain, iii) exhibits size-dependent access to cerebral perivascular spaces, ii) can be enhanced by osmotic strategies to improve perivascular access for large substances, iv) involves receptor-mediated entry of species-matched IgG into the perivascular spaces, and v) is significantly reduced within the brain in disease, in this case a model of primary brain cancer. We also demonstrated perivascular distribution of endogenous IgG in the brain, which, in combination with the intrathecal data, suggests these pathways are available to therapeutic antibodies in the CSF. These experiments have revealed several delivery factors that may determine the success or failure of intra-CSF clinical trials for biologics—successful delivery may rely on smaller macromolecules that efficiently access perivascular spaces and diffuse into the parenchyma or species-specific binding that improves perivascular access and distribution, but failure may be attributed to poor delivery of large macromolecules which are unable to access perivascular spaces or significant disease pathology that disrupts CNS transport. We hypothesize perivascular access is key to therapeutic delivery because this rapid transport is likely scalable to large human brains, as demonstrated in larger mammals (Rennels *et al.*, 1985; Jolly *et al.*, 2011; Samaranch *et al.*, 2013). Indeed, rapid perivascular transport along the vasculature could deliver drugs to the entire brain if: i) the perivascular spaces around every vessel in the brain are accessed to the level of the capillary and ii) the therapeutic substance is capable of diffusing out of the perivascular space into the neuropil (as each neuron in the brain is only ~10-20 μm from a capillary

(Wolak & Thorne, 2013)). Our data supports the possibility that pericapillary transport is possible for macromolecules ~4.5-13.5 nm in diameter.

The experiments of the present work also revealed additional questions which are of interest to pursue in future studies, which will be the focus of the remainder of the Epilogue. Focusing first on Chapter 2, there are a clear number of manipulations to the CSF-infusion paradigm that would provide useful information, including site of administration, patient position, and volume/rate of administration. A few studies have demonstrated how the site of administration (e.g., intracerebroventricular (ICV) versus lumbar intrathecal) in rodents may influence distribution, with the most apparent difference being kinetics of distribution (e.g., time it takes administered substance to reach the cranial CSF, e.g., (Yang *et al.*, 2013)). Trials in humans appear to use both routes frequently. For example, the enzyme cerliponase alfa (for treatment of neuronal ceroid lipofuscinosis type 2, a genetic whole-brain disorder) is infused into the ventricles (ICV), which hopefully targets as much of the brain as possible (BioMarin Pharmaceuticals, 2017). The antisense oligonucleotide nusinersen (for treatment of spinal muscular atrophy) is administered intrathecally at the level of the lumbar spinal cord and the primary targets are the spinal cord motor neurons (Biogen, 2016). However, the clinical trial using an antisense oligonucleotide for the potential treatment of Huntington's disease (a whole-brain disease) is also being delivered by lumbar intrathecal injection (and is produced by the same company as nusinersen). It is unclear whether the route of administration is governed by company preference (as it may coincidentally appear) or by experimental evidence of delivery. In addition to the site of administration, the patient position during and after the administration may cause differences in drug distribution within the CNS (as demonstrated in rats (Lee *et al.*, 2015)) but it is unclear if patient position is a controlled variable in the clinical trials. Lastly, optimal volumes and rates of delivery into the CSF in humans is understudied, though it has been explored in rodents (Xu *et al.*, 2011). Unfortunately, most clinical trial details (available at clinicaltrials.gov) regarding route, patient position, and volume/rate of administration are poorly described or not mentioned at all; indeed, many trials state 'intrathecal' delivery is used (indicating administration into the thecal sac, the dura enveloping the spinal cord and cauda equina), but further investigation (e.g., discovery of a published manuscript or abstract relating to trial) reveals ICV delivery via an Ommaya reservoir is the actual route. One must hope that these factors are indeed controlled variables. In any case, we need to determine the parameters of administration that will provide the best possible delivery, consistently, while minimizing risks and possible complications (e.g, potential for infection with indwelling catheters or invasiveness of procedures).

Additional studies of molecular size and binding capacity are also of great interest. The probes used in our studies ranged from 4.5 nm to 13.5 nm and showed strikingly different brain distribution, particularly in terms of access to the perivascular spaces. Additional probes encompassing a wider breadth of molecular sizes (i.e., 1 nm to 20 nm to µm in size) and geometries (e.g., rod-shaped) representing the majority biologics would help further characterize perivascular accessibility. Additionally, our data demonstrated that full-length IgG (and nanoparticles, Chapter 6) did not easily exit the perivascular spaces and diffuse across the astrocyte basement membrane into the surrounding neuropil, suggesting a size-dependent barrier. Knowledge of the size 'cutoff' for penetration through this basement membrane (and other basement membranes in the CNS) is important. In the present work all tracers were non-targeted and remained primarily extracellular, so further investigation of, for example, targeted monoclonal antibodies or enzymes which require cellular internalization are of great interest. Indeed, ICV-infusion of brain-derived neurotrophic factor demonstrated significant binding to endogenous receptors that greatly impeded penetration into the brain, but could be blocked to allow for improved brain distribution (Yan *et al.*, 1994; Croll *et al.*, 1998).

We demonstrated that pores or 'stomata' are present in the leptomeningeal cells around blood vessels on the surface of the brain, separating the CSF from the perivascular space. We hypothesize that these pores and their associated connective tissue may act to sieve molecules, allowing smaller substances in the CSF preferred entry into the perivascular space. Future examination of human tissue for these pores would be extremely valuable. We also showed that intrathecal co-infusion of mannitol potentially manipulates these cells (and/or their stomata) to increase access to the perivascular spaces for the larger IgG. Additional studies which would provide valuable information include: determining the mechanism of enhancement, investigating the optimal timing of administration, and probing the size range of molecules enhanced by mannitol infusion. As to the first point, we have performed preliminary scanning electron microscopy studies on two rats which were intrathecally-infused with hyperosmolar mannitol and found no obvious structural differences, but rigorous qualitative or quantitative studies of stomata size, number, density, or morphology have not been performed. It is also possible that intrathecal mannitol causes increased vesicular transport across leptomeningeal cells toward the perivascular spaces, as increased transcytosis has been demonstrated for the BBB with hyperosmolar arabinose (Vorbrodt *et al.*, 1994). As to the second point, we demonstrated that *co-administration* of hyperosmolar mannitol over the 50-minute infusion was capable increasing tracer delivery. However, knowledge of the optimal timing of mannitol administration (e.g., pre- or co-infusion) and the length of effect (expected to be < 1 hour based on the effect of mannitol on the BBB (Rapoport *et al.*, 1980)) would be exceedingly helpful. Lastly, it is of interest to determine the size-range of molecules that benefit from intrathecal mannitol infusion. Our preliminary experiments showed that intrathecally-infused molecules which entered the perivascular spaces relatively well (single-domain antibody and rat IgG) did not obviously benefit from intrathecal mannitol co-infusion, while the larger non-binding IgG experienced improved delivery. Substances the size of the nanoparticles used here (13.5 nm, Chapter 6) or greater (e.g., the size of viral vectors) would be primary candidates for these studies.

Fluids and tracers appear to be cleared from the CNS via several routes. A very interesting study would be a quantitative analysis of tracer drainage along each route, e.g., the percentage of the administered dose reaching the nasal mucosa, cervical lymph nodes, arachnoid villi/granulations, dural lymphatics, or other cranial/spinal nerve associated routes. These, however, would be incredibly difficult experiments to perform due to the interconnectedness of these routes (which are also likely to have very different kinetics) and their widespread, pervasive, and complex anatomy (which poses a number of questions, e.g., How does one quantify clearance along minuscule dural lymphatic vessels around nerves? or How does one unambiguously sample the nasal mucosa?). A few studies have attempted this type of investigation in rats (Boulton *et al.*, 1999) and sheep (Boulton *et al.*, 1996) but only focused on apparently major clearance routes, likely due to the stated difficulties distinguishing other routes (arachnoid/blood drainage versus cervical/spinal lymph drainage).

Chapter 3 provided critical discussion regarding the recently proposed ‘glymphatic’ hypothesis (Iliff *et al.*, 2012; Nedergaard, 2013; Jessen *et al.*, 2015). A critical component of the hypothesis is the involvement of the aquaporin-4 water channel localized to astrocyte end feet which wall-off the vasculature from the brain parenchyma. A recent study has failed to demonstrate differences in CSF-to-brain transport of intrathecal tracers in aquaporin-4 mice and rats (Smith *et al.*, 2017) thus additional replication studies will need to be performed to determine the role of aquaporin-4 in CNS transport. It is crucial that more experiments are conducted to understand changes in CSF physiology and flow dynamics in aquaporin-4 deficient animals and whether any compensatory changes in the brain/CSF occur. One aspect of the 'glymphatic' hypothesis that we feel that our data can address is the suggested 'bulk flow' of fluid through the neuropil. We developed a method to characterize diffusion gradients at the brain-CSF interface (Wolak *et al.*, 2015; Pizzo *et al.*, 2018) based on an older method using radiolabeled compounds (Patlak & Fenstermacher, 1975). An excellent fit between the data and the modeled diffusion coefficients suggests that the transport occurring at the brain surface is indeed diffusion. In theory, the same technique could be applied to the diffuse gradients around perivascular spaces observed for the single-domain antibody. However, the assumptions of the diffusion models we used may not truly be valid for this case, thus the infusion paradigm and model would need to be developed further. This could shed light on whether the transport of molecules out of the perivascular space and into the brain parenchyma are indeed diffusive in nature, or whether the bulk flow suggested by the 'glymphatic' hypothesis is possible.

In Chapter 4 we first revealed that species-matched rat IgG possessed an enhanced ability to enter the perivascular spaces from the CSF compared to a species-matched IgG and demonstrated that perivascular access was significantly reduced when an excess of unlabeled rat IgG was co-infused. This suggested that a Fc receptor-mediated mechanism shuttled IgG into the perivascular spaces, probably for the physiological purpose of surveillance for antigens. We speculate that FcRn is involved in transcytosis of IgG due to its transcytotic role elsewhere in the body (e.g., (Hemmings & Brambell, 1961; Brambell, 1969; Simister *et al.*, 1996)), but each step should be unambiguously demonstrated. Confocal imaging could demonstrate if colocalization of IgG and FcRn occur and electron microscopy could confirm if vesicular transport occurs; immuno electron microscopy could also be a useful tool for these studies. Alternatively, antibodies that specifically bind to only FcRn or only Fcγ receptor (e.g., (Adolfsson *et al.*, 2012)) could help probe which receptors are involved. Also, our study utilized a polyclonal mixture of IgGs, but monoclonal antibodies are used therapeutically. There are a number of IgG-specific factors that have been demonstrated to impact IgG interactions with Fc receptors, and thus may result in altered CSF-to-brain distribution, including IgG isotype, glycosylation, and receptor affinity (Jefferis, 2012). It would be of great interest to study each of these factors. In particular, we have speculated a role for FcRn in the transcytosis of IgG from the CSF into the perivascular spaces, thus it would be intriguing to study the delivery of (engineered) antibodies with various affinities for FcRn.

Our first experiments in a disease model were also described in Chapter 4. Infusions of rat IgG (which showed exceptional perivascular access in normal rats) into rats bearing human glioma tumors showed a widespread *reduction* in perivascular signal and a lack of IgG signal within the tumor borders. Several factors which could contribute to these transport alterations include tumor pressure, tumor type/invasiveness, and structural changes within the tumor or adjacent brain. It has been demonstrated that the interstitial pressure of the tumor can greatly exceed that of the surrounding brain due in part to leaky tumor vasculature allowing fluid to flow across the blood-tumor barrier and a lack of lymphatic drainage (Baxter & Jain, 1989; Ferretti *et al.*, 2009;

Stylianopoulos *et al.*, 2013). This might suggest that intrathecal IgG coming from the CSF would be pushed away from the tumor and intrathecal mannitol may encourage this tumor → CSF gradient. An interesting experiment would be to administer systemic mannitol (or another hyperosmolar solution) to reverse this gradient, perhaps encouraging CSF → tumor transport of fluid. Indeed, it has been demonstrated that tumor interstitial pressure appears to be reduced in patients receiving mannitol, dexamethasone, and furosemide to decrease brain edema (Boucher *et al.*, 1997). The cell line (U87) and method of cell culture used in our study created isolated large tumor masses in the brain of rodents; this is not representative of many glioblastomas in humans which display irregular borders and tumor cells infiltrating along the vasculature. Future studies could investigate the impact of cell lines/patient-derived tumor cells grown in spheroid culture or genetically engineered animal models with *de novo* brain tumor growth on the brain and tumor distribution of intrathecally-administered macromolecules. Additionally, the structural changes to the meninges and perivascular space associated with brain tumors and the expression of Fc receptors in brain tumors/adjacent normal brain are not well-studied but could severely impact perivascular access and transport and are of significance to investigate.

Chapter 5 revealed that endogenous serum proteins (IgG and albumin) are readily detected in the brain tissue of normal animals and we discussed possible routes for serum proteins to enter the brain (e.g., across the choroid plexus). Some of the results are preliminary and require further replication and co-labeling with cell markers for other cell types in the brain, namely astrocytes and microglia/macrophages. An in-depth investigation of the proteins and receptors that bind to IgG and albumin in the brain (e.g., FcRn) is certainly warranted, thus we have been investigating this in our laboratory. However, it would be of interest to conduct these studies in numerous rodent strains (as differences have been reported, e.g., in (Hazama *et al.*, 2005)) and most importantly, in human brain tissue as well. It would be exciting to demonstrate whether similar perivascular localization of IgG occurs in the human brain, which may also suggest a mechanism for human IgG to enter the perivascular space and thus provide greater hope for widespread distribution of intrathecal IgG in humans.

Chapter 6 demonstrated the distribution of the largest molecule we studied, a 13.5 nm nanoparticle labeled for MRI and fluorescence detection. This showed the phenomenal capacity to correlate across techniques, highlighting the importance of combined low- and high-resolution techniques for distribution studies. Interestingly, there were a fair number of perivascular profiles in these animals with signal often reaching far along the length of the vessel. This more 'consistent' signal along the perivascular spaces may be due to the significantly longer distribution time for the nanoparticles (150 minutes) versus our other tracers (80 minutes). Thus, it would be quite interesting to study the distribution of our protein tracers (single-domain antibody, goat IgG, and rat IgG) at different time points following intrathecal infusion.

The present experiments are likely representative of how many proteins, depending on their size and binding characteristics, distribute between the CSF and brain. Thus, drugs that enter the CSF from any route of administration would be expected use these same mechanisms of distribution, i.e., systemically administered antibodies may reach the CSF and distribute along perivascular spaces (though at significantly lower concentrations than in the blood, see Chapter 5). The fact that many systemic antibody trials for Alzheimer's disease have failed to reach their clinical end points (e.g., (Moreth *et al.*, 2013)) may thus suggest that: i) insufficient quantities of the antibody are reaching the brain, ii) distribution of the antibodies from CSF-to-brain is poor due to disease pathology, iii) the antibodies are not efficacious, or iv) the antibody target is not sufficiently contributing to disease/its removal does not alleviate disease. Insufficient delivery of the antibody to the brain seems highly likely, considering preclinical studies have demonstrated efficacy using intraparenchymal injection of antibodies in rodents (e.g., (Wilcock *et al.*, 2003; Sudduth *et al.*, 2013)). A very exciting possibility for biotherapeutic drug delivery to the brain via the CSF is gene therapy. While the size of the vectors used to deliver a transgene are large (Davidson & Breakefield, 2003) and would not be expected to distribute well within the parenchyma, a fascinating strategy could be to target vectors to large CSF-contacting surfaces of the brain (e.g., meninges, choroid plexus epithelial cells, or ependymal cells), where a transgene could be expressed and a protein (or modified/reduced size product) secreted (e.g., (Yamazaki *et al.*, 2014; Hironaka *et al.*, 2015)). Thus our data could also describe how proteins secreted into the CSF are expected to distribute throughout the brain, and highlights potential barriers to delivery.

Altogether this collection of studies has provided some clarity regarding the pathways by which the CSF and the brain communicate, illuminating how therapeutic substances administered into the CSF may also access the brain tissue. It is apparent that much work is left to be done in this exciting area with the hope that each new piece of information can aid in the interpretation of clinical trial results and provide guidance for how to improve future studies.

References

Adolfsson O et al. (2012). An effector-reduced anti-β-amyloid (Aβ) antibody with unique aβ binding properties promotes neuroprotection and glial engulfment of Aβ. *J Neurosci* **32,** 9677–9689.

Baxter LT & Jain RK (1989). Transport of fluid and macromolecules in tumors. I. Role of interstitial pressure and convection. *Microvasc Res* **37,** 77–104.

Biogen (2016). SPINRAZA (nusinersen) injection, for intrathecal use. *Highlights Prescr Inf.*

BioMarin Pharmaceuticals (2017). BRINEURA (cerliponase alfa) injection, for intraventricular use.

Boucher Y, Salehil H, Witwerl B, Harsh G & Jain R (1997). Interstitial fluid pressure in intracranial tumours in patients and in rodents. *Br Joumal Cancer* **75,** 829–836.

Boulton M, Flessner M, Armstrong D, Mohamed R, Hay J & Johnston M (1999). Contribution of extracranial lymphatics and arachnoid villi to the clearance of a CSF tracer in the rat. *Am J Physiol* **276,** R818-23.

Boulton M, Young A, Hay J, Armstrong D, Flessner M, Schwartz M & Johnston M (1996). Drainage of CSF through lymphatic pathways and arachnoid villi in sheep: measurement of 125I-albumin clearance. *Neuropathol Appl Neurobiol* **22,** 325–333.

Brambell FW (1969). The transmission of immune globulins from the mother to the foetal and newborn young. *Proc Nutr Soc* **28,** 35–41.

Croll SD, Chesnutt CR, Rudge JS, Acheson A, Ryan TE, Siuciak JA, DiStefano PS, Wiegand SJ & Lindsay RM (1998). Co-infusion with a TrkB-Fc receptor body carrier enhances BDNF distribution in the adult rat brain. *Exp Neurol* **152,** 20–33.

Davidson BL & Breakefield XO (2003). Viral vectors for gene delivery to the nervous system. *Nat Rev Neurosci* **4,** 353–364.

Ferretti S, Allegrini PR, Becquet MM & McSheehy PM (2009). Tumor interstitial fluid pressure as an early-response marker for anticancer therapeutics. *Neoplasia* **11,** 874–881.

Hazama GI, Yasuhara O, Morita H, Aimi Y, Tooyama I & Kimura H (2005). Mouse brain IgG-like immunoreactivity: Strain-specific occurrence in microglia and biochemical identification of IgG. *J Comp Neurol* **492,** 234–249.

Hemmings WA & Brambell FW (1961). Protein transfer across the foetal membranes. *Br Med Bull* **17,** 96–101.

Hironaka K, Yamazaki Y, Hirai Y, Yamamoto M, Miyake N, Miyake K, Okada T, Morita A & Shimada T (2015). Enzyme replacement in the CSF to treat metachromatic leukodystrophy in mouse model using single intracerebroventricular injection of self-complementary AAV1 vector. *Sci Rep* **5,** 13104.

Iliff JJ, Wang M, Liao Y, Plogg BA, Peng W, Gundersen GA, Benveniste H, Vates GE, Deane R, Goldman SA, Nagelhus EA & Nedergaard M (2012). A paravascular pathway facilitates CSF flow through the brain parenchyma and the clearance of interstitial solutes, including amyloid β. *Sci Transl Med* **4,** 147ra111.

Jefferis R (2012). Isotype and glycoform selection for antibody therapeutics. *Arch Biochem Biophys* **526,** 159–166.

Jessen NA, Munk ASF, Lundgaard I & Nedergaard M (2015). The Glymphatic System: A Beginner's Guide. *Neurochem Res* **40,** 2583–2599.

Jolly RD, Marshall NR, Perrott MR, Dittmer KE, Hemsley KM & Beard H (2011). Intracisternal enzyme replacement therapy in lysosomal storage diseases: Routes of absorption into brain. *Neuropathol Appl Neurobiol* **37,** 414–422.

Lee H, Xie L, Yu M, Kang H, Feng T, Deane R, Logan J, Nedergaard M & Benveniste H (2015). The Effect of Body Posture on Brain Glymphatic Transport. *J Neurosci* **35,** 11034–11044.

Moreth J, Mavoungou C & Schindowski K (2013). Passive anti-amyloid immunotherapy in Alzheimer's disease: What are the most promising targets? *Immun Ageing* **10,** 1.

Nedergaard M (2013). Garbage truck of the brain. *Science (80-)* **340,** 1529–1530.

Patlak CS & Fenstermacher JD (1975). Measurements of dog blood-brain transfer constants by ventriculocisternal perfusion. *Am J Physiol* **229,** 877–884.

Pizzo ME, Wolak DJ, Kumar NN, Brunette E, Brunnquell CL, Hannocks M-J, Abbott NJ, Meyerand ME, Sorokin L, Stanimirovic DB & Thorne RG (2018). Intrathecal antibody distribution in the rat brain: surface diffusion, perivascular transport and osmotic enhancement of delivery. *J Physiol* **596,** 445–475.

Rapoport SI, Fredericks WR, Ohno K & Pettigrew KD (1980). Quantitative aspects of reversible osmotic opening of the blood-brain barrier. *Am J Physiol* **238,** R421-31.

Rennels ML, Gregory TF, Blaumanis OR, Fujimoto K & Grady PA (1985). Evidence for a “paravascular” fluid circulation in the mammalian central nervous system, provided by the rapid distribution of tracer protein throughout the brain from the subarachnoid space. *Brain Res* **326,** 47–63.

Samaranch L, Salegio EA, San Sebastian W, Kells AP, Bringas JR, Forsayeth J & Bankiewicz KS (2013). Strong Cortical and Spinal Cord Transduction After AAV7 and AAV9 Delivery into the Cerebrospinal Fluid of Nonhuman Primates. *Hum Gene Ther* **24,** 526–532.

Simister NE, Story CM, Chen HL & Hunt JS (1996). An IgG-transporting Fc receptor expressed in the syncytiotrophoblast of human placenta. *Eur J Immunol* **26,** 1527–1531.

Smith AJ, Yao X, Dix JA, Jin B & Verkman AS (2017). Test of the “glymphatic” hypothesis demonstrates diffusive and aquaporin-4-independent solute transport in rodent brain parenchyma. *Elife*; DOI: 10.7554/eLife.27679.

Stylianopoulos T, Martin JD, Snuderl M, Mpekris F, Jain SR & Jain RK (2013). Coevolution of solid stress and interstitial fluid pressure in tumors during progression: implications for vascular collapse. *Cancer Res* **73,** 3833–3841.

Sudduth TL, Greenstein A & Wilcock DM (2013). Intracranial injection of Gammagard, a human IVIg, modulates the inflammatory response of the brain and lowers Aβ in APP/PS1 mice along a different time course than anti-Aβ antibodies. *J Neurosci* **33,** 9684–9692.

Vorbrodt AW, Dobrogowska DH, Tarnawski M & Lossinsky AS (1994). A quantitative immunocytochemical study of the osmotic opening of the blood-brain barrier to endogenous albumin. *J Neurocytol* **23,** 792–800.

Wilcock DM, DiCarlo G, Henderson D, Jackson J, Clarke K, Ugen KE, Gordon MN & Morgan D (2003). Intracranially administered anti-Abeta antibodies reduce beta-amyloid deposition by mechanisms both independent of and associated with microglial activation. *J Neurosci* **23,** 3745–3751.

Wolak DJ, Pizzo ME & Thorne RG (2015). Probing the extracellular diffusion of antibodies in brain using in vivo integrative optical imaging and ex vivo fluorescence imaging. *J Control Release* **197,** 78–86.

Wolak DJ & Thorne RG (2013). Diffusion of macromolecules in the brain: implications for drug delivery. *Mol Pharm* **10,** 1492–1504.

Xu S, Wang L, El-Banna M, Sohar I, Sleat DE & Lobel P (2011). Large-volume Intrathecal Enzyme Delivery Increases Survival of a Mouse Model of Late Infantile Neuronal Ceroid Lipofuscinosis. *Mol Ther* **19,** 1842–1848.

Yamazaki Y, Hirai Y, Miyake K & Shimada T (2014). Targeted gene transfer into ependymal cells through intraventricular injection of AAV1 vector and long-term enzyme replacement via the CSF. *Sci Rep* **4,** 5506.

Yan Q, Matheson C, Sun J, Radeke MJ, Feinstein SC & Miller JA (1994). Distribution of intracerebral ventricularly administered neurotrophins in rat brain and its correlation with trk receptor expression. *Exp Neurol* **127,** 23–36.

Yang L, Kress BT, Weber HJ, Thiyagarajan M, Wang B, Deane R, Benveniste H, Iliff JJ & Nedergaard M (2013). Evaluating glymphatic pathway function utilizing clinically relevant intrathecal infusion of CSF tracer. *J Transl Med* **11,** 107.